Quantifying the interference achieved by cementless tibial trays and its effect on primary stability

By

Lauren S Wearne
BEng (Biomed/Hons I) / BS (Physics)

Principal Supervisor: Associate Professor Egon Perilli
Associate Supervisor: Professor Mark Taylor

Thesis
Submitted to Flinders University
for the degree of

Doctor of Philosophy
Medical Device Research Institute
College of Science and Engineering
11 June 2024

CONTENTS

ABSTRACT

Cementless tibial trays rely on osseointegration to achieve long-term fixation; creating a biological bond with the implant that strengthens over time. The mechanical environment during this period is essential in facilitating, or hindering, this growth. However, registry data alludes to a lack of primary stability, with cementless tibial components currently having a higher initial failure rate compared to their cemented counterparts in the first 4.5 years. Little is known about the interaction between the interference fit, employed during surgery, and the resulting primary stability, or, more generally, the initial mechanical environment that surrounds the implant. With the recent advancement of large-gantry micro-computer tomography (micro-CT) systems and digital volume correlation (DVC), such analysis is now possible experimentally.

The aim of this PhD was to quantify the initial mechanical environment surrounding a cementless titanium tibial tray. Micro-CT scans of seven cadaveric tibiae were performed when the tibiae were intact, following resection, and, once implanted with a commercially available cementless tibial tray, during two-time elapsed mechanical load sequences that replicated stair descent (SD, 0-2.5BW) and deep knee bend (DKB, 0-3.5BW). The established experimental protocol and subsequent analysis permitted quantification of the resected surface deviation, the actual interference fit, the post-implantation residual strain field, and, during the time-elapsed mechanical load sequence, the relative motion across the entire bone-implant interface and the minimum principal strain component in the surrounding cancellous bone.

Limited initial contact (54.4 %) occurred between the bone and the tibial tray, which, in part, was due to the undulating resected surface (R^2 = 0.219, p < 0.001). Residual strains were found in the surrounding peri-prosthetic bone following impaction, highlighting the importance of including damage criteria in finite element models of this period. The actual interference fit was significantly related to both this residual strain (R^2 = 0.450, p < 0.001) and the relative motion at the bone-implant interface when loaded (R^2 = 0.109 - 0.248, p < 0.035), with greater bone-implant overlap related to higher compression of cancellous bone and reduced relative motion (greater stability) at each load case. The relative motion across the majority (> 78.6 %) of the bone-implant interface remained below 150 μm during time elapsed loading, sufficiently low for (in principle) enabling osseointegration according to reported values in the literature. High minimum principal strain values were extracted in the cancellous bone in close contact with and up to 3.14 mm from the bone-implant interface. After the first load sequence (SD, maximum load of 2.5BW), residual strains in the peri-prosthetic bone and permanent tray migration were found; providing a potential mechanism for the high initial migration of cementless tibial trays seen clinically. Taken together, these results provide a comprehensive analysis of the initial mechanical environment following the implantation of a clinically successful cementless tibial tray.

DECLARATION

I certify that this thesis does not incorporate without acknowledgment any material previously submitted for a degree or diploma in any university; and the research within will not be submitted for any other future degree or diploma without the permission of Flinders University; and, to the best of my knowledge and belief, does not contain any material previously published or written by another person except where due reference is made in the text.

Lauren S Wearne

11th June, 2024

ACKNOWLEDGEMENTS

Firstly a big thank you to my two supervisors Egon and Mark. Egon, this has very much been a team effort and thank you for seeing, right from the start, what it could be. Few PhD students are given as many opportunities as I have been, and a lot of that comes down to you. So thank you for presenting me with them and encouraging me to peruse the others. To Mark, thank you for investing in me, not just as a "student" but a person beyond that. Thank you for all the additional guidance and time that you've given during this PhD. Sorry for not getting the word "squidgey" in here but I hope you'll accept it in the acknowledgements.

To Greg, thank you for all the encouragement and belief that you've given. It has been a privilege to learn from you and understand the importance of translating this work away from "engineering speak". I'm excited to see where this goes moving forward.

To Dave, Kenneth, John and MDRI on the whole, thank you for the advice and encouragement throughout. It means a lot to have such kind people to look up to, and be looked out for, during both my under-grad and now. Also, a big thank you to ARC CMIT for the mentorship and opportunities given from within this community.

To the Round Table, thank you for making every day (or at least a part of everyday (lunch + treaties)) enjoyable. So few people genuinely love their work environment, so thank you for being the exception to this. A special thank you to Sophie for the generosity and kindness that you have shown throughout. A Fleabag quote that always comes front of mine is "what a lovely thick neck" but that doesn't really seem all that appropriate here.

To all my housemates over the years, thank you for every meal you've made, for bringing my clothes in off of the line in the rain and hanging it up during the rain. To friends, family and the footy girls, thank you for making life outside (late but) always worth the wait.

To Cathy and Tony, thank you for being such a big part of our lives. Ella and I are so lucky to have an additional set of parents, so thank you for giving us that.

To Ella, thank you for always making me clam, always being on the other side of the phone and making me laugh every time we speak. I am so grateful that, out of everyone in the world, I get you as a sister – how lucky am I?

To Mum and Dad, thank you for always surrounding us in so much love and giving us the true essence of the word "home" in every way. You give us the confidence to go out and seek the oyster, knowing that we will be loved beyond measure no matter what. Thank you.

LIST OF PUBLICATIONS

PEER-REVIEWED JOURNAL ARTICLES

1. **Wearne LS**, Rapagna S, Taylor M, Perilli E (2022). Micro-CT scan optimisation for mechanical loading of tibia with titanium tibial tray: A digital volume correlation zero strain error analysis. *Journal of the Mechanical Behavior of Biomedical Materials*, 134:105336.

2. **Wearne LS**, Rapagna S, Awadalla M, Keene G, Taylor M, Perilli E (2024). Quantifying the immediate post-implantation strain field of cadaveric tibiae implanted with cementless tibial trays: A time-elapsed micro-CT and digital volume correlation analysis during stair descent. *Journal of the Mechanical Behavior of Biomedical Materials*, 151: 106347.

3. **Wearne LS**, Rapagna S, Keene G, Taylor M, Perilli E. Quantifying the interference fit of cementless tibial trays and its effect on the initial mechanical environment. *In submission to a peer-reviewed journal*.

4. **Wearne LS,** Rapagna S, Awadalla M, Keene G, Taylor M, Perilli E. Quantifying the contribution of interference to the primary stability of cementless tibial trays: a micro-CT and digital volume correlation analysis. *In preparation for submission to a peer-reviewed journal*.

5. Herath S, **Wearne LS**, Wilson C, Hobbs D, Taylor M, Thewlis, D. Bone density changes in the proximal tibia after a primary total knee replacement: a systematic review. *In preparation for submission to a peer-reviewed journal*.

NATIONAL AND INTERNATIONAL CONFERENCE PRESENTATIONS

1. **Wearne LS,** Rapagna S, Awadalla M, Keene G, Taylor M, Perilli E (2023). Assessing the initial mechanical environment of cadaveric tibiae with cementless tibial trays during stair descent and deep knee bend. Australian and New Zealand Orthopaedic Research Society, 28th Annual Scientific Meeting, Auckland, New Zealand. ***Podium Presentation.***

2. **Wearne LS,** Rapagna S, Keene G, Taylor M, Perilli E (2023). Variation in interference fit of cementless tibial trays and its effect on post-implantation strain field: a micro-CT and digital volume correlation analysis. Australian and New Zealand Orthopaedic Research Society, 28th Annual Scientific Meeting, Auckland, New Zealand. ***Poster Presentation.***

3. **Wearne LS**, Rapagna S, Awadalla M, Keene G, Taylor M, Perilli E (2023). Primary stability of cementless tibial trays during stair descent and deep knee bend: a micro-CT and DVC analysis. European Society of Biomechanics, 28th Annual Congress, Maastricht, The Netherlands. ***Podium Presentation.***

4. **Wearne LS,** Rapagna S, Awadalla M, Keene G, Taylor M, Perilli E (2023). Compression of cancellous bone under cementless tibial tray depending on the activity undertaken: a time-elapsed internal strain distribution analysis through micro-CT and digital volume correlation. Orthopaedic Research Society ORS 2023 Annual Meeting, Dallas (TX), USA. ***Poster Presentation.***

5. **Wearne LS,** Rapagna S, Awadalla M, Keene G, Taylor M, Perilli E (2022). Titanium press-fit tray implanted in human tibia: a zero-strain micro-CT and digital volume correlation analysis. Australian and New Zealand Society of Biomechanics, 13th Australasian Biomechanics Conference, Brisbane (QLD), Australia. ***Podium Presentation, Winner Best Orthopaedic Biomechanics Presentation.***

6. **Wearne LS,** Rapagna S, Awadalla M, Keene G, Taylor M, Perilli E (2022). Micro-CT imaging a press-fit tray implanted in human tibia: a zero-strain digital volume correlation analysis at organ level. Australian and New Zealand Orthopaedic Research Society, 27th Annual Scientific Meeting, Gold Coast (QLD), Australia. ***Podium Presentation, Winner PhD Award.***

7. **Wearne LS,** Rapagna S, Awadalla M, Keene G, Taylor M, Perilli E (2022). Internal strain field of a human tibia with titanium tibial tray during stair descent: a micro-CT and DVC analysis. European Society of Biomechanics, 27th Annual Congress, Porto, Portugal. ***Poster Presentation***.

8. *Wearne LS,* Rapagna S, Taylor M, Perilli E (2021). Titanium press-fit tray implanted in human tibia: a zero-strain micro-CT and digital volume correlation analysis. Australian and New Zealand Society of Biomechanics, 12th Australasian Biomechanics Conference, online. ***Poster, Winner People's Poster Choice Award.***

9. **Wearne LS,** Rapagna S, Taylor M, Perilli E (2021). Micro-CT imaging a press-fit tray implanted in human tibia: a zero-strain digital volume correlation analysis at organ level. Australian and New Zealand Orthopaedic Research Society, 26th Annual Scientific Meeting, online. ***Podium Presentation, Finalist PhD Award.***

10. **Wearne LS,** Rapagna S, Taylor M, Perilli E (2021). Human Tibia implanted with titanium press-fit tray: A micro-CT zero-strain analysis with digital volume correlation. European Society of Biomechanics, 26th Annual Congress, Milan, Italy (online). ***Podium Presentation***.

11. **Wearne LS,** Rapagna S, Taylor M, Perilli E (2021). Titanium press-fit implantation in human tibia imaged via micro-CT: a zero-strain analysis using digital volume correlation. Australian Orthopaedic Association SA/NT Branch Meeting, Adelaide (SA), Australia. ***Podium Presentation***.

12. **Wearne LS,** Rapagna S, Taylor M, Perilli E (2020). Micro-CT Imaging of a Press-Fit Implant in Human Tibia: A Zero-Strain Analysis using digital volume correlation. ToScA Global 2020 Online Edition. Webinar Sep 2020. ***Lightning Talk***.

HONOURS AND AWARDS

1. **Travel Award** ($300 AUD), Australian and New Zealand Orthopaedic Research Society, 28th Annual Scientific Meeting, December 2023, Auckland, New Zealand.

2. **Winner of a Graduate Women SA Centenary Scholarship** ($1,500 AUD), received from The Australian Federation of University Women. June 2023.

3. **Best Oral Presentation in Orthopaedic Biomechanics** ($500 AUD)**,** Australian and New Zealand Society of Biomechanics, 13th Australasian Biomechanics Conference, November 2022, Brisbane (QLD) Australia.

4. **Recipient of Conference Support** ($1,500 AUD), Flinders University College of Science and Engineering. February 2023.

5. **PhD Student Award** ($500 AUD), Australian and New Zealand Orthopaedic Research Society, 27th Annual Scientific Meeting, August 2022, Gold Coast (QLD) Australia.

6. **Travel Award** ($300 AUD), Australian and New Zealand Orthopaedic Research Society, 27th Annual Scientific Meeting, August 2022, Gold Coast (QLD) Australia.

7. **Best 7 minutes Presentation, Winner** ($300 AUD), Flinders University Engineered Systems, December, 2021, Adelaide (SA) Australia.

8. **People's Choice Poster Award** ($300 AUD), Australian and New Zealand Society of Biomechanics, 12th Australasian Biomechanics Conference, December 2021, online.

9. **PhD Student Award Finalist**, Australian and New Zealand Orthopaedic Research Society, 26th Annual Scientific Meeting, October 2021, online.

10. **Research Higher Degree Scholarship**, Australian Government Department of Education, March 2020.

LIST OF FIGURES

LIST OF TABLES

ABBREVIATIONS

2D	Two-dimensional
3D	Three-dimensional
ADLs	Activities of Daily Living
Al Tb	Aluminium tube
AOANJRR	Australian Orthopaedic Association national joint replacement registry
A-P	Anterior-posterior
BMD	Bone mineral density
BV/TV	Bone volume fraction (bone volume / total volume)
BW	Body weight
CT	Computer tomography
DIC	Digital image correlation
DKB	Deep knee bend
DVC	Digital volume correlation
FE	Finite element
I-E	Internal - external
LVDT	Linear variable differential transducer
MAER	Mean absolute error
Micro-CT	Micro-computer tomography
M-L	Medio-lateral
P3	Minimum principal strain component
PL1	Preload 1
PL2	Preload 2
PMMA	Poly-methyl-methacrylate
PSA	Percentage surface area
ROI	Region of interest
RSA	Roentgen Stereophotogrammetry Analysis
Std dev	Standard deviation
SD	Stair descent
SDER	Standard deviation of error
SMI	Structural model index
Tb.Th	Trabecular thickness
Tb.N	Trabecular number
Tb.Sp	Trabecular separation
TKA	Total knee arthroplasty
VOI	Volume of interest
vs	versus

CHAPTER 1: INTRODUCTION

1.1 MOTIVATION

Over 59,000 Australians received a primary total knee arthroplasty (TKA) in 2022, with the number only expected to increase (AOANJRR, 2022). Currently, cemented fixation is considered the gold standard and accounts for 62.5 % of all TKAs performed in Australia (AOANJRR, 2022). Proponents of cementless tibial trays cite improved bone stock retention at the time of revision. Furthermore, the concerns surrounding cement fixation, including micro-crack development in the cement mantle and stress shielding, leading to bone resorption and loss of fixation with time, are mitigated by cementless fixation. With a younger and more active patient cohort, there is a renewed interest in cementless tibial components (AOANJRR, 2022, AJRR, 2022). This is reflective in recent registry data, where their use has increased in Australia from 9.8% in 2018 to 18.6% in 2022 (AOANJRR, 2022).

Whilst long-term success rates at fifteen and nineteen years are comparable between cemented and cementless tibial components (Baker et al., 2007, AOANJRR, 2020c), cementless tibial components currently have a higher failure rate within the first 4.5 years compared to their cemented counterparts, after which it is lower (AOANJRR, 2020c, AOANJRR, 2022). Aside from aseptic loosening and infection, such early failure alludes to insufficient primary stability.

Long-term fixation of cementless tibial components relies on the apposition of bone directly onto the implant surface after implantation, creating a biological bond that strengthens over time. An initial favourable mechanical environment is essential in achieving osseointegration. An interference fit is introduced during the surgery, whereby the bone is undercut relative to the implant geometry, to provide sufficient primary stability, and hence facilitate osseointegration. The interference fit helps to ensure direct contact between implant and bone and, theoretically, results in a compressive response in the surrounding bone that grips onto to the implant.

The interplay between the interference fit and the resulting mechanical response of bone remains unknown. Furthermore, inconsistent roughness and flatness of the resected surface (Toksvig-Larsen and Ryd, 1991, Delgadillo et al., 2020), damage caused by the impaction process (Berahmani et al., 2017, Rapagna et al., 2019, Bishop et al., 2014, Damm et al., 2015, Damm et al., 2017), and, alignment of the prosthesis to the tibia all introduce surgical variability that can alter the nominal interference fit.

Previous experimental studies on cementless knee replacements have assessed primary stability through various metrics, such as the force required to implant the device (push-in force: (Campi et al., 2018, Bishop et al., 2014, Damm et al., 2015, Damm et al., 2017)) or remove it (pull-out force: (Campi et al., 2018, Bishop et al., 2014, Damm et al., 2015, Damm et al., 2017, Berahmani et al., 2017)). The most common metric for assessing primary stability of cementless tibial trays is the

relative motion between the tray and underlying bone, referred to as micromotion (Lee et al., 1991, Miura et al., 1990, Kraemer et al., 1995, Stern et al., 1997, Sala et al., 1999, Meneghini et al., 2011, Bhimji and Meneghini, 2012, Bhimji and Meneghini, 2014, Chong et al., 2010, Van Valkenburg et al., 2016, Small et al., 2016, Navacchia et al., 2018, Han et al., 2020, Sánchez et al., 2021). Whilst simplistic, there is a direct correlation between inducible micromotion, being recoverable micromotion, and osseointegration. Fundamental work by Pilliar et al. (1986) and Søballe et al. (1992) reports that osseointegration can occur when micromotion remains below 50 µm, and fibrous tissue attachment instead can occur when micromotion exceeds 150 µm. Whilst numerous experimental studies and associations to interference fit, implant design, implant surface finish and loading protocols exist, they are limited to peripheral (surface) measurements only. It has previously not been possible to experimentally assess the micromotion across the entire bone-implant interface for tibial components. Furthermore, the effect of the interference fit on primary stability for cementless knee components has been assessed by modifying the intended (or nominal) interference fit through altered implant design (Berahmani et al., 2015a, Sánchez et al., 2021) or resection depths (Damm et al., 2015, Damm et al., 2017). However, the intended interference fit is known to differ to the interference fit achieved (Berahmani et al., 2018).

Computational (finite element (FE)) models of tibiae with cementless tibial components are able to predict the mechanical environment surrounding the entire bone-implant interface, providing an insight into the possible initial environment under complex loading scenarios. However, the models are limited, often not including an interference fit (Taylor et al., 2012, Chong et al., 2010), or modelling a fit smaller than used clinically (Dawson and Bartel, 1992, Hashemi and Shirazi-Adl, 2000, Yang et al., 2020), and are sensitive to chosen friction coefficients, material properties and contact conditions. Furthermore, without experimental data, it is difficult to validate these models (Yang et al., 2021), relying on external (surface) measurements (Completo et al., 2007, Completo et al., 2008, Gray et al., 2008), or comparisons to failure and migration rates within joint replacement registries (Taylor et al., 1998, Perillo-Marcone et al., 2004) or the regional development of fibrous tissue from retrieval studies (Dawson and Bartel, 1992).

With the recent advancement of large gantry micro-computer tomography (micro-CT) systems and digital volume correlation (DVC) it is now possible to quantify experimentally the internal mechanical environment of large specimens (Kusins et al., 2019, Kusins et al., 2022, Zhou et al., 2020b, Tozzi et al., 2016, Hussein et al., 2012, Palanca et al., 2016a, Danesi et al., 2016). The aim of this thesis is to undertake such an analysis on cadaveric tibiae with a cementless tibial component. There are a number of challenges introduced in undertaking such an analysis, including the size of the organ and the presence of a large metallic implant. Whilst theoretically possible, to the best of the author's knowledge, this type of analysis, prior to this thesis, has not been undertaken.

1.2 AIMS AND SIGNIFICANCE OF RESEARCH

The overall aim of this thesis is to quantify the interference fit achieved for cementless tibial components and the immediate post-implantation mechanical environment surrounding the implant. This will be undertaken through micro-CT imaging of cadaveric specimens intact, after preparation for TKA, and, when implanted with a commercially available cementless tibial component, during two time-elapsed mechanical load sequences. Through the acquired datasets, the following will be performed:

1) Assessing the possibility of employing DVC analysis on micro-CT datasets of cadaveric tibiae with a commercially available cementless tibial tray to quantify the immediate mechanical environment (**Chapter 3 (Study 1)** and **Chapter 4**).

2) Evaluating the interference fit achieved between cementless tibial trays and cadaveric tibiae prepared for TKA, thereby taking into account resection variability and implant alignment (**Chapter 5 (Study 2)**). Relationships between the interference fit and the post-impaction residual strain field will also be quantified.

3) Experimentally quantifying the relative motion between a cementless tibial component and underlying bone across the entire bone-implant interface during two time-elapsed mechanical load sequences that replicate stair descent (SD) and deep knee bend (DKB) (**Chapter 6 (Study 3)**). Relationships between the actual interference fit, the percentage of tray-to-bone contact, the residual post-impaction strain field and bone volume fraction to the quantified relative motion will be assessed. The permanent tray migration following SD will also be analysed.

4) Extracting the internal compressive strain field of tibial cancellous bone for cadaveric tibiae with a cementless tibial tray during SD and DKB (**Chapter 7 (Study 4)**). The residual strain present in the cancellous bone after the first day of testing (SD, maximum load of 2.5BW) will also quantified.

Such results will increase our understanding of the surgical variability and primary stability of cementless tibial components, **providing an insight into the initial mechanical environment surrounding a cementless tibial component after implantation**. Relationships between surgical variability (actual interference fit and resected surface roughness), post-impaction residual strain and primary stability (full-field compressive strains and relative motion at the bone-implant interface) will be explored to provide a better understanding of the interplay between them. Results will be discussed in regard to registry data, Roentgen Stereophotogrammetric Analysis (RSA) studies and current FE models. The methodology produced and understanding gained from this work can be used in analysis of different surgical techniques, building FE models that are better informed and validated, and assisting in developing physiotherapy guidelines.

1.3 OUTLINE OF THE THESIS

Chapter 1: Introduction

Details the motivation, aims and significance of the research produced for this thesis.

Chapter 2: Background

Provides an overview of the knee, total knee arthroplasties (TKAs) and bone of the tibia. A literature review is undertaken for factors influencing primary stability, and how primary stability is currently being assessed in both experimental and computational studies. The possibility of, and complications associated with, using micro-computer tomography (micro-CT) and digital volume correlation (DVC) to assess the primary stability of cementless tibial trays are also discussed.

Chapter 3, Study 1: Micro-CT scan optimisation for mechanical loading of tibia with titanium tibial component: A digital volume correlation zero strain error analysis

Determines the feasibility of the proposed experimental configuration by assessing the zero-strain errors during time-elapsed mechanical loading and concomitant micro-CT imaging of a cadaveric tibia with a metallic (titanium) tibial component (Aim 1). Four different scanning configurations were considered, that assessed the influence of X-ray voltage, scan time and presence of a 2 mm thick aluminium cylinder (as required for mechanical loading of long bones in this study).

Chapter 4: Time-elapsed micro-CT scanning and digital volume correlation analysis of cadaveric tibiae with cementless tibial tray

Details the experimental protocol that formed the basis of the subsequent studies, including the potting procedure and micro-CT imaging of the seven acquired cadaveric specimens (Aim 1). The analysis of this captured data forms Chapters 5 (Study 2), 6 (Study 3) and 7 (Study 4).

Chapter 5, Study 2: Quantifying the interference fit of cementless tibial trays: a cadaveric micro-CT and digital volume correlation analysis

Explores the actual interference fit achieved for seven cadaveric tibiae with cementless tibial components, the roughness of the resected surface and the resulting percentage surface area of the tibial tray in initial contact with the resected surface (Aim 2). The residual strain induced in the surrounding cancellous bone from the impaction was quantified. Relationships between actual interference fit and induced strain are investigated.

Chapter 6, Study 3: Contribution of the actual interference fit of cementless tibial components to their relative motion

Quantifies the relative motion between cementless tibial components and underlying bone for seven cadaveric specimens as they are exposed to two time-elapsed mechanical load sequences that replicate SD and DKB (Aim 3). Full-field relative motion is extracted across the entire interface for each load step through DVC. The permanent subsidence of the component after the first time-elapsed sequence (SD, maximum 2.5BW) is quantified. Relationships between the relative motion

across the bone-implant interface and the actual interference fit, percentage implant-bone contact and post-impaction residual strain field are also explored.

Chapter 7, Study 4: Quantifying the cancellous bone mechanical environment following TKA of cementless tibial trays during simulated stair descent and deep knee bend: full-field strain analysis through time-elapsed micro-CT imaging and DVC

Computes the minimum principal strain component of the cancellous bone surrounding a cementless tibial TKA component for seven cadaveric specimens during the two time-elapsed mechanical load sequences (SD and DKB, Aim 4). The residual strain induced after completion of the first load sequence is quantified and compared to migration patterns reported in clinical studies.

Chapter 8: Discussion and Future Directions

The principal findings and significance to the orthopaedic research community of this work are discussed, along with its limitations and the recommendations for future research stemming from this thesis.

CHAPTER 2: BACKGROUND

2.1 ANATOMY

2.1.1 Knee Anatomy

The knee is a diarthrodial joint (Figure 2. 1), composed of the distal femur, proximal tibia and the patella (Paschos and Prodromas, 2019). There are two articulating surfaces: the tibiofemoral joint and the patella-femoral joint. The tibiofemoral joint is exposed to high loads with up to four times body weight (BW) being applied during activities of daily living (ADLs), and much greater in moments of instability (5.5 BW) (Kutzner et al., 2010, Saxby et al., 2016).

The mechanical axis of a healthy knee is defined as a straight line passing from the centre of the femoral head, through the knee to the centre of the ankle. Most people naturally present with a varus knee, with the mechanical axis of the femur deviating medially by 1.2 ± 2.2 ° relative to the mechanical axis of the tibia in the coronal plane (Hsu et al., 1990). In a native healthy knee, typically 60-80% of load passing through the knee is distributed through the medial condyle (Andriacchi et al., 1986, Hsu et al., 1990).

The knee is often represented as a simple hinge joint, with just flexion-extension (F-E) included, even though it is recognised as one of the most complex joints of the body (Andriacchi et al., 1986). Whilst F-E is the primary motion of the knee, such models overlook the anterior-posterior (A-P) translation of the femur on the tibia, the abduction-adduction motion and internal-external (I-E) rotation occurring at this joint (Figure 2. 1).

As the knee flexes, the femur rolls posteriorly on the tibial plateau, which progresses to a gliding motion after 20-30˚ of flexion (Andriacchi et al., 1986). Concurrently, there is a passive I-E rotation due to the larger lateral condyle of the femur and an external adduction moment (Andriacchi et al., 1986). Consequentially, during flexion there is a posterior translation of the point of loading of the femur on the tibia, with the medial condyle translating posteriorly by 1.5 mm, and lateral femoral condyle translating further up to 15 mm (Freeman and Pinskerova, 2005). The varus alignment of the knee also introduces an adduction moment in activities that have a temporary single leg stance (such as gait and stair climbing (Kutzner et al., 2010)), with again, more load passing through the medial condyle of the knee (Andriacchi et al., 1986).
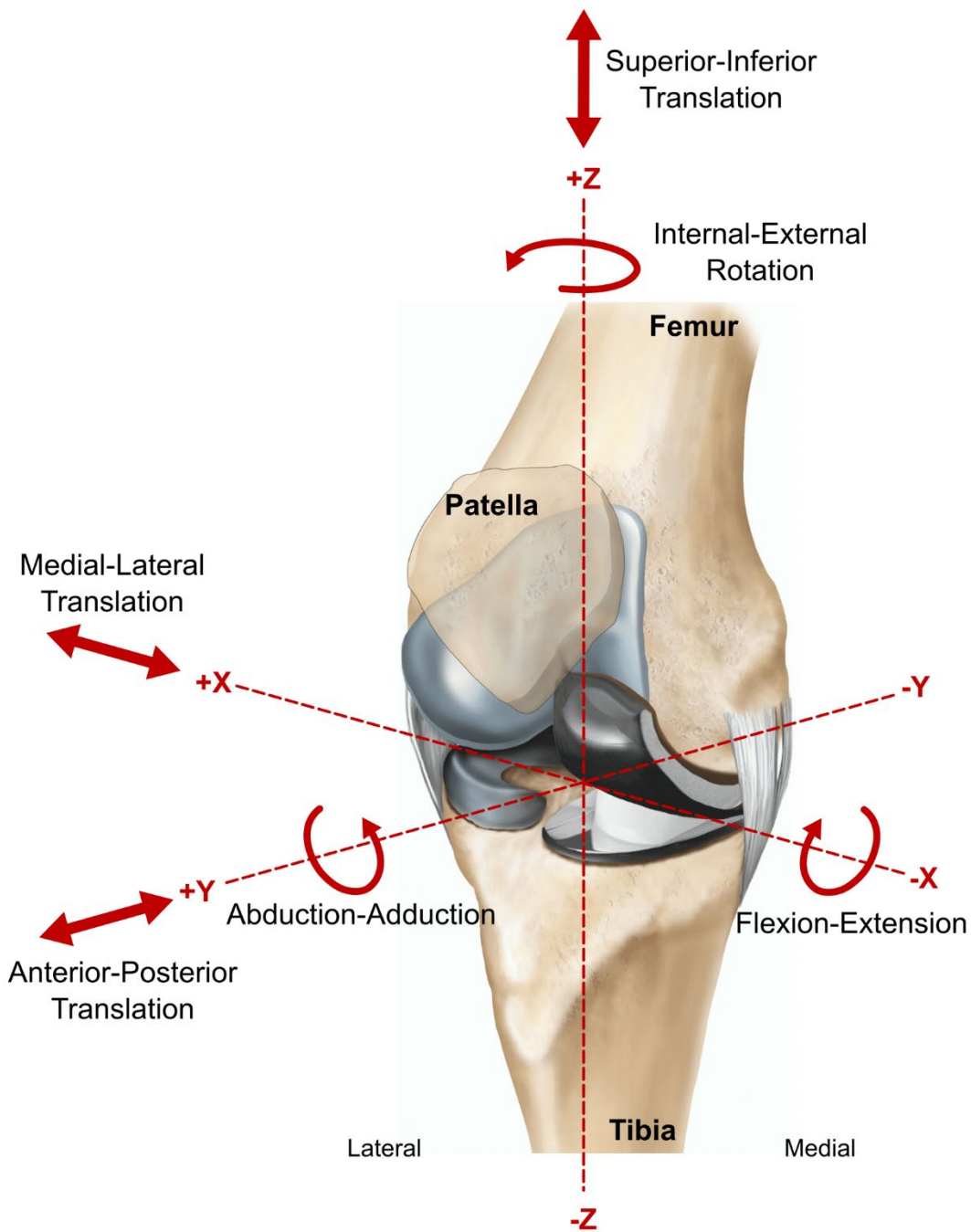
Figure 2. 1: Knee anatomy and joint coordinate system, showing (left) the native knee and right a knee replacement. Motions of the joint include: superior-inferior translation, internal-external (I-E) rotation, medial-lateral (M-L) translation, flexion-extenion (F-E), anterior-posterior (A-P) translation and abduction-adduction. Figure amended from (Culley, 2022) with reprinting rights bought from MedicalStockImages.net.

2.1.2 Total Knee Arthroplasties

Total knee arthroplasties (TKA) offer pain relief and improved knee functionality to patients with late-stage osteoarthritis, whom account for 97.8 % of the presenting patients in Australia (AOANJRR, 2022). The number of primary TKAs performed annually is increasing, with a conservative model predicting over 1.5 million procedures annually in America alone by 2050 (Inacio et al., 2017). The demographic is also changing: we are receiving primary TKAs younger and are living for longer (Kurtz et al., 2009). As such, the importance of achieving long term fixation becomes increasingly pressing.

During TKA, the articulating surfaces of the femur and tibia, and commonly (in Australia) the patella, are replaced with separate components. It is a successful procedure, increasing the quality of life for recipients, with 95.3 % of modern components lasting longer than 10 years (AOANJRR, 2022). However, for the revisions that do occur, the tibial component has been recognised as the problematic component (Andriacchi et al., 1986, Sharkey et al., 2002, Nelissen et al., 1998).

Mechanical fixation of the implants can be achieved via two means: cemented or cementless. Cemented fixation has been considered the gold standard and is the most commonly performed fixation technique (AOANJRR, 2022). However, concern surrounds microcrack accumulation in the cement mantle (Gao et al., 2019), and stress shielding resulting in bone resorption and loss of fixation with time in service (Completo et al., 2008, Miller et al., 2014). These issues become more pressing considering the changing patient demographic, with which a longer time in service and higher activity levels can be expected (Kurtz et al., 2009). Cementless tibial components achieve long-term fixation through (ideally) bone ingrowth, whereby there is direct apposition of bone onto the implant surface, resulting in a biological fixation that strengthens over time. There has been renewed interest in cementless tibial components in recent years, with their use increasing by 5 fold in American registries since 2015 and close to 2 fold in Australian registries since 2018 (AJRR, 2022, AOANJRR, 2022).

Studies show no difference in long-term revision rates between cementless and cemented implants in matched patient cohorts (Baker et al., 2007, Choy et al., 2014). However, cementless TKAs have a higher initial failure rate within the first 1.5 – 3.5 years (AOANJRR, 2020c, AOANJRR, 2022). After 4.5 years, the revision rate for cementless TKA components is lower than their cemented counterparts (AOANJRR, 2022). As stated by the Australian Orthopaedic Association (AOA), such early revision alludes to "failure to gain fixation" (AOANJRR, 2020c).

When successfully fixated through osseointegration, "excellent" outcomes are reported for cementless tibial trays (Berger et al., 2001, Restrepo et al., 2021). Modern cementless designs have revision rates comparable to cemented devices at short- and mid-term follow-up (Restrepo et al., 2021, Zhou et al., 2018), although longer studies are still needed (Haddad and Plastow, 2020, Zhou et al., 2018). For bony fixation to occur, there must be sufficient mechanical stability in the

immediate post-operative period, without which, fibrous tissue attachment may instead form. Occurrences of fibrous tissue attachment have been found in retrieval studies of failed cementless tibial components (Baker et al., 2007, Berger et al., 2001). As highlighted by multiple authors (Taylor and Tanner, 1997, Pijls et al., 2012, Pijls et al., 2018, Ryd et al., 1995, Curtis et al., 1992, Viceconti et al., 2006, Kuzyk and Schemitsch, 2011, Mueller et al., 2013, Taylor and Prendergast, 2015), the long-term success of cementless tibial components is dependent on the initial mechanical environment surrounding the implant.

2.1.3 Knee Joint Biomechanics After TKA

Early TKAs were designed as a hinge joint, permitting only flexion and extension (Prendergast, 2001). As these designs constrained the A-P translation and I-E rotation of the knee, it is unsurprising that high revision rates were reported (Andriacchi et al., 1986).

The exact motion of the replaced joint is dependent on many factors, including patient attributes (Meric et al., 2015, Bergmann et al., 2014, Fitzpatrick et al., 2014b), surgical variability (Fitzpatrick et al., 2012) and the components' design, particularly the conformity of the articulating surfaces (Fitzpatrick et al., 2012, Prendergast, 2001). Whilst the time course and magnitude may vary between patients, the four common motions of F-E, A-P translation, varus-valgus (V-V) motion and I-E rotation still exist in the replaced joint (Bergmann et al., 2014, Dreyer et al., 2022).

The forces acting at the tibiofemoral joint are a result of these kinematics, produced by both external and internal forces. External forces include those resulting from the weight of the patient, the ground reaction force, and the force attributed to limb acceleration (Andriacchi et al., 1986). Internal forces are produced internally by the body, being those produced by contracting muscles, tension from ligaments and, subsequently, joint contact forces (Andriacchi et al., 1986).

Much insight into the kinetics acting on the tibial component during common ADLs has been gained through the development of instrumented implants (Kutzner et al., 2010, Bergmann et al., 2014). The three force components ($+F_x,\ +F_y,\ +F_z$, acting in the lateral, anterior and superior direction respectively) and three moments ($+M_x,\ +M_y,\ +M_z$ corresponding to F-E, V-V and I-E rotation, respectively) have been recorded as patients with a TKA undertook common ADLs, including a one- and two-legged stance, sit down and up, deep knee bend, gait and stair ascent and descent. Resultant forces generated across the knee during the eight activities were typically within the range 2.2-3.5BW, however peak forces of 4.0BW were recorded. The inferior force, $-F_z$, was the largest component across all activities by a factor of 10-20 (Kutzner et al., 2010).

An important aspect of knee biomechanics that was not captured by the hinge-joint design of early TKAs is the A-P translation of the femur on the tibial component. In a validated FE study, Fitzpatrick et al. (2013) reported increased posterior translation with increasing knee flexion, particularly after post-cam engagement. For the eight designs assessed in their study, this

occurred between 23-89° (Fitzpatrick et al., 2013). The common ADLs of sit up, sit down and deep knee bend achieve such knee flexion (Kutzner et al., 2010), thereby exposing the tray to a posterior point of loading. Posterior translation of the medial femoral condyle was reported to be as great as 7.1 mm and lateral posterior translation as great as 15.6 mm from the centre of the tibial component (Fitzpatrick et al., 2013).

During both stair climbing and gait, an anterior translation of loading can also occur between contralateral toe off and contralateral heal strike (Kutzner et al., 2010).The extent of translation (both anterior and posterior) is dependent on patient attributes (muscle strength and ligament tension and their insertion sites), achieved joint alignment, the femoral condyle radii in the sagittal plane, the degree of tibial insert conformity and the bearing (fixed bearing or rotating platform) (Fitzpatrick et al., 2012, Fitzpatrick et al., 2014b, Fitzpatrick et al., 2013). This A-P translation of the femur on the tibial component can induce a sagittal rocking motion of the tray, with anterior-edge lift-off and posterior-edge subsidence. Such a motion is well documented within the literature (Bhimji and Meneghini, 2012, Bhimji and Meneghini, 2014, Chong et al., 2010, Fitzpatrick et al., 2014a, Han et al., 2020, Quevedo González et al., 2019, Sánchez et al., 2021) and seen clinically (Figure 2. 2) with fibrous tissue growth across the anterior and posterior edges of retrieved tibial components (Restrepo et al., 2021, Sumner et al., 1995).
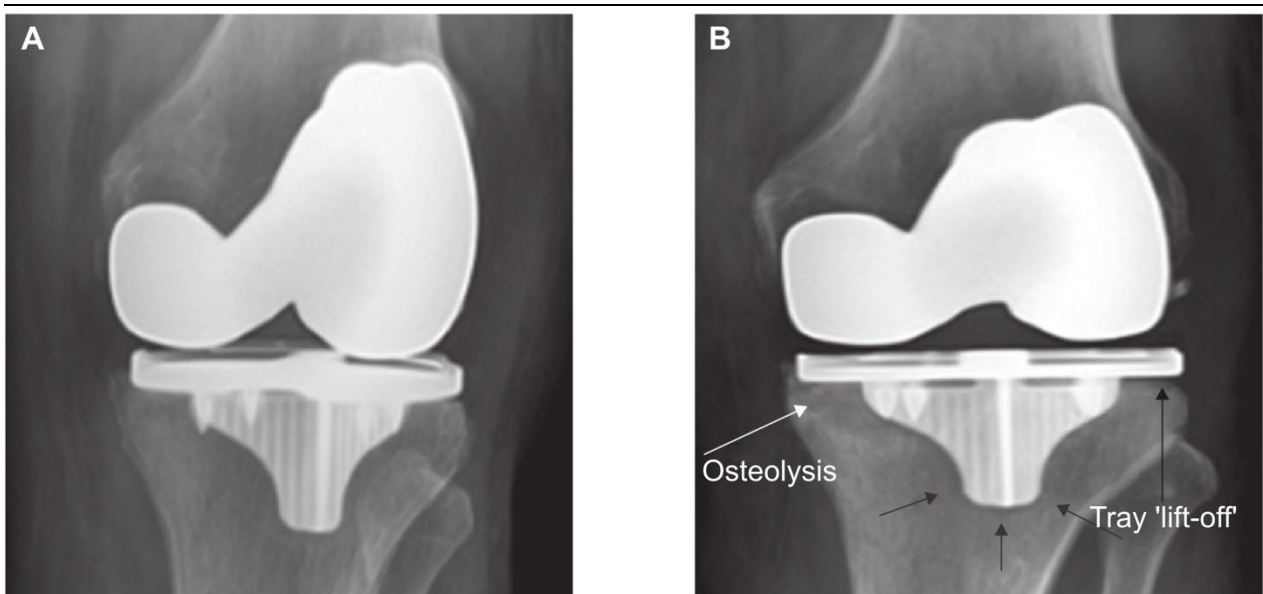
Figure 2. 2: Radiographs taken of a cementless total knee arthroplasty in a 75 year old male patient, taken A) immediately post-operatively and B) at the time of revision. Revision was performed 4 months after the operation as the component was loose. Radiolucent lines were found around the bottom of the stem (black arrows), with posterior subsidence (white arrow) and anterior lift-off (black arrow to the right).
Figure from Restrepo et al. (2021). Reprinted with permission from British Editorial Society of Bone & Joint Surgery.

2.1.4 Mechanical Properties of Bone

Unlike cemented devices, cementless tibial components are in intimate contact with the underlying bone. This is primarily a bed of cancellous bone, exposed during the resection, with varying mechanical properties across the plateau. The mechanical properties of bone in contact with the implant is important to both the primary stability and the long-term success of the device.

The proximal tibia consists of a thin wall of cortical bone surrounding a bed of cancellous bone. At a cellular level, bone consists of a mineralized inorganic matrix of hydroxyapatite $(Ca_{10}(PO_4)_6(OH)_2)$, type 1 collagen fibers and various proteins. Differences in their arrangement, density and architecture result in varying mechanical properties at the apparent level (5-10 mm).
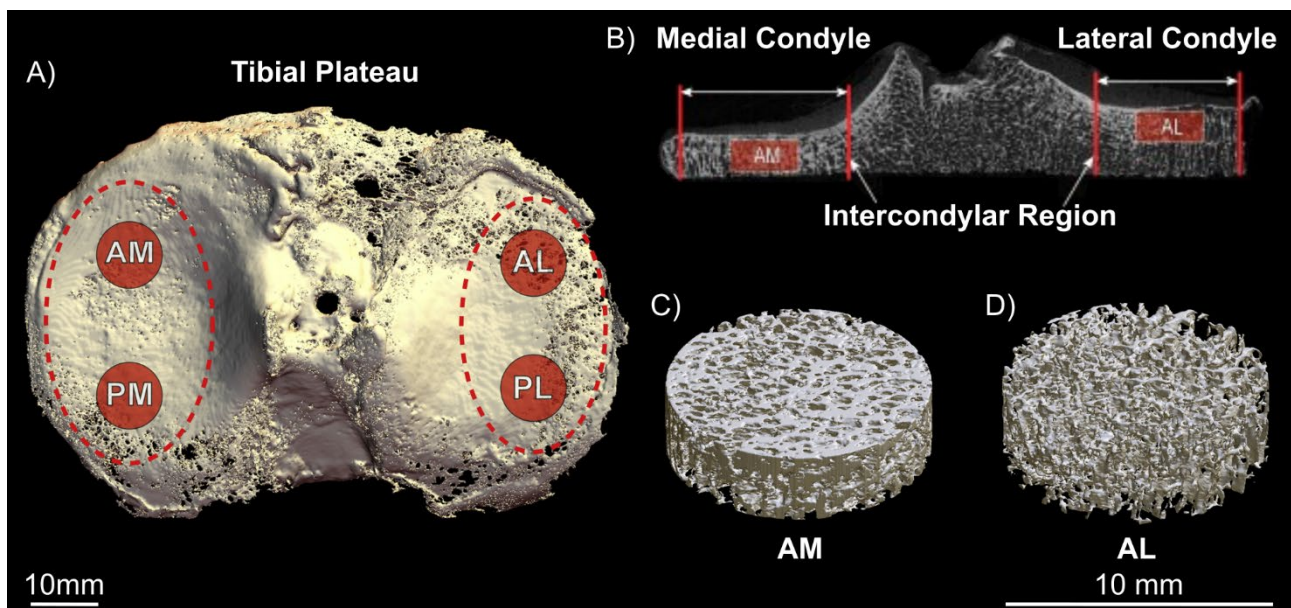
Figure 2. 3: Cancellous bone distribution in the proximal tibia. A) A 3D reconstruction of a right osteoarthritic tibial plateau removed during TKA surgery. Dashed red ellipses define the medial (left) and lateral (right) condyle. B) Micro-CT coronal cross-section across the anterior-medial (AM) and anterior-lateral (AL) regions. C,D) 3D reconstructions of the AM and AL regions, where AM (C) has a high BV/TV (42 %) and more plate-like structure and AL (D) has a lower BV/TV (13 %) and more rod-like structure.
Figure amended from Roberts et al. (2018). Reprinted with permission from Elsevier.

Cancellous bone, or trabecular bone, is arranged into a system of interconnected plates and rods (shown in Figure 2. 3), the arrangement being heavily dependent upon the everyday loading it is exposed to (Roberts et al., 2018). The mean intercept length (MIL) is a morphometric parameter (Whitehouse, 1974), from which the fabric tensor describing the tissue's orientation in space can be extracted. The resulting mechanical properties of cancellous bone vary, from nearly isotropic to highly anisotropic depending on this arrangement, the density and the region (Odgaard, 1997, Morgan et al., 2018).

Cancellous bone is a non-linear viscoelastic material, displaying both stress- and strain- relaxation (Morgan et al., 2018). It does not exhibit a distinct linear region within its stress-strain curve (Morgan et al., 2018), though it is often modelled as a linearly elastic material (Viceconti et al., 2006, Chong et al., 2011, Chong et al., 2010, Perillo-Marcone et al., 2004, Hashemi and Shirazi-

Adl, 2000, Kelly et al., 2013, Taylor et al., 1998, Quevedo González et al., 2023, Quevedo González et al., 2019, Innocenti et al., 2009). Yield stress is often used when defining the strength of bone and used to mechanically assess bone quality (Keaveny, 2001).The yield stress of the tissue is typically taken as the 0.2% offset stress on a stress-strain curve, with the elastic modulus (often referred to as Young's modulus or just the modulus) taken as the slope (Keaveny, 2001). The yield stress of trabecular bone is higher in compression (proximal cadaveric tibia: 3.77 - 9.18 MPa (Sanyal et al., 2012)) than in tension, and lowest in shear (1.82 - 3.16 MPa (Sanyal et al., 2012)) (Morgan and Keaveny, 2001, Morgan et al., 2018, Ciarelli et al., 1991).

Whilst representative values are included above for human cancellous bone of the proximal tibia, the yield stress of cancellous bone at an apparent level is difficult to define as it is dependent on the material properties of trabeculae (tissue level), the anatomical site (Morgan 2001)(Morgan and Keaveny, 2001), and its structural properties. The bone volume and architecture of cancellous bone alone can contribute to as much as 70-90% of its elastic modulus and yield stress (Morgan et al., 2018). As such, there is a large range of reported values within the literature (Helgason et al., 2008), with reported values of the elastic modulus of human cancellous bone ranging from 10 – 30,000 MPa and strength ranging from 1 to 30 MPa (Morgan et al., 2018).

When using yield stress to define the strength of cancellous bone, it is dependent on its density, volume fraction and elastic modulus. However, when instead using yield strain to define the strength of cancellous bone, it is found to be relatively isotropic and homogeneous within a site (Morgan et al., 2003, Morgan and Keaveny, 2001). Hence, the dependence of bone strength on orientation and density can largely be mitigated (Bayraktar et al., 2004). Lower density bone does have anisotropic yield strains, however they only differ by up to approximately 10% between the different loading directions (Morgan et al., 2018). For cadaveric femoral necks, the reported compressive yield strain of human trabecular bone is -8,300 ± 1,500 με (-7,800 to -10,000 με (Bayraktar et al., 2004)).

2.1.4.1 Post-Yield Behaviour

When bone exceeds its yield point, there is a zero-strain offset whereby the bone remains in a deformed state even as the load is removed. The yielded bone is still able to mechanically function with comparable (although reduced) strength, however at this strain offset and with decreased modulus (Keaveny et al., 1994), resulting in an increased hysteresis loop. Even when compressed to 150,000 – 500,000 με (15 – 50 %), cancellous bone is still able to take substantial loads (Keaveny et al., 1994, Morgan et al., 2018). Due to the consistency of these changes, Keaveny et al. (1994) proposed that the post-yield behaviour of cancellous bone should be considered a tissue property.

2.1.5 Quantifying Bone Properties

The mechanical properties of bone within 100-200 µm of the bone-implant interface are critically important to the implant's stability (Mathieu et al., 2014). However, little is known about them (Steiner et al., 2015) and it currently not possible to ascertain them directly. As a result, associations between apparent densities and morphometric parameters to strength have been investigated and subsequently used.

2.1.5.1 Bone Mineral Density

Bone mineral density (BMD) can be acquired clinically from calibrated computer-tomography (CT) scans by converting the grey-levels (Hounsfield units) of the CT images to BMD through phantom- or tissue based-calibration. Phantom calibration remains the gold standard, whereby the scan is acquired with an inline calibration phantom. The phantom, typically of calcium hydroxyapatite or hydrogen phosphate (Eggermont et al., 2019), provides known densities within the image dataset, allowing conversion of grey-levels to mineral densities, including BMD. However, as the name suggests, this relies on the scans being acquired with a phantom in place. Phantomless calibration instead employs the grey-levels of specific tissues within the scan to generate a calibration function, promoting its ease of use. It relies on the assumption that the relative tissue densities will remain comparable between patients. Eggermont et al. (2019) found that including cortical bone, in addition to air, fat and muscle, when generating the calibration function did not improve the accuracy in comparison to phantom-based calibration, potentially due to the large variability between patients. In considering fat, blood, muscle, urine and air, Winsor et al. (2021), in retrospectively studying 258 patients, found that air and fat had the greatest inter- and intra-operator repeatability, whilst urine had the worst. Numerous tissue combinations have been used to calibrate CT scans, including: fat and muscle; air and blood; air and fat; air, fat and muscle; air, fat, muscle and blood; air, fat, blood, muscle and cortical bone (Winsor et al., 2021).

Once the grey levels of the CT scan are converted, the extracted BMD values can be directly exported to finite element (FE) models and mechanical properties assigned. The relationship between elastic modulus (E) and BMD (ρ) is dependent on the anatomical site (Helgason et al., 2008). For the tibia, specifically, this has been calculated as $E = 15{,}520\,\rho^{1.93}$ (Morgan et al., 2003). It is now becoming common practice to build patient- or specimen-specific FE models based on these relationships (Viceconti et al., 2006, Chong et al., 2011, Chong et al., 2010, Perillo-Marcone et al., 2004, Taylor et al., 2012, Quevedo González et al., 2023, Fitzpatrick et al., 2014a, Quevedo González et al., 2019).

However, BMD measurements cannot distinguish micro-architecture and are influenced by imaging artifacts (including metal artifacts in the vicinity of implants). These factors are important when considering the tibial component: the loading transferred from a tibial implant (often metal with observed image artefacts (Karbowski et al., 1999)), is predominately to cancellous bone

(Bloebaum et al., 1994, Hashemi and Shirazi-Adl, 2000), of which micro-architecture is a key component for strength (Keaveny, 2001).

2.1.5.2 Trabecular Bone Morphometric Parameters

The strength of trabecular bone is highly dependent upon its micro-architecture (Keaveny, 2001). Three-dimensional (3D) analysis of the structure of trabecular bone is possible through micro-computer tomography (micro-CT) quantified morphometric parameters, with some parameters providing a potentially better prediction of ultimate load than BMD from CT or Dual Energy X-ray Absorptiometry (DEXA) (Perilli et al., 2012, Mittra et al., 2008, Ulrich et al., 1997). Micro-CT derived morphometric parameters reported within the literature include:

Bone volume fraction (BV/TV, %): a measure of the total segmented bone volume (BV) within the volume of interest, expressed as a fraction of the tissue volume (TV) (Parfitt et al., 1987, Perilli et al., 2006). BV/TV has been reported as a strong predictor for ultimate load (Perilli et al., 2012) and can explain up to 85 % of the variation in cancellous bone elastic properties (Ulrich et al., 1997).

Trabecular Thickness (Tb.Th, μm): a measure of the average width of the trabeculae, calculated with either 2D or 3D (sphere-fitting) methods (Parfitt et al., 1987, Hildebrand and Rüegsegger, 1997). Statistically significant associations have been found between Tb.Th and crack initiation (Turunen et al., 2020).

Trabecular Separation (Tb.Sp, μm): the average space between trabeculae struts, calculated either with 2D or 3D (sphere-fitting) methods (Parfitt et al., 1987, Hildebrand and Rüegsegger, 1997).

Trabecular Number (Tb.N, mm^{-1}): the number of trabeculae per unit length (typically mm^{-1}) (Parfitt et al., 1987). Tb.N has been found to better correlated to ultimate strength than Tb.Th (Mittra et al., 2008).

Whilst the importance of micro-architecture to the mechanical properties of trabecular bone has been identified and tools for morphometric analysis developed, mathematical equations relating these parameters to yield stress are yet to be derived and are not widely employed.

2.1.6 Bone Distribution in the Proximal Tibia

The focus of this thesis will be on the cancellous tissue of the proximal tibia, accounting for 94% of the surface area of the resected bone (Bloebaum et al., 1994). The cancellous bone at the proximal tibia redistributes knee joint loading, dispersing the compressive forces from the medial and lateral femoral condyles (Capozza et al., 2010). The distribution of trabecular bone is reflective of this loading (Roberts et al., 2018).

Through indentation tests, the penetration strength (reflective of ultimate axial compressive stress, in MPa) of cancellous bone immediately under the subchondral bone, and then moving distally away, has been quantified (Harada et al., 1988, Hvid and Hansen, 1985). From these studies, it has been found that stronger bone exists in the regions under the medial and lateral condyles (Figure 2. 4), with the medial bone typically being stronger by a factor of 1.7 (range: 0.8-2.5) (Harada et al., 1988, Hvid and Hansen, 1985). In the intercondylar region of the proximal tibia, where there is no direct loading from the two femoral condyles, there is reduced cancellous bone strength (Harada et al., 1988, Hvid and Hansen, 1985).
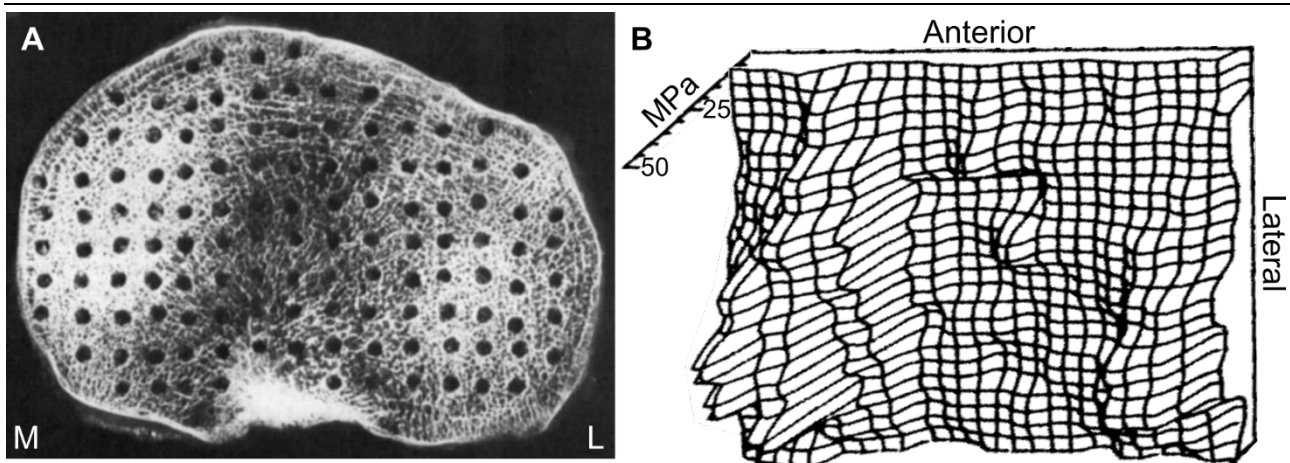
Figure 2. 4: Bone distribution of the proximal tibial. A) Contact radiograph of a right proximal tibia, showing increased cancellous bone density under the medial (M) and lateral (L) condyles. A thin wall of cortical bone surrounds the cancellous bone. The measurement locations for the bone strength testing are visible. B) the bone strength (in MPa), measured via penetration tests, across the proximal tibia, again with greater strength correlating to areas of greater cancellous bone density.
Figure amended from Hvid and Hansen (1985). Reprinted with permission from John Wiley and Sons.

Cancellous bone is strongest within the first 5.00 mm from the subchondral bone plate (Harada et al., 1988, Hvid and Hansen, 1985). Distally from this point, its strength and density decreases as, conversely, the cortical wall becomes thicker and stronger (Takechi, 1977, Capozza et al., 2010). The depth of the resected cut also therefore dictates the mechanical properties of the exposed surface. Depending on the age, region, gender and depth of the resection, the ultimate strength of the cancellous bone of the proximal tibia can vary by a factor of 17.7 transversely (Hvid and Hansen, 1985)), and, decrease by a factor of 3.55 within the first 5.00 mm (Harada et al., 1988).

Osteoarthritis, the leading reason for undergoing TKA in Australia (AOANJRR, 2022), changes the mechanical properties of this tissue. Sclerotic bone, predominately found in late stage osteoarthritis, is stiffer than healthy bone (Loeser et al., 2012) and typically occurs in higher incidence on the medial tibial condyle to the lateral (Purcell et al., 2022, Finlay et al., 1982), although dependent on knee joint alignment (Roberts et al., 2017, Rapagna et al., 2021). Depending on the state of the disease, the surgeon may have to increase the depth of the resected cut to remove such bone.

2.2 PRIMARY STABILITY OF CEMENTLESS TIBIAL IMPLANTS

Primary stability refers to the initial mechanical interlock achieved between implant and bone before any biological fixation occurs, whether that be bony ingrowth or fibrous tissue fixation. It is dependent on the strain state induced in the surrounding bone and the frictional parameters at the interface. Adequate primary stability facilitates osseointegration by providing a mechanically favourable environment for the formation of an initial unmineralized extracellular matrix (ECM) on the implant surface and its subsequent mineralisation.

The induced strain field following implantation of the tibial component should lie within the safety margin as defined by Huiskes (1993), whereby there is sufficient strain within the surrounding cancellous bone to provide stability but not too great to cause gross failure. Whilst the theory exists, the strain required to achieve this balance remains unknown. The induced strain is made up of four components: the elastic strain, the inelastic strain due to permanent damage, the inelastic strain due to plastic flow and the recoverable strains due to viscous creep (Jepsen et al., 2009). It is believed that stability is provided by the elastic and recoverable strains (Dawson and Bartel, 1992, Curtis et al., 1992). The compressive strains following implantation within the bone result in frictional resistance that prevents movement between the implant and surrounding bone, thereby permitting osseointegration (Dawson and Bartel, 1992, Damm et al., 2017). Due to the viscoelastic nature of cancellous bone, it is not known how long the stability provided by the residual elastic components following the surgery last (Bishop et al., 2014, Norman et al., 2006, Berahmani et al., 2015a).

Secondary stability is achieved at the onset of a permanent biological fixation. For the ideal case of osseointegration, this occurs when the newly developed immature woven bone is remodelled to lamellar bone. Within rat models, remodelling of the woven bone occurred as early as four weeks post operatively and extended up to 16 weeks (typically 8 weeks and beyond), defining the end of the primary stability period (Brånemark et al., 1997). The bony fixation will continue to remodel over the lifetime of the implant, being one of the reported benefits of cementless implants.

2.3 FACTORS INFLUENCING PRIMARY STABILITY

2.3.1 Surgical Factors

2.3.1.1 Interference Fit

During surgery an interference fit is employed whereby the tibia is under-resected relative to the implant geometry. This ensures bone-to-implant contact and, theoretically, establishes radial and circumferential strains by compressing the bone to achieve proper seating. Primary stability is thought to be generated through the elastic component of this induced response (Jepsen et al., 2009).

Increased stability of cementless components corresponding to increased interference has been reported in the literature (Berahmani et al., 2015a, Norman et al., 2006, Curtis et al., 1992, Damm et al., 2015). However, a complex relationship between interference fit and achieved stability is apparent. Reported benefits are often dependent on additional factors, including implant surface roughness or morphology (Berahmani et al., 2015a, Damm et al., 2017), bone density and/or volume (Damm et al., 2017), and bone relaxation (Berahmani et al., 2015a, Norman et al., 2006). Some studies found no difference in stability with varied nominal interference fit (Gebert et al., 2009) whilst others report a negative trend between stability and nominal interference fit (Sánchez et al., 2021).

The desired overlap, in millimetres (mm), between implant and resected bone is termed the **nominal interference fit**. Surgical variation (including cutting error and implant positioning) and bone damage are known to occur during implantation. The effect that this has on the achieved bone-implant overlap and the resulting issue response remains largely unknown. The **actual interference fit** refers to the overlap (in mm) achieved and is dependent on the accuracy of the resection and the alignment of the implant to the cut guides (Damm et al., 2015, Berahmani et al., 2018). Whilst for femoral components, Berahmani et al. (2018) reported an inhomogeneous actual interference fit across the bone-implant interface, with some gaps present. In their *ex-vivo* study on cancellous bone cubes, Damm et al. (2015) reported an actual interference fit that could be as low as 30% of the nominal interference fit.

Whilst it is believed that the elastic response of the surrounding cancellous tissue contributes to implant stability, permanent bone deformation is inflicted during the impaction process. Aside from the abrasion of the resected surface during impaction (Bishop et al., 2014, Damm et al., 2015, Damm et al., 2017), multiaxial and confined compression in the surrounding cancellous bone results in pressure induced yielding¸ that extends past the bone- implant interface (Dawson and Bartel, 1992, Berahmani et al., 2015a, Kelly et al., 2013, Rapagna et al., 2019). The **effective interference fit** refers specifically to the elastic deformation of bone following the impaction. It is dependent on the extent of induced permanent damage, the surface morphology of the implant

and the density of the surrounding bone (Bishop et al., 2014, Damm et al., 2017, Berahmani et al., 2015a, Berahmani et al., 2018). Little is known about the interplay between nominal interference fit, actual interference fit, the elastic response and the permanent deformation, and, furthermore, how the latter two contribute to primary stability separately.

2.3.1.2 Cut Accuracy Across the Resected Surface

The resected surface refers to the horizontal cut made across the proximal tibia, upon which the tray of the implant will come to sit. Ideally, the resected surface will be minimally rough (difference between highest and lowest points) and flat (standard deviation between surface point heights)(Toksvig-Larsen and Ryd, 1991). Such a resection provides complete contact between the implant tray and underlying bone. This is an important factor in cementless tibial components, in which osseointegration is desired. Furthermore, unlike for cemented tibial components, the absence of cement is not able to fill any surface irregularities. Complete contact has important implications in preventing the cancellous bone in contact with the implant from overloading and encouraging osseointegration.
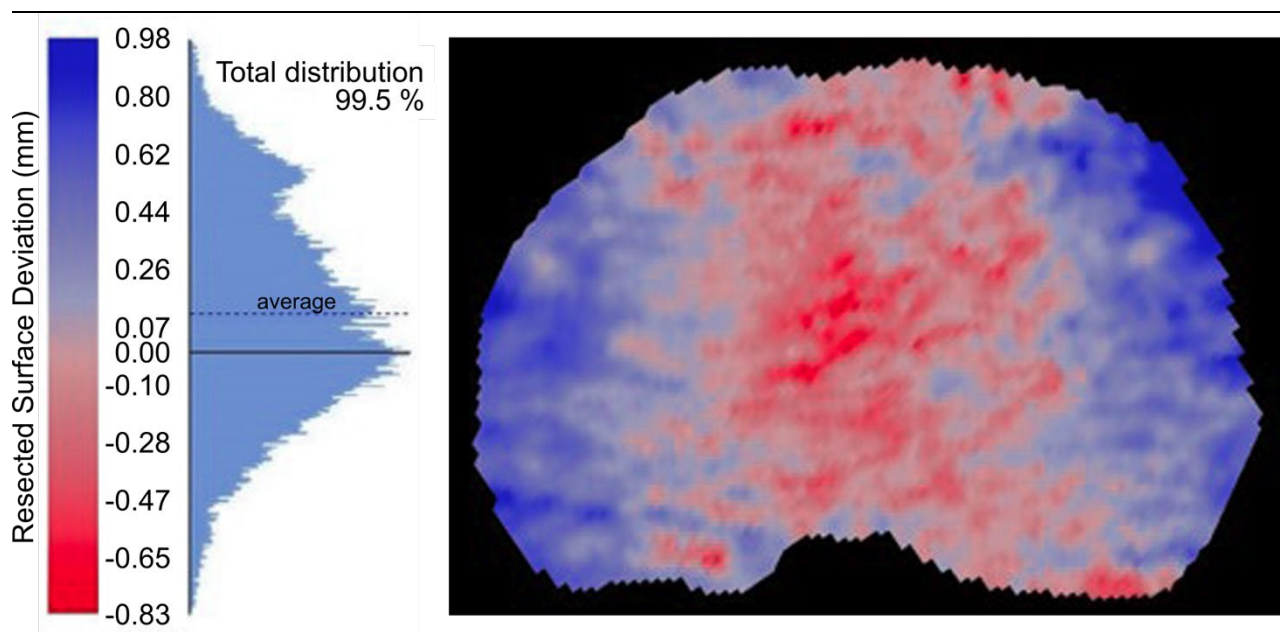
Figure 2. 5: Resected surface roughness, displaying peaks (blue) and low points (red). Here a typically distribution, as reported within the literature, is shown, with a central dipping in the intercondylar region. Figure amended from Delgadillo et al. (2020). Reprinted with permission from Elsevier.

Three studies undertaken on cadaveric tibiae reported roughness values between 0.56-2.57 mm and flatness between 0.10-0.40 mm (Toksvig-Larsen and Ryd, 1991, Toksvig-Larsen and Ryd, 1994, Delgadillo et al., 2020), with comparable surface patterns. As depicted in Figure 2. 5, a consistent dipping of the resected surface in the central cancellous bed, between the anterior cruciate ligament and posterior cruciate ligament zones, was reported (Toksvig-Larsen and Ryd, 1994, Delgadillo et al., 2020). It is hypothesized that this stems from the surgical technique, whereby the oscillating blade is pulled down into the softer cancellous bone of the intercondylar region (Delgadillo et al., 2020).

A rough surface limits the contact between the tray and underlying bone, with as little as 0.2% of bone in initial contact (Delgadillo et al., 2020). The bone in contact with the implant is exposed to substantially higher stresses than if complete (100 %) contact were achieved. The subsequent stresses are sufficiently high to place the cancellous bone at risk of yielding (Taylor et al., 1998). This may explain in part the high initial subsidence of cementless tibial components reported clinically (Koster et al., 2023).

The minimum contact required to achieve adequate fixation is not known from the literature, with some authors reporting that fixation is not jeopardized by the presence of some gaps (Rao et al., 2010) and others reporting that it is (Viceconti et al., 2006, Viceconti et al., 2001).

2.3.1.3 Tibial Component Alignment

Tibial component alignment refers to both the planar positioning and the rotational alignment of the tibial component with respect to the anatomical knee. Issues with malalignment result from detrimental changes to the induced stress or strain field within the bone and additional shear forces at the bone-implant interface (Green et al., 2002, Berend et al., 2010, Werner et al., 2005, Bottlang et al., 2006). In *ex-vivo* and *in-silico* studies, misalignment has been associated with increased micromotion (Navacchia et al., 2018, Hashemi and Shirazi-Adl, 2000) and torsional moments (Kessler et al., 2006) at the bone-implant interface. Furthermore, due to the variation in trabecular bone strength and density across the proximal tibia (Harada et al., 1988, Capozza et al., 2010, Hvid, 1988), planar misalignment can compromise the strength of the supporting bone. A heightened risk of trabecular bone overloading has been reported for misaligned components (Frost, 1987, Kessler et al., 2006, Taylor and Tanner, 1997, Berend et al., 2010).

Clinically, misalignment can result in early prosthetic failures and patient pain (Bargren et al., 1983), however, detrimental effects are not consistently found (Parratte et al., 2010). Developments in computer-aided and robot-assisted joint replacements may reduce these incidences, with the Australian National Joint Registry finding a lower revision rate with the use of robotic assistance (AOANJRR, 2022).

2.3.1.4 Tibial Component Sizing

Achieving cortical contact by the tibial implant component is a preference by some orthopaedic surgeons. Whilst cortical bone of the proximal tibia is relatively thin (reported as 0.5mm (Capozza et al., 2010)), achieving cortical contact ensures increased surface coverage by, and therefore underlying support to, the tibial component (Quevedo González et al., 2023). However, the clinical benefits are limited. An RSA study has found no difference in migration rates of cementless tibia trays for those that did have medial cortex contact to those that did not (Linde et al., 1991).

2.3.2 Micromotion

Micromotion refers to the recoverable relative motion between the implant and underlying bone. It is believed that with sufficient primary stability, such motion will be suppressed. In many studies, primary stability is defined solely on the basis of micromotion (Viceconti et al., 2006, Norman et al., 2006, Camine et al., 2016). There is a clear clinical association with this claim; fundamental work by Pilliar et al. (1986) and Søballe et al. (1992) reported bony ingrowth in regions where micromotion was less than 50 µm and fibrous tissue development where they exceeded 150 µm. Based on such claims, the potential for osseointegration could solely be assessed by the surface micromotion, and many studies have used these limits for such analysis (Sala et al., 1999, Chong et al., 2010, Fitzpatrick et al., 2014a, Sánchez et al., 2021, Quevedo González et al., 2019, Taylor et al., 2012). A recent review by Kohli et al. (2021) has discredited a universal limit of tolerable micromotion for osseointegration, instead reporting a complex system that is dependent on many implant and external environmental factors. Furthermore, low levels of micromotion may be beneficial for osseointegration by simulating a fracture healing response (Wazen et al., 2013). However, it is largely accepted that reducing micromotion assists in bony ingrowth.

Since telemetric data has become available through instrumented knee replacements (Kutzner et al., 2010, Bergmann et al., 2014), a number of experimental (Van Valkenburg et al., 2016) and FE models (Taylor et al., 2012, Fitzpatrick et al., 2014a, Quevedo González et al., 2019) have employed their loading profiles, or variations of them (Navacchia et al., 2018, Han et al., 2020, Sánchez et al., 2021, Yang et al., 2020) when assessing micromotion. Consequently, micromotions have been quantified at discretised time points of common ADLs, including stand to sit, stair ascent and descent, deep knee bend (DKB) and gait. Prior to telemetric loading profiles, other papers have employed dynamic loading protocols to simulate gait (Chong et al., 2010) and stair climbing (Bhimji and Meneghini, 2012). A finding common amongst these papers is that the largest micromotions occur when high moments and shear loads combine with low axial forces (Taylor et al., 2012, Fitzpatrick et al., 2014a, Quevedo González et al., 2019). In considering the loading profiles of ADLs, such instances occur during gait and stair ascent and descent, with stair climbing commonly associated with greatest micromotion (Bhimji and Meneghini, 2014, Bhimji and Meneghini, 2012, Chong et al., 2010, Han et al., 2020, Taylor et al., 2012). Whilst the micromotion magnitude may vary, a sagittal rocking motion of the tray is commonly reported across these activities, with anterior edge lift-off and posterior-edge seating (Bhimji and Meneghini, 2012, Bhimji and Meneghini, 2014, Chong et al., 2010, Fitzpatrick et al., 2014a, Han et al., 2020, Quevedo González et al., 2019, Sánchez et al., 2021).

If 50 µm micromotion is taken as the upper permissible limit for osseointegration (Pilliar et al., 1986), the recorded micromotions in several of these papers are sufficient to hinder osseointegration, in at least one of the loading scenarios or measured location (Bhimji and Meneghini, 2012, Taylor et al., 2012, Fitzpatrick et al., 2014a, Chong et al., 2010, Han et al., 2020,

Sánchez et al., 2021, Navacchia et al., 2018, Quevedo González et al., 2019, Yang et al., 2020). Whether osseointegration will occur or not cannot be guaranteed based on the assessed micromotion alone (Kohli et al., 2021). Kohli et al. (2021) reported incidences of successful osseointegration even in the presence of higher micromotion when there was: infrequent loading during the initial period, a rest period following initial loading and hydroxyapatite coating on the implant.

2.3.3 Bone Quality

Cementless tibial components come into intimate contact with cancellous bone, exposed during the resection. The properties and quantity of this peri-prosthetic bone therefore dictates the mechanical environment across the bone-implant interface, with implications to both the initial primary stability and longer-term migration. Due to difficulties in measuring the strength of bone in contact with the implant in both clinical and lab studies, bone quality has been indicated by its density and morphometric parameters.

In a population-based FE analysis, tibiae at higher risk of localised failure at the bone-implant interface had a mean modulus (276 MPa) that was half that of those in the lower risk group (590 MPa) (Galloway et al., 2013). In experimental *ex-vivo* studies, greater bone density has been associated with increased mechanical fixation (both push-in and pull-out forces) (Damm et al., 2017, Berahmani et al., 2017, Berahmani et al., 2015a, Mueller et al., 2013, Burgers et al., 2010) and reduced micromotion (Meneghini et al., 2011, Berahmani et al., 2017, Kohli et al., 2021). Furthermore, greater bone density appears to protect against permanent damage from occurring during impaction (Berahmani et al., 2018) and pull-out tests, whereby there is better recruitment of trabeculae further away from the bone-implant interface (Mueller et al., 2013).

Correlations have been found between peri-prosthetic BMD and cementless tibial component migration in Roentgen Stereophotogrammetric Analysis (RSA) studies. Continuous migration, being migration that pursues after the first post-operative year, can be detrimental to the long-term success of the implant, with increased incidences of loosening and revision reported (Ryd et al., 1995). Both Andersen et al. (2017) and Li and Nilsson (2000) reported a negative relationship between migration of cementless tibial components and BMD, with lower BMD being associated with higher net migration at all time points of their separate two-year studies. However, the contribution of BMD to migration was low, accounting for a maximum of 27 % (Andersen et al., 2017), highlighting a complex system. Still, some authors recommend reserving cementless TKA for patients with higher bone density (Sharkey et al., 2002), although a threshold has not been suggested, and there does not appear to be a defined limit that ensures no continuous migration (Andersen et al., 2017).

These studies are also subject to the same limitations discussed previously for assessing the mechanical properties of cancellous bone. Clinical studies often report on DEXA derived areal

BMD (Andersen et al., 2017, Berahmani et al., 2018, Berahmani et al., 2017, Berahmani et al., 2015a, Li and Nilsson, 2000), therefore not separating cortical and trabecular bone nor capturing the 3D architecture of the latter. Two papers (Mueller et al., 2013, Damm et al., 2017) quantified morphometric parameters of their bone samples, including trabeculae bone volume (BV), BV/TV, and, Tb.Th, Tb.Sp and Tb.N (see *2.1.5.2 Trabecular Bone Morphometric Parameters* for their definitions), however only used BV and BV/TV in their analysis of implant stability. Limitations in assessing the mechanical properties of bone in intimate contact with the tibial component may be why some studies find no contribution, or inconsistent contribution, of these properties of bone to primary stability (Damm et al., 2017, Sánchez et al., 2021, Berahmani et al., 2017).

2.3.4 Tibial Component Design

A large body of research exists surrounding the design, surface topography and surface finish of cementless tibial components. Correlations have been drawn between these factors to the induced stress or strain field (Taylor and Prendergast, 2015, Hashemi and Shirazi-Adl, 2000, Dawson and Bartel, 1992, Bottlang et al., 2006), implant micromotions (Kohli et al., 2021, Taylor et al., 2012, Meneghini et al., 2011, Bhimji and Meneghini, 2014, Kraemer et al., 1995, Miura et al., 1990, Stern et al., 1997, Sala et al., 1999, Lee et al., 1991), damage caused during impaction (Bishop et al., 2014, Gao et al., 2019, Damm et al., 2015, Wennerberg and Albrektsson, 2009, Norman et al., 2006) and recruitment of osteogenic cells (Kohli et al., 2021, Søballe et al., 1992). Such analysis or comparison is beyond the scope of this study.

A wide range of implants exist on the market, with the AOANJRR reporting 28 cementless femoral and tibial component combinations for modern devices that were used in over 400 procedures in 2021 (AOANJRR, 2022). Of these 28 different combinations, 14 combinations have data on 15 years revision rates ranging between 3.7 % (NexGen TM LPS tibial component and NexGen LPS femoral component) to 13.1 % (Columbus tibial and femoral component). Only 3 combinations have 20-year revision rates: a NexGen tibial component and NexGen CR femoral component (5.7 % 20-year revision, both Zimmer Biomet); a LCS tibial component and LCS CR femoral component (8.8 %, both DePuy Synthes); and, a MBT Duofix tibial component and LCS CR femoral component (9.8 %, both DePuy Synthes).

Advancements in manufacturing, namely 3D printing porous surfaces and additive manufacturing, have recently been gaining popularity. Such technologies produce a surface that morphologically represents cancellous bone (and with comparable stiffness), thereby promoting osseointegration (Hasan et al., 2020). Furthermore, the costs of 3D printing have decreased substantially in the past two decades, making their use more widespread (Hasan et al., 2020). Clinical results are promising, with 2- and 5-year revision rates (reflective of the critical period for primary stability) comparable to cemented components (Zhou et al., 2018, Restrepo et al., 2021).

2.4 LIMITATIONS IN ASSESSING PRIMARY STABILITY

2.4.1 Experimental Methodologies

2.4.1.1 Mechanical Fixation

Whilst not specifically undertaken for cementless tibial TKA components, mechanical fixation strength refers to methods that assess the primary stability of an implant via its force resistance. Forces measured in the literature for uni-compartmental knee replacement, dynamic hip screws, femoral components and stems, acetabulum cups, and excised bone cubes with pegs include push-in force (Bishop et al., 2014, Damm et al., 2017, Mueller et al., 2013, Norman et al., 2006, Campi et al., 2018), pull-out force (Bishop et al., 2014, Berahmani et al., 2015a, Damm et al., 2015, Damm et al., 2017, Søballe et al., 1992, Campi et al., 2018, Berahmani et al., 2017), and resistance to torque (Curtis et al., 1992, Gebert et al., 2009, Ryd et al., 1999). In each instance, load is applied directly to the component, whilst the bone is secured. Fixation properties, including ultimate shear strength, ultimate yield strength, torque capacity, apparent stiffness and energy absorption, can be extracted or estimated when load deformation curves are recorded.

A fundamental flaw of mechanical fixation assessments is that they often assess failure loads as a result of non-physiological loading. Whilst previous results have found a direct relationship between pull-out force and primary stability (Berahmani et al., 2015a), such analysis has two limitations. Firstly, crack propagation at the bone-implant is unstable once initiated (Gao et al., 2019). Secondly, primary stability is provided by the elastic deformation of bone (Jepsen et al., 2009), rather than the failure strength as is being assessed through such methods (Gebert et al., 2009). Stability at physiologically relevant load cases, as occurring post-operatively, should instead be assessed.

Development of sophisticated imaging tools has allowed for some such analysis to occur (Marter et al., Mueller et al., 2013, Berahmani et al., 2017). Berahmani et al. (2017), through synchronising digital image correlation (DIC) with loading, assessed the force required to induce micromotions of 50 µm (taken as the limit of osseointegration) and 150 µm (growth of fibrous tissue) for two cementless femoral components. Clinically relevant and significantly different forces were required between the two implants to induce such micromotions (50 µm: 501 N (Attune) vs 263 N (LCS), p = 0.015; 150 µm: 784 N (Attune) vs 322 N (LCS), p = 0.002) (Berahmani et al., 2017). Such a difference was not found when the pull-off force was assessed (p = 0.757) (Berahmani et al., 2017), highlighting the issues of crack propagation.

2.4.1.2 Micromotion

As discussed previously, micromotion is a metric commonly used to assess primary stability, with direct correlations to previously accepted osseointegration limits. Micromotion measurements have been undertaken experimentally for cementless tibial components through linear-variable differential transducers (LVDTs) and other extensometers (Lee et al., 1991, Miura et al., 1990, Kraemer et al., 1995, Stern et al., 1997, Sala et al., 1999, Meneghini et al., 2011, Bhimji and Meneghini, 2012, Bhimji and Meneghini, 2014, Chong et al., 2010, Van Valkenburg et al., 2016), and more recently DIC (Small et al., 2016, Navacchia et al., 2018, Han et al., 2020, Sánchez et al., 2021). Much insight has been gained through these studies, as included in the preceding sections. However, these methods fall short of the system requirements for assessing micromotion as stipulated by Viceconti et al. (2000). Firstly, as it appears that even a small area of fibrous tissue fixation (developed as a result of excessive micromotion) can result in compromised implant stability (Viceconti et al., 2001, Baker et al., 2007), full field micromotions need to be extracted across the entire interface. Secondly, with the proposed osseointegration limit of 150 μm (Søballe et al., 1992, Pilliar et al., 1986), these systems should have an accuracy below 15 μm (<10%) (Viceconti et al., 2000).

LVDTs and other extensometers are limited to the surface of the specimen, and, are only able to capture micromotion at a discrete number of peripheral locations at the bone-implant interface. As inherent in the name, they are limited to linear displacement, therefore only capturing one component of micromotion. Additionally, such sensors require an external frame, which may introduce an unknown level of compliance (Sala et al., 1999), and, in some instances, may amplify the recorded motions due to an offset (Bhimji and Meneghini, 2012, Bhimji and Meneghini, 2014, Sala et al., 1999). These issues surrounding the external frame can be mitigated with careful configuration and error assessment (Monti et al., 1999), providing a precise measurement tool for relative motion, however still only at the location where they are applied.

DIC provides a continuous, non-contact micromotion measurement, with resolution finer than 10 μm (Small et al., 2016, Berahmani et al., 2017). DIC (and LVDTs) are not able to distinguish between relative bone-implant micromotion and underlying bone deformation, introducing uncertainties in the results (Berahmani et al., 2017, Monti et al., 1999). In order to get 3D measurements spanning the whole periphery of the interface, either multiple trials (Small et al., 2016, Sánchez et al., 2021) or multiple cameras (Han et al., 2020) are required, which is not always possible (Berahmani et al., 2017). None of the found studies assessed a complete outer perimeter. Of these papers, Han et al. (2020) measured the largest continuous region, including two posterior and six anterior regions through 30° zonal arcs, amalgamating to two thirds of the periphery.

Few published experimental studies exist that quantify micromotion between implant and bone across the internal interface. For femoral stems and bone replicas, internal shear micromotion has been measured by drilling 3.75 mm holes through the cortical bone. This exposed the internal interface, from which radial micromotion was measured with an LVDT anchorage system (Monti et al., 1999, Monti et al., 2001b, Monti et al., 2001a). As with all LVDTs, the measurements were limited to one direction, being axial rotation, and, to the discrete locations where the sensors were attached. The system was able to achieve an experimental error of 3.5 μm (Monti et al., 1999). In comparison to the detrimental micromotion limits for osseointegration (150 μm) this is low, however, when comparing this error to the measured shear micromotion during the data collection, which remained below 8 μm in all but one specimen (Monti et al., 2001b, Monti et al., 2001a), this is notable. Furthermore, the potential effect on the micromotion due to the damage induced by drilling the holes was not discussed.

A recent body of work by Gortchacow et al. (2011), Camine et al. (2016), Camine et al. (2018) experimentally extracted the internal micromotion between a femoral stem and the cadaveric host bone. Here, radiopaque beads were adhered to the cadaveric cavity after which a time-elapsed mechanical load sequence with concurrent micro-CT imaging was undertaken. 3D rigid co-registration of the micro-CT datasets was performed to align the femoral stems in the loaded and unloaded scans. Micromotion was then extracted as the 3D vector displacement of the bone beads when unloaded to loaded. This method, whilst experimentally extracting the internal micromotions, still has limitations. The extracted micromotions were not between bone and implant, but displacement of bone only, with the assumption of implant rigidity. It is therefore dependent on the accuracy of the 3D rigid co-registration between scans and the fixation of the markers into the bone. The latter was tested in their accuracy and precision tests, the errors of which were sufficiently low (accuracy (bias) ≤ 5.1 μm and precision (repeatability) ≤ 10.6 μm (Camine et al., 2016)). However, this did not assess the accuracy of the 3D rigid co-registration as the specimen (to the best of this author's knowledge) was not moved between unloaded scans. As such, the accuracy of the whole analysis technique, being how the subsequent measurements were made, was not assessed. Furthermore, 313 micromotion measurement points were extracted in their compression test, and full-field micromotion was calculated by extrapolating between. Whilst this is a substantially greater number of measurement points than other experimental tests, it is not known how evenly these points were distributed across the whole cavity and regions with a high micromotion gradient may be missed (Viceconti et al., 2000).

To the best of the author's knowledge, no experimental work has yet been undertaken to quantify the micromotion between a cementless tibial tray and underlying bone internally, with the published work so far being restricted to external (circumferential) measurements only.

2.4.1.3 Strain measurements

Strain gauges have long been considered the "gold standard" of strain measurement, with comprehensive protocols developed (Finlay et al., 1982, Grassi and Isaksson, 2015). However, measurement points are limited and localised to placement of the strain gauge. As the mechanical response of cancellous bone to the impaction is highly localised to the bone-implant interface (Kelly et al., 2013, Dawson and Bartel, 1992, Rapagna et al., 2019), it is not be possible to place strain gauges closes enough to, and obtain sufficient measurement points, to capture the high strain gradient (Completo et al., 2008). Furthermore, strain gauges often reinforce the bone due to their non-negligible-stiffness (Cristofolini et al., 2010b), and may miss areas of high strain (Completo et al., 2007, Gray et al., 2008).

DIC can be used to capture 2D or 3D surface strains on cadaveric specimens, again providing a non-contact and continuous measurement. The use of DIC for strain measurements is still subjected to the same limitations as its use for micromotion: requiring multiple cameras for 3D analysis and multiple trials for full-peripheral measurements (Grassi and Isaksson, 2015). Until recently, strain measurements extracted through DIC were only used qualitatively (Den Buijs and Dragomir-Daescu, 2011, Helgason et al., 2014). As the spatial resolution and frame rate of cameras improve, quantitative analysis is now possible (Grassi and Isaksson, 2015, Palanca et al., 2016b). However, its use in orthopaedic applications is still limited. Rather, DIC is used in the validation process of FE models through a micromotion analysis. With the models validated, a stress or strain analysis is then performed (Yang et al., 2020, Yang et al., 2021).

Continuum-level strains can be measured through a photoelastic resin coating applied to the tibial cortex. Here, the tibia is cleaned and a layer of photoelastic resin (contoured to the shape of the bone) is bonded with epoxy cement. Shear strains across the surface of the resin, inferring the strains at the cortex of the bone, are measured through a refraction polariscope. For tibiae, this technique has been employed to assess stress shielding and surgical mal-alignment (Berend et al., 2010, Kessler et al., 2006, Green et al., 2002, Small et al., 2010, Small et al., 2011), however, there are limitations. Assessing strain magnitudes is limited to shear strains only, and, due to the reinforcement effect provided by the resin, these values can be reduced by between 1 to 33.4 % (Cristofolini et al., 1994, Glisson et al., 2000). The magnitude of the principal strains can only be extracted through the addition of strain gauges, which need to specifically be compliant with the resin (Glisson et al., 2000). The use of photoelastic resin is therefore recommended for assessing relative shear strain intensity across the cortex, rather than strain magnitudes (Glisson et al., 2000).

As with micromotion measurements, both photoelastic resin and strain gauges are restricted to superficial measurements only. This is a major limitation when assessing the initial mechanical

environment: cancellous bone of the tibia is the principal load bearer (Hashemi and Shirazi-Adl, 2000).

Digital volume correlation (DVC) is a relatively new technique in the study of biomechanics that quantifies the internal displacements, at apparent level, of biological structures from cross-sectional image sets of the specimen in a reference and deformed state. The internal strain of the specimen can then be calculated as the displacement gradient, providing experimentally derived continuous, full-field calculations. In biomechanics, it has been employed to extract internal strain fields for specimens at organ level (Hussein et al., 2012, Palanca et al., 2016a, Tozzi et al., 2016, Dall'Ara et al., 2017, Boulanaache et al., 2020, Zhou et al., 2020b, Martelli et al., 2021, Rapagna et al., 2019, Palanca et al., 2021, Kusins et al., 2019, Kusins et al., 2022), for constructs consisting of bone - screw (Le Cann et al., 2017, Le Cann et al., 2020), bone-dental implant (Zhou et al., 2020a) or bone - implant (polyethylene component (Zhou et al., 2020b, Boulanaache et al., 2020)), for bone augmented with cement (Palanca et al., 2016a, Danesi et al., 2016) and for bone-metal interfaces (Sukjamsri et al., 2015, Marter et al., 2020). Whilst theoretically possible, it has thus far not been undertaken for cadaveric tibiae implanted with commercially available cementless tibial components, or, generally speaking, for long bones at organ level with metal joint replacement components. Such a setup introduces a number of complications, as will be discussed within *2.5 Possibilities and Complications with Digital Volume Correlation*.

2.4.2 Finite Element Models

FE models are able to address some of the limitations met by the current experimental work; predicting internal full-field strain and stress states, and bone-implant micromotion across the entire interface. Through their use, complex loading scenarios can be simulated and the sensitivity to specific parameters can be individually analysed, both of which would be difficult to achieve experimentally.

Previous models commonly represented cancellous bone with homogeneous material properties (Dawson and Bartel, 1992, Taylor et al., 1998, Viceconti et al., 2006). It is now common practice to directly extract the heterogeneous elastic modulus of bone through CT derived equations. However, cancellous bone is often assumed to be isotropic (Viceconti et al., 2006, Chong et al., 2011, Chong et al., 2010, Perillo-Marcone et al., 2004, Hashemi and Shirazi-Adl, 2000, Kelly et al., 2013, Taylor et al., 1998, Quevedo González et al., 2023, Quevedo González et al., 2019, Innocenti et al., 2009) and linearly elastic, with only a few studies including post-yield behaviour (Kelly et al., 2013, Soltanihafshejani et al., 2021, Soltanihafshejani et al., 2023). As such, bone's anisotropic behaviour, viscoelasticity and failure response are all simplified or disregarded. A new body of work is emerging with the development of crushable foam (CF) models, whereby an isotropic hardening response is introduced (Kelly et al., 2013, Soltanihafshejani et al., 2021, Lee et al., 2017, Soltanihafshejani et al., 2023). Such models are reported as being able to better

represent the mechanical properties of bone, particularly its post-yield behaviour (Kelly et al., 2013, Soltanihafshejani et al., 2021, Lee et al., 2017). Due to the damage of cancellous bone known to occur during the impaction process, authors have flagged its importance when modelling the initial mechanical environment surrounding an implant. Unfortunately, these models are dependent on extracting material properties (compressive elastic modulus, Poisson's ratio in uniaxial compression, yield stress in both uniaxial compression and confined compression) through *ex-vivo* mechanical testing (Soltanihafshejani et al., 2023), thus limiting their use.

FE models are also highly sensitive to friction coefficients used (Hashemi and Shirazi-Adl, 2000), implant material rigidity (Gray et al., 2008) and bone-implant bonding (Dawson and Bartel, 1992). When simulating cementless tibial components in the immediate post-operative period (prior to any biological attachment), most FE studies model the interaction between implant and bone as frictional, but ignore an interference fit (Viceconti et al., 2006, Chong et al., 2010, Hashemi and Shirazi-Adl, 2000, Taylor et al., 2012, Taylor et al., 1998, Quevedo González et al., 2023, Fitzpatrick et al., 2014a, Quevedo González et al., 2019). There are very few studies that do include an interference fit (Kelly et al., 2013, Dawson and Bartel, 1992), and often those modelled are smaller than what is clinically employed (Navacchia et al. (2018): interference of 0.05, 0.10 and 0.15 mm; Yang et al. (2020): interference of 0.002, 0.005, 0.010, 0.025, 0.050 and 0.100 mm modelled; in comparison to clinically employed levels of: 1.00 – 2.00 mm (DePuy Synthes, 2016, DePuy Synthes, 2023)). When assessing the primary stability of cementless tibial components it is important that the mechanical interaction between the implant and bone is properly represented.

To determine the correct selection of parameters, and justification for assumptions made, FE models need be validated against controlled *ex-vivo* experimental results (Viceconti et al., 2005), which is not always undertaken (Dawson and Bartel, 1992, Taylor et al., 1998, Perillo-Marcone et al., 2000, Perillo-Marcone et al., 2004, Perillo-Marcone and Taylor, 2007, Taylor et al., 2012, Kelly et al., 2013, Fitzpatrick et al., 2014a, Navacchia et al., 2018, Quevedo González et al., 2019, Quevedo González et al., 2023). Loading boundary conditions of the experiment must be replicated, which is often hard to explicitly extract from the experimental data (Gray et al., 2008). Alignment between comparison points is also essential, thereby limiting comparisons currently to superficial measurements only. The relevance of validating surface values to internal strains and full-field micromotion is not known (Pal and Gupta, 2020). As such, an inability to experimentally extract internal measurements limits not just the experimental studies, but also limits the validation of FE studies.

2.5 POSSIBILITIES AND COMPLICATIONS WITH DIGITAL VOLUME CORRELATION

Digital volume correlation (DVC), originally conceived by Bay et al. (1999), is an image mapping tool that utilises time-elapsed mechanical loading with concurrent 3D imaging to extract internal displacement and resultantly calculate internal strain fields (Figure 2. 6). Volumetric imaging modalities include computer tomography (CT: high-resolution peripheral quantitative (HR-pQCT), and micro-CT imaging), neutron tomography and magnetic resonance imaging (MRI). DVC offers great potential in experimentally analysing the initial mechanical environment surrounding cementless tibial components by extracting internal displacement vectors, from which micromotion and strain values can be calculated.
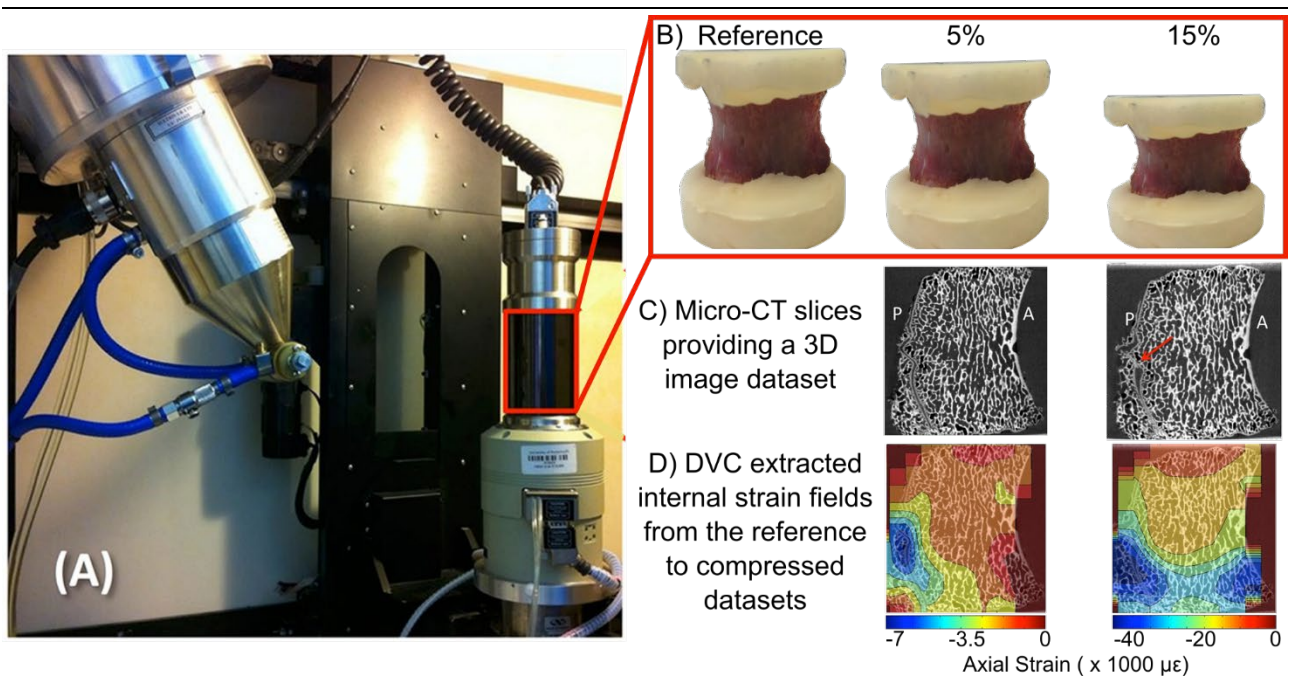
Figure 2. 6: Process for capturing internal full-field strains through DVC: A) Mechanical loading rig within the micro-CT system. B) Specimen (porcine vertebra) within the loading rig, in the reference state and then after 5 % and 15 % compression. C) Micro-CT datasets acquired at each of the load steps, sagittal cross-section only shown for the loaded steps. D) The extracted DVC internal strain fields at each load step.
Figure amended from Tozzi et al. (2016). Reprinted with permission from John Wiley and Sons.

The accuracy and precision of DVC is assessed by performing a zero-strain error analysis, where repeated scanning of the specimen in an unloaded condition is undertaken. As the specimen is unloaded, extracted values that deviate from zero are deemed errors, with the mean an indicator of the measurement's accuracy, and the standard deviation an indicator of the measurement's precision. It has been suggested that these errors should be less than 10 % of the yield strain of bone (Liu and Morgan, 2007, Tozzi et al., 2017) and less than 10 % of the micromotion value indicated for fibrous tissue formation (Viceconti et al., 2000), placing them below 780 to 1,000 µε and 15 µm, respectively (Bayraktar et al., 2004, Pilliar et al., 1986, Søballe et al., 1992). The accuracy and precision of DVC is dependent primarily upon the desired spatial resolution of the extracted field and the quality of the input images (i.e. signal to noise ratio) (Roberts et al., 2014,

Croom et al., 2020, Dall'Ara and Tozzi, 2022), which, for the given application (cadaveric tibia and cementless tibial component), presents multiple complications.

2.5.1 DVC analysis of large specimens using micro-CT datasets

There are several difficulties in obtaining images of sufficient signal to noise ratio for a specimen as large as a proximal cadaveric tibia (approximately 85 mm diameter, 180 mm height) and with a large metal component. DVC analysis has been employed on time-elapsed micro-CT datasets of various organs (Hussein et al., 2012, Tozzi et al., 2016, Kusins et al., 2019, Kusins et al., 2022, Le Cann et al., 2020, Palanca et al., 2016a, Danesi et al., 2016, Sukjamsri et al., 2015, Boulanaache et al., 2020, Zhou et al., 2020a, Zhou et al., 2020b, Du et al., 2015, Jackman et al., 2016). With the development of large gantry micro-CT systems, it is now possible to obtain relatively high resolution scans (33.5 – 39 µm/pixel), permitting organ-level DVC analysis of vertebrae (Hussein et al., 2012, Tozzi et al., 2016) and scapula (specifically the glenoid (Boulanaache et al., 2020, Zhou et al., 2020b)). The extracted strain fields of the referenced studies have a spatial resolution between 1.00 – 4.8 mm and DVC strain errors less than 1,000 µε, enabling analysis of bone within its elastic region (Liu and Morgan, 2007, Tozzi et al., 2017). Theoretically, large gantry micro-CT systems would allow analysis of lower-body long bones, with an internal chamber size permitting specimens up to a diameter 240 mm and height 400 mm (Nikon Metrology, 2020). DVC analysis has been undertaken on cadaveric proximal femurs using synchrotron imaging, whereby a 146 x 146 x 131 mm field of view (FOV) was possible with 30 µm/pixel resolution (Martelli et al., 2021). Whilst the achieved scans were of a high resolution, due to the memory size of the produced datasets (160 GB (Martelli and Perilli, 2018)) and processing restrictions, they had to be down sampled to 120 µm/pixel with a resulting strain field spatial resolution of 6 mm (and precision 760 µε). Whilst hypothetically possible, the size of proximal cadaveric tibiae, and the required mechanical loading rig to induce deformations, presents challenges in achieving manageable high-resolution datasets, that has so far, not been achieved within the literature.

Micro-CT images are produced from the attenuation of X-rays by the interacting matter of the material in their path. Through cross-section image reconstruction, most commonly a filtered back projection algorithm (Hendee and Ritenour, 2003, Feldkamp et al., 1984), the greylevels of the produced tomography slices are representative of the material's attenuation coefficient, μ. The attenuation coefficient is proportional to the material's atomic number (Z) through a power relationship, and inversely proportional to the X-ray beam energy (Stock, 2009). Issues arise when the atomic number of adjacent materials vary substantially, as is the case for cadaveric bone with metal implants. Of three materials commonly used for tibial components (cobalt-chromium alloys, stainless steel and titanium alloys (Cowin, 2001)), titanium (and its alloys) has the lowest attenuation coefficient at $\mu_{Titanium\,(100\,keV)} = 1.22\,cm^{-1}$ (Hubbell and Seltzer, 1996). However, this is still markedly higher than that of bone (Figure 2. 7): $\mu_{Cortical\,Bone\,(100\,keV)} = 0.352\,cm^{-1}$ (Hubbell and Seltzer, 1996). Such differences in attenuation coefficients for materials in the same scan (and

depending on their thicknesses) can result in incomplete attenuation profiles (Barrett and Keat, 2004) and streaking of the cross-section image through beam hardening, scattering, nonlinear partial volume effect and noise, which are all generally termed together as metal artefact (Li et al., 2014). Furthermore, the mechanical loading rigs employed for long bones must be sufficiently strong to impose physiologically relevant loads. Consequently, the walls of micro-CT compatible compression chambers for long bones have been made of aluminium (Martelli and Perilli, 2018, Martelli et al., 2021, Boulanaache et al., 2020), which introduces further attenuation of the X-ray beams ($\mu_{Aluminium\,(100\,keV)} = 0.462\,cm^{-1}$ (Hubbell and Seltzer, 1996)). As the accuracy and precision of DVC analysis is linked to the noise vs. signal of the images (Roberts et al., 2014, Dall'Ara and Tozzi, 2022), the presence of a large metal component, such as a titanium tibial component, and the required mechanical testing rig could compromise such an analysis. DVC analysis using micro-CT datasets on cadaveric bone with metal (TiZr) implants has thus far only been undertaken on smaller components (screws: Ø 2.6 mm (Le Cann et al., 2020), dental implants: Ø 4.1 mm (Du et al., 2015, Zhou et al., 2020a)), where the attenuation is hence lower. These cited authors still reported metal artefact, which may have been the underlying cause of their higher errors (1,060 – 7,400 µε).
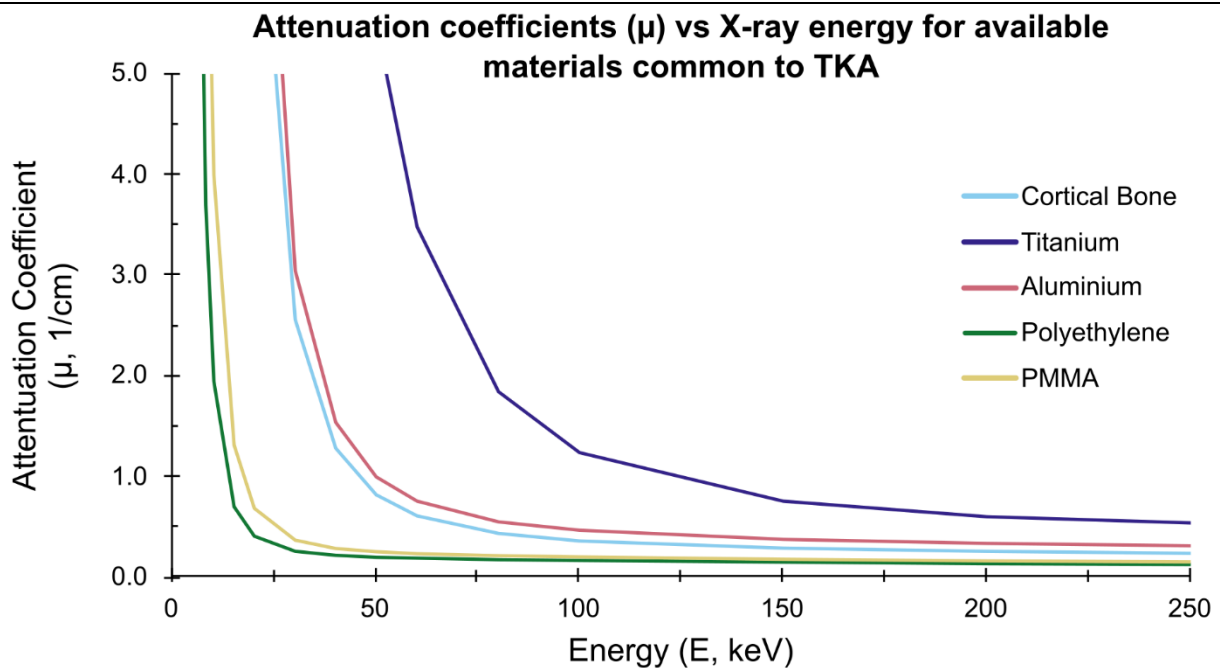
Figure 2. 7: Attenuation coefficients of materials common to TKA against X-ray beam energies (as available: Hubbell and Seltzer (1996)).

Synchrotron micro-CT imaging permits relatively short scanning times due to their high X-ray beam flux. Aside from excised bone biopsies (Comini et al., 2019, Dall'Ara et al., 2017, Peña Fernández et al., 2018, Turunen et al., 2020), DVC has been undertaken on synchrotron-acquired datasets to study the fracture initiation and propagation of the proximal femur (Martelli et al., 2021). As the attenuation coefficient (Figure 2. 7) of a material is dependent on the beam's energy through an inverse power law (Stock, 2009), the applicability of using a synchrotron to acquire micro-CT

images of large metallic components would need to be verified: whilst at the synchrotron a high beam flux can be achieved, the energy of the beam is capped (maximum beam energy of 120 keV at the Australian Synchrotron (Lewis, 2005)).

The aforementioned DVC studies on metallic components ((Le Cann et al., 2020, Du et al., 2015, Zhou et al., 2020a)) were acquired through micro-CT imaging at relatively low source power and energy, potentially due to system limitations (maximum power: 10-20 W and energy: 160-180 keV (Zeiss, 2023, Waygate Technologies, 2023)). Recent developments in efficient heat dissipation of the X-ray tube has resulted in increased power generation and reduced focal size (Li et al., 2008). Large gantry micro-CT scanners are now available commercially that can achieve X-ray beam energies of 225 keV and power 225 W, allowing for larger specimens to be scanned with greater penetration through denser materials (Nikon Metrology, 2020). Whilst this technology is now available, to the best of the author's knowledge, no study has yet been undertaken using micro-CT imaging combined with DVC to investigate the primary stability of cementless tibial components.

2.6 SUMMARY

Cementless tibial components for TKA potentially minimise bone loss over the life of the implant and alleviate issues associated with cement fixation, including debris accumulation and stress-shielding. These factors become increasingly important considering the younger and more active patient cohort, whom are more likely to require a revision surgery within their lifetime. However, cementless tibial components currently have a higher failure rate within the first 1.5-3.5 years, whereby after 4.5 years their revision rate is lower than their cemented counterparts. Such early failure alludes to an inability to gain fixation.

The mechanical environment surrounding the implant in the immediate post-operative period is essential to its long-term success. Sufficient primary stability facilitates bony ingrowth, forming a strong biological fixation that strengthens with time. During surgery, an interference fit is employed to achieve such stability, by under cutting the bone relative to the geometry of implant. Due to this overlap, there is theoretically an elastic mechanical response in the surrounding cancellous bone, which, along with friction at the bone-implant interface, provides primary stability. However, little is known about the interaction between the interference fit and primary stability, or more generally, the initial mechanical environment.

The interference fit achieved differs to the intended (nominal) interference fit due to surgical variation (including variation in the resected surface and alignment of the tray) and the damage induced during impaction. Experimental studies that have investigated the interference fit often do so by changing the nominal interference fit, thereby not acknowledging these variations. Few FE models with cementless tibial components include an interference fit, and, those that do, use interferences that are often lower than what's employed clinically.

Various aspects of primary stability have been assessed experimentally though mechanical fixation and micromotion, however these have limitations. Mechanical fixation assesses the fixation strength at failure loads, with clinically little relevance. Sufficient primary stability can be assessed though micromotion suppression, and, whilst previously established osseointegration thresholds have limitations, it is generally accepted that reduced micromotion is beneficial for bony ingrowth. However, experimental studies are limited to external measurements only and often at discrete locations. FE models can provide micromotion measurements across the entire bone-implant interface, and furthermore, assess the mechanical response of bone by extracting full-field strain, stress and stress energy density fields, often under complex loading simulations. However, the lack of experimental data limits the ability to validate these models. The relevance of validating FE models, from which calculations on the internal environment are made, against superficial measurements is not known. Due to the assumptions made on the interference fit, chosen friction parameters and the linear-elastic material properties of bone modelled (in an environment where damage is known to be inflicted), this validation is essential.

Digital volume correlation undertaken on micro-CT datasets provides an experimental means to extract full-field internal displacements, from which micromotion across the entire bone-implant interface and internal strain could be extracted. Whilst micro-CT imaging and DVC analysis has been performed at organ level, there is yet to be a study undertaken on a specimen as large as cadaveric tibiae with a metallic tibial component. Such a scenario introduces complexities in achieving micro-CT images of sufficient signal-to-noise ratio, known to impact the errors of DVC.

In this thesis, a large-gantry micro-CT system, available at Flinders University, will be used to address the above challenges, and, subsequently perform the following analysis: **quantifying the immediate mechanical environment surrounding a cementless tibial component**.

Chapter 3 (Study 1) assesses the possibility of employing DVC on micro-CT datasets of a cadaveric tibia implanted with a cementless tibial component through a zero-strain error analysis. The study concludes that, although there is a compromise between experimental requirements and errors, it is possible to obtain accuracy and precision sufficiently low for analysis of bone within its elastic region. **Chapter 4** details the subsequent experimental protocol employed within this thesis. **Chapter 5 (Study 2)** assesses surgical variation by quantifying the roughness of the resected surface and the actual interference fit achieved between cadaveric tibiae and a cementless tibial component. The residual strain induced within the cancellous bone following impaction is also analysed, and relationships to surgical variation and bone morphometry are assessed. **Chapter 6 (Study 3)** extracts the relative motion between implant and underlying bone across the entire interface when exposed to two time-elapsed mechanical load sequences that replicate stair descent (SD) and deep knee bend (DKB). The influence of actual interference fit, induced cancellous bone damage and bone morphometry are explored. And finally, **Chapter 7 (Study 4)** computes the internal strain field of cancellous bone of proximal tibiae with a cementless tibial component during the time-elapsed mechanical load sequences of SD and DKB. The regional dissipation of strain moving away from the implant is explored and associations are made to clinical observations.

Study 1: Micro-CT scan optimisation for mechanical loading of tibia with titanium tibial component: A digital volume correlation zero strain error analysis

Work in this chapter has been published in the following journal article:

Wearne LS, Rapagna S, Taylor M, Perilli E (2022). Micro-CT scan optimisation for mechanical loading of tibia with titanium tibial tray: A digital volume correlation zero strain error analysis. *Journal of the Mechanical Behavior of Biomedical Materials*, 134:105336.

Please refer to the Appendix at the end of this thesis for a detailed outline of the author's contribution to this study.

ABSTRACT

The primary stability of cementless tibial components for total knee arthroplasty (TKA) is achieved by introducing an interference fit between bone and implant. The internal cancellous bone strains induced during this process and during initial loading have yet to be quantified experimentally. Advances in large-gantry micro-CT imaging and digital volume correlation (DVC) allow quantification of these strains. However, before undertaking such analysis, experimental requirements and DVC performance need to be examined, particularly considering the presence of a large orthopaedic implant (tibial component). The aim of this study was to assess the DVC zero-strain accuracy (mean absolute error (MAER)) and precision (standard deviation of error (SDER)) on a cadaveric human tibia implanted with a titanium cementless implant across four plausible scanning configurations, using a cabinet micro-CT system (Nikon XTH 225ST). The scanning protocols varied in rotation step and resulting scanning time (106 min vs. 66 min), presence or absence of a 2 mm-thick aluminium cylinder for mechanical testing, and X-ray tube voltage (150 kVp vs. 215 kVp). One proximal tibia was implanted and micro-CT scanned (42 µm/pixel), with repeated scanning and specimen repositioning in between. DVC (DaVis, LaVision, direct correlation) was performed on nine cubic volumes of interest (VOIs: 13.4 mm side-length) and across the entire proximal tibia. Strain errors were comparable across the four scanning configurations and sufficiently low for assessing bone within its elastic region in VOIs (MAER = 223 - 540 µε; SDER = 88 - 261 µε) and at organ level (MAER = 536 µε; SDER = 473 µε). Whilst the investigated experimental conditions, including a large titanium implant, present added complexity for DVC analysis, scans of sufficient quality can be achieved, reaching a compromise between the DVC requirements and the wanted application. The approach used for choosing the X-ray source settings considering the transmitted X-ray signal intensity and source power, is also discussed.

KEYWORDS

3.1 INTRODUCTION

For the potential benefits of cementless tibial TKA components listed in Chapter 2, little is understood about the initial mechanical interaction between the bone and the implant. Recent advancements in large gantry micro-CT systems and digital volume correlation (DVC), are, at least in theory, permitting experimental analysis of this initial mechanical environment. By obtaining micro-CT datasets of cadaveric tibiae with cementless tibial components under load, DVC is, in principle, able to track the grey levels of the specimens' structure to obtain the internal strain field. Before proceeding with such an experiment, the accuracy (mean absolute error: MAER) and precision (standard deviation of error: SDER) associated with DVC should be quantified via a zero-strain load case (Liu and Morgan, 2007, Tozzi et al., 2017).

There are several challenges in obtaining micro-CT images with sufficiently high signal to noise ratio and spatial resolution for DVC analysis (Roberts et al., 2014). These challenges are further accentuated for large specimens (such as the tibia: a long bone at organ level) and when imaging with metallic orthopaedic implants. Furthermore, to induce the bone deformations, a mechanical loading device with sufficient mechanical strength to replicate in-vivo loads is required. Previously, this has been achieved for long-bones (femur) using a mechanical loading rig with an aluminium cylinder (Martelli and Perilli, 2018). The presence of a large metallic orthopaedic implant, such as a titanium tibial TKA component, and an aluminium cylinder for mechanical testing as presented in this thesis, further increases the overall attenuation of the X-ray beam (Li et al., 2008) (attenuation coefficients μ: $\mu_{Titanium\,(100\,keV)} = 1.22\,cm^{-1}$, $\mu_{Aluminium\,(100\,keV)} = 0.462\,cm^{-1}$, $\mu_{Cortical\,Bone\,(100\,keV)} = 0.352\,cm^{-1}$ (Hubbell and Seltzer, 1996)). The micro-CT system must therefore 1) have a sufficiently large gantry size to accommodate both the specimen and the mechanical loading rig, and, 2) have sufficiently high power to penetrate through the implant and the loading rig due to the additional X-ray beam attenuation that they cause. Large-gantry micro-CT systems, in principle, allow such an experiment, having a gantry size and sufficient X-ray source power (Kusins et al., 2019).

Whilst possible in principle, to the best of this author's knowledge, no study has yet been undertaken that used a large-gantry micro-CT system to perform this type of analysis. Previous papers using DVC have mitigated the issue of increased attenuation by removing the metallic implant components before scanning (Rapagna et al., 2019, Boulanaache et al., 2020), replicating an implant with a hollow aluminium pin (Marter et al., 2020) or a thin (150 µm) titanium coating (Sukjamsri et al., 2015), or, by employing neutron scanning on smaller components (screws) (Le Cann et al., 2017, Le Cann et al., 2020). It is therefore not known if a sufficient signal to noise ratio is obtainable from a large-gantry micro-CT system, with the aim of performing DVC analysis on a proximal tibial with a titanium implant within its elastic region.

There are a number of reported scanning configurations that can help to improve the signal-to-noise ratio (Croom et al., 2020, Gillard et al., 2014, Hussein et al., 2012). However, these are often at odds with practical requirements of time-elapsed mechanical loading, namely reducing scanning time and maintaining tissue integrity. The quality of the reconstructed image may be improved by increasing the exposure time, the number of projections and/or image frame averaging (Croom et al., 2020), however, at the expense of increasing total scanning time. This in turn exposes the biological specimen to an extended period of dehydration and increased radiation, both with possible detrimental consequences to the mechanical integrity of bone (Martin and Sharkey, 2001, Peña Fernández et al., 2018).

The aim of this study is thus to assess the associated DVC zero-strain errors (MAER and SDER) across four plausible micro-CT scanning configurations that consider: the number of projection images and their corresponding scanning times (106 min vs 66 min); the presence or absence of a 2 mm thick aluminium cylinder used for mechanical testing; and an increased X-ray tube voltage (from 150 kVp to 215 kVp). The reference condition was the specimen scanned in air at 150 kVp, with the longer acquisition time (106 min). This study therefore assesses the potential of using DVC to experimentally quantify the immediate mechanical environment between tibia and cementless tibial components, considering the experimental complexities that are introduced in such a scenario. The approach used for choosing the X-ray source settings considering the transmitted X-ray signal intensity and source power, is also discussed.

3.2 MATERIALS AND METHODS

3.2.1 Specimen

One cadaveric human proximal tibia (height: 176 mm, width: 74 mm; ethics received from the Human Research Ethics Committee, 17/SAC/350) was cleaned of all soft tissue and the distal end was potted in poly-methyl-methacrylate (PMMA), with the tibia's mechanical axis aligning to the vertical axis. The proximal end was resected and a cementless titanium tibial component (Attune Affixium Cementless Fixed Bearing Knee, DePuy Synthes Joint Reconstruction), consisting of a central keel (of diameter 21.3 mm and length 44.1 mm) and four surrounding cylindrical pegs (of diameter 7.3 mm and length 10.1 mm), was inserted. The specimen was placed in an air-tight sealed plastic bag for scanning.

3.2.2 Micro-CT Scanning

Micro-CT imaging was performed with a large-volume micro-CT system installed at Flinders University (Nikon XT H 225 ST, Nikon Metrology, Tring, Hertfordshire, UK; 4056 x 4056 pixel array detector), at four different scanning configurations, detailed in Table 3. 1. The first scan configuration (Table 3. 1, #1: Air, 150 kVp, 34.1 W, 3185 projection images, Sn 0.25 mm filter, 106 min scan time) was considered as the baseline scan: the bone specimen surrounded only by air has conditions that provide a higher signal compared to a scan of a specimen placed in the aluminium cylinder, and, 3185 projections over 360 degrees is the scan setting recommended in published guidelines (du Plessis et al., 2017) and also by the manufacturer (Nikon Metrology, 2018). Subsequent scans considered a shortened scan time (of interest for preserving the biological specimens) by reducing the number of projections, the presence of a hollow aluminium cylinder (Al Tb), with 2 mm wall thickness (as required for mechanical loading of large specimens (Martelli and Perilli, 2018)), and, increased X-ray source voltage to 215 kVp (potentially improving X-ray penetration (Rawson et al., 2020)). All scans were performed with 2 x detector binning (equivalent to a 2028 x 2028 pixel array), 2.0 sec exposure and an isotropic pixel size of 42 μm.

Table 3. 1: Four Micro-CT (Nikon XT H225 ST) Scan Configurations Considered.

#1: Air, 150 kVp, 34.1 W, 3185 projections, Sn 0.25 mm filter, 106 min scan time
#2: Air, 150 kVp, 34.1 W, 2000 projections, Sn 0.25 mm filter, 66 min scan time
#3: Al Tb, 150 kVp, 42.0 W, 2000 projections, Sn 0.25 mm filter, 66 min scan time
#4: Al Tb, 215 kVp, 42.0 W, 2000 projections, Sn 0.50 mm filter, 66 min scan time

The scan configurations considered different number of projection images (3185 vs. 2000 projections, corresponding to 106 min vs 66 min scan times), the presence of a 2 mm thick aluminium cylinder (Aluminium Tube: Al Tb; as required for mechanical loading), and a higher voltage (increased from 150 kVp to 215 kVp, aimed at improving penetration). #1 was taken as the baseline, providing the ideal scenario, with the sealed specimen surrounded by air, with more projection images captured (default number suggested by micro-CT software).

The tibia was placed on the rotation stage with the tibial anatomical long axis aligned with the micro-CT system's vertical rotation axis (Figure 3. 1). As the aim of this work is to assess the zero-strain error associated with DVC, one repeated scan at each configuration was undertaken on the following day, with specimen repositioning between.
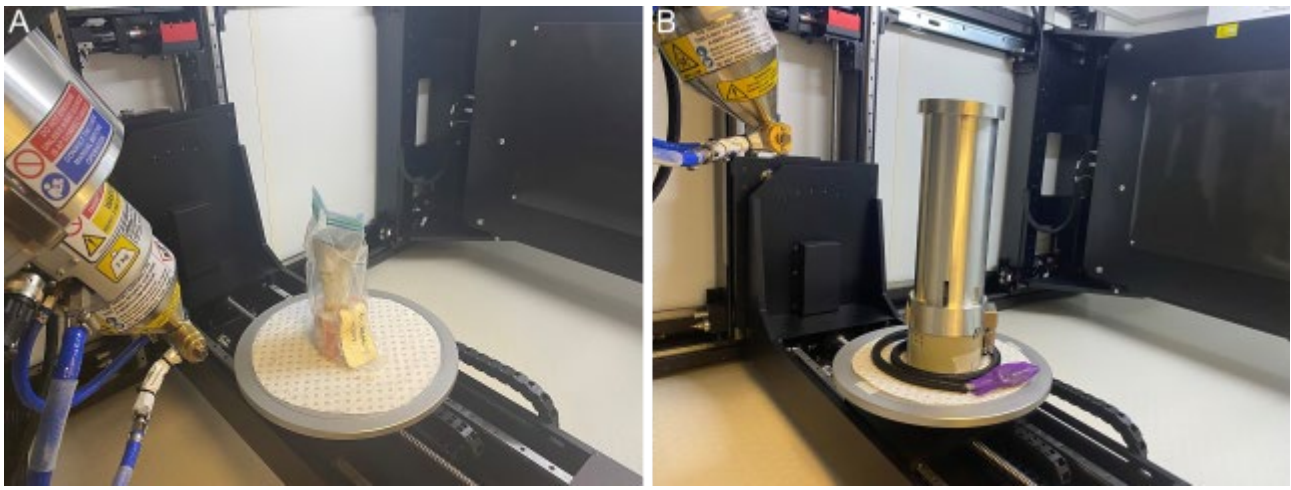
Figure 3. 1: Experimental setup of the cadaveric proximal tibia placed in the micro-CT. A) in air for scan configuration #1 and #2 (Table 3. 1), and B) within the 2 mm thick aluminium cylinder, as required for mechanical loading, for scanning configurations #3 and #4 (Table 3. 1). In both setups, the mechanical axis of the tibia was aligned to the vertical rotation axis of the micro-CT system.

3.2.3 Cross-section image reconstruction and image registration

Reconstruction of the cross-section images was performed using a filtered-back projection algorithm (software CT Pro 3D, Nikon Metrology, UK) with low-level beam hardening correction (Level 2). No noise reduction or additional filters were applied. Each reconstructed image stack consisted of 1,700 consecutive cross-section axial images, each 2028 x 2028 pixels (corresponding to 85.2 x 85.2 mm), saved in 8-bit greyscale format, generating a dataset occupying 6.51 GB. Three-dimensional (3D) rigid co-registration was performed between the first scan and the repeated scan of each scan configuration (software DataViewer, version 1.5.4.0, Skyscan-Bruker, Kontich, Belgium), by aligning a 320 x 320 x 320 pixels (13.4 mm side length) region of interest located distally in the tibial metaphysis, away from the implant (Rapagna et al., 2019).

3.2.4 Image masking for DVC

3.2.4.1 Tibia Isolation

In preparation for DVC, a custom mask (software CTAnalyser, 1.17.2.2, Skyscan- Bruker) for each scan configuration was applied to the cross-sectional slices to remove pixels external to the tibial cortex. This process involved forming a mask over the tibial cortex (binarising bone, despeckling and applying a "ROI shrink-wrap" software feature): all pixels within remained, whilst pixels external to the tibial cortex were set to a greylevel of 0 (background).

3.2.4.2 Mitigating Marrow Movement

A custom CT Analyser and MATLAB (2019b, MathWorks) protocol was written to mask marrow that was not present in both the initial and repeated scan for each scan configuration (Figure 3. 2).
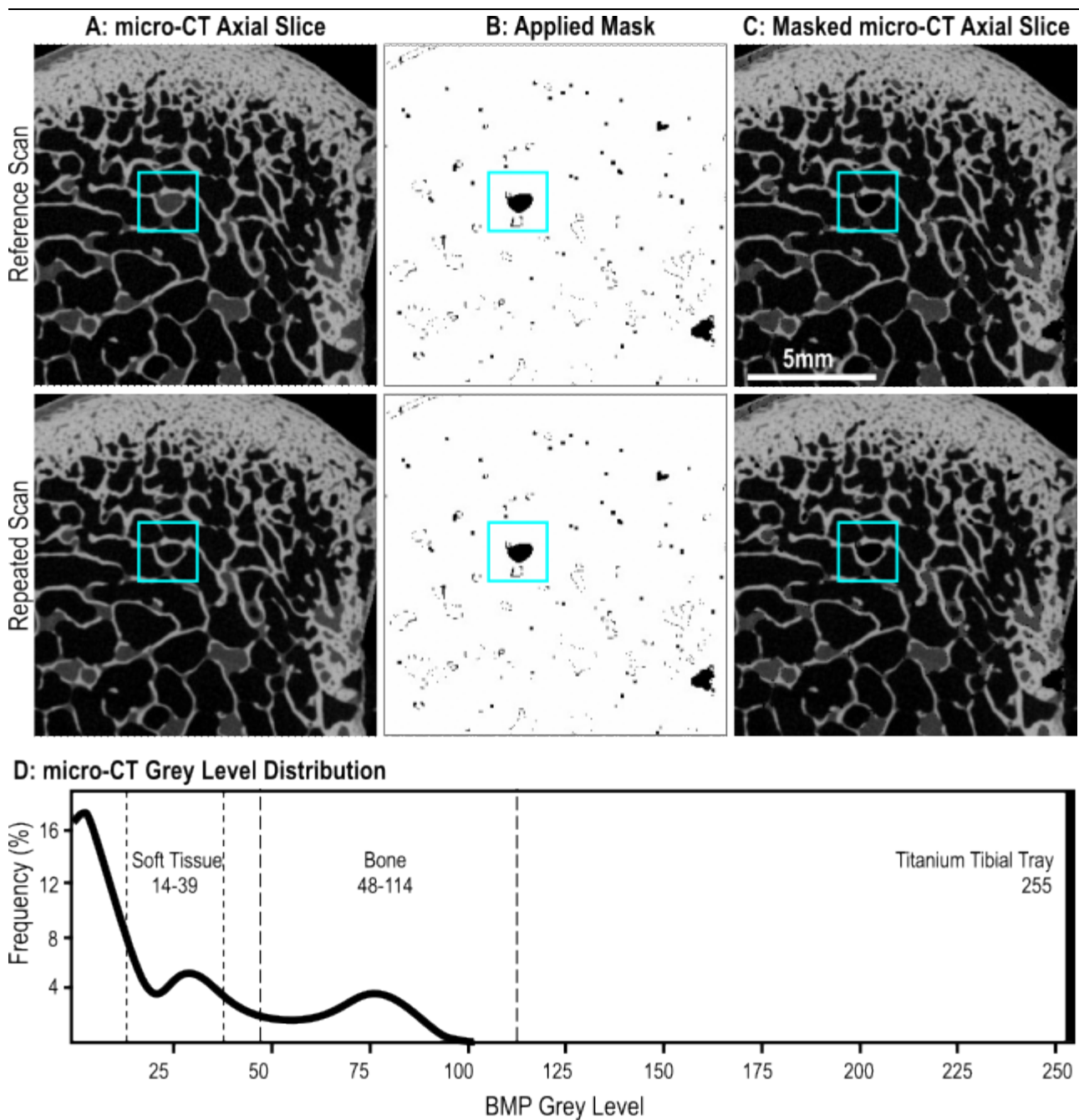
Figure 3. 2: Mitigating the influence of possible soft tissue movement prior to DVC analysis. Micro-CT cross-sectional images of the reference (top) and repeated scan (middle) were masked to remove marrow not present in both images. A) Examplar cross-sectional axial image (320 x 320 pixels) for the reference (top) and repeated (middle) scan. Highlighted by square boxes are examples of marrow movement, where here marrow is present in the reference scan but not the repeated scan. B) Constructed mask, showing regions to keep in white and to remove in black (MATLAB 2019b). C) The cross-sectional images from A) once the mask has been applied. As highlighted, the inconsistent marrow is removed from both images. D) example of a grey-level histogram of a cross-sectional image for scan configuration #1. The threshold levels used to binarise Soft Tissue and Bone are indicated by the dashed lines.

This was a multistep process which consisted of segmenting soft tissue (binarising soft tissue, despeckling and morphological function (opening, 1pixel)) and, separately, segmenting bone (binarising bone and despeckling). MATLAB code was executed that compared segmented soft tissue in each axial image of the reference and repeated scan dataset: for each pixel where soft tissue was not present in both, and consisted of bone in neither, the pixel was masked (greylevel 0, mask Figure 3. 2B, resulting dataset Figure 3. 2C).

3.2.5 Digital Volume Correlation Application

3.2.5.1 Cubic Volumes of Interest

Nine cubic volumes of interest (VOI, 13.4 x 13.4 x 13.4 mm (320 x 320 x 320 pixels)) were virtually selected (software CTAnalyser) from the masked image datasets for every scanning configuration. Five VOIs contained trabecular bone only and four were centred on each of the titanium implant pegs, with surrounding trabecular bone (Figure 3. 3D).
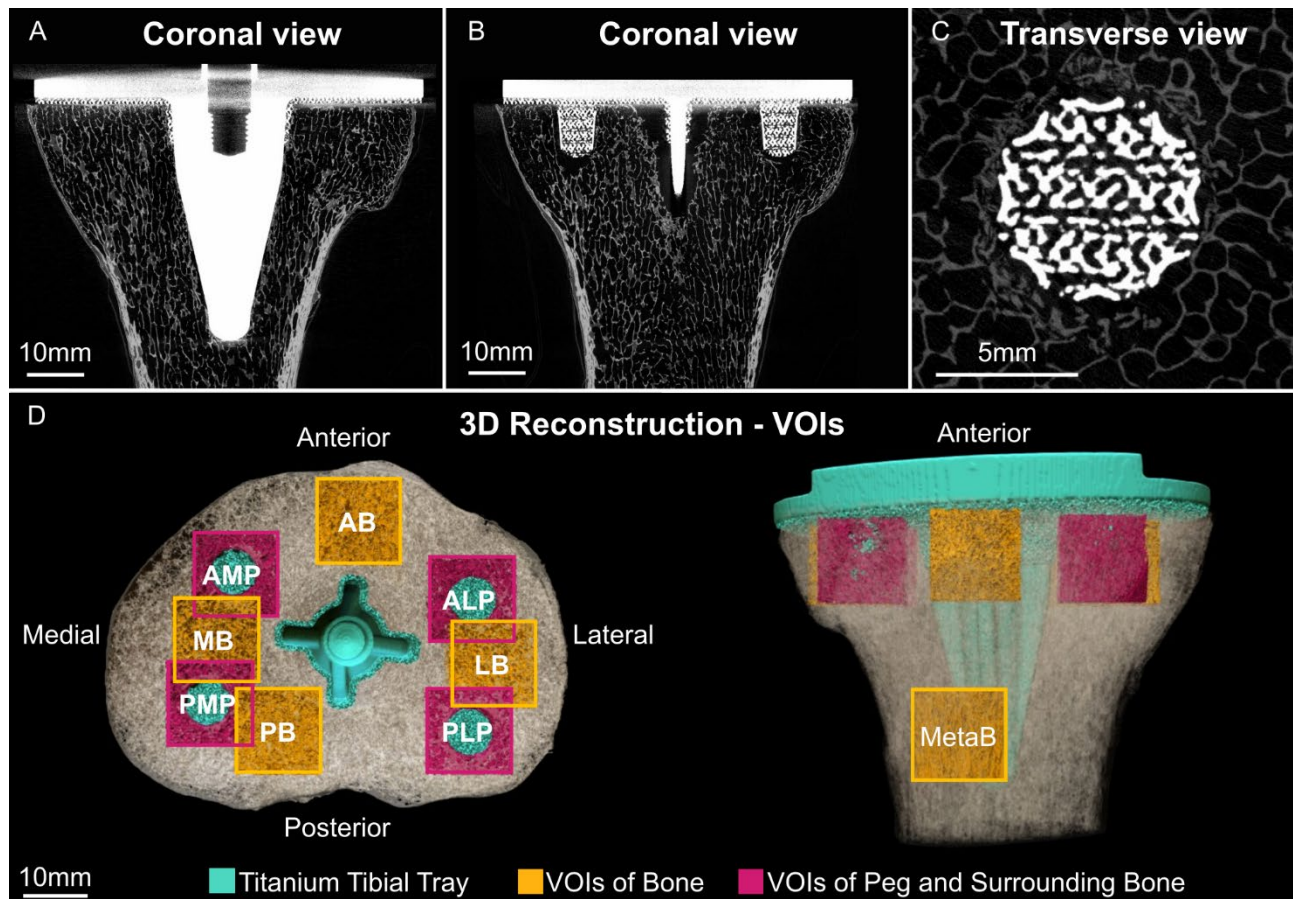
Figure 3. 3: Micro-CT Images and Volume of Interest Selection. A) and B) Coronal micro-CT images (42 µm/pixel) of the cadaveric tibia implanted with a titanium tibial component, C) transverse micro-CT image of the anterior-lateral peg (ALP) volume of interest (VOI), displaying bone and implant contact. D) Three-dimensional reconstruction of the tibia and implant (in blue colour), showing the nine virtually segmented VOIs consisting either of bone (in orange colour) or centered on peg with surrounding bone (in pink colour). MetaB: Metaphysis bone VOI; AB: anterior bone VOI; PB: posterior bone VOI; LB: lateral bone VOI; MB: medial bone VOI; ALP: anterior-lateral peg VOI; PLP: posterior-lateral peg VOI; AMP: anterior-medial peg VOI; PMP: posterior-medial peg VOI.

DVC analysis (direct correlation) was performed via the commercially available DaVis program (DaVis, 8.3.1, LaVision) on each VOI. A three-step multipass sequence (128 pixels (5.38 mm), 64 pixels (2.69 mm), 28 pixels (1.18 mm)), each with 3 passes and 0 % overlap (similar to Rapagna et al. (2019)), was executed. The final subvolume side length size of 28 pixels (1.18 mm) was selected, as a compromise between resolution and accuracy (Dall'Ara et al., 2014).

Strain errors associated to each scan configuration were quantified through the scalar quantities MAER (Equation 3. 1) and SDER (Equation 3. 2), as an assessment of accuracy and precision, respectively, across all six strain components (Liu and Morgan, 2007, Tozzi et al., 2017, Rapagna et al., 2019). The correlation coefficient (r), an indicator of DVC's ability to correlate the subvolumes of the reference to the target scans (Gillard et al., 2014), was also recorded for each scan configuration.

Equation 3. 1: Mean Absolute Error (MAER)   *Equation 3. 2: Standard Deviation of Error (SDER)*

$$MAER = \frac{1}{N}\sum_{k=1}^{N}\left(\frac{1}{6}\sum_{c=1}^{6}|\varepsilon_{c,k}|\right)$$

$$SDER = \sqrt{\frac{1}{N}\sum_{k=1}^{N}\left(\frac{1}{6}\sum_{c=1}^{6}|\varepsilon_{c,k}| - MAER\right)^2}$$

ε = strain; c = independent strain component; k = measurement point (subvolume); N = number of measurement points (number of subvolumes).

3.2.5.2 Organ-level Analysis

After performing the DVC analysis on the VOIs for the four scanning configurations, DVC was extended to organ level analysis (volume 2028 x 2028 x 1345 pixels (85.2 x 85.2 x 56.5 mm)) for the last scan configuration (#4). Due to the larger dataset size, a six-step multipass sequence was employed (208 pixels (8.74 mm), 136 pixels (5.71 mm), 96 pixels (4.03 mm), 64 pixels (2.69 mm), 44 pixels (1.85 mm) and 28 pixels (1.18 mm) subvolume side length). As in the nine VOIs, direct correlation with 0% overlap was executed at a final strain field resolution of 1.18 mm.

Strain values extracted across the titanium tibial component were masked, to only consider strain values associated with bone. The mask was produced by segmenting the titanium tibial component from the cross-section axial images (binarising the titanium tibial component, followed by despeckling, applying morphological operations and the "ROI shrink-wrap" plug-in feature (software CTAnalyser)).

Strain errors were quantified through the metrics MAER and SDER, and the average correlation coefficient across the proximal tibia was calculated.

3.2.6 Statistical Analysis

The extracted MAER, SDER and the correlation coefficients for all VOIs at each scan configuration were tested for assumptions of normality (Shapiro-Wilk test) and sphericity (Mauchly's test). Differences in MAER, SDER and the correlation coefficient across the four scanning configurations were tested using a repeated measures ANOVA. Where significance was found, paired t-tests were employed between the baseline scan (Air, 150 kVp, 34.1 W, 3185 projections, Sn 0.25 mm filter, 106 min scan time) and each of the three subsequent scan configurations, with Bonferroni adjustment (3 planned comparisons). In all tests, alpha level was set to $p < 0.05$ (Bonferroni adjustment, $p < 0.0167$).

For each scanning configuration, a further analysis was performed, to investigate whether the accuracy (MAER) and precision (SDER) were significantly different between the 5 VOIs that contained solely bone and the 4 VOIs that contained the 7.3 mm titanium peg and bone, by using a Mann-Whitney test. All statistical analysis was performed on IBM SPSS Statistics (version 25).

3.3 RESULTS

MAER and SDER of all scan configurations met the assumptions of normality and sphericity. The correlation coefficients of all scan configurations were normally distributed, however did not meet the assumption of sphericity ($p = 0.002$). As such, post-hoc Wilcoxon Sign Rank tests were performed between the baseline correlation coefficient to that of the three subsequent scan configurations, with Bonferroni adjustment.
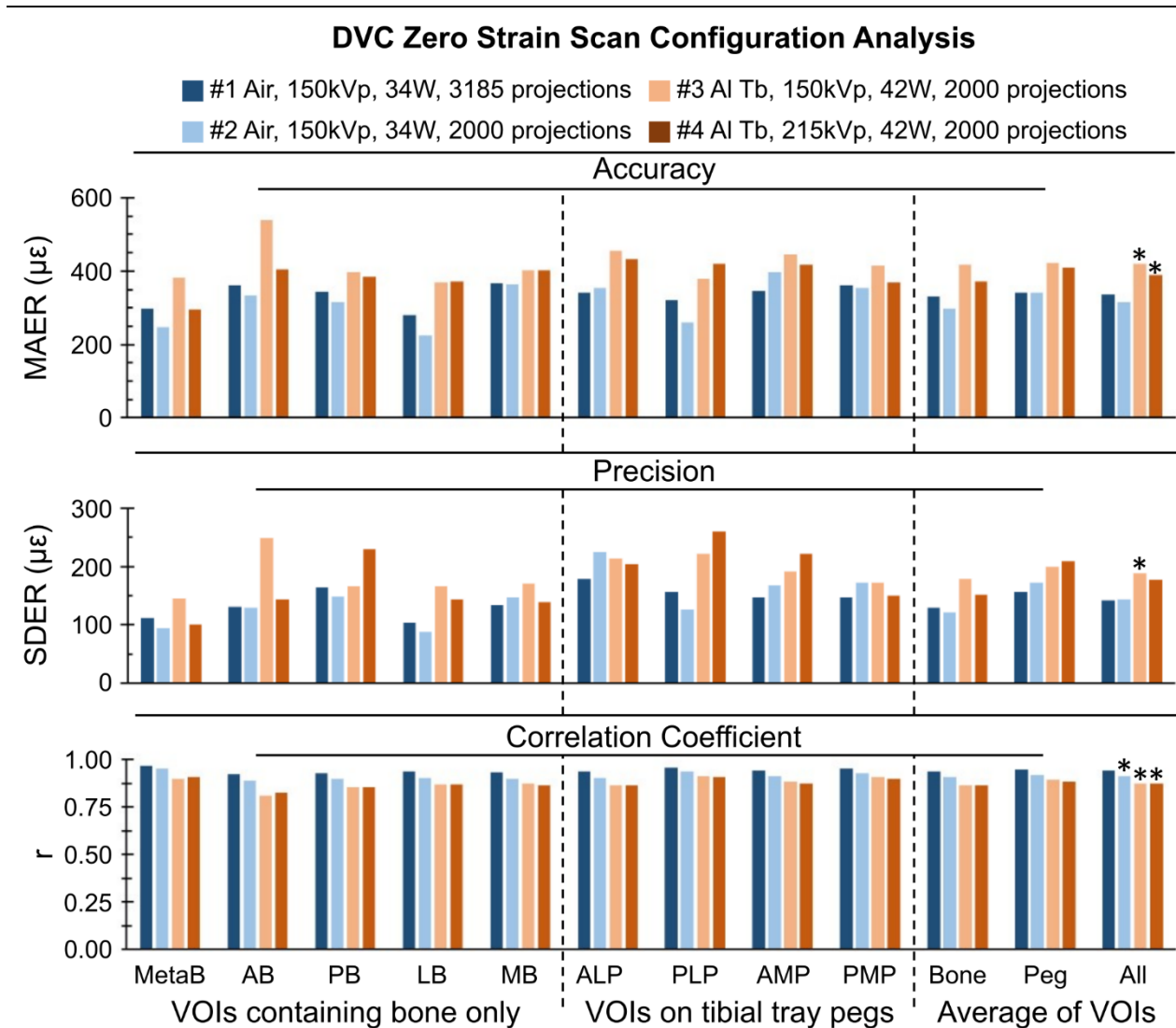
Figure 3. 4: Zero-strain error comparison of the four scanning configurations. Comparing the accuracy (mean absolute error (MAER), top), precision (standard deviation of error (SDER), middle) and correlation coefficient (r, bottom) for the nine volumes of interest (VOIs) of each of the four scanning configurations. On the far right, averages for these VOIs, considering VOIs of bone, VOIs centering on an implant peg with surrounding bone, and all VOIs
*: Statistically significant difference to the baseline scan (Air, 150 kVp, 34 W, 3185 projections).
MetaB: Metaphysis bone VOI; AB: anterior bone VOI; PB: posterior bone VOI; LB: lateral bone VOI; MB: medial bone VOI; ALP: anterior-lateral peg VOI; PLP: posterior-lateral peg VOI; AMP: anterior-medial peg VOI; PMP: posterior-medial peg VOI; Al Tb: Aluminium Tube.

Across all four scan configurations (36 VOIs: 9 VOIs per scan, 4 scan configurations), the MAER ranged between 223 and 540 με (average ± standard deviation: 365 ± 62 με, Figure 3. 4) and SDER between 88 and 261 με (163 ± 43με). The average accumulated error (MAER + SDER) was 528 ± 99 με. The correlation coefficients were in the range r = 0.81 - 0.97 (0.90 ± 0.04). For the considered baseline scan (scan configuration #1: in air, at 150 kVp voltage and 3185 projections, 106 min scan time) the values were MAER = 335 ± 30 με, SDER = 142 ± 24 με, r = 0.94 ± 0.01.

3.3.1 Rotation Step on Strain Errors

Compared to the baseline scan, reducing the number of projections to 2000 (increasing the rotation step to 0.18°, scan configuration #2) did not show significant differences in MAER (317 ± 59 με, p = 0.157) or SDER (144 ± 42 με, p = 0.780), whereas there was a statistically significant decrease in DVC correlation coefficient (r = 0.91 ± 0.02, p = 0.007).

3.3.2 Two-mm thick Aluminium Cylinder

Scanning the specimen within the 2 mm thick aluminium cylinder (Al Tb) using 2000 projections, at both 150 kVp (scan configuration #3, MAER: 421 ± 54 με, p < 0.001) and 215 kVp (scan configuration #4, MAER: 388 ± 41 με, p = 0.003), showed a significant increase in MAER compared to the baseline scan. There was also a statistically significant increase in SDER at 150 kVp (#3: 188 ± 34 με, p = 0.003), but not at 215 kVp (#4: 177 ± 54 με, p=0.026). The correlation coefficients at both 150 kVp (r = 0.88 ± 0.03, p = 0.008) and 215 kVp (r = 0.87 ± 0.03, p = 0.007) decreased significantly, compared to the baseline scan.

3.3.3 Comparison of VOIs containing bone to those containing titanium peg and bone

For each scanning configuration, when comparing the VOIs containing bone to those containing the 7.3 mm diameter titanium peg and bone, no statistically significant difference was found in MAER, SDER and correlation coefficients. However, both MAER and SDER, showed a tendency to be slightly higher (by 25 με and 40 με, respectively, values averaged over all 4 configurations) for VOIs centred on the pegs compared to those only containing bone.

3.3.4 Organ-level DVC Analysis

In performing DVC analysis on the entire proximal tibia (scan configuration #4: aluminium cylinder, at 215 kVp, 66 min scan time), MAER was 536 µε (Figure 3. 5) and SDER 437 µε. The average correlation coefficient across the proximal tibia was r = 0.88.
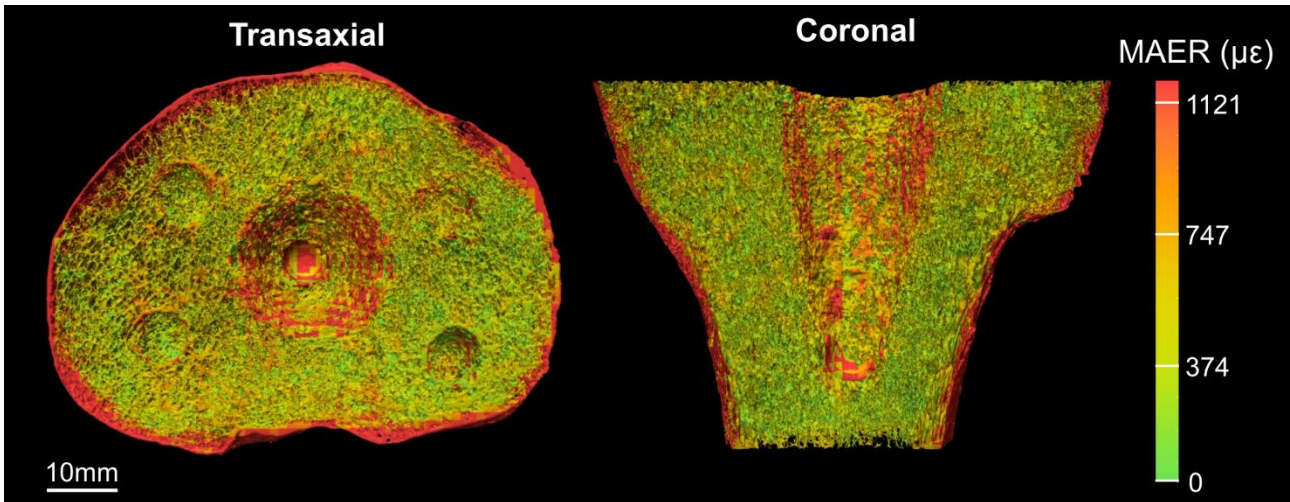
Figure 3. 5: Accuracy projection of DVC analysis across the entire proximal tibia. Specimen scanned in the aluminium cylinder, at 215 kVp, with a scan time of 66 min (scan configuration #4). Colour representing the mean absolute error (MAER).

3.4 DISCUSSION

The focus of DVC error minimisation should always be on the application: here, the mechanical investigation into how materials internally respond when subjected to load. As such, the chosen scanning configuration needs to not only minimize the errors associated with DVC, but also consider experimental requirements, including the necessary hardware (such as a mechanical load rig) and the possibility of a shorter scan time for preservation of the biological specimen. This is further complicated with the additional complexities of scanning large cadaveric specimens with metallic orthopaedic implants. The aim of this study was to investigate four plausible micro-CT scanning configurations for the desired application of mechanically loading a cadaveric tibia implanted with a titanium cementless tibial component.

With the specimen scanned in air, the accuracy (MAER) and precision (SDER) were comparable across the two numbers of projection images (3185 projections (106 min) and 2000 projections (66 min)). Both were sufficiently low for analysis of bone within its elastic region, by being less than 10 % of the yield strain of bone (< 7,800 – 10,000 µε (Bayraktar et al., 2004)), as has been suggested in the literature (Liu and Morgan, 2007). Whilst an interlaboratory experiment reported an increase in DVC errors with increasing rotation step (decreasing number of projections) (Croom et al., 2020), here a shorter scan time of 66 min, preferable for cadaveric tibiae, is still deemed suitable for analysis of bone's elastic region. Guidelines recommend that the number of projections be equal to or greater than the width of the examined specimen (in pixels), multiplied by $\pi/2$ (du Plessis et al., 2017). As our specimen maximum width was 1,750 pixels (74 mm), this would result in 2750 projections (0.13° rotation step, 92 min scanning time). The manufacturer software (CT Pro 3D, Nikon) by default considers the entire pixel array width in the calculation, equating to 3185 projections suggested (rotation step of 0.11°, 106 min scan time), taken as the baseline configuration in this study. Our results show that a reduced number of projections of 2000 (0.18°, 66 min) can be deemed sufficient for DVC analysis in this scenario.

The four scanning configurations assessed here were selected based on 1) the transmitted X-ray signal intensity and 2) the source power. As recommended by others (du Plessis et al., 2017, Stock, 2009), transmission intensity through the specimen was kept between 10 % to 90 % of areas with maximum transmission (the background). Considering the attenuation of the X-ray beams by the proximal tibia, the titanium tibial tray, and, in scans #3 and #4, the aluminium cylinder, sufficient penetration was achieved through either increased X-ray source current (flux) or increased voltage. Both of these parameters are factors of the source power, which leads to the second consideration. Depending on the system, the focal spot size increases with source power above a certain threshold (Rueckel et al., 2014, du Plessis et al., 2017, Nikon Metrology, 2018). If the focal spot size becomes larger than the pixel size, it dominates (hence worsens) the spatial resolution of the image (du Plessis et al., 2017). For the given micro-CT system and wanted spatial resolution of 42 µm/pixel, it was required that the source power likewise remains under 42 W. The

requirements of sufficient transmission intensity (> 10% of the maximum transmitted intensity) and capped source power (< 42 W) dictated the scanning configurations.

To determine the effects of each parameter (exposure time, number of projections, X-ray tube current, X-ray tube voltage, and presence or absence of the aluminium cylinder), a parametric study would be required. This was not the aim of this functional study.

The aluminium cylinder, required for performing mechanical testing on human cadaveric organs (Martelli and Perilli, 2018), induced larger errors compared to the specimen scanned in air, at both the source voltages considered (150 kVp and 215 kVp). However, whilst these were statistically significant, they would not have experimental consequences moving forward: all errors were sufficiently low for analysis of bone in its elastic region even when extended to organ level analysis (Figure 3. 5).

Compared to VOIs containing only bone, and although not statistically significant, slightly higher errors were observed for VOIs containing bone and tibial component titanium pegs, where a discontinuity of material arises. Palanca et al. (2016a) observed localised errors in augmented porcine vertebrae between bone and bone cement. However, the errors of such regions in both their study and this study remain sufficiently low for analysis of bone in its elastic region.

Few other studies have comparable experimental requirements, in terms of organ size and the presence of orthopaedic components or biomaterials. Kusins et al. (2019), using the same cabinet micro-CT scanner as employed here, examined cadaveric scapulae (37 µm/pixel) at organ level for DVC analysis. However, their analysis considered displacement rather than strain, making direct comparison of errors difficult, and furthermore, the specimens did not have an implant (whether metallic or otherwise). Whereas previous papers show that cabinet micro-CT imaging combined with mechanical loading of large specimens is possible (Hussein et al., 2012, Palanca et al., 2016a, Rapagna et al., 2019, Kusins et al., 2019, Boulanaache et al., 2020), they likewise do not have a metallic orthopaedic component as big as a titanium tibial component in their scanning volume.

In this study, a spatial resolution of 42 µm/voxel was used to scan a cadaveric tibia with titanium tibial component at the organ level, which is comparable to the voxel size of forementioned studies (33.5-60.7 µm/voxel). Across all four scanning configurations assessed, a DVC resolution of 1.18 mm incurred an accuracy between 223 and 540 µε (365 ± 62 µε) and precision between 88 and 261 µε (163 ± 43 µε), in the VOIs, and an accuracy of 536 µε and precision of 473 µε, at organ level. With the added complexities of the titanium tibial component and the size of the long bone, these errors remain comparable to those of previous papers on time-lapsed mechanical testing of bone, where DVC resolution ranged from 0.644 mm to 6.0 mm, with reported accuracy 215 to 1,200 µε and precision 68 to 630 µε (Hussein et al., 2012, Palanca et al., 2016a, Rapagna et al., 2019, Kusins et al., 2019, Boulanaache et al., 2020).

There are a number of limitations present within this study. Firstly, scan setting analysis was only undertaken on a single cadaveric tibia. As the errors associated with DVC could depend on tissue micro-architecture (Liu and Morgan, 2007, Tozzi et al., 2017), multiple (nine) regions were examined, to account for possible bone variation. Secondly, the cadaveric specimen used within this study has been used extensively during previous experimental work, in which mechanical loading was applied. However, the purpose of the present study was to compare scanning configurations in zero-strain conditions and not to examine tissue performance. Lastly, the scan parameters investigated here are not exhaustive. When selecting scan configurations, the end application must be considered. The configurations analysed within this study were intended to offer a compromise between scan quality (hence DVC error minimisation (Roberts et al., 2014)) and the requirements for mechanical loading a human tibia implanted with a titanium tibial component, including hardware and maintaining tissue integrity. Depending on the intended experiment, other scan parameters may be assessed.

3.5 CONCLUSION

The results from this work demonstrate the possibility of assessing the internal strain field within the elastic region of a human cadaveric tibia implanted with a titanium tibial component, while scanned in an aluminium cylinder for mechanical loading. Differences were investigated across four plausible scanning configurations in a zero-strain condition. Whereas an increased rotation step (shorter scan time: 66 min compared to 106 min) did not significantly influence the accuracy (MAER) and precision (SDER), the addition of the aluminium cylinder, required for mechanical loading, gave slightly higher errors, depending on the setting. However, the four scanning configurations assessed were all suitable for analysis of bone strain within its elastic region, with errors less than 10 % of its yield strain. Whilst the investigated experimental conditions, including a titanium implant, present added complexities for DVC analysis, scans of sufficient quality can be achieved, thereby reaching a compromise between the requirements of DVC and its wanted application.

Time-elapsed micro-CT scanning and digital volume correlation analysis of cadaveric tibiae with cementless tibial tray

The protocol presented in this chapter encapsulates the experimental work undertaken during this PhD candidature, and forms the basis for the analysis detailed within the three following chapters:

Chapter 5, Study 2: Interference fit of Cementless Tibial components

Chapter 6, Study 3: Relative Motion

Chapter 7, Study 4: Internal Strain field

Please refer to the Appendix at the end of this thesis for a detailed outline of the author's contribution to this study.

Since confirming within Chapter 3 the possibility of employing micro-CT imaging and DVC to analyse the bony mechanical environment surrounding a commercially available cementless tibial component, such an analysis followed. The work undertaken within this thesis is based on micro-CT imaging of cadaveric tibiae and a commercially available cementless component. The tibiae, once implanted, were subjected to two time-elapsed mechanical load sequences, with concomitant micro-CT scanning, that replicated stair descent (SD) and deep knee bend (DKB). From the acquired micro-CT datasets, analysis of the interference fit, post-impaction strain, and mechanical environment under loading (internal strain and relative motion between bone and implant) was undertaken.

This chapter details the experimental work, establishing the protocol that was used for the following studies. A roadmap of the experimental procedure is included within Figure 4. 1. Reference to this chapter will be made within each of the subsequent studies.

Cadaveric tibia procured.
Placed within the freezer.

Tibia defrosted in saline solution.
Tibia stripped of all soft tissue and cut to 174mm in length.
Tibia returned to the freezer.

Intact Tibia Micro-CT Scanning
Higher resolution scan: 23 µm/pixel
Lower resolution scan: 184 µm/pixel

Tibia defrosted in saline solution.
TKA preparation and resection performed.
Tibia returned to the freezer.

Resected Tibia Micro-CT Scanning
Higher resolution scan: 46 µm/pixel
Lower resolution scan: 184 µm/pixel spatial resolution

Proximal 160 mm of tibia isolated and distal end potted.
Tibia returned to the freezer.

Tibia defrosted in saline solution.
TKA implantation of cementless tibial component performed.
Implanted tibia returned to the freezer.

Tibia defrosted in saline solution.
Time-elapsed Mechanical Load Sequence with Micro-CT Scanning: SD
All micro-CT scans were performed at a spatial resolution of 46 µm/pixel
Cyclic Preloading
0.0BW (PL1); scan
0.0BW (PL2- baseline); scan
0.5BW; scan
1.0BW; scan
1.5BW; scan
2.5BW; scan

Tibiae returned to a saline bath and stored in a fridge (+4°C) overnight to rehydrate.

Time-elapsed Mechanical Load Sequence with Micro-CT Scanning: DKB
All micro-CT scans performed at a spatial resolution of 46 µm/pixel
Cyclic Preload
0.0BW (preload - baseline); scan
0.5BW; scan
1.0BW; scan
1.5BW; scan
2.5BW; scan
3.5BW; scan
Tibia returned to the freezer.

Figure 4. 1: Experimental procedure undertaken for each of the seven cadaveric tibiae. Specimens, when returned to the freezer, were stored at -20°C in the Advanced Surgical Training facility, Flinders University. SD: stair descent; BW: bodyweight; PL1: preload 1; PL2: preload 2; DKB: deep knee bend.

4.1 SPECIMENS

Seven human cadaveric shanks were sourced from donors (Table 4. 1) aged between 44-58 years (ave ± std dev: 52 ± 6 years) and weighing between 48-104 kg (78 ± 19 kg). To ensure bone quality, male specimens were selected with a body mass index (BMI) greater than 17 (25.9 ± 6.8 kg.m^{-2}) and with no reported period of prolonged bed rest prior to death. Ethics approval was provided by the Southern Adelaide Clinical Human Research Ethics Committee (HREC 186.20). The shanks were stripped of all soft tissue and the proximal tibiae (approximately 174 mm in length) were extracted.

Table 4. 1: Donor summaries. All were male and required a size 7 tibial component, as assessed by the surgeon (GK).

Specimen	Age (years)	Weight (kg)	Height (cm)	BMI (kg.m^{-2})
Tibia A	55	48	168	17.1
Tibia B	51	64	180	19.5
Tibia C	44	82	178	25.8
Tibia D	45	97	170	33.5
Tibia E	58	81	170	28.2
Tibia F	58	104	173	35.0
Tibia G	52	67	179	21.9

A surgeon (GK), experienced with cementless TKA, performed the resections and impactions, following standard surgical procedure for a commercially available titanium tibial component (Attune Affixium Cementless Fixed Bearing Knee, DePuy Synthes Joint Reconstruction (DePuy Synthes, 2016)). Each tibia was sized by the surgeon, with all tibiae requiring a size 7 tibial component. Following guidelines, peg guides were over drilled relative to the peg length. The keel guide was prepared by firstly drilling a hole into the central cancellous bed and then employing a keel punch to impact the cancellous bone (DePuy Synthes, 2016).

Following the resection, the distal end of each tibia was removed (so that the specimens were approximately 160 mm in length) and the tibiae were potted, distally, in PMMA, keeping 98 mm as free length (approximately). Micro-CT scans, detailed below, were taken of the tibiae when intact, resected, and, once implanted with the cementless tibial component, during the time elapsed mechanical load sequences.

4.1.1 Cementless Tibial component

The commercially available Attune Affixium Cementless Fixed Bearing Knee System tibial component (Figure 4. 2) was used in this study. The tibial component is made of a titanium alloy (ASTM F3001) and consists of a central keel and four surrounding cylindrical pegs (DePuy Synthes, 2016). For a size 7 implant, as sized for all tibiae of this study, the tibial component was 74 mm wide and 50 mm deep, with a keel of diameter 21.3 mm and length 44.1 mm, and, each peg of diameter 7.3 mm and length 10.1mm.
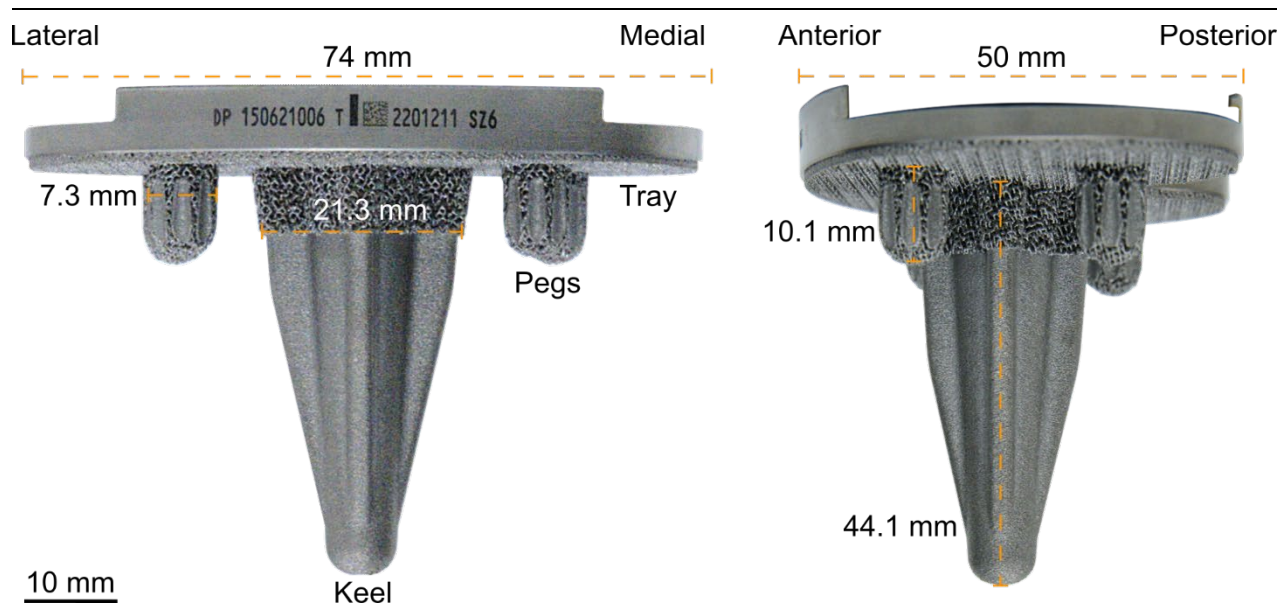
Figure 4. 2: Attune Affixium Cementless Fixed Bearing Tibial Tray, including a central keel (21.3 mm wide, 44.1 mm long) and four surrounding pegs (7.3 mm, 10.1 mm). Dimensions shown for a size 7 component.

The nominal radial interference fit differs across this tibial component. For the pegs, a nominal radial interference of 1.0 mm is intended, with overdrilling at the bottom resulting in no interference (DePuy Synthes, 2016). For the keel, the interference varies across the feature, between 1.19 mm to 2.0 mm, with a median interference of 1.2 mm (DePuy Synthes, 2023). Across the tray, there is no nominal interference fit, with the surgical guidelines instructing impaction until the implant is "fully seated" (DePuy Synthes, 2016).

4.2 MICRO-CT SCANNING

Micro-CT scans of each tibia were undertaken using a large-gantry micro-CT system (Figure 4. 3, Nikon XT H 225 ST, Nikon Metrology, as in Chapter 3). Scans were obtained with the tibiae intact (at 23 µm/pixel (Figure 4. 4A) and 184 µm/pixel), after resection (at 46 µm/pixel (Figure 4. 4B) and 184 µm/pixel), and then when implanted (at 46 µm/pixel, Figure 4. 4B and Figure 4. 5) for two separate time-elapsed mechanic load sequences that replicated SD and DKB. For each load sequence, activity six micro-CT scans (at 46 µm/pixel) were acquired. This amounted to 112 micro-CT datasets (16 datasets per tibia for 7 tibiae).

All scans were obtained with the long axis of the tibiae aligned to the rotation axis of the micro-CT stage (Figure 4. 3B) and placed within a 2 mm thick aluminium cylinder, as required for mechanical testing (Figure 4. 6).
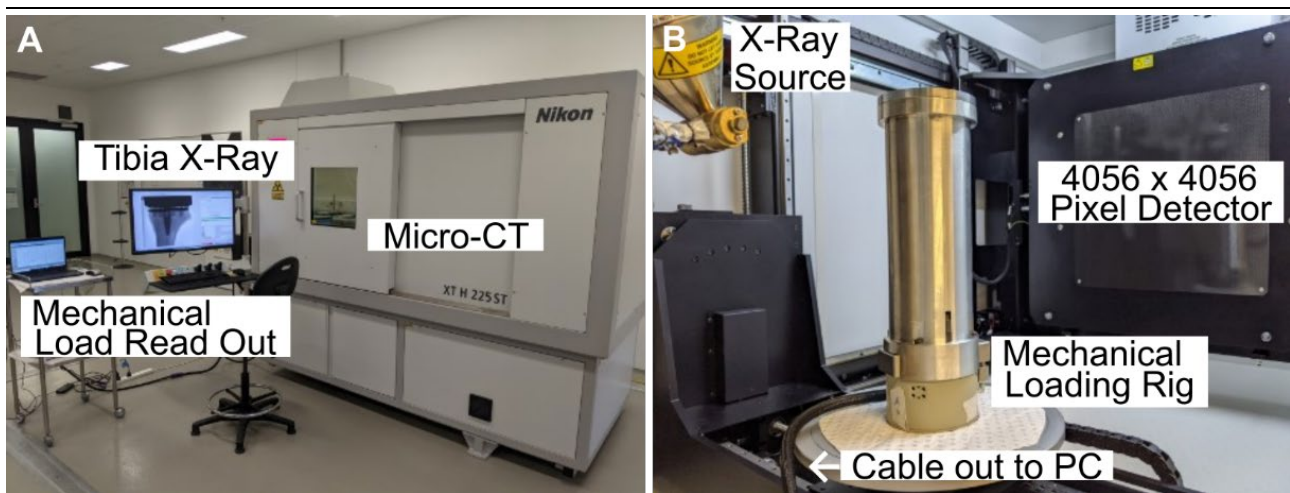
Figure 4. 3: Experimental setup for time-elapsed mechanical loading with micro-CT imaging. A) within the Micro-CT Laboratory. X-ray projection of the tibia with cementless tibial component visible. B) Inside the large gantry micro-CT system (Nikon XT H 225 ST). Mechanical loading rig, with tibia inside, shown placed on the micro-CT stage. The long axis of the tibia was aligned to the rotation axis of the stage.

4.2.1 Intact Tibia Micro-CT Scans

With the intent to perform bone micro-architecture quantification of the tibiae when intact, intact tibia scans were obtained at an isotropic spatial resolution of 23 µm/pixel with an 85 min scan time (source voltage: 215 kVp, current: 107 µA, power: 23 W, 1 x detector binning, corresponding to 93 x 93 mm field of view, 0.1 mm Sn filter, exposure time 2.83 sec, and 1800 projections over 360°). A second, lower resolution (184 µm/pixel) and faster (4 min scan time) micro-CT scan was also obtained directly after (voltage: 150 kVp, current: 307µA, power: 46 W, 4 x detector binning, corresponding to 187 x 187 mm field of view, 0.25 mm Sn filter, exposure time: 0.5 sec and 500 projections). The purpose of this scan was to determine the mechanical axis of the tibia by creating an intact STL model.
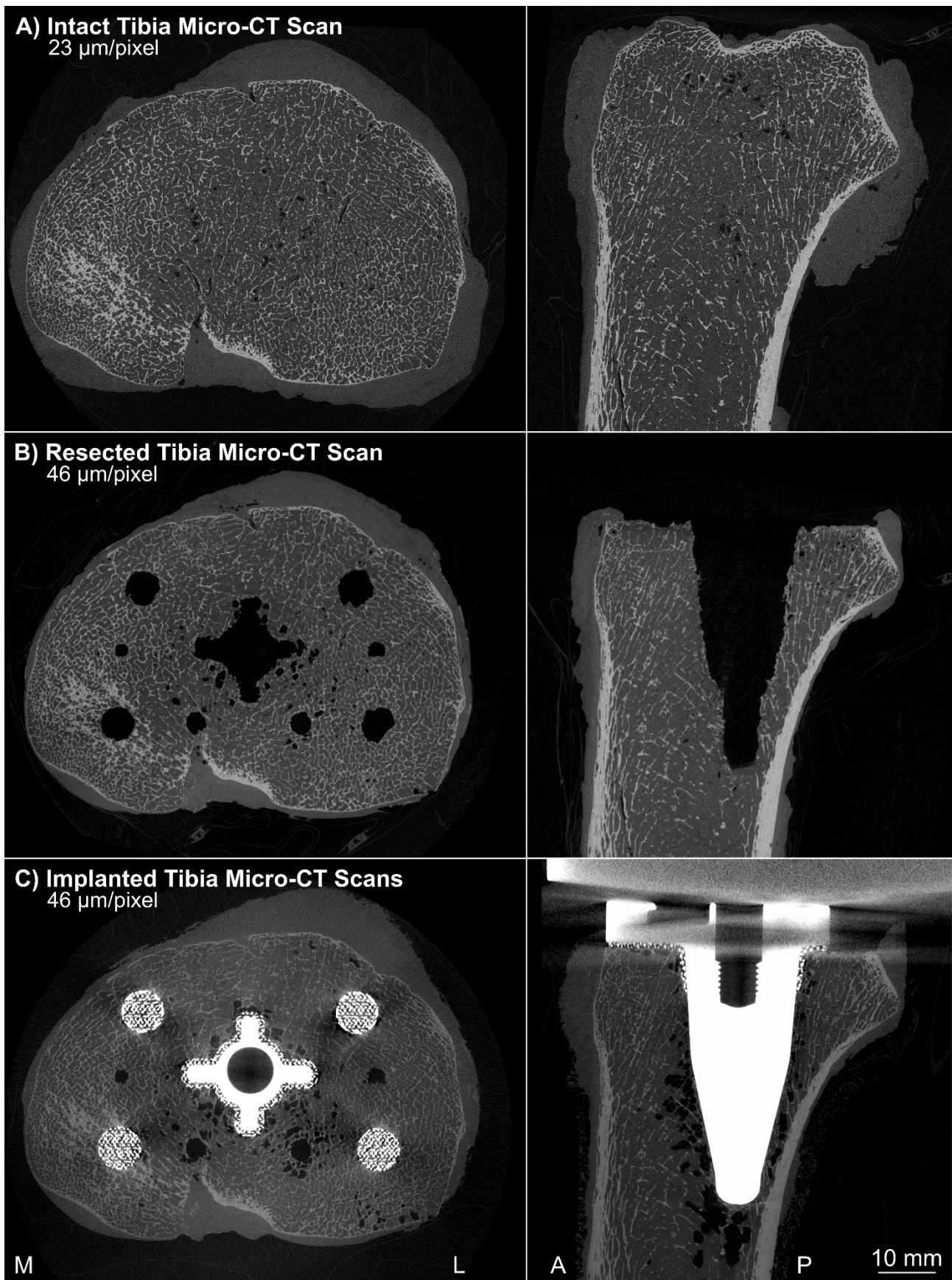
Figure 4. 4: Micro-CT images of the tibia (Tibia G) in the transverse (left) and sagittal (right) plane when A) intact (at 23 µm/pixel), B) resected (at 46 µm/pixel) and C) following implantation with a commercially available cementless tibial tray (at 46 µm/pixel, shown for SD PL2).
Medial: M; lateral: L; anterior: A; posterior: P.

4.2.2 Resected Tibia and Time-elapsed Micro-CT (Loaded) Scans

Micro-CT scans of the tibiae resected and then during the time-elapsed mechanical load sequence were obtained with the same scanning configuration. Due to the tibiae being implanted in the latter, the selected scanning configuration needed to contend with the additional X-ray attenuation of the titanium implant. As a result, 2 x detector binning was used (corresponding to 93 x 93 mm field of view) for a spatial resolution of 46 µm/pixel and a 67 min scan time (voltage: 215 kV, current: 214 µA, power: 46 W, 0.5 mm Sn filter, exposure time: 1.0 sec, and 2000 projections).

Another lower resolution micro-CT scan (184 µm/pixel) of the tibiae resected was taken, with the same scanning configuration detailed above for the lower resolution intact tibia scan. The purpose of this scan was likewise to create an STL model, here of the resected tibia, for the potting procedure detailed below.
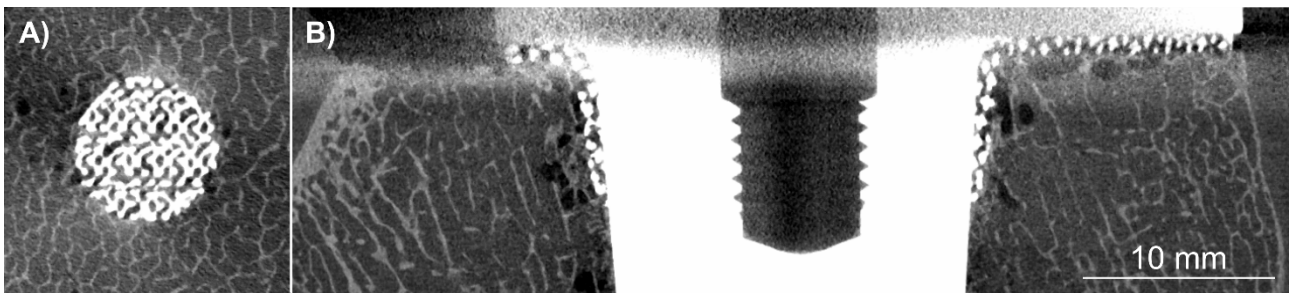
Figure 4. 5: Micro-CT image of the bone-implant interface of A) the posterior-lateral peg (transverse plane) and B) the proximal keel (sagittal plane). Extracted from Figure 4. 4C, but here shown at full resolution.

4.3 MICRO-CT IMAGE RECONSTRUCTION

Reconstruction of the cross-sectional images for all datasets was performed using a filtered-back projection algorithm (software CT Pro 3D, Nikon Metrology UK) with low level beam hardening correction (level 2). No noise reduction or additional filters were applied during the reconstruction process. The images were saved in 8-bit grayscale format, generating datasets occupying approximately 45 GB for the intact datasets at 23 µm/pixel resolution, 5.5 GB for the resected and impacted datasets (resolution: 46 µm/pixel) and 0.4 GB for the lower resolution (184 µm/pixel) intact and resected datasets.

4.4 TIME-ELAPSED MICRO-CT IMAGING WITH MECHANICAL LOADING

4.4.1 The Loading Rig

Mechanical loading of the implanted tibiae was performed using a Deben CT5000 loading device (Deben Ltd, UK), fitted with a custom-built aluminium cylinder of 2 mm wall thickness (Figure 4. 6). The load was applied to the tibia by applying a vertical displacement to the lower compressive platen, via a software-driven optically-encoded motor. The resulting mechanical loading rig with custom cylinder provided up to 3000 N uniaxial compression over a 10 mm travel range, with an internal chamber of height 186 mm (176 mm at full compression) and diameter of 90 mm.

To replicate the two activities of SD and DKB in a quasi-static uniaxial loading configuration, upper loading platens were fabricated from stainless steel with two stainless steel prongs (Ø 5 mm), protruding by 8 mm (Figure 4. 6, inset). The position of the prongs mimicked the averaged central contact point of the medial and lateral femoral condyles on the tibial component during SD and DKB based on data from a validated musculoskeletal model (Baldwin et al., 2012). For SD, the medial prong was posteriorly offset by an intended 9.92 mm and the lateral prong posteriorly offset by an intended 11.74 mm. For DKB, this was further posteriorly offset, with the medial prong posteriorly offset by an intended 14.6 mm and the lateral prong by an intended 18.7 mm.
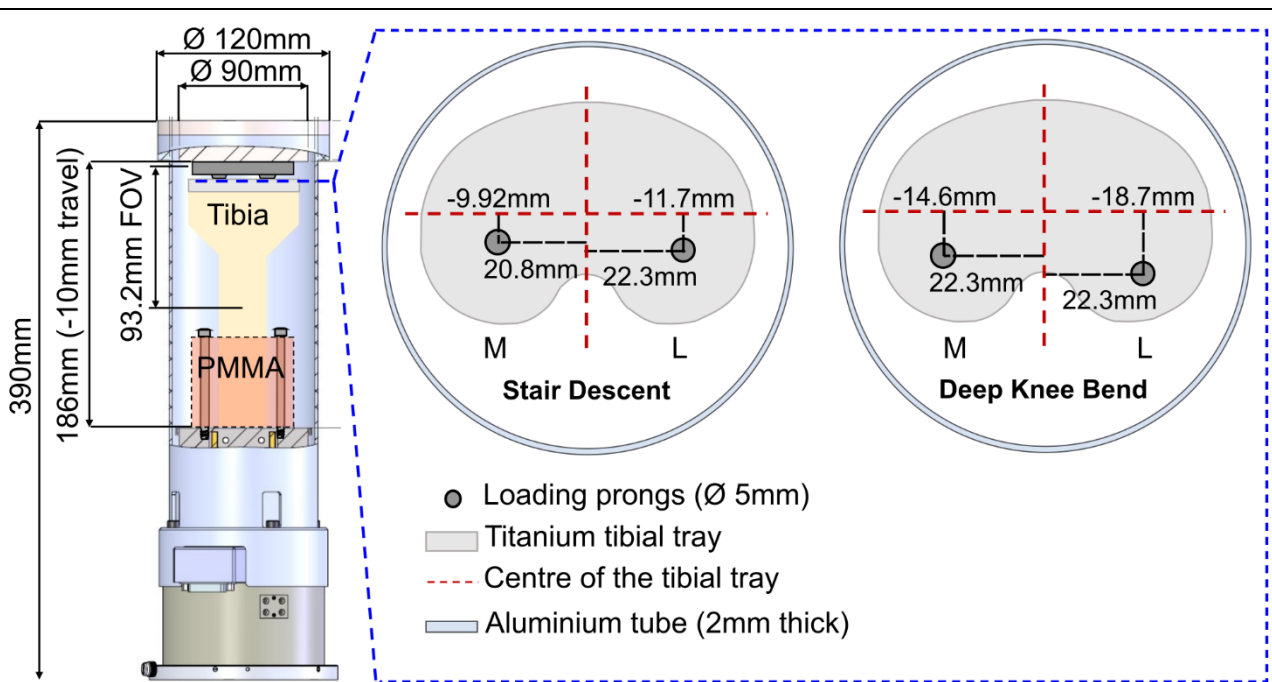
Figure 4. 6: Schematic inside the mechanical loading rig (Deben CT5000), fitted with a custom built aluminium cylinder. The setup of a tibia is shown, screwed onto the lower compressive stainless steel platen. The inset shows the position of the loading prongs (two stainless steel rods: 5 mm diameter, protruding by 8 mm) fixed onto the superior compressive stainless steel platen. Prong positions replicated femoral condyle loading points during stair descent (SD, middle) and deep knee bend (DKB, right). Offset values reported relative to the centre of the implant. Load was applied to the tibia by applying a vertical displacement to the lower compressive platen, via a software-driven optically-encoded motor.

4.4.2 Potting

The distal end of each tibia was potted in cement (poly methyl methacrylate (PMMA)) once resected, which dictated its position within the loading rig for the time-elapsed mechanical load sequence. It was desirable to have the implanted position of the tray horizontal to mitigate the X-ray scatter noise due to the presence of the large (74 mm wide) titanium implant within the micro-CT images. Furthermore, the alignment of the tibia (and tibial component) to the upper loading platens of the mechanical loading rig (Figure 4. 6, inset) was also determined by the potting procedure. To ensure correct positioning of the tibia (and tibial component), custom 3D printed guides were made to hold each tibia in the correct position as the cement cured.

To produce the guides, an STL model of a size 7 tibial component was built and oriented to align with the upper platen loading prongs (Figure 4. 7A). A 3D surface model (.STL file format) of each resected tibia was produced from reconstructed cross-sections of the resected low-resolution (184 μm/pixel) micro-CT scan and then rigidly transformed onto the aligned tibial component (MATLAB 2022b *pcregistration*), performing a virtual implantation (Figure 4. 7B). Using the transformed 3D model of the tibia, potting guides were 3D printed (Figure 4. 7C) and the distal 60 mm of the resected tibia was potted in PMMA (Figure 4. 7D, E). Four screw guides extended through the height of the PMMA, allowing the specimen to be rigidly screwed onto the lower platen of the loading rig for mechanical testing.
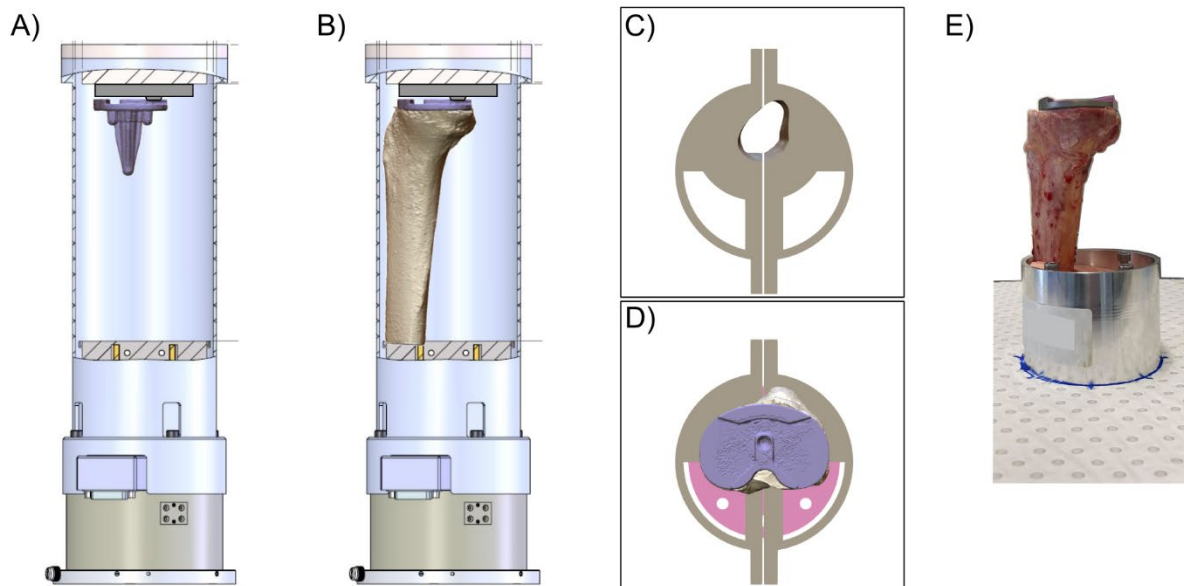
Figure 4. 7: The potting procedure. A) An STL of the tibial component was orientated to align with the upper loading platen (with protruding prongs) of the Deben Stage. B) An STL of the resected tibia was rigidly transformed, performing a virtual "implantation" to the aligned tibial component. C) Potting guides were produced and D) held the metaphysis of the tibia in place as the PMMA cured. E) photograph of the tibia once potted (and implanted).

4.4.2.1 Alignment Errors

From the cross-section images of the loaded baseline micro-CT scans (SD (PL2) and DKB 0.0BW), where the tibiae were potted and implanted, some alignment errors were observed. Errors were defined as a deviation between the wanted position of the loading prongs relative to the implant, to what was actually obtained. The average and largest deviations (anterior-posterior (A-P) and medio-lateral (M-L)) from the intended medial and lateral prong position for the two activities is included in Table 4. 2.

Table 4. 2: Alignment Errors: prong position deviation. Deviations displayed as ave (max).

	SD		DKB	
	Medial Prong	**Lateral Prong**	**Medial Prong**	**Lateral Prong**
A-P Deviation (mm)	1.27 (3.97)	1.80 (3.92)	1.15 (2.79)	1.24 (3.39)
M-L Deviation (mm)	0.93 (2.79)	0.97 (2.78)	0.64 (1.23)	0.80 (1.30)

In addition, only lateral-prong contact was observed during the SD loading configuration for Tibia C. This was rectified before the second day of testing (DKB configuration), where both medial and lateral - prong contact was observed. Whilst every effort was made to ensure that the tibial component was positioned as flat as possible, with specimen, surgical and experimental variability, this can be challenging to obtain (Cristofolini et al., 2010a).

4.4.3 Time-elapsed Micro-CT Imaging with Mechanical Loading

The mechanical loading procedure spanned two days for each tibia, where, on the first day, the upper loading platen for SD was used (Figure 4. 6, inset middle), and on the second, the upper loading platen for DKB (Figure 4. 6, inset right).

The tibiae, with titanium implant, were thawed in saline solution for 24 hours prior to the first day of testing. The tibiae were returned to a saline bath and kept in a fridge at 4° overnight between the first and second day to rehydrate. Throughout testing, specimens were kept wrapped in saline soaked gauze surrounded by cling-wrap, to maintain hydration. After unwrapping the specimen at the end of testing on each day, the tibiae were observed to still be wet.

On the morning of testing (for both SD and DKB), the tibiae were removed from the solution, wrapped in saline-soaked gauze and cling film, before the distal PMMA-potting was screwed onto the mechanical loading stage. The mechanical loading rig containing the tibia was placed within the large gantry micro-CT system, with the long axis of the tibia aligned to the rotation axis of the micro-CT stage (Figure 4. 3B). A cyclic preload, consisting of 20 repetitions from 50 N to 0.5BW of the donor, was applied prior to mechanical testing.

The time-elapsed mechanical testing consisted of six steps taken sequentially at increasing load increments scaled to the bodyweight (BW) of the donor. At each load step, a micro-CT scan was

taken after a 20 min relaxation period, using the scanning configuration detailed above (section 4.2.2). For SD these load steps were: 0.0BW (preload 1 (PL1)), 0.0BW (preload 2 (PL2)), 0.5BW, 1.0BW, 1.5BW, and 2.5BW. For DKB: 0.0BW (preload), 0.5BW, 1.0BW, 1.5BW, 2.5BW, and 3.5BW. The applied loads at 3.5BW DKB ranged from 1,542 N (Tibia A) to 2,924 N (Tibia F). The axial force-time curve was monitored during the experiment and recorded for each tibia using a laptop computer. Repeated scanning (preload 1 and 2 during SD) of the tibia in an unloaded condition was taken for zero-strain DVC error analysis (Tozzi et al., 2017, Wearne et al., 2022).

All seven specimens completed the time-elapsed mechanical load sequence and no gross failure was observed.

4.5 DIGITAL VOLUME CORRELATION ANALYSIS

DVC is able to extract both the rigid and non-rigid deformation by tracking the grey levels of a specimen's structure between a baseline to target micro-CT dataset. As included within Table 4. 3, DVC was employed to extract the internal residual strain field post-impaction (Chapter 5), and, for the time-elapsed mechanical load sequence, the relative motion between implant and underlying bone (Chapter 6) and, the internal strain field (Chapter 7). The same DVC configuration and subvolume masking was employed in each of these analyses, as described below. Within the subsequent chapters (5, 6 and 7), the baseline micro-CT dataset and the target micro-CT dataset will be specified.

Table 4. 3: Performed DVC analyses. Baseline scans are the reference dataset during DVC analysis.

Baseline Scan	Target Scan	Analysis
SD 0.0BW (PL2)	SD 0.0BW (PL1)	Zero-strain error analysis
Resected Scan	SD 0.0BW (PL2)	Post-impaction residual strain field
SD 0.0BW (PL2)	SD {0.5 - 2.5BW}	Time-elapsed mechanical load sequence during SD
SD 0.0BW (PL2)	DKB PL	Permanent tray subsidence and residual strain after SD 2.5BW
DKB 0.0BW	DKB {0.5 - 3.5BW}	Time-elapsed mechanical load sequence during DKB

4.5.1 Image Preparation for DVC Analysis

DVC assumes a continuous material within each subvolume. To separate the implant and bone into separate DVC subvolumes, all image stacks were shifted in the proximal-distal direction prior to DVC analysis. This resulted in the bone-tray interface of the implanted scans aligned with a DVC subvolume boundary in the transverse plane. This was achieved by deleting between 14 - 32 micro-CT slices, depending on the specimen. As a result, the slice containing the bone-tray interface was at a multiple of 34 pixels (being the side length of the final DVC subvolume) from the distal slice of the image stack.

As within Chapter 3, the effect of marrow movement was mitigated in each DVC analysis by masking marrow that was not present in both the baseline and target dataset. The same method described in 3.2.4 Image masking for DVC: Mitigating Marrow Movement was employed here. Please refer to that section for more details.

4.5.2 DVC Analysis

DVC analysis (direct correlation) was performed using the commercially available program DaVis (8.3.1, LaVision) between the baseline to target datasets to extract the internal vector and strain fields. A five-step iterative progression was used (176 pixels (8.10 mm), 112 pixels (5.15 mm), 76 pixels (3.50 mm), 52 pixels (2.39 mm), and 34 pixels (1.56 mm)) with 2 passes at each step and 0 % overlap (Wearne et al., 2022). Algorithmic masking was applied to remove pixels corresponding

to air or background (grey level values less than 20). The final spatial resolution of the extracted strain field was 34 pixels (1.56 mm), as a compromise between spatial resolution and accuracy (Dall'Ara et al., 2014). Displacement vectors (components U_x, U_y, U_z), normal strain fields (ε_{xx}, ε_{yy}, ε_{zz}), shear strain fields (ε_{xy}, ε_{yz}, ε_{zx}) and the correlation coefficient (r) field across the entire datasets were extracted.

Following standard notation for displacement, U_x, U_y and U_z are used here for the extracted displacement vectors. In the DaVis software, these are reported as V_x, V_y and V_z.

4.5.3 DVC Subvolume Masking

The extracted vector and strain fields included subvolumes across the tibia, across the implant and external to the tibial cortex. Masks were produced from the micro-CT slices to identify subvolumes of these three regions. Furthermore, subvolumes with a bone volume fraction (BV/TV) less than 5 % were observed to have a higher associated error. The resected micro-CT dataset of each tibia was employed to binarise bone and perform this additional masking. Lastly, masks were produced to isolate subvolumes of the tibia in direct contact with the implant (Radial 1, 0.00 – 1.56 mm from the bone-implant interface), and then moving radially outwards by 2 subvolumes (Radial 2: 1.56 – 3.13 mm from the bone-implant interface) and 3 subvolumes (Radial 3: 3.13 – 2.69 mm from the bone-implant interface). For each region, binarised image datasets were produced (all within software CTAnalyser, 1.17.7.2), where a greylevel value of 1 identified pixels within that region, and a greylevel of 0 identified pixels outside of that region. An exemplar image of each region is included below in Figure 4. 8 (top), with the corresponding DVC mask (bottom).

As undertaken within Chapter 3: *3.2.4 Image masking for DVC*, the tibia and implant were segmented by identifying the tibial cortex (Figure 4. 8A): thresholding bone, despeckling (20 voxels in 3D), and applying a "ROI shrink-wrap" software feature (stretching over holes of 74 pixels in 2D). The produced mask encapsulated both the tibia and, when present, the implant. Pixels had a greylevel value of 1 if they fell within this space.

To create the BV/TV mask, the resected micro-CT dataset of each tibia was binarised for bone (Figure 4. 8B) by applying a 3D median filter (1 voxel), thresholding for bone and despeckling (10 voxels in 3D).

The tibial component was segmented to create one full solid object in each loaded (implanted) micro-CT dataset by thresholding for implant, despeckling (5 pixels in 2D), opening (morphological operation where one pixels is removed, and then added, to the boundary pixel), closing (morphological operation where four pixels where added, and then removed, from the surface), applying a "ROI shrink-wrap" feature (stretching over holes of 14 pixels in 2D), and, dilation by one pixel. A pixel value of 1 (white, Figure 4. 8C) in the segmented images corresponded to where the implant was, and, 0 (black, Figure 4. 8C) outside of the implant.

Subvolumes in direct contact with the implant were those within 1.56 mm from the bone-implant interface, being within 34 voxels of the segmented implant. To produce the Radial 1 images (Figure 4. 8D), the binarised implant images were read into CTAnalyser and a 3D expansion by 34 voxels was applied. For Radial 2, this expansion was 68 voxels and, for Radial 3, 102 voxels.
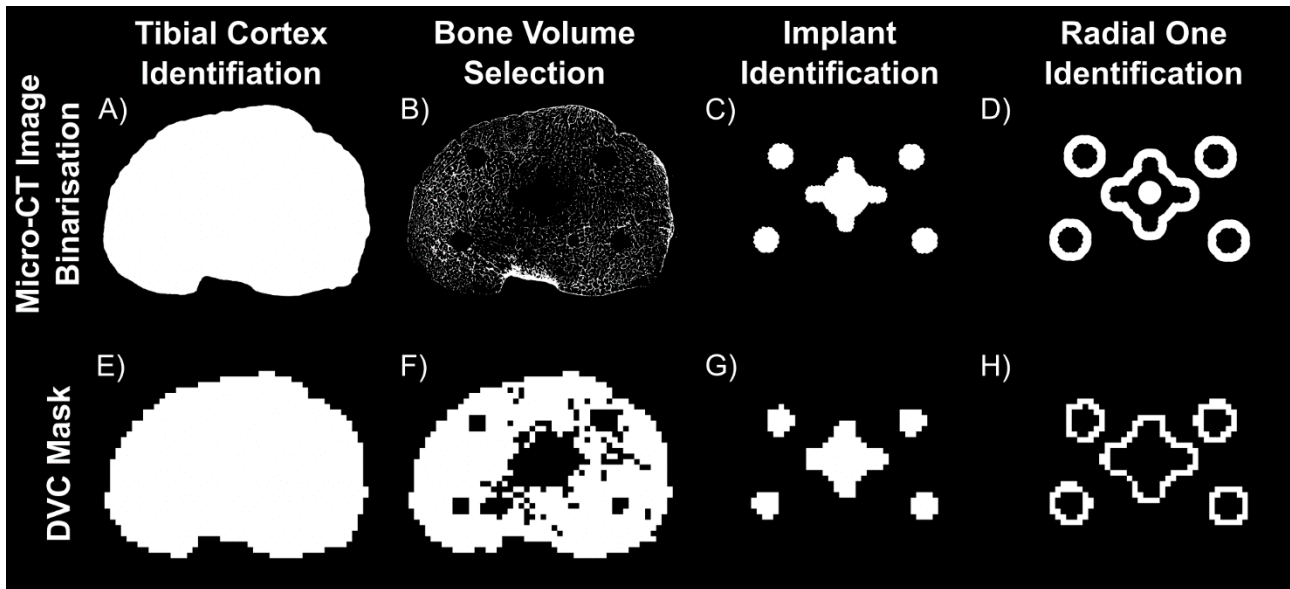
Figure 4. 8: DVC subvolume masking. Top: producing masks from micro-CT images by A) segmenting the tibia (including implant), B) binarising bone, taken from the resected scan, C) segmenting the implant and D) isolating voxels within 1.56 mm (34 voxels) of the bone-implant interface (3D space). Pixels with a greylevel of 1 (white) identify those within the respective regions, whereas pixels with a greylevel of 0 (black) are outside. Bottom: the corresponding DVC masks to identify regions are shown for E) subvolumes within the tibial cortex, F) subvolumes with a bone volume fraction greater than 5 % G) subvolumes of the implant and H) subvolumes of the tibia in direct contact with the implant (Radial 1). Tibial subvolumes were identified through the logic of the masks: E & F ⌐ G. For Radial 1 subvolumes, the logic of the masks employed was: E & F ⌐ G & H.
Exemplar images shown for Tibia G (BMP slice number 1310; DVC Z coordinate = 39).
&: "and" logic operator; ⌐: "and not" logic operator

DVC masks (Figure 4. 8E, F, G, H) were produced from the above binarised micro-CT images (Figure 4. 8A, B, C, D) in MATLAB (R2021b) through a custom written script. To identify subvolumes of the tibia, only those that contained, by volume, more than 90% of voxels pertaining to the tibia, were considered (i.e., those containing more than 10% of voxels external to the tibia or across the tibial tray were excluded). These subvolumes were identified in a multi-step approach, as follows:

Subvolumes of the tibia and implant construct (Figure 4. 8E), were identified as subvolumes that existed completely within the tibial cortex segmented images. **Implant subvolumes** (Figure 4. 8G) were identified as those that contained 10 % or more implant by volume from the segmented image datasets of the implant. **Tibia subvolumes** were then defined as those within the tibia and implant construct (Figure 4. 8E), that had an overall bone volume fraction greater than 5 % (Figure 4. 8F), but were not across the implant (Figure 4. 8G). Expressed in form of logical operators, this was written as: Figure 4. 8: E & F ⌐ G (& : *and* logic operator, ⌐: *and not* logic operator). **Radial 1 subvolumes** (Figure 4. 8H) were defined as subvolumes of the tibia that were at least 50% by

volume within 1.56 mm from the bone implant interface (logically: E & F ⊢ G & H). The same logic was used for Radial 2 and Radial 3. Extracted subvolumes more than 4.69 mm away from the bone-implant interface were not included in any subsequent analysis.

4.5.4 DVC Error Analysis

Using the experimental protocol established within this chapter, a zero-strain error analysis was performed to calculate the accuracy (MAER) and precision (SDER) of the system to be used in the following chapters. For each tibia, SD 0.0BW (PL1, target) dataset was rigidly co-registered to SD 0.0BW (PL2, baseline) dataset and DVC analysis was performed to extract the displacement vectors (U_x, U_y, U_z), the normal strain fields (ε_{xx}, ε_{yy}, ε_{zz}), the shear strain fields (ε_{xy}, ε_{yz}, ε_{zx}) and the correlation coefficient (r) field across the entire datasets. Masking of the DVC datasets was performed using the protocols detailed above. As the tibiae were in unloaded conditions, displacement vectors and strain values that deviated from zero were considered errors.

Strain MAER (Equation 3. 1) and SDER (Equation 3. 2) were calculated as indicators of the systems accuracy and precision, respectively (Tozzi et al., 2017, Wearne et al., 2022), for subvolumes of Radial 1, 2, and 3. Zero-strain error analysis across the seven tibiae and within the three VOIs (Radial 1, 2 and 3, Table 4. 4) resulted in a strain accuracy (MAER) of 439 ± 76 με (ave ± std dev) and precision (SDER) of 200 ± 54 με. The largest MAER value was 547 με (Tibia C, Radial 2) and SDER 336 με (Tibia B, Radial 1). Such errors are sufficiently low for analysis of bone within its elastic region, by being less that 10 % of the yield strain of bone (Liu and Morgan, 2007, Roberts et al., 2014).

Micromotion for subvolume k, ΔU_k, was calculated as the difference in relative motion of the implant to the tibia (Radial 1) across the three vector components (please refer to Chapter 6, Study 3: Relative Motion for a more indepth explanation of how micromotion was calculated). As the tibia and implant are unloaded and the two scans are rigidly co-registered, vector components that deviate from zero are errors. The associated micromotion error was taken as the absolute uncertainty of these values:

$$\Delta U_{x,k} = \left| U_{x,k,Implant} \right| + \left| U_{x,k,Tibia} \right|$$
$$\Delta U_{y,k} = \left| U_{y,k,Implant} \right| + \left| U_{y,k,Tibia} \right|$$
$$\Delta U_{z,k} = \left| U_{z,k,Implant} \right| + \left| U_{z,k,Tibia} \right|$$

where $\left| U_{c,k,Implant} \right|$ is the extracted vector magnitude for component c of the implant and $\left| U_{c,k,Tibia} \right|$ of the tibia for subvolume k during the zero-strain error analysis.

MAER and SDER for micromotion was hence calculated as:

Equation 4. 1: Micromotion Mean Absolute Error (MAER)

$$MAER = \frac{1}{N}\sum_{k=1}^{N}\left(\frac{1}{3}\sum_{c=1}^{3}|\Delta U_{c,k}|\right)$$

Equation 4. 2: Micromotion Standard Deviation of Error (SDER)

$$SDER = \sqrt{\frac{1}{N}\sum_{k=1}^{N}\left(\frac{1}{3}\sum_{c=1}^{3}|\Delta U_{c,k}| - MAER\right)^{2}}$$

ΔU = micromotion; c = independent micromotion component (x, y, z); k = measurement point (subvolume); N = number of measurement points (number of subvolumes).

Across the interface, the micromotion accuracy was 12.81 ± 6.89 µm and precision was 2.99 ± 1.59 µm. The largest MAER value was 26.87 µm (Tibia E) and SDER was 5.46 µm (Tibia B), Table 4. 4. MAER for Tibia E was the only error value (MAER or SDER) that exceeded 15.0 µm. Such values are sufficiently low to discriminate micromotions detrimental to osseointegration, by being less than 10 %, on average, of the reported osseointegration threshold (150 µm (Søballe et al., 1992)) (Viceconti et al., 2000).

As such, the use of DVC within the following studies of this thesis was deemed acceptable.

Table 4. 4: The accuracy and precision of strain (columns 2: 4) and micromotion (column 5) calculated for each region and specimen. The errors are calculated from a zero-strain error analysis (SD 0.0BW (PL2) vs SD 0.0BW (PL1)), where, as the tibiae are unloaded, any deviation from zero is considered an error. Reported as MAER ± SDER.

Tibia	Strain Uncertainties			Micromotion Uncertainties
	Radial 1 (µε)	Radial 2 (µε)	Radial 3 (µε)	(µm)
A	405 ± 159	396 ± 169	307 ± 116	8.21 ± 1.45
B	535 ± 219	539 ± 220	374 ± 146	14.85 ± 5.46
C	495 ± 216	498 ± 237	333 ± 180	6.66 ± 1.74
D	455 ± 169	437 ± 169	329 ± 122	9.60 ± 1.74
E	444 ± 336	473 ± 290	370 ± 198	26.87 ± 4.83
F	477 ± 232	516 ± 234	353 ± 149	14.06 ± 3.13
G	528 ± 232	547 ± 237	416 ± 178	9.40 ± 2.58
Radial Average MAER ± SDER	**477 ± 223**	**487 ± 22**	**354 ± 155**	
Total Average MAER ± SDER			**439 ± 200**	**12.81 ± 3.00**

MAER: mean absolute error; SDER: standard deviation of error.

Study 2: Quantifying the interference fit of cementless tibial trays: a cadaveric micro-CT and digital volume correlation analysis

The work presented in this chapter is in preparation for submission as a manuscript to a peer-reviewed journal.

Wearne LS, Rapagna S, Keene G., Taylor M, Perilli E (2024). Quantifying the interference fit of cementless tibial trays and its effect on the initial mechanical environment. *In submission at a peer-reviewed journal.*

Please refer to the Appendix at the end of this thesis for a detailed outline of the author's contribution to this study.

ABSTRACT

Cementless tibial components rely on sufficient primary stability and direct bone-implant contact to achieve osseointegration. To ensure this, an interference fit is introduced during surgery, whereby there is an overlap between the resected tibia and the component's geometry. However, due to surgical variation and induced damage during impaction, the actual interference fit achieved differs to what was intended. Little is known about the actual interference fit of cementless tibial components and its interplay to the induced mechanical response of the surrounding cancellous bone. The aim of this study was 1) to quantify the actual interference fit achieved across seven cadaveric tibiae with a commercially available cementless tibial component (Attune Affixium Cementless Fixed Bearing Knee, DePuy Synthes Joint Reconstruction) and 2) to assess its effect on the post-impaction cancellous bone strain. Bone micro-architecture was also determined from micro-CT scans of the intact tibiae as a metric for bone quality.

The tibiae were micro-CT scanned intact (at 23 μm/pixel), once prepared for TKA (46 μm/pixel) and following impaction of a titanium cementless tibial component (46 μm/pixel). The actual interference fit was defined as the distance between the bony surface of the prepared tibia to the impacted position of the tibial component, with a positive value denoting an interference and a negative value a gap. To quantify the mechanical response of cancellous bone to implantation, digital volume correlation (DVC) was performed between the resected and implanted micro-CT datasets, by extracting the minimum principal strain field.

An inhomogeneous actual interference fit was found across the pegs and keel (median ± std dev: 0.70 ± 0.27 mm) that was lower than the intended interference in all specimens. Limited interference (0.02 ± 0.12 mm) was found directly under the tray, which was related to the undulating resected surface (R^2 = 0.219, p < 0.01). Peaks and low points limited the percentage of the implant's tray in direct contact with bone to 54.4 %. A mechanical response in the surrounding cancellous bone was elicited after the impaction, with residual strains highest for bone closest to the pegs and keel (median ± std dev: -9,529 ± 2,959 με). The compressive strains, capturing both elastic and permanent deformation, were significantly related to the actual interference fit within 3.14 mm from the bone-implant interface (R^2 = 0.269 – 0.450, p < 0.001), whereby with increased interference there was an increased mechanical response in the cancellous bone. Bone volume fraction was not significantly related to the compressive strains at any distance from the bone-implant interface (p > 0.45). Insight here is provided into the interaction between surgical variability and the resulting mechanical response of the cancellous bone surrounding a cementless tibial TKA component. A complex interaction is apparent, whereby only 45 % of the mechanical response (residual strains) could be attributed to the actual interference fit.

5.1 INTRODUCTION

Cementless tibial total knee arthroplasty (TKA) components, and cementless prosthesis in general, rely on generating hoop stresses in the peri-implant bone to provide sufficient primary stability for osseointegration. During the surgery, an interference fit is introduced, whereby the tibia is under resected relative to the component geometry. The intended overlap is known as the *nominal interference fit* and the intent of this is twofold; firstly, it ensures direct contact between implant and bone, and secondly, induces a mechanical response within the peri-prosthetic bone. The elastic component of the latter is believed to provide stability by theoretically "gripping" onto the implant (Huiskes, 1993). However, the interference fit achieved during surgery differs to the nominal interference fit due to surgical variation and induced damage and the extent of mechanical response is not known.

The term *actual interference fit*, as coined by Berahmani et al. (2018), defines the overlap between implant and bone attained from the resection. This therefore takes into account any cut surface variation and misalignment between implant and bone. For tibial components, surgical error and variation have been assessed across the resected surface by quantifying the roughness and flatness of the cut (Toksvig-Larsen and Ryd, 1991, Toksvig-Larsen and Ryd, 1994, Delgadillo et al., 2020). Whilst surgical variation of tibial components has been recorded, to the best of the author's knowledge, no study has assessed its effect on the actual interference fit of cementless tibial components.

The intention of the interference fit is to achieve a mechanical interlock between the cementless tibial component and neighbouring cancellous bone. However, during the impaction process, bone may become abraded or compacted (Damm et al., 2017). This reduces the actual interference fit and induces damage that extends further than the bone-implant interface (Berahmani et al., 2018, Rapagna et al., 2019). The resulting strain field, being the mechanical response of the cancellous bone to the actual interference fit, has not been previously quantified for cementless tibial components experimentally. It is therefore unknown if the theoretical purpose of the interference fit, being to ensure bone-implant contact and elicit an elastic mechanical response in the surrounding cancellous bone, is achieved. By undertaking micro-CT scans of tibiae once resected and then after impaction (with a tibial component in place), this study employs digital volume correlation (DVC) to quantify the compressive response of the cancellous bone at organ level from the impaction process.

The aim of this study was 1) to quantify the actual interference fit achieved across seven cadaveric tibiae with a commercially available cementless tibial component (Attune Affixium Cementless Fixed Bearing Knee, DePuy Synthes Joint Reconstruction) and 2) to assess its effect on the post-impaction cancellous bone strain. Bone micro-architecture was also determined from micro-CT scans of the intact tibiae as a metric for bone quality.

5.2 MATERIALS AND METHODS

The analysis undertaken in this study employed the micro-CT datasets of the tibiae when intact (at 23 µm/pixel resolution), resected (at 46 µm/pixel resolution) and once implanted (SD PL2). Details of the datasets can be found within section:

4.2 Micro-CT Scanning. During all scans, the tibiae were placed within the aluminium tube of the mechanical loading rig (section: *4.4.1 The Loading Rig*). All seven tibiae (section: *4.1 Specimens*) were included in this analysis. Please refer to the sections listed for methodology details.

5.2.1 Nominal Interference Fit

The employed tibial component (Attune Affixium, more details section: *4.1.1 Cementless Tibial component*) has a nominal radial interference of 1.00 mm on the sides of each peg (DePuy Synthes, 2016). The peg guides are over drilled relative to the peg length, resulting in no interference distally.

The nominal interference varies across the surface of the keel from 1.19 mm to 2.00 mm (DePuy Synthes, 2023). The median interference across the keel is 1.2 mm. The keel guide is prepared by firstly drilling a hole into the central cancellous bed and then employing a keel punch to impact the cancellous bone (DePuy Synthes, 2016).

Across the tray, there is no nominal interference, with the surgical guidelines instructing impaction until the implant is "fully seated" (DePuy Synthes, 2016).

5.2.2 Co-Registration of the Micro-CT Datasets

The intact and resected datasets were rigidly co-registered to the implanted scan (SD PL2. DataViewer, version 1.5.4.0, Skyscan-Bruker). 3D co-registration was performed by aligning the distal region within the tibial metaphysis, which did not contain the implant or implant guiding holes. A 3D median filter with a round kernel of 1 voxel radius was applied to reduce image noise (smoothing). As detailed below, these co-registered datasets were used to quantify the bone microarchitecture variability, actual interference fit, the resected surface roughness and flatness, and, to extract the post-impaction residual strain fields.

5.2.3 Assessing Bone Morphometry

Morphometric analysis was undertaken on the intact dataset as an indicator of bone quality (Perilli et al., 2012), calculating the bone volume fraction (bone volume to total volume: BV/TV)).

Following co-registration and smoothing (median filter, 1 voxel), the intact scans were binarised for bone (filtering (median filter of 1 voxel), thresholding, despeckling, closing (CT Analyser version 1.17.7.2)). VOIs were created to isolate peri-prosthetic bone that existed where the implant came to sit, being inside the anterior-medial peg (Peg_AM), the anterior-lateral peg (Peg_AL), the posterior-medial peg (Peg_PM), the posterior-lateral peg (Peg_PL), and the Keel.

For peri-prosthetic bone across the tibial baseplate (Figure 5. 1A: Tray), a VOI was created, of 5 mm height, that encapsulated the cancellous bone across the plateau. The mid-plane of the VOI aligned with the cutting plane. 3D morphometric analysis was subsequently undertaken.

The Tray VOI was then further divided into six regions (Figure 5. 1B): the anterior-medial quadrant of the Tray (Tray_AM), the anterior intercondylar region of the Tray (Tray_AIC), anterior-lateral quadrant of the Tray (Tray_AL), the posterior-medial quadrant of the Tray (Tray_PM), the posterior intercondylar region of the Tray (Tray_PIC), posterior-lateral quadrant of the Tray (Tray_PL). 3D morphometric analysis was undertaken on each tray VOI.
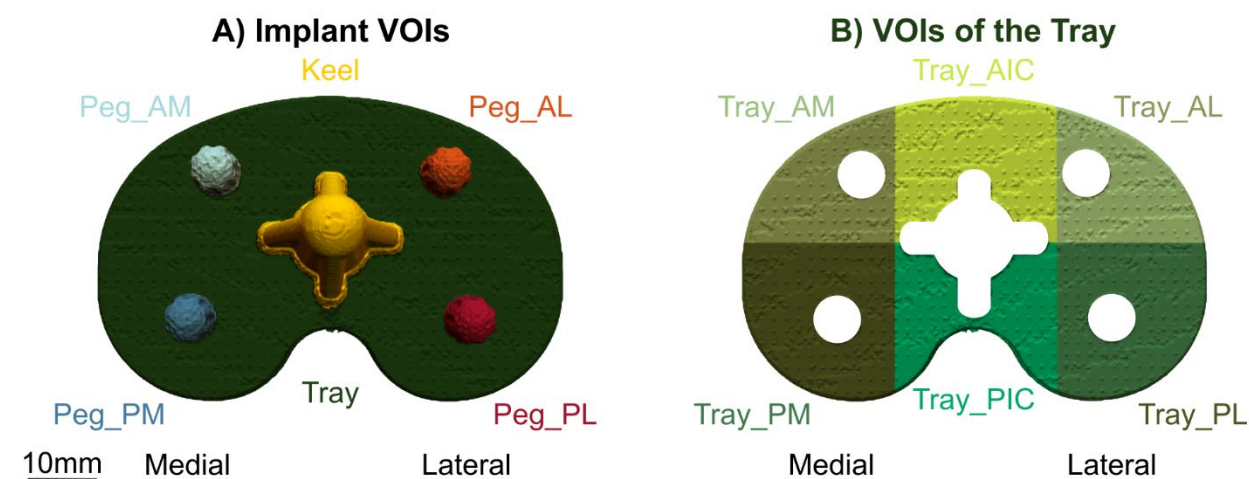
Figure 5. 1: A) The six volumes of interest (VOIs) sectioned across the implant: the anterior-medial peg: Peg_AM; the anterior-lateral peg: Peg_AL; the posterior-medial peg: Peg_PM; the posterior-lateral peg: Peg_PL; the keel: Keel and the tray: Tray. B) The Tray VOI was then further subdivided into 6 VOIs: subvolumes in contact with the anterior-medial quadrant: Tray_AM; the anterior-intercondylar region: Tray_AIC; the anterior-lateral quadrant: Tray_AL; the posterior-medial quadrant: Tray_PM; the posterior-intercondylar region: Tray_PIC; and the posterior-lateral quadrant: Tray_PL.

5.2.4 Quantifying Actual Interference Fit

The actual interference fit was defined as the distance between the bony surface of the tibia after TKA preparation and the seated surface of the tibial component. Depending on the region, this was calculated via different methods.

5.2.4.1 Pegs and Keel

A continuous bone boundary (referred to as BoneBoundary) was developed around the drill holes made for each of the pegs (Peg_AL, Peg_AM, Peg_PL, Peg_PM) and the keel (Keel) following a similar method to Berahmani et al. (2018). The BoneBoundary reflected the resected cut. For this, VOIs surrounding each of these fixation features were extracted from both the resected and impacted (SD PL2) scans (peg VOIs: 340 x 340 x 340 voxels, keel VOIs: 646 x 646 x 1020 voxels). Bone within the resected scan (Figure 5. 2A) was binarised (thresholded for bone and despeckling) and followed by a 2-dimensional (2D) closing to produce a continuous surface along the resected cut (Figure 5. 2B, blue ring). The resultant BoneBoundary surface was saved as an STL model.

An STL model of the implant within each of the five VOIs was also created, by binarising the implant from the impacted scan (SD PL2) for each specimen (thresholding for implant, despeckling (5 voxels in 2D), morphological operations to close over implant pores (opening by 1 pixel in 2D, closing by 4 pixels in 2D, ROI shrink-wrap of 14 pixels in 2D), Figure 5. 2D (orange ring)).

To calculate the actual interference fit, the normal surface deviation between the BoneBoundary STL and implant STL was extracted (Simpleware ScanIP Medical P-2019.09). The implant STL was set as the reference surface, with the BoneBoundary STL forming the target surface. The surface deviation (mm) was calculated for every triangulation point across the implant surface. A positive value denoted an interference (blue, Figure 5. 2E) and a negative value a gap between implant and bone (red, Figure 5. 2E).
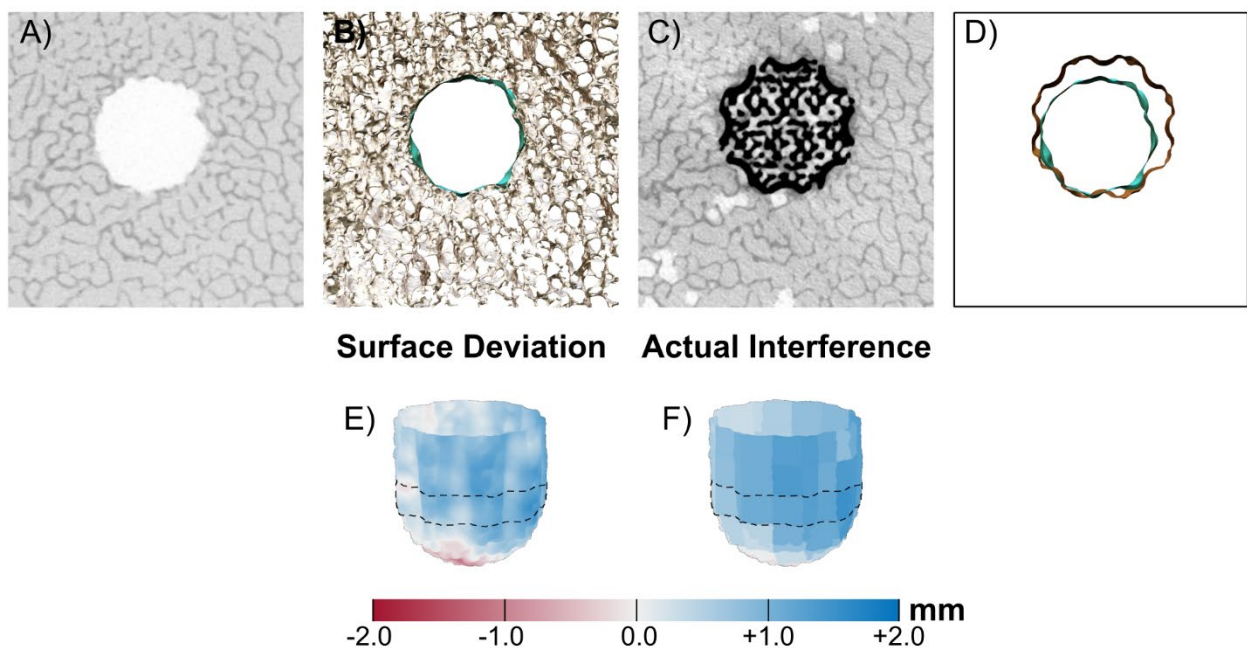
Figure 5. 2: Quantifying the actual interference fit for peg and keel VOIs. Methodology shown for Tibia D, Peg_AL. From the resected micro-CT dataset (A), a continuous BoneBoundary was developed (B). Similarly, from the impacted micro-CT dataset (B), the implant surface was extracted (D, orange). The surface deviation between the BoneBoundary and implant STL (D) was extracted across the entire VOI (E, slice shown by the dashed line). The actual interference fit was taken as the peak (98th percentile) surface deviation within a DVC subvolume (F, slice shown by the dashed line).

Based on the grid system established by the DVC post-impaction residual strain field, see below, the actual interference fit for each subvolume was calculated (Figure 5. 2F). This was taken as the 98th percentile of the surface deviation for the implant triangulation points that fell within that subvolume, being a 34 x 34 x 34 voxel cube.

Sensitivity Analysis

A sensitivity analysis was undertaken to assess the effect of the threshold window when binarising bone and implant on the resultant actual interference fit, respectively. Here, for the four peg VOIs of Tibia D, the threshold window for bone and implant was altered by ±1% (Figure 5. 3) (Hara et al., 2002, Rapagna et al., 2022), and the actual interference fit was subsequently calculated following the same method as detailed above.

B		Bone	Implant
Chosen Threshold Boundaries		55 – 139	190 – 255
	-1%	53 – 137	188 – 255
	+1%	57 – 141	192 - 255
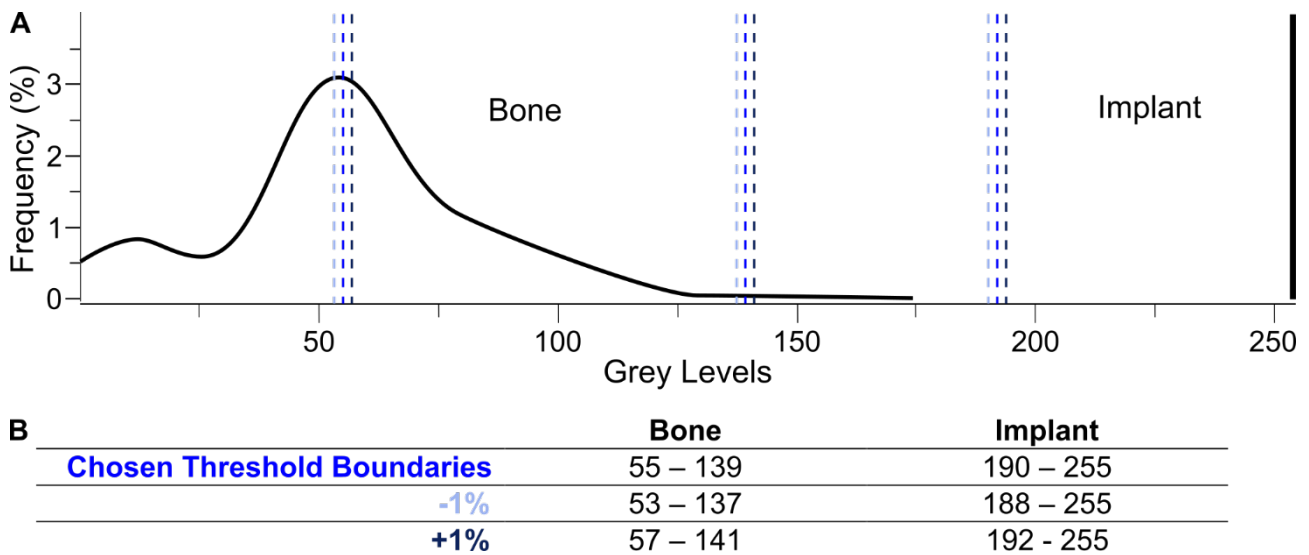
Figure 5. 3: Actual interference fit sensitivity analysis: threshold window. A) Example of a grey level histogram (256 grey levels) taken from a transaxial slice (1330) of Tibia D. Boundaries used to threshold Bone (55 – 139) and Implant (190 – 255) are shown by the central blue dashed lines. Sensitivity analysis was undertaken by shifting these boundaries by -1% (-2 grey levels; light blue) and +1% (+2 grey levels; dark blue), the threshold values included in B). The quantified actual interference fit was most sensitive to the threshold window chosen for bone, with an average (± std dev) difference of 0.0352 ± 0.0215 mm between the lower and upper threshold boundaries, equating to a difference of 6.62 ± 6.91 % of the calculated actual interference fit. Across the four pegs, the average actual interference for Tibia D using the chosen threshold boundaries was 0.630 ± 0.152 mm (Table 5. 1, row 4). Shifting the bone threshold window by -1% (-2 grey levels) resulted in an increased average interference of 0.641 ± 0.141 mm, whilst shifting the threshold window by +1% (+2 grey levels) resulted in a decreased average actual interference of 0.605 ± 0.156 mm. The effect of the threshold window of the implant to the actual interference was much lower, with a difference of 0.000501 ± 0.001943 mm between lower and upper windows, being a variation of 0.091 ± 0.281% of the calculated actual interference. These variations in actual interference due to chosen threshold windows for both bone and implant were deemed acceptable as they are several factors smaller than the actual interference calculated in this study.

5.2.4.2 Tibial Tray

For the actual interference fit directly under the tibial tray (Tray, Figure 5. 4A), a different method was employed compared to the pegs and keel, as it was not possible to produce the same BoneBoundary STL for this region. Instead, the actual interference fit was quantified as the superior-inferior distance for each Tray subvolume between the most proximal occurrence of bone within the resected dataset and the most distal occurrence of tray in the implanted dataset (custom script, MATLAB R2021b).
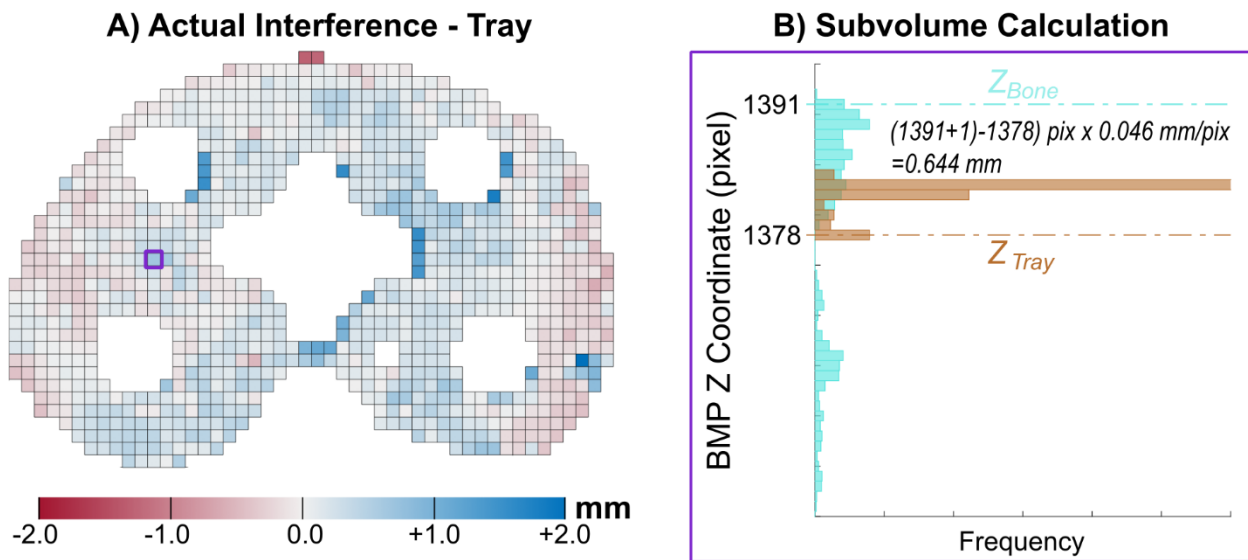
Figure 5. 4: Quantifying Actual Interference fit across the Tray A) distribution of actual interference fit across the Tray VOI of Tibia D, and, B) how it was calculated: the superior-inferior distribution of bony (blue) and implant (orange) pixels for the selected subvolume. The actual interference fit (calculation shown) is quantified as the distance between these two.

To calculate, the scan of the resected tibia was binarised for bone (thresholding for bone followed by despeckling (10 voxels in 3D), CTAnalyser, 1.17.2.2, Skyscan- Bruker) and the impacted scan binarised for the implant (thresholding for implant, despeckling (5 voxels in 2D), morphological operations to close over implant pores (opening by 1 pixel in 2D, closing by 4 pixels in 2D, ROI shrink-wrap of 14 pixels in 2D)).

Moving distally through the segmented resected dataset, the first occurrence of bone for every pixel in an XY plane was recorded. According to the established DVC grid system, the most proximal occurrence of bone for each subvolume, Z_{Bone}, was taken as the 98th percentile proximal position of bony points that occurred within that 34 x 34 pixel square (Figure 5. 4B, blue line). Conversely for the implant, moving proximally through the segmented implant dataset, the first occurrence of implant for every pixel in an XY plane was recorded. The most distal occurrence of implant for each subvolume, Z_{Tray}, was taken as the 2nd percentile distal position of implant points that occurred within that 34 x 34 pixel square (Figure 5. 4B, orange line).

The actual interference fit was quantified as the superior-inferior distance between these two occurrences (Equation 5. 1), with a positive value denoting an interference and a negative value a gap. When Z_{Bone} and Z_{Tray} occur at the same superior-inferior position, there is an overlap of 1 pixel (0.046mm). Therefore, a vertical offset of 1 pixel was added to the bone occurrence.to correctly represent this overlap.

Equation 5. 1: Calculating the actual interference fit (in mm) across the Tray

$$\left((Z_{Bone} + 1) - Z_{Tray}\right) \times 0.046 \; mm/pixel$$

Where Z_{Bone}: proximal occurrence of bone within the subvolume (pixel), Z_{Tray}: distal occurrence of tray within the subvolume (pixel).

Consequently, each subvolume across the Tray had an actual interference fit value, quantifying the overlap between the Tray and the underlying bone for that region (34 x 34 pixels (1.56 x 1.56 mm)) of the interface. The percentage of Tray in contact with bone was calculated, being the percentage of subvolumes within Tray that had an actual interference fit ≥ 0.00mm to the total number of subvolumes within Tray. This was repeated, for subvolumes with an actual interference fit between -0.300 mm to 0.00 mm (a gap between the Tray and underlying bone up to 300μm) and between -0.300mm to -0.500mm (a bone-tray gap between 300 to 500μm), defining the lower and upper permissible gaps for bone apposition on the implant surface, respectively (Carlsson et al., 1988, Dalton et al., 1995, Dalury, 2016). These values (PSA ≥ 0.00 mm, -0.300 ≤ PSA < 0.00mm, -0.500 ≤ PSA < -0.300mm and PSA < -0.500mm) were calculated across the entire Tray, and then for each of the 6 VOIs of the Tray (Tray_AM, Tray_AIC, Tray_AL, Tray_PM, Tray_PIC, Tray_PL, Figure 5. 1B).

5.2.4.3 Resected Surface Analysis

To calculate the roughness and the flatness of the resected tibia surface, the plane of best fit was calculated for all proximal bony points (Z_{Bone}) (MATLAB 2021b, custom script). The normal deviation of each proximal bony point to the plane of best fit was calculated, with a negative value denoting over-resected bone (inferior to the plane of best fit) and a positive value denoting under-resected bone (superior to the plane of best fit). The resected surface roughness was calculated as the range (2nd to 98th percentile) of surface deviation across the plane of best fit and the flatness as the standard deviation of surface deviation across the plane of best fit (Toksvig-Larsen and Ryd, 1994, Delgadillo et al., 2020).

5.2.5 Post Impaction Strain Field: DVC Analysis

DVC analysis was performed to extract the post-impaction residual strain field, being the minimum principal strain component between the resected scan (baseline) and impacted scan (SD PL2, target) for each tibia. The same configuration detailed in *4.5 Digital Volume Correlation Analysis* was employed, however, algorithmic masking was applied to remove both pixels associated with air (a grey level less than 20) and also the titanium tibial component (grey level greater than 170).

From the DVC analysis, the extracted normal (ε_{xx}, ε_{yy}, ε_{zz}) and shear (ε_{xy}, ε_{yz}, ε_{zx}) strain fields were used within this study. Principal strain components were calculated in MATLAB (R2021b) as the eigenvalues of the Cartesian strain matrix for subvolumes across the tibia, with the minimum principal strain component describing apparent compression. Masking (detailed within *4.5.3 DVC Subvolume Masking*) was applied to isolate tibial subvolumes, with a bone volume fraction greater than 5 %, within Radial 1 (0.00 – 1.56 mm from the bone-implant interface), Radial 2 (1.56 – 3.13 mm from the bone-implant interface) and Radial 3 (3.13 – 2.69 mm from the bone-implant interface). Each radial VOI was further divided into the different subregions (Figure 5. 1A): subvolumes in direct contact with Peg_AM, Peg_AL, Peg_PM, Peg_PL, and the Keel, and, those directly under the tibial baseplate (Tray). The Tray VOI was also further divided into 6 VOIs: Tray_AM, Tray_AIC, Tray_AL, Tray_PM, Tray_PIC, and Tray_PL (Figure 5. 1B).

5.2.6 Matching Actual Interference fit Subvolumes to Post-Impaction Subvolumes

The subvolumes with an actual interference fit measurement occurred within the tibial component space, whilst the post-impaction strain values occurred within the cancellous bone (and thus external to the component). To align the actual interference fit to the induced post-impaction strain, a "*k-nearest neighbour (knn)*" search (MATLAB, R2021b) was employed. This matched post-impaction strain subvolumes to the closest actual interference fit subvolume.
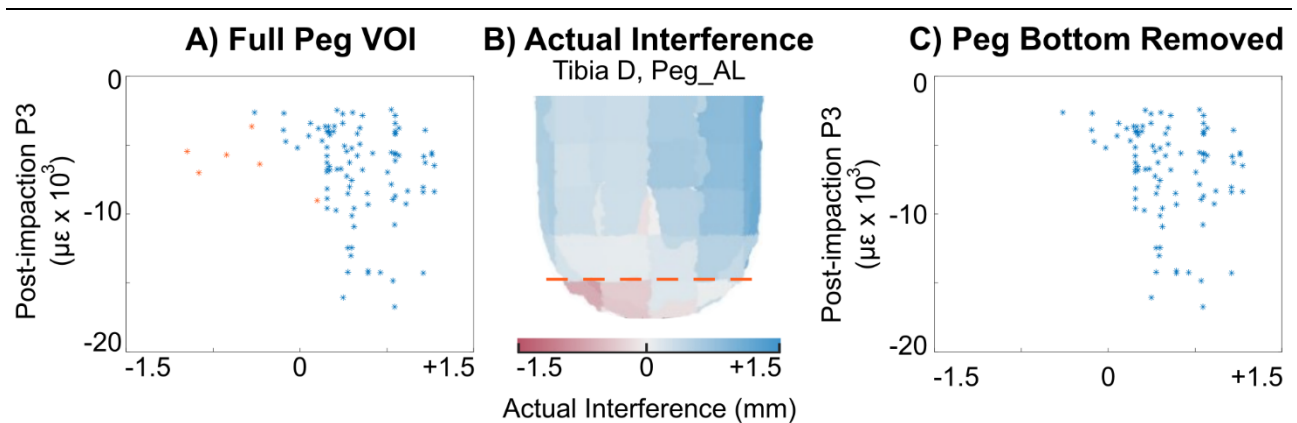
Figure 5. 5: Bone debris accumulation in Peg VOIs: data masking. A) Subvolume scatter plot of the actual interference fit vs. post-impaction minimum principal strain component (P3). Subvolumes existing at the distal tip of the peg are highlighted. B) Actual interference fit across the VOI (Tibia D, Peg_AL), orange dashed horizontal line separating the distal tip of the peg. C) the same scatter plot of A, however with subvolumes below the orange line masked.

Scatter plots of the actual interference fit *vs.* post-impaction minimum principal strain were created for each VOI, with every subvolume forming a data point (Figure 5. 5A). Some unexpected instances were observed in which compressive bone strains occurred even though there was a gap between bone and implant (actual interference fit < 0.00 mm). Upon inspecting the corresponding micro-CT images, such instances were mainly limited to the distal tip of the implant pegs. Following surgical guidelines, the peg guides were over-drilled in relation to the peg length to avoid "bottoming-out" (DePuy Synthes, 2016). This was quantified within the actual interference fit: where there was a gap at the distal tip of the implant (subvolumes below the orange line, Figure 5. 5B). After the impaction, an accumulation of debris was visible in the micro-CT images within these regions resulting in high minimum principal strains. For the analysis moving forward, measurements (both actual interference fit and post-impaction strain) associated with the distal tip of the pegs were masked (Figure 5. 5D). The presented results do not include these subvolumes unless otherwise specified.

5.2.7 Statistical Analysis

5.2.7.1 Bone Morphometry

A one-way analysis of variance (ANOVA) for repeated measures was performed to assess if there was a statistically significant regional variation of BV/TV across the specimens, with, in the first test, the implant VOIs (Peg_AM, Peg_AL, Peg_PM, Peg_PL and Keel) being the independent variable and their BV/TV the dependent variable. A second test was run to assess the regional variation in BV/TV across the Tray VOIs, with the Tray VOIs (Tray_AM, Tray_AIC, Tray_AL, Tray_PM, Tray_PIC and Tray_PL) being the independent variable and their BV/TV being the dependent variable.

Significance was set to $p < 0.05$. Where significance was found, post-hoc analysis was undertaken with Bonferroni adjustment, to determine where statistically significant differences arose.

5.2.7.2 Resected Surface

Distribution maps of the surface deviation were created across the resected surface, showing areas of over-resection and under-resection relative to the cutting plane of best fit.

An additional linear regression was undertaken for the tray VOIs (7 tibiae x 6 tray VOIs = 42 data points), with the median BV/TV and the resected surface deviation as the predictor variables and median actual interference fit as the predicted variable. Significance (alpha level) was set to $p < 0.05$.

5.2.7.3 Actual Interference Fit and Post-Impaction Residual Strain Field

For each of the 11 VOIs, the median and standard deviation of the actual interference fit and post-impaction strain were calculated for each radial (Radial 1, 2 and 3) boundary. For the six tray VOIs, the median and standard deviation of the resected surface deviation was also calculated. To

assess the contribution of actual interference fit and BV/TV to the post-impaction residual strain field, a linear regression analysis was performed. The median actual interference fit values and BV/TV for each VOI (77 data points) were predictor variables and the VOI post-impaction strain median values were the predicted variable (*fitlm*, MATLAB, 2021b). This analysis was undertaken for each of the radial boundaries. Significance (alpha level) was set to $p < 0.05$.

5.3 RESULTS

5.3.1 Bone Morphology

As seen in Figure 5. 6, the specimens presented regional variations in bone micro-architecture. The repeated measures ANOVA, with Greenhouse-Geisser correction, for the implant VOIs found statistically significant differences in BV/TV (p = 0.001). Post-hoc analysis revealed that the BV/TV of Keel (median ± std dev: 8.2 ± 3.4 %) was consistently lower than all other VOIs (p < 0.031). The BV/TV of the Peg_AL (11.7 ± 3.9 %) was also lower than other VOIs, and reached significance against Peg_PL (p < 0.001, 22.1 ± 4.5 %) and Peg_AM (p = 0.002, 19.8 ± 2.1 %).

Regional variations in BV/TV across the Tray VOIs were also found (p < 0.001, Greenhouse-Geisser correction). Through post-hoc analysis, statistically significant regional variation occurred across the entire anterior portion of the Tray, with Tray_AM (21.4 ± 3.1 %) having a greater BV/TV than both Tray_AL (p = 0.038, 16.6 ± 3.0 %) and Tray_AIC (p = 0.001, 12.3 ± 2.6 %). Tray_AIC had the lowest BV/TV of the six regions, which was statistically significantly lower to all other VOIs (p < 0.017). The region with the highest BV/TV was the posterior-medial VOI directly under the tray (Tray_PM), that had a median BV/TV of 24.7±5.4 %.

Within the micro-CT scans, Tibia E was observed to have some areas void of cancellous bone (possible lesions) in the proximal anterior-lateral region that extended to the metaphysis. This was reflected within the BV/TV of the Peg_AL (7.6%), Keel (4.4%) and Tray_AIC (8.3%) VOIs.
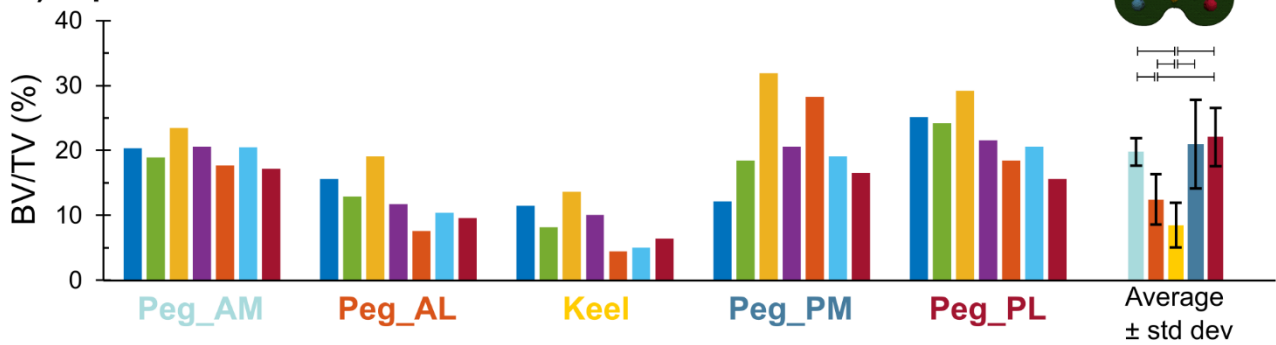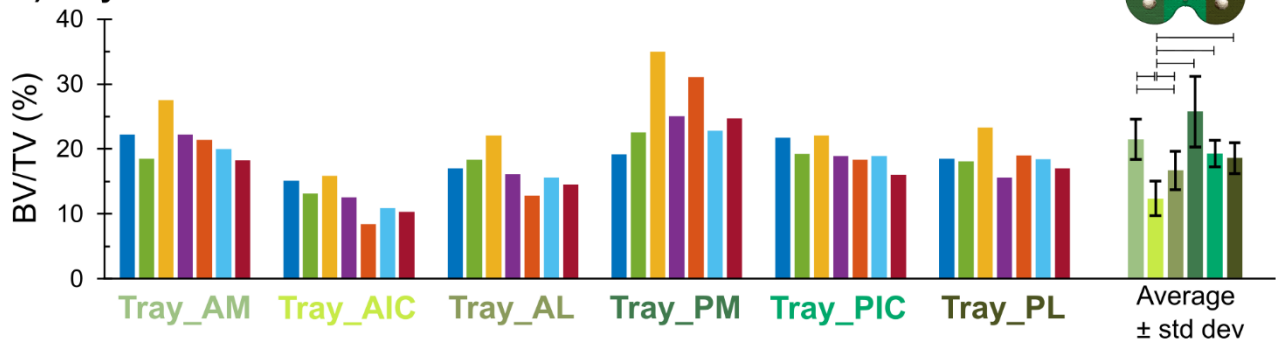
Figure 5. 6: Analysis of regional variation of tibial bone volume fraction of A) the implant volumes of interest (VOIs) and B) the Tray VOIs. Average ± std dev (error bars) for each VOI included in the plot to the right. Statistically significant differences of BV/TV signified by the horizontal bar.

Anterior-medial peg: Peg_AM; anterior-lateral peg: Peg_AL; keel: Keel; posterior-medial peg: Peg_PM; posterior-lateral peg: Peg_PL. For the tray: the anterior-medial quadrant: Tray_AM; the anterior-intercondylar region: Tray_AIC; the anterior-lateral quadrant: Tray_AL; the posterior-medial quadrant: Tray_PM; the posterior-intercondylar region: Tray_PIC; and the posterior-lateral quadrant: Tray_PL.
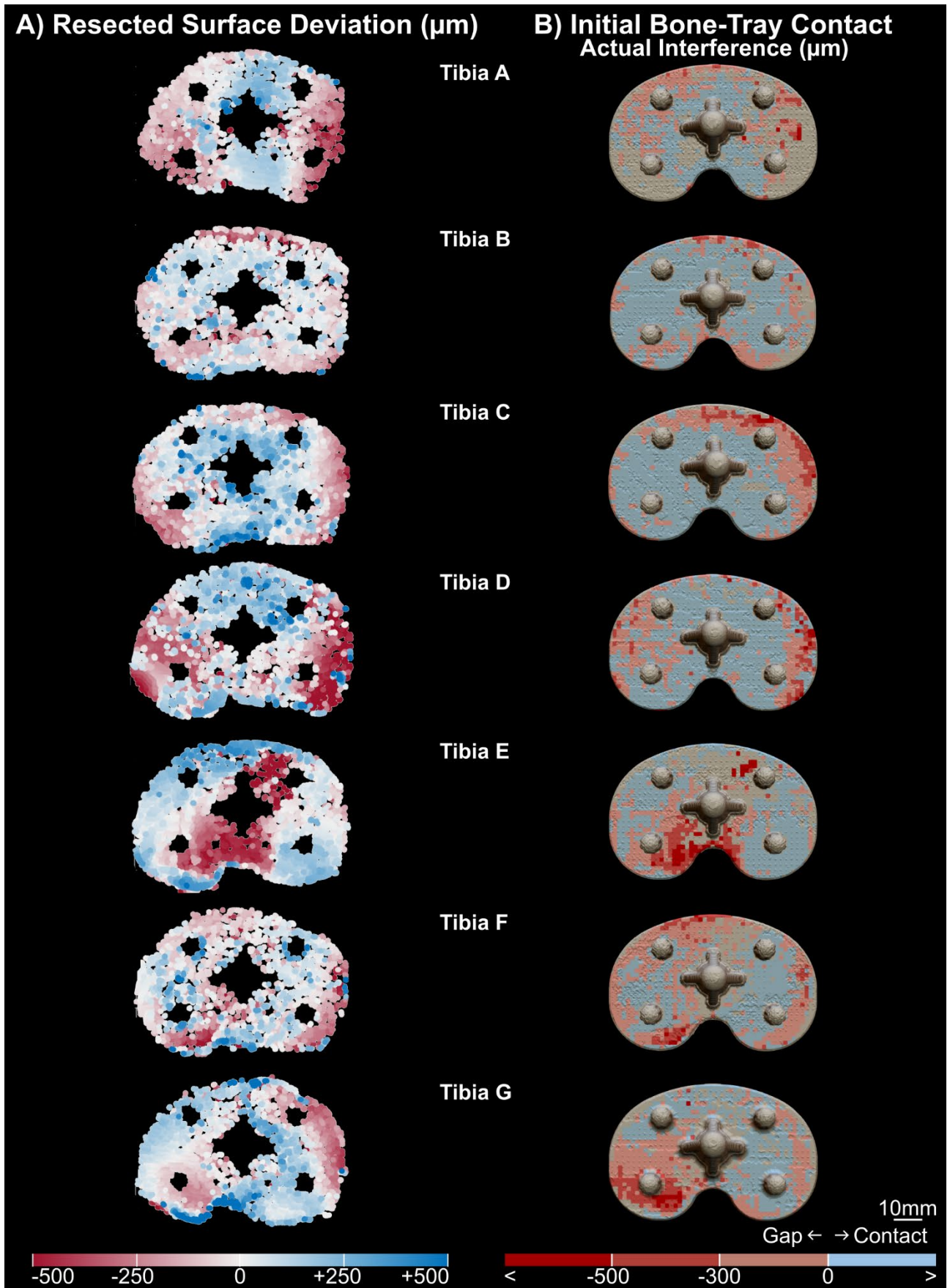
Figure 5. 7: A) The surface deviation across the resected cut and B) the initial contact between the tibial tray and underlying bone for each of the seven tibiae. Blue colour shows A) peaks in the resected surface and B) areas of bone-implant contact, whilst red colour displays A) low points in the resected surface and B) areas of bone-implant gaps. Due to masking, some subvolumes do not have an associated value calculated. In such instances, there is no representative colour, resulting in A) a black region and B) a grey region.

84
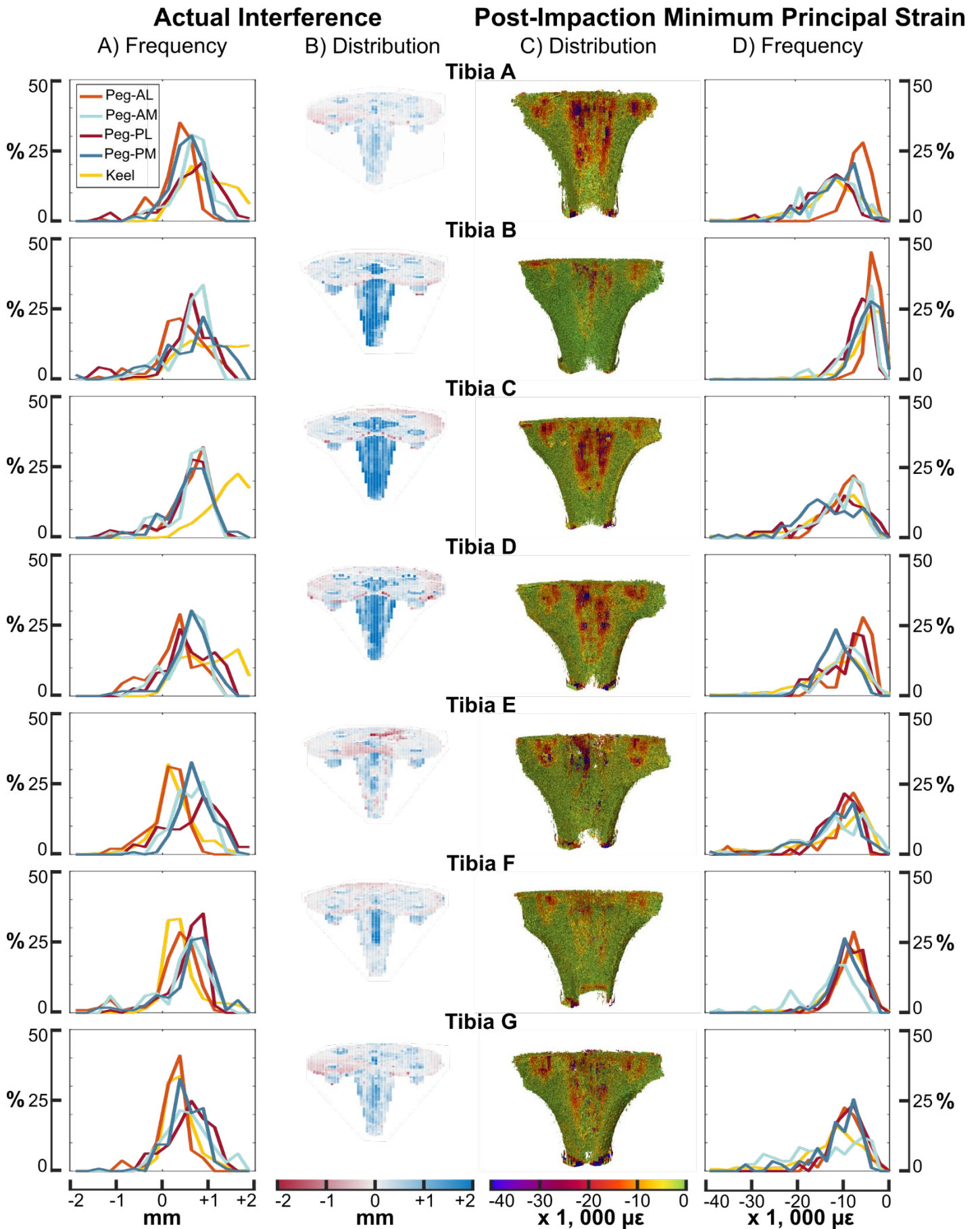
Figure 5. 8: Frequency and distribution plots of actual interference fit and post-impaction residual strain. The post-impaction minimum principal strain frequency plot is shown for subvolumes in direct contact with the tibial component (Radial 1).

5.3.2 Tibial Tray Surface Roughness

The median roughness across the resected surface of the seven tibiae was 2.44 ± 0.41 mm and flatness 0.180 ± 0.037 mm. No consistent regional pattern of peaks (resected surface above the plane of best fit) and low points (resected surface below) was observed between the specimens (Figure 5. 7A). For Tibia E, regions void of cancellous bone were associated with low points (Figure 5. 7A red regions), however, they did not appear to affect the roughness (2.44 mm) or flatness (0.221 mm).

There was no statistically significant relationship between BV/TV and the resected surface deviation ($p = 0.23$, $R^2 = 0.0349$).

5.3.3 Actual Interference Fit

The actual interference fit across the surface of the tibial component was inhomogeneous (Figure 5. 8A, B, Equation 5. 1). An interference (actual interference fit > 0.00 mm) was found across all pegs and keel (median ± std dev: pegs: 0.70 ± 0.25 mm and keel: 0.95 ± 0.50 mm). However, in all tibiae, the actual interference fit was less than the nominal interference fit (interference of 1.00 mm for the pegs and 1.2 mm for the keel) with the median interference value across a fixation feature (a peg or keel) being as little as 20.8 % of the nominal interference (Tibia E, Keel: 0.21 mm).

The median actual interference fit under the tray was 0.02 ± 0.12 mm for the seven tibiae, denoting little to no interference. For six of the seven tibiae, at least one region of the tray had a negative median value fit, representing a gap. A significant relationship was found between the resected surface deviation and actual interference fit ($R^2 = 0.219$, $p < 0.01$), however, not between the actual interference fit and BV/TV ($p = 0.77$).

After impaction, approximately half of the Tray (54.4 ± 8.2 %) was in contact with bone (range: 50.3 - 70.6 %, Figure 5. 7B, blue). The large majority of the Tray (90.4 ± 5.0 %) was within 0.300 mm from the resected surface, which increased to 97.3 ± 2.9 % within 0.500 mm.

Table 5. 1: Median VOI actual interference fit (mm) between the tibial component and seven tibiae, with a positive value denoting an interference, and, a negative value, a gap. The median and standard deviation (median ± std dev) for the peg, keel and tray VOIs are displayed in the bottom row. Tray cells are shaded to highlight interference (blue), contact (no colour) and gaps (red).

Tibia	Peg AM	Peg AL	Peg PM	Peg PL	Keel	Tray AM	Tray AIC	Tray AL	Tray PM	Tray PIC	Tray PL
A	0.886	0.450	0.553	0.744	0.951	-0.092	-0.046	-0.184	0.000	0.184	0.046
B	0.703	0.563	0.887	0.775	1.095	0.000	0.128	0.046	0.092	0.000	0.092
C	0.802	0.795	0.863	0.766	1.513	0.000	0.092	-0.184	0.046	0.184	0.138
D	0.689	0.404	0.724	0.704	1.058	0.046	-0.037	0.092	0.138	0.184	0.000
E	0.949	0.248	0.718	0.666	0.208	0.138	0.046	0.000	0.000	-0.368	-0.092
F	0.737	0.472	0.864	0.687	0.313	0.046	-0.092	0.046	-0.092	0.000	0.000
G	0.693	0.289	0.569	0.626	0.327	0.046	0.000	0.046	0.109	-0.046	-0.276
Median	0.704 ± 0.246				0.951 ± 0.499	0.023 ± 0.116					

5.3.4 Post-Impaction Strain

All tibiae showed a compressive mechanical response of cancellous bone following impaction (Figure 5. 8C, D). Large minimum principal strain values were extracted, with peak (90th percentile) VOI values ranging from -4,534 to -34,057 µε for subvolumes in direct contact with the tibial component (Radial 1). The median compressive strains of cancellous bone were much greater around the Peg and Keel VOIs (median ± std dev pegs: -9,363 ± 3,022 µε and Keel: -10,668 ± 2,919 µε) than under the tray (-3,725 ± 1,841 µε).

The induced mechanical response had largely dissipated by Radial 3 (3.14 – 4.69 mm from the bone-implant interface, Figure 5. 9). The median values in the VOIs ranged from -469 to -8,161 µε (median ± std dev: -3,140 ± 1,210 µε) within this boundary and were comparable across all regions.

Multi-linear regression revealed a significant relationship between the actual interference fit, being the predictor variable, and the post-impaction residual strain field (predicted variable) within VOIs of Radial 1 (within 1.56 mm from the bone-implant interface: R^2 = 0.450, p < 0.001) and Radial 2 (from 1.56 – 3.14 mm from the bone-implant interface:R^2 = 0.269, p < 0.001), indicating an increase in compressive strains with increased interference. This relationship dissipated by Radial 3 (3.14 – 4.69 mm from the bone-implant interface: R^2 = 0.005, p = 0.59), potentially indicating the end of the impaction zone.

BV/TV was not a significant predictor of the post-impaction residual strain field in any boundary from the implant (Radial 1: p = 0.89; Radial 2: p = 0.45; Radial 3: p = 0.75).
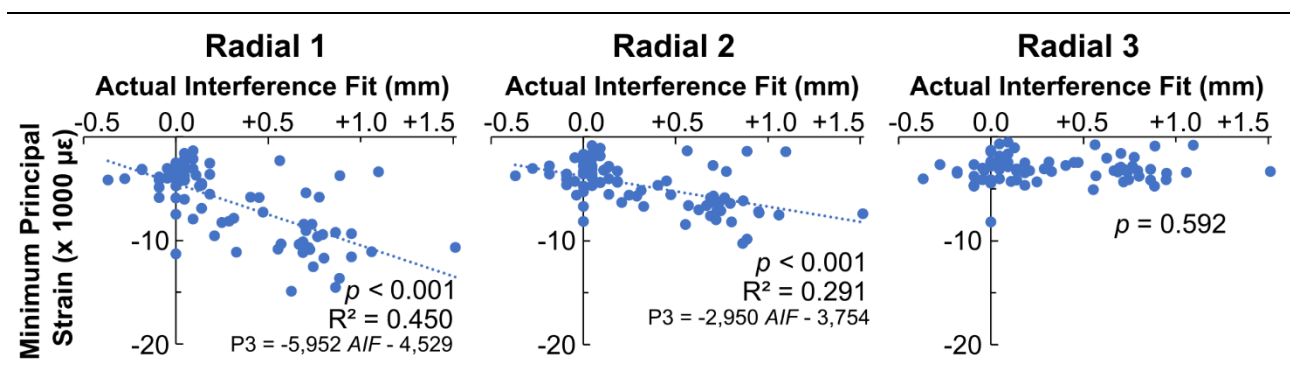
Figure 5. 9: Dissipation of residual post-impaction strain within the Radial 1, Radial 2 and Radial 3. Regression equation included for instances (Radial 1 and 2) where a statistically significant relationship between actual interference fit (AIF) and minimum principal strain (P3) were found.

5.3.5 DVC Analysis: Correlation Coefficient

The DVC correlation coefficients were assessed as an indicator DVC's ability to correlate the resected to impacted datasets, with a value of 1.0 denoting a perfect match (LaVision, 2017). Within Radial 1, being those subvolumes in direct contact with the implant, the median correlation coefficient of the DVC analysis was 0.49 ± 0.10. For the same regions, but when including the distal tip of the pegs, the correlation coefficient was 0.51 ± 0.10. The lowest correlation coefficient

for a VOI was 0.22 (Tibia B, Tray_AIC). The median correlation coefficient within Radial 2 (1.56 – 3.14 mm from the bone-implant interface) was 0.78 ± 0.08, and Radial 3 (3.14 – 4.69 mm from the bone-implant interface) was 0.84 ± 0.04. Within these regions, there was no difference in correlation coefficients when including the distal tip of the peg.

5.4 DISCUSSION

This study quantified the actual interference fit achieved between a commercially available cementless tibial TKA component and seven cadaveric tibia. The corresponding mechanical response of the cancellous bone in immediate contact with, and then extending away, from the implant was extracted through DVC analysis.

Across all seven tibiae, an interference (actual interference fit > 0.00 mm) was found in all peg (median ± std dev: 0.70 ± 0.25 mm) and keel VOIs (0.95 ± 0.50 mm). As similarly observed by Berahmani et al. (2018), there was large variation in the actual interference fit across the implant, both intra- and inter- tibia. Across a single fixation feature (Tibia G, Peg_PL), the actual interference fit could range from -0.40 to 1.42 mm (Figure 5. 8 A), highlighting an inhomogeneous distribution. In inspecting the bone boundary and implant STL models, this variation was due to numerous factors, including bone distribution and misalignment between the implant drill guides to the impacted position of the implant.

The quantified actual interference fit was substantially smaller than the nominal interference fit, intended to be 1.00 mm across the surface of the pegs and between 1.19 – 2.00 mm across the keel (median nominal keel interference 1.20 mm (DePuy Synthes, 2023)). Berahmani et al. (2018) in their study on press-fit femoral components, similarly reported an inhomogeneous actual interference fit distribution. However, that study found that the average actual interference fit was close to the nominal interference fit (average actual interference: 1.48 ± 0.27 mm; nominal interference: 1.50 mm). Part of the discrepancy between the nominal and actual interference fit quantified here could be the nature of the peg drills and keel punch, in comparison to the planar resection performed for femoral components. The actual interference fit achieved here may be lower than the nominal interference fit due to additional shearing occurring at the bone boundary during this preparation. After preparation, bone debris was observed here in the peg drill and keel punch.

Across the resected surface of the tray the interference was found to be small, with a median value of 0.02 ± 0.12 mm. This is unsurprising, considering that surgical guidelines recommend impacting until complete seating of the tibial tray (DePuy Synthes, 2016). In the instance of a perfectly flat resected surface, this would result in uniform contact across the tibial surface. Here however, peaks and low points were quantified across the resected surface of all seven tibiae, with a median roughness of 2.44 ± 0.41 mm and flatness 0.180 ± 0.037 mm. Such findings are comparable to other studies, reporting roughness between 0.56 - 2.57 mm and flatness between 0.10 – 0.40 mm (Delgadillo et al., 2020, Toksvig-Larsen and Ryd, 1991, Toksvig-Larsen and Ryd, 1994). Other authors reported a consistent pattern of over resection (a low point) in the central intercondylar region as the oscillating blade is pulled down into the softer cancellous bed (Delgadillo et al., 2020). Such a conjecture was not supported by the findings of this study, where no statistically significant relationship was found between bone volume fraction and resected surface deviation.

Only one tibia, Tibia E, displayed such a pattern and that could largely be associated to the observed regions void of bone (possible lesions) within the anterior-lateral region of this specimen. Three tibiae (Tibia A, C and D) displayed the opposite pattern, with under-resection (peaks) centrally and over-resection (low points) occurring medially and laterally. Berahmani et al. (2018) likewise reported no correlation between bone density (BMD) and cutting error. The lack of relationship found in this study could be in part due to *ex-vivo* nature of the experimental design, where the tibiae being stripped of all soft tissue prior to resection. This provided the surgeon with unrestricted view and access to the entire plateau, which would not be the case *in-vivo*. Surgical blade stiffness could also contribute to deflection (Toksvig-Larsen and Ryd, 1994), which was not assessed in this study.

A weak but statistically significant relationship was found between the surface deviation of the resected cut and the actual interference fit (R^2 = 0.219, *p* < 0.01): denoting that peaks and low points prevent complete seating of the tray. After impaction, only 54.4 ± 8.2 % of the tibial tray surface was initially in contact with the underlying bone. This may expose the cancellous bone in contact with the implant to increased bone stresses, found by Taylor et al. (1998), in their finite element study on cementless tibial components, to be sufficiently high to cause permanent damage. Within a Roentgen Stereophotogrammetric Analysis (RSA) study of a similar tray design (Attune, Depuy Synthes), high subsidence rates were reported within the first 3 months post-surgery (Koster et al., 2023). The high initial rate could be in consequence of the limited contact between tray and underlying bone; to achieve complete seating of the tray permanent deformation may be required. As found in this study, a virtually introduced subsidence of 0.300 mm would result in over 90% of the tibial tray surface being in contact with bone (90.4 ± 5.0 %), increasing to over 95% with 0.500 mm subsidence (97.3 ± 2.9 %). The previously mentioned RSA study found that after the initial 3 month period, the subsidence rate stabilised and was negligible in the second year post-surgery (Koster et al., 2023), potentially reflective of seating being achieved. Similar migration patterns have likewise been reported for other devices (Hasan et al., 2020).

There was a residual compressive strain response of cancellous bone quantified directly after the impaction in all seven tibiae. The compression was concentrated around the pegs and keel (median: -9,529± 2,959 µε) in comparison to directly under the tray (-3,781 ± 1,841 µε) for bone in direct contact with the tibial component (within 0.00 – 1.56 mm from the bone-implant interface) and within 1.56 – 3.14 mm from the interface (pegs and keel: -6,299 ± 2,104 µε; tray: -3,553 ± 1,436 µε). By 3.14 – 4.69 mm from the bone-implant interface (Radial 3), the compression was comparable across the entire implant surface (pegs and keel: -3,208 ± 1,032 µε; tray: -3,020 ± 1,352 µε), alluding to the ability of cancellous bone to redistribute the strain and suggesting the boundary of the impacted bone region. Previous work, although on a femoral component, has similarly reported that the (residual) mechanical response of bone to the impaction extends from the bone -implant interface, to similar depths of 1.7 to 2.3 mm (Rapagna et al., 2019).

This quantified mechanical response encapsulates both the elastic and permanent deformation of bone, with only the former reported as contributing to the primary stability of these devices (Jepsen et al., 2009, Gebert et al., 2009). During the impaction of cementless tibial components, a multiaxial stress state develops due to confined loading that results in pressure-dependent yielding of cancellous bone (Kelly et al., 2013). Within this study, it was not possible to "unload" the cancellous bone by removing the implant (as done by others (Berahmani et al., 2018, Rapagna et al., 2019)). However, previous studies have reported recovery by 70-80 % of permanent strains (Jepsen et al., 2009). Due to the magnitude of the compressive strains extracted within 3.14 mm from the bone-implant interface (Radial 1 and Radial 2), it could be predicted that yielding, to some extent, has occurred. In such an instance, the mechanical properties of the cancellous bone in intimate contact with the tibial component would alter, resulting in decreased modulus and (slightly) decreased strength (Keaveny et al., 1994).

Bone debris were also visualised within the micro-CT datasets, confirming that permanent deformation (through both compaction and abrasion) had occurred. Damm et al. (2017) and Bishop et al. (2014), in their studies on bone cores, both reported on the accumulation of bone debris around the implant, the extent of which increased with increasing nominal interference fit (Bishop et al., 2014) and penetrated up to 0.900 mm from the bone-implant interface (Damm et al., 2017). Whilst not linked to the primary stability of cementless devices, abrasion and compaction of cancellous bone could still be beneficial to the long-term success of the device by stimulating a quicker osteogenic response (Bosshardt et al., 2011).

A moderate-to-weak (statistically significant) relationship was quantified here between the actual interference fit and post-impaction strain, with increasing interference corresponding to increasing post-impaction residual strain within 0.00 – 1.56 mm (Radial 1: R^2 = 0.450, $p < 0.01$) and 1.56 – 3.14 mm (Radial 2: R^2 = 0.296, $p < 0.01$) from the bone-implant interface. This indicates that increased actual interference fit is related to an increased mechanical response of bone, capturing both the elastic and permanent response. However, varying post-impaction residual strain values were found at comparable actual interference fits. As such, a particular interference fit could not guarantee a particular extent of mechanical response. This highlights the complexity of the tissue response and how other additional factors, not quantified here, could contribute to the compressive response of the cancellous bone. The relationship between actual interference fit and post-impaction residual strain was not significant by 3.14 mm from the bone-implant interface (Radial 3: p = 0.592, R^2 = 0.00515), again potentially highlighting the end of the impaction zone.

Bone volume fraction (BV/TV), taken as an indicator of bone quality, did not relate to the post-impaction residual strain field at any distance from the bone-implant interface. Whilst no statistically significant relationship was found, observations were made from the micro-CT datasets. The Keel VOI consistently had the lowest BV/TV (8.5 ± 3.4 %) in comparison to other VOIs for all tibiae. The

compressive response of cancellous bone extracted by DVC around the Keel was similar to that across the pegs (which sat in regions of higher BV/TV (19.0 ± 5.9 %)). In comparing the pre- to post- impaction scans, it was observed that a layer of debris surrounded the keel. This follows standard surgical procedure, whereby a keel punch is used to impact bone prior to implantation (DePuy Synthes, 2016). The extracted strain values in that region may instead be associated with debris movement. Such an observation also highlights the limitation of employing DVC for this type of analysis.

DVC was used to extract the internal strain of bone, in immediate contact with the implant and then extending further away. DVC uses the grey levels of the specimen's structure to extract a displacement field (Bay et al., 1999), and thereby calculate a strain value for each subvolume. Within the setup of this experiment, this introduces a number of limitations. Firstly, whilst algorithmic masking was employed to remove the implant from DVC analysis, the presence of the large titanium implant increased the grey level values of the bone close to the implant (extending by approximately 20 pixel (0.92 mm) from the interface), making it harder for DVC to identify the same features. This is reflected in the lower DVC correlation coefficients extracted for subvolumes in direct contact with the tibial component (Radial 1), with a median correlation coefficient of 0.49 ± 0.10, compared to the higher correlation coefficients in subvolumes further from the implant (Radial 2: 0.78 ± 0.08; Radial 3: 0.84 ± 0.04). Secondly, DVC relies on trackable features. Shearing occurred during the impaction process, removing trabeculae and adding debris to individual subvolumes. It was observed that debris accumulation often resulted in high compressive strain values, as noted around the distal tips of the pegs. However, these subvolumes with debris accumulation did not have lower DVC correlation coefficients than subvolumes without; by removing subvolumes at the distal tip of the pegs from the analysis, the median correlation coefficient of subvolumes assessed actually *worsened (decreased)*. As such, and as undertaken within the methods, it was not possible to mask subvolumes based on the correlation coefficient as other authors recommend (Gillard et al., 2014). Whilst a threshold of acceptable values varies in the literature (0.6 to 0.9 (Dall'Ara and Tozzi, 2022, Gillard et al., 2014)), the correlation coefficients within Radial 1 are low and the extracted strain magnitudes should be treated with caution. The micro-CT datasets need be viewed alongside the extracted strain calculations to ascertain their values in areas of high impaction. Masking here was applied based on logic (over drilling of the peg guides is part of the surgical technique) and observations (bone debris was seen to accumulate within these regions). The correlation coefficients here are within the range (0.50 to 0.75) reported by Rapagna et al. (2019) on their study of femurs before and after impaction of a femoral components, with the similar conclusions regarding the limitation of DVC when extracting strain values in regions with high deformation. In such situations, the benefit of DVC is that the values are extracted from micro-CT datasets, allowing the operator to visualise the bone before and after impaction and to make informed decisions.

5.5 CONCLUSION

An inhomogeneous actual interference fit was found across the pegs and keel of a commercially available cementless tibial component once implanted in seven cadaveric tibiae. The actual interference was lower than the intended interference in all specimens. The tray came to rest on the peaks of the resected surface, limiting the percentage of tray surface in direct contact with bone to 54 %, which could theoretically increase to 97 % with 0.500 mm of subsidence. This could be reflective of the high migration reported in the literature for cementless tibial components in the initial 3 months post-implantation (Koster et al., 2023). After impaction, residual compressive strains were extracted in the cancellous bone, which were highest for bone closest to the pegs and keel, and extended up to approximately 3.14 mm from the bone-implant interface. The compressive strains, capturing both elastic and permanent deformations, of this bone could not be fully explained by the actual interference fit and the bone volume fraction in that region alone, highlighting the complexity of this interaction. DVC, as employed here, offers the potential to experimentally assess the deformation inflicted during the impaction process for cancellous bone in direct contact with the implant. However, the extracted strain values need to be assessed alongside the images.

Study 3: Contribution of the actual interference fit of cementless tibial components to their relative motion

The work presented in this chapter is in preparation for submission as a manuscript to a peer-reviewed journal.

Wearne LS, Rapagna S, Awadalla M, Keene G, Taylor M, Perilli E. Quantifying the contribution of interference fit to the primary stability of cementless tibial trays: a micro-CT and Digital Volume Correlation analysis. *In preparation for submission to a peer-reviewed journal*.

Please refer to the Appendix at the end of this thesis for a detailed outline of the author's contribution to this study.

ABSTRACT

An interference fit is employed for cementless tibial TKA components to ensure sufficient stability in the initial-post operative period. With sufficient primary stability, detrimental levels of micromotion are suppressed, thereby facilitating osseointegration. However, previous experimental limitations have prevented quantification of micromotion across the entire bone-implant interface. Furthermore, the effect of an interference fit is often assessed by changing the nominal interference fit, which differs from that achieved. The aim of this study was 1) to experimentally quantify the micromotion across the entire interface of a cementless tibial component and underlying bone for seven cadaveric tibiae through micro-CT imaging and DVC and 2) to assess the relationship between actual interference fit and observed micromotion. The effect of residual post-impaction strain and BV/TV on micromotion was also assessed.

Micro-CT scans were taken of seven cadaveric tibiae, when intact, following resection and, once implanted with a cementless TKA component, during two time-elapsed mechanical load sequences that replicated stair descent (SD, 0.0 – 2.5BW) and deep knee bend (DKB, 0.0-3.5BW). Actual interference fit was quantified as the overlap between the resected surface of the tibiae following TKA preparation and the position of the implant once impacted. DVC was employed to extract the post-impaction internal strain field and the relative motion at the bone-implant interface for each load case.

A sagittal rocking motion of the tray was quantified in both activities, with anterior tray lift-off and posterior subsidence (migration) that increased linearly with increased load. Posterior subsidence was the dominant motion of the tray across all seven specimens in both activities, with up to -168 μm of subsidence quantified. Tray lift-off was enhanced in the central and lateral anterior regions during DKB in comparison to during SD. With 69.7 ± 25.4 % of the bone-implant interface having a relative motion less than 50 μm at peak load cases, it largely remained within the limits considered permissible to osseointegration (Pilliar et al., 1986). Increased interference was related to reduced relative motion between the implant and underlying bone for all but one load case, whilst neither the post-impaction residual strain field nor regional BV/TV were related to relative motion. This work finds that the induced damage following impaction may not be detrimental to the achieved stability. Furthermore, the mechanical interlock provided by the interference fit may last longer (beyond 24 hrs) than previously reported, with the relationship between increased interference and reduced relative motion still found on the second day of testing.

6.1 INTRODUCTION

Successful fixation of cementless tibial components is defined by osseointegration: the direct ingrowth of bone into the implant's surface. Sufficient primary stability, being the initial mechanical interlock between implant and bone, can assist successful osseointegration by suppressing micromotions. The primary stability of tibial components has therefore often been assessed directly with micromotion as the defining metric. Whilst the limits of tolerable micromotion for osseointegration are not conclusive (Kohli et al., 2021), it is generally accepted that reduced micromotion is beneficial.

The implanted tibial component is subjected to a complex loading pattern that results in a posterior translation of the point of loading from the femur as the knee flexes (Fitzpatrick et al., 2013). Motions with a high degree of flexion, such as stair descent (SD) and deep knee bend (DKB) (both common activities of daily living), can accentuate this posterior translation. Consequentially a sagittal rocking motion of the tray has been reported during these activities, whereby there is anterior edge lift-off and posterior-edge seating (Chong et al., 2010, Taylor et al., 2012, Han et al., 2020, Yang et al., 2021). If sufficiently large, this may jeopardise the fixation of the implant, resulting in fibrous tissue development rather than osseointegration.

As discussed in the preceding chapter, primary stability is generated during surgery by employing an interference fit. Whilst numerous studies exist that correlate interference fit with implant stability, both computational (Dawson and Bartel, 1992, Yang et al., 2020) and experimental (Damm et al., 2017, Berahmani et al., 2015a, Norman et al., 2006, Bishop et al., 2014, Berahmani et al., 2018, Sánchez et al., 2021, Gebert et al., 2009), the reported effect of interference fit on micromotion remains inconclusive. For experimental studies, micromotion measurements were previously restricted to the external bone-implant interface measurements (Han et al., 2020, Yang et al., Sánchez et al., 2021) and often at discrete locations (Miura et al., 1990, Kraemer et al., 1995, Stern et al., 1997, Sala et al., 1999, Chong et al., 2010). Furthermore, the effect of interference fit in experimental studies is typically tested by varying the nominal interference fit (Sánchez et al., 2021, Campi et al., 2018, Berahmani et al., 2015a, Gebert et al., 2009, Norman et al., 2006), which differs to the interference fit actually achieved (Berahmani et al., 2017, Berahmani et al., 2018, Damm et al., 2015, Damm et al., 2017). Computational models are able to extract micromotion across the entire interface, however they often ignore an interference fit between implant and bone altogether (Chong et al., 2010, Taylor et al., 2012, Fitzpatrick et al., 2014a, Quevedo González et al., 2019, Yang et al., 2020), or, employ one that is smaller than seen clinically (Navacchia et al., 2018). Furthermore, only a few FE studies are experimentally validated (Chong et al., 2010, Navacchia et al., 2018, Yang et al., 2020), and, with the currently available experimental data, it is difficult to do so properly. As such, there are currently no studies, to the best of this author's knowledge, that have assessed the effect of clinical-levels of interference fit on full-field micromotions between a cementless tibial component and underlying bone.

The aim of this study was therefore 1) to experimentally quantify the micromotion across the entire interface of a cementless tibial component and underlying bone for seven cadaveric tibiae and 2) to assess the relationship between actual interference fit and observed micromotion. The effects of residual post-impaction strain and BV/TV on micromotion were also examined.

6.2 MATERIALS AND METHODS

This study utilised the micro-CT datasets of the tibiae when resected and once implanted during the time-elapsed mechanical load sequences for both SD and DKB (section:

4.2 Micro-CT Scanning). Here, the tibiae were potted (*4.4.2 Potting*) and placed within the mechanical loading rig (*4.4.1 The Loading Rig*). All seven tibiae (*4.1 Specimens*) were included in this analysis. Please refer to the relevant sections of this thesis for methodology details.

6.2.1 Co-Registration of Micro-CT Datasets

The 0.0BW scan taken at the start of each testing day (SD 0.0BW (PL2) and DKB 0.0BW) became the respective baseline scans for the two activities. The loaded scans (SD: 0.5 – 2.5 BW; DKB: 0.5 – 3.5BW), being the target datasets, were rigidly co-registered in 3D to their baseline scan (software DataViewer, version 1.5.4.0, Skyscan-Bruker). To quantify any permanent relative motion (termed migration) of the tray after the first day of testing, the DKB 0.0BW scan was also rigidly co-registered to the SD baseline scan.

Registration was performed by aligning the distal region within the tibial metaphysis, which did not contain the implant or implant guiding holes. After co-registration a 3D median filter with a round kernel of 1 pixel was applied to the image datasets (software CTAnalyser, 1.17.2.2, Skyscan-Bruker).

6.2.2 Bone Volume Fraction

The bone volume fraction (BV/TV) previously calculated in Chapter 5 was used here and for the same VOIs (Figure 5. 1: anterior-medial peg (Peg_AM), the anterior-lateral peg (Peg_AL), the posterior-medial peg (Peg_PM), the posterior-lateral peg (Peg_PL), the Keel, and, for the Tray, the anterior-medial quadrant (Tray_AM), the anterior intercondylar region (Tray_AIC), anterior-lateral quadrant (Tray_AL), the posterior-medial quadrant (Tray_PM), the posterior intercondylar region (Tray_PIC), posterior-lateral quadrant (Tray_PL)). Please refer to *5.2.3 Assessing Bone Morphometry* for details.

6.2.3 Actual Interference Fit

As per Chapter 5, the actual interference fit was defined as the overlap between the resected surface of the tibia and tibial component once implanted. The median and standard deviation calculated previously for each VOI were used within this study. Please refer to *5.2.4 Quantifying Actual Interference Fit* for further details.

For tray VOIs (Tray_AM, Tray_AIC, Tray_AL, Tray_PM, Tray_PIC, Tray_PL), the percentage of implant in contact with the underlying bone was calculated. This was calculated as the percentage of subvolumes of that region with an interference (actual interference fit > 0.00 mm) to the total number of subvolumes within that region. Subvolumes with an actual interference fit between 0.00

and -0.300 mm were identified (denoting a gap of up to 300 μm between implant and bone, marking the lower limit gap size for osseointegration (Carlsson et al., 1988)), as were subvolumes with an actual interference fit between -0.300 and -0.500 mm (denoting a gap of 300 to 500 μm, marking the upper limit gap size for osseointegration (Dalton et al., 1995)) and subvolumes with an actual interference fit greater than -0.500 mm (denoting a gap larger than 500 μm, above the tolerable gap size for osseointegration).

6.2.4 Post-impaction Residual Strain

As within Chapter 5, the minimum principal strain component of the post-impaction residual strain field within the cancellous bone of each tibia following impaction was extracted (*5.2.5 Post Impaction Strain Field: DVC Analysis*). The median and standard deviation of the minimum principal strain component from these datasets has been calculated for each VOI. Only calculations for subvolumes in direct contact with the tibial component (Radial 1) are considered within this study. Please refer to the relevant section for further details.

6.2.5 Relative Motion

The term "relative motion" has been employed within this study for the captured motion between the implant and the bone, as it encapsulates both the recoverable motion (termed micromotion within the literature) and permanent migration. Within this study it was not possible to separate the two components during each load case.

The relative motion was calculated for each of the sequential load steps detailed within *4.4.3 Time-elapsed Micro-CT Imaging with Mechanical Loading*. As described previously, two time-elapsed mechanical load sequences were undertaken per tibia, with the first representing SD and the second DKB. Each load sequence consisted of 6 increasing and discrete load steps; 0.0BW to 2.5BW for SD, and, 0.0BW to 3.5BW for DKB.

6.2.5.1 DVC Analysis

DVC analysis was undertaken using the configuration included in *4.5 Digital Volume Correlation Analysis* for each of the co-registered pairs detailed in *6.2.1 Co-Registration of Micro-CT Datasets*. This resulted in 10 DVC analyses per tibia (nine load steps and one residual). At each load step, displacement vectors (U_x, U_y, U_z) across the entire datasets were extracted. To calculate the relative motion between the implant and bone, the vector fields only of tibial subvolumes in direct contact with the implant (Radial 1) and subvolumes of the implant were used (*4.5.3 DVC Subvolume Masking*).

6.2.5.2 Calculating relative motion across the bone-tray interface

For every tibia subvolume in direct contact with the tibial component, the closest implant subvolume was identified through a "knnsearch" (MATLAB 2021b, query point: tibia subvolumes, input data: implant subvolumes). The relative displacement between the tibia subvolume and the

corresponding implant subvolume was calculated through vector subtraction: $+\Delta U_x$ denoted lateral tray movement, $+\Delta U_y$ denoted posterior tray movement, and $+\Delta U_z$ denoted tray lift-off, whilst a $-\Delta U_x$ denoted medial tray movement, $-\Delta U_y$ denoted anterior tray movement, and $-\Delta U_z$ denoted tray subsidence of a subvolume. Relative motion between implant and bone was calculated as the length of the resultant vector: $\Delta U = \sqrt{\Delta U_x^2 + \Delta U_y^2 + \Delta U_z^2}$. This was undertaken for each load case.

The percentage surface area (PSA) of the implant that had a relative motion less than 50 μm, and, greater than 150 μm was calculated, being considered as the lower and upper limits of tolerable micromotion for osseointegration, respectively (Pilliar et al., 1986, Søballe et al., 1992). This was calculated as the percentage of subvolumes that had an associated relative motion below 50 μm and above 150 μm, separately, to the total number of tibia subvolumes in contact with the tray (Radial 1) for that specimen.

6.2.5.3 Volume of Interest Selection

The same VOIs across the tibial component defined within Chapter 5 were also employed here. For the implant (Figure 5. 1A) that is: the relative motion between the anterior-medial peg and surrounding bone (Peg_AM), between the anterior-lateral peg and surrounding bone (Peg_AL), between the keel and surrounding bone (Keel), between the posterior-medial peg and surrounding bone (Peg_PM), between the posterior-lateral peg and surrounding bone (Peg_PL) and between the tray and underlying bone (Tray). For each VOI, and during each load case, the median and standard deviation of relative motion were calculated. The PSA with a relative motion below 50 μm and above 150 μm for each VOI was calculated, as above.

The Tray VOI was then further separated into six VOIs, as within Chapter 5 (Figure 5. 1B), being the anterior-medial quadrant (Tray_AM), the anterior intercondylar region (Tray_AIC), the anterior-lateral quadrant (Tray_AL), the posterior-medial quadrant (Tray_PM), the posterior intercondylar region (Tray_PIC), and, the posterior -lateral quadrant (Tray_AL). The median and standard deviation of relative motion and the PSA within the above listed bounds for each VOI was calculated. In addition, the median and standard deviation values for the relative vertical motion (ΔU_z component) were also calculated, denoting tray lift-off (+) and subsidence (-).

6.2.6 Statistical Analysis

6.2.6.1 Contribution of actual interference fit, post-impaction residual strain and bone volume fraction to relative tray motion

Linear regression ("fitlm", MATLAB 2021b) was used to assess if there was a relationship between the relative motion of the implant (predicted variable) and the actual interference fit, the post impaction strain and the bone volume fraction (predictor variables). The median values of each variable for every VOI of the implant (Peg_AM, Peg_AL, Peg_PM, Peg_PL, Keel, Tray_AM,

Tray_AIC, Tray_AL, Tray_PM, Tray_PIC, Tray_PL) formed a datapoint (amounting to a total of 77 datapoints (11 VOIs x 7 tibiae)). This was undertaken separately for each load case.

Linear regression was also employed separately for VOIs of the Tray (Tray_AM, Tray_AIC, Tray_AL, Tray_PM, Tray_PIC, Tray_PL), with the response variable being the median relative vertical motion, ΔU_z, at each load case. In the first set of tests, the median actual interference fit for each VOI was used as a predictor variable. In the second set of tests, the percentage of contact between the implant to bone for each Tray VOI was used instead. In both sets of tests, the median post-impaction residual strain was also included as a predictor variable. Bone volume fraction was not included as this was a directional test.

For all statistical analyses, the significance level was set to 5 % ($p < 0.05$). Where significance was found, the relative motion was plotted against the respective predictor variable and a linear line of best fit was included.

6.2.6.2 Comparison of activities to relative motion
A Wilcoxon-signed rank test ("signrank", MATLAB 2021b) was employed to compare the relative motion between SD and DKB for implant VOIs (Peg_AM, Peg_AL, Peg_PM, Peg_PL, Keel, Tray, 42 datapoints per test). This was undertaken for each comparable load step (e.g. for SD 0.5WB vs DKB 0.5BW), with significance set to 5 %. The null hypothesis was that there was no difference in relative motion between the two activities.

Wilcoxon signed rank tests were also employed to compare the relative vertical motion of the Tray VOIs (Tray_AM, Tray_AIC, Tray_AL, Tray_PM, Tray_PIC, Tray_PL) during SD to DKB. This was undertaken separately for each VOI at each load case (7 datapoints per test), for example, comparing the relative vertical motion of Tray_AM during SD to DKB at 0.5BW loading was one test. Again, a significance level of 5 % was used, with the null hypothesis being that there was no difference in relative vertical motion between the two activities.

6.3 RESULTS

Relative motion was quantified between the tibial component and underlying bone during every load case for each specimen. Whilst the magnitude varied between tibiae, there was an approximately linear increase in relative motion with applied load as shown by the exemplar specimen (Tibia E) in Figure 6. 1. A comparable trend was seen for all specimens.
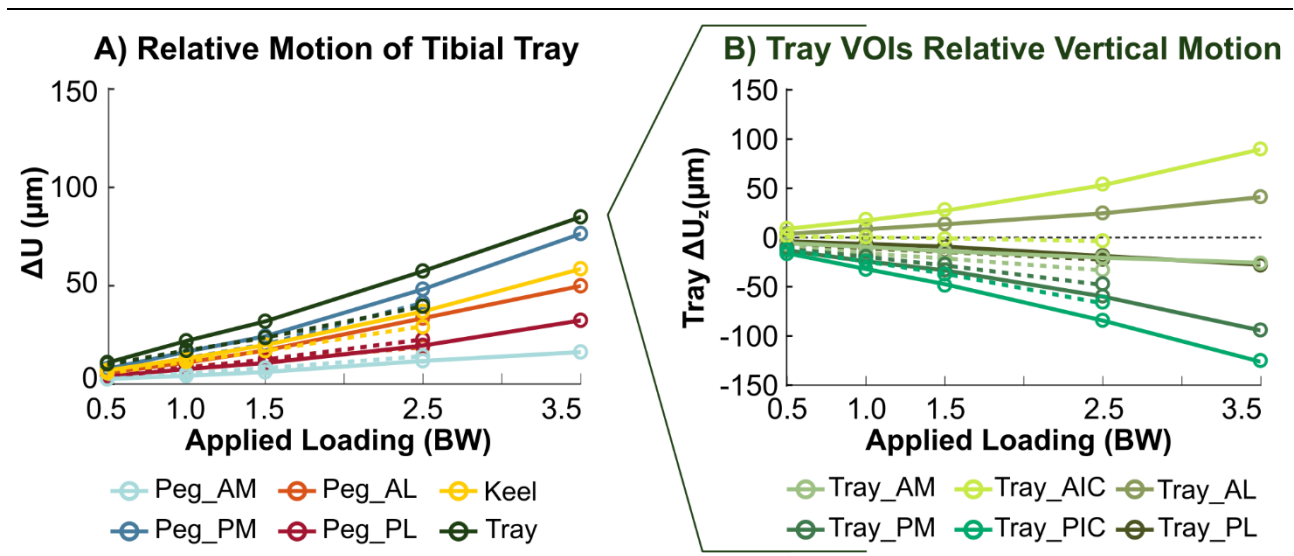
Figure 6. 1: Progressive relative motion (ΔU) between the implant and underlying bone for an exemplar specimen (Tibia E) for A) the 6 volumes of interest (VOIs) of the implant and B) the relative vertical motion (ΔU_z) for the six VOIs across the Tray. Stair descent (SD) is represented by the dashed line and deep knee bend (DKB) by the solid line.
VOIs of the implant: the anterior-medial peg: Peg_AM; the anterior-lateral peg: Peg_AL; the keel: Keel; the posterior-medial peg: Peg_PM; the posterior-lateral peg: Peg_PL and the across the tray: Tray
VOIs of the tray: anterior-medial quadrant: Tray_AM; anterior-intercondylar region: Tray_AIC; posterior-lateral quadrant: Tray_AL; posterior-medial quadrant: Tray_PM; posterior-intercondylar region: Tray_PIC; posterior-lateral quadrant: Tray_PL.

At maximum loads, the majority of the implant surface (median ± std dev: 69.7 ± 25.4 %; range: 19.3 – 96.2 %) had a relative motion less than 50 μm for the seven specimens (Figure 6. 2A). The pegs had the greatest PSA with relative motion less than 50 μm (95.5 ± 33.3 %; range: 6.74 – 100 %), followed by the Keel (79.3 ± 24.2 %; range: 35.0 – 100 %) and then the Tray (53.0 ± 29.4 %; range: 3.17 – 90.8 %). The relative motion remained below 150 μm across 78.6 %, or greater, of the bone-implant interface at maximum loads, rendering (in principle) the majority of the implant surface within the micromotion limits permissible to osseointegration (Søballe et al., 1992). Relative motion did not exceed 150 μm prior to 1.5BW (Figure 6. 2).
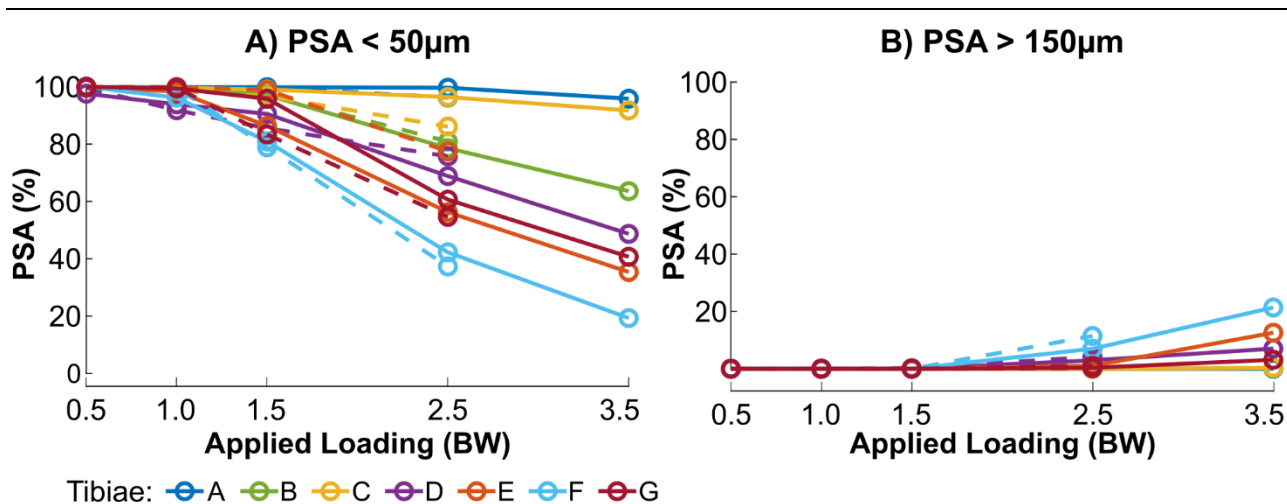
Figure 6. 2: Percentage of implant surface area (PSA) permissible to osseointegration, with a relative motion A) less than 50 µm, and B) greater than 150 µm at each load step. Stair descent (SD) is represented by the dashed line and deep knee bend (DKB) by the solid line.

A comparable distribution of relative vertical motion of the Tray was observed across the specimens (Figure 6. 3). Posterior VOIs of the Tray consistently displayed subsidence, with the largest subsidence occurring in the posterior medial (Tray_PM) and posterior central regions (Tray_PIC). Conversely, the anterior regions displayed a combination of both lift-off and subsidence, depending on the specimen. The extent of anterior subsidence was always less than that of posterior subsidence. Of the VOIs, Tray_AIC had the largest lift-off, with median lift-off of 22.2 ± 56.0 µm at the highest load steps.

Tibia C was the only specimen where lift-off was recorded for a posterior VOI (Tray_PM, only during SD). This could be explained by the large lateral migration of the tibial component, potentially in consequence of an experimental artefact (discussed in *4.4.2.1 Alignment Errors*).

Permanent relative motion between the implant and underlying bone occurred after the first day of testing, where a final load step of SD 2.5BW was applied. For all of the seven tibial components, the median permanent relative motion was 10.7 ± 15.6 µm, with the median vertical migration (ΔU_z) of the Tray VOI being -8.47 ± 26.0 µm, therefore demonstrating overall subsidence of the Tray. The greatest vertical migration occurred for Tibia G at (median ± std dev) -42.3 ± 44.9 µm, with Tray_PIC subsiding by -87.6 µm. Across the seven specimens, the distribution of permanent relative vertical migration matched the motion of the tray during SD (Figure 6. 3B & C).
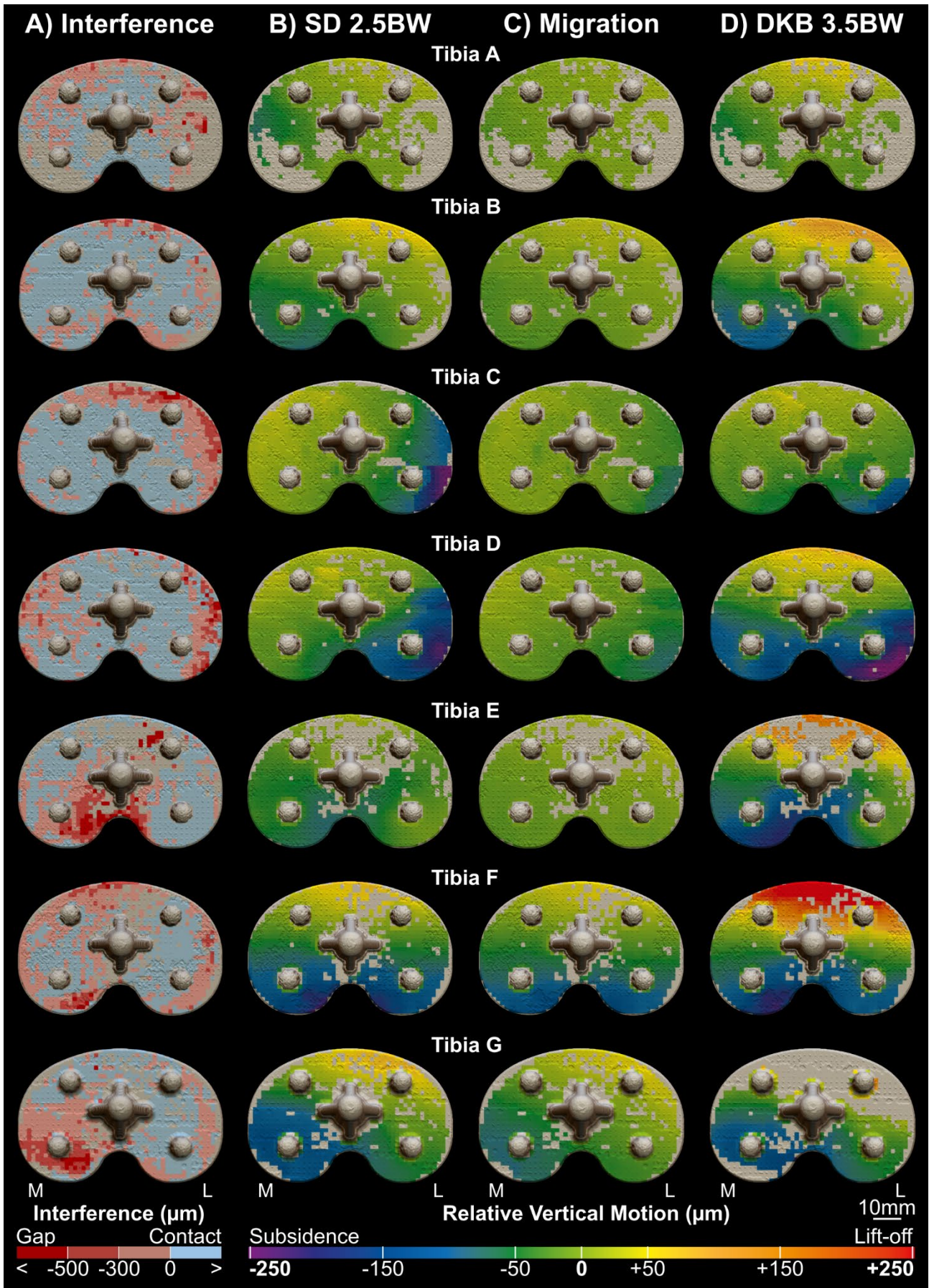
Figure 6. 3: Tray-bone contact and relation-motion distributions for the seven cadaveric tibiae. A) contact between the tray to underlying bone, displaying interference (>0.00), a gap between 0 to 300 µm, a gap between 300 to 500 µm and a gap greater than 500 µm, and, the vertical motion (ΔU_z) of the tray B) during stair descent (SD) at 2.5BW, C) after SD (migration) and D) during deep knee bend (DKB) at 3.5BW.

6.3.1 Relationships between relative motion and actual interference fit, post-impaction residual strain and bone volume fraction

Actual interference fit was a predictor of implant relative motion in the all load cases except SD 2.5BW (R^2 and p values included within Table 6. 1). A negative relationship was observed, with greater interference corresponding to reduced relative motion. Neither BV/TV nor post-impaction residual strain were predictors of relative motion at any load case. Exemplar plots of each linear regression for the load case of DKB 3.5BW are included in Figure 6. 4.

Table 6. 1: The results of the linear regression analysis for relative motion to the predictor variables of bone volume fraction (BV/TV), actual interference fit (AIF) and post-impaction residual strain.

Load Case		BV/TV	Actual Interference Fit (AI)	Post-Impaction Residual Strain
SD	0.5BW	0.001 (0.554)	0.248 (< 0.001)* $\Delta U = -5AI + 8$	0.101 (0.834)
	1.0BW	0.005 (0.594)	0.132 (0.016)* $\Delta U = -9AI + 15$	0.059 (0.994)
	1.5BW	0.006 (0.548)	0.109 (0.035)* $\Delta U = -13AI + 24$	0.052 (0.930)
	2.5BW	0.010 (0.424)	0.080 (0.055)	0.032 (0.894)
DKB	0.5BW	0.000 (0.814)	0.151 (0.002)* $\Delta U = -5AI + 9$	0.037 (0.390)
	1.0BW	0.001 (0.705)	0.187 (< 0.001)* $\Delta U = -11AI + 17$	0.049 (0.385)
	1.5BW	0.004 (0.441)	0.191 (< 0.001)* $\Delta U = -16AI + 24$	0.046 (0.305)
	2.5BW	0.012 (0.225)	0.190 (< 0.001)* $\Delta U = -32AI + 47$	0.044 (0.278)
	3.5BW	0.020 (0.136)	0.178 (< 0.001)* $\Delta U = -49AI + 72$	0.039 (0.256)

*Reported as R^2 (p), where * denotes a statistically significant coefficient of determination for that load case (significance level set to p < 0.05). Regression equations are included for instances where a statistically significant relationship was found.*
AIF: actual interference fit (mm); ΔU: relative motion (μm)
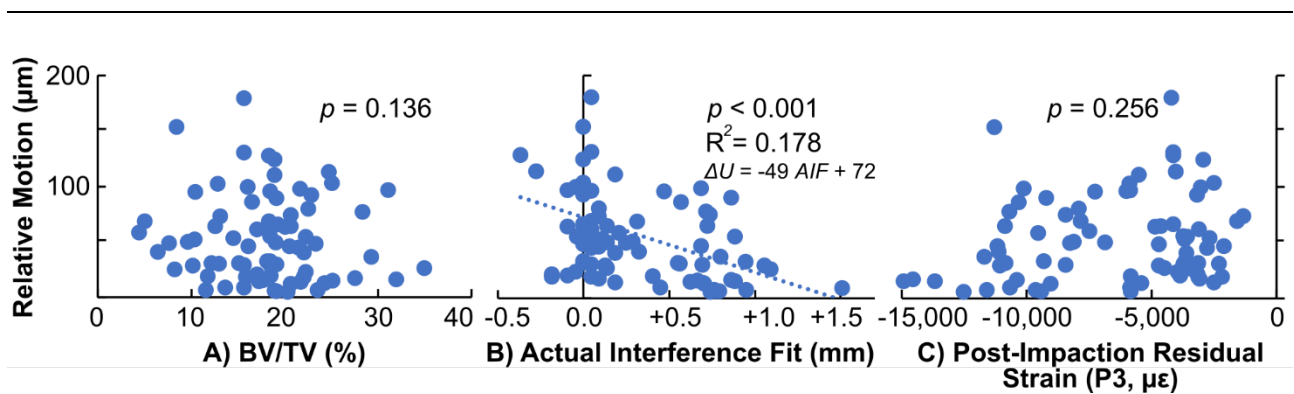
Figure 6. 4: Relationship between predictor variables and relative motion during DKB 3.5BW, being A) BV/TV to relative motion, B) actual interference fit to relative motion and C) post-impaction residual strain (minimum principal strain, P3) to relative motion. Where a statistically significant relationship between the predictor variables and relative motion was found, the regression equation is included.
ΔU: relative motion (mm); AIF: actual interference fit.

A co-location was apparent between areas of the tray that had a gap (negative actual interference fit, reds: Figure 6. 3 A) and tray subsidence (dark blue / purple: Figure 6. 3 B, C, D). This however did not reach statistical significance in any load case when actual interference fit or percentage tray contact were used as predictor variables for relative vertical tray motion. There did not appear to be a minimum percentage tray contact that prevented tray subsidence. The post-impaction residual strain was not a predictor to relative vertical tray motion at any load case.

6.3.2 Comparison of relative motion during SD and DKB

The regional distribution of relative motion was comparable between SD to DKB at each load step (shown for SD 2.5BW: Figure 6. 3 B; DKB 3.5BW: Figure 6. 3 D). In considering the relative vertical motion of the tray, greater lift-off was apparent during DKB in the anterior central (Tray_AIC: median ± std dev at SD 2.5BW vs DKB 2.5BW: 9.02 ± 16.2 µm vs 21.9 ± 41.3 µm) and anterior lateral (Tray_AL: -10.2 ± 25.5 µm vs 18.8 ± 19.7 µm) region, reaching statistical significance in the latter (p = 0.047, Figure 6. 5). This statistically significant difference in ΔU_z for Tray_AL occurred at each load step, with DKB having greater lift-off.
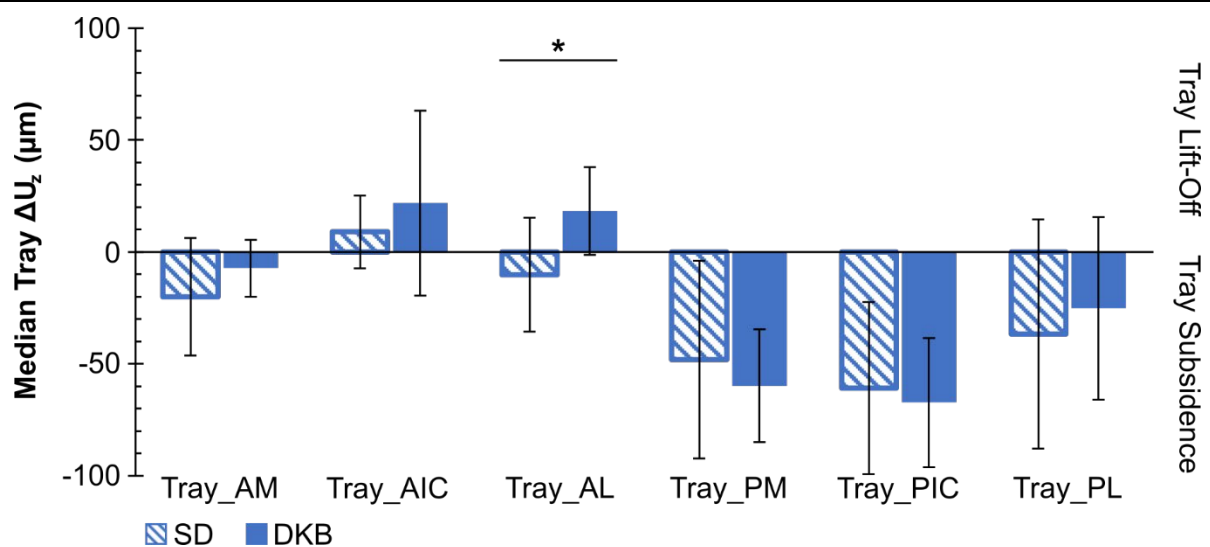
Figure 6. 5: Comparison of vertical tray motion in stair descent to deep knee bend: median relative vertical motion (ΔU_z) of the volumes of interest (VOIs) of the Tray at 2.5BW during each activity.
* denotes a statistically significant difference between SD and DKB for the specified VOI.
Stair descent: SD; deep knee bend: DKB
VOIs of the tray: anterior-medial quadrant: Tray_AM; anterior-indercondylar region: Tray_AIC; posterior-lateral quadrant: Tray_AL; posterior-medial quadrant: Tray_PM; posterior-indercondylar region: Tray_PIC; posterior-lateral quadrant: Tray_PL.

6.4 DISCUSSION

This is the first paper, to the best of the author's knowledge, that has experimentally quantified the relative motion between a cementless tibial component and the underlying bone across the entire interface at sufficiently high spatial resolution (Viceconti et al., 2000). This relative motion encapsulates both the inducible (recoverable) micromotion and the permanent migration of the implant as it settles into the cancellous bone bed below. A recent review by Kohli et al. (2021) concluded that there is no universal limit of tolerable micromotion for osseointegration. However, the previously defined limits for inducible micromotion by Pilliar et al. (1986) and Søballe et al. (1992) resulting in osseointegration (< 50 μm) and fibrous tissue development (> 150 μm), respectively, have been used extensively within the literature. Furthermore, these limits are in good agreement with a post-mortem retrieval study on femoral stems; osseointegration was reported for areas with micromotion less than 40 μm, and fibrous tissue development for areas with micromotion greater than 150 μm (Engh et al., 1992). As such, the two limits have been employed within this study. Based on these established limits and the fact that the quantified relative motion includes permanent migration, the majority of the bone-implant interface remained sufficiently stable for osseointegration across the testing.

An increase (approximately linear) in relative motion was found with applied load magnitude (simulating SD and DKB) across the seven tibiae. For the majority of specimens, the relative motion at or below 1.5BW, in both loading sequences, was within the limits considered conducive to osseointegration (< 150 μm, Figure 6. 2) (Søballe et al., 1992, Pilliar et al., 1986). The quantified relative motion began to exceed the limits considered favourable for osseointegration (> 50 μm) at 1.0BW for both activities and exceeded limits considered tolerable for osseointegration (and hence favourable for fibrous tissue fixation (> 150 μm)) at 1.5BW, however only during DKB. It could therefore be predicted that the inducible micromotion, of which the above osseointegration limits are based, would remain sufficiently low for bony ingrowth, even at the higher load cases. Others (Han et al., 2020, Kohli et al., 2021) have recommended reducing loading in the immediate post-operative period, until secondary stability is achieved through bony ingrowth (mature bone occurring after 8 weeks (Bosshardt et al., 2017)). Based on the relative motion values quantified here, and taking a conservative approach, it could likewise be recommended to limit loading to below 1.5BW within the immediate post-operative period.

The pegs, as a fixation feature, displayed greatest stability, with the relative motion remaining under 150 μm across all load cases. The increased stability provided by pegs has similarly been reported by FE studies (Taylor et al., 2012, Dawson and Bartel, 1992) and retrieval studies (Sumner et al., 1995). In considering the two peak load cases (SD 2.5BW and DKB 3.5BW), the relative motion across 69.7 ± 25.4 % of the implant surface remained below 50 μm, with only 1.61 % (range: 0.00 – 32.1 %) of the implant surface exceeding the upper limit of osseointegration (> 150 μm). This is within the range reported by FE studies for cementless tibial components when

considering both 50 μm (PSA < 50 μm : 11 – 85 ± 16 %) and 150 μm (PSA > 150 μm: 1 ± 2 – 16%) as tolerable limits (Chong et al., 2010, Fitzpatrick et al., 2014a, Quevedo González et al., 2019, Taylor et al., 2012). Furthermore, the results are in good agreement with a recent retrieval study on modern cementless tibial components, where 65 ± 19 % of the tray surface displayed bony ongrowth (Purcell et al., 2022). Whilst this reported percentage of osseointegration is higher than previous retrieval studies (Sumner et al., 1995), that study considered implants that were collected during revision surgery after having a short time in-service (average: 39 months), and therefore could display a worse-case scenario.

A comparable pattern was found for the relative vertical motion across the tibial trays in all specimens. Subsidence was the main component of this movement and occurred primarily in the posterior region. Interestingly, there was little difference in the relative motion when comparing SD to DKB. No increased posterior subsidence was found (Figure 6. 5) during DKB, however, there was increased lift-off in the anterior regions, reaching statistical significance in the anterior-lateral region (Tray_AL) for all load cases ($p \leq 0.047$). For both activities, the occurrence of anterior lift-off and posterior subsidence, to varying degrees, portrays a sagittal rocking motion of the tray.

The sagittal rocking motion of the tray found here has likewise been reported by other studies during both stair climbing (Chong et al., 2010, Taylor et al., 2012, Navacchia et al., 2018, Quevedo González et al., 2019, Yang et al., 2021, Han et al., 2020) and DKB (Taylor et al., 2012, Navacchia et al., 2018, Yang et al., 2021, Sánchez et al., 2021), with some papers reporting a difference in micromotion between the two (Yang et al., 2021, Taylor et al., 2012). The extent of relative vertical motion reported here is lower than two other recent *ex-vivo* publications. Han et al. (2020) reported average posterior subsidence of -125 ± 23 μm for seven cadaveric specimens after a battery of testing that included preload, stair descent and gait. Furthermore, their applied loads were lower to avoid tibial failure; scaled to 50 % of telemetrically derived values (Kutzner et al., 2010). Sánchez et al. (2021) for both high (700 μm) and clinically employed levels (350 μm) of nominal interference, reported average posterior subsidence of -143.3 μm during squat. As found in this study, tray subsidence was the dominant tray motion reported.

The present study, due to requirements of micro-CT imaging and the employed mechanical loading rig, was limited to a static and uniaxial load. Numerous FE studies have reported that peak micromotion occurs during incidences that couple high moments with low axial load (Taylor et al., 2012, Fitzpatrick et al., 2014a, Quevedo González et al., 2019), which could not be assessed here. Interestingly, the study by Sánchez et al. (2021), quantifying micromotion with DIC during dynamic loading, did not posteriorly offset the load during squat. Instead, the mating femoral component (flexed at 92°) sat in the deepest dwell points of the tibial component, therefore applying the load centrally. With their comparably high levels of micromotion reported, this further highlights the potential impact of moments. Other studies have reported that the cyclic translation of the loading

points, occurring during repetitive motions (such as gait) whereby there is a recurring anterior-posterior translation (Fitzpatrick et al., 2013), contributes to larger micromotions (Van Valkenburg et al., 2016, Quevedo González et al., 2019). Incidences of high moments coupled with low axial loads and incidences of cyclic load translation were not captured within this experimental configuration, which may explain the lower relative motions.

Permanent migration was assessed after the first day of testing (when a maximum of SD 2.5BW was applied), by comparing the unloaded scans taken at the start of the first and second day. This was the only load case (SD PL2 vs DKB PL) in which the permanent migration could be separated from the total relative motion. All implants displayed some extent of permanent migration after the first day of testing, with a median (± std dev) implant migration of 10.7 ± 15.6 μm. As with the loaded relative motion, the vertical motion was the largest contributor, and a permanent sagittal rocking motion was observed through posterior subsidence and anterior lift-off of the tray, as similarly reported in RSA studies (Li and Nilsson, 2000). Posterior tray regions displayed the largest permanent subsidence and were comparable across the three VOIs (median ± std dev: Tray_PM = -17 ± 3 μm; Tray_PIC = -13.8 ± 29.7 μm; Tray_PL = -15.45 μm). Furthermore, permanent lift-off occurred in two anterior regions: Tray_AIC = 6.44 ± 11.1 μm and Tray_AL = 6.18 ± 16.7 μm. Han et al. (2020) reported a similar migration pattern in their study of gait and SD, however to a greater extent (posterior seating: -162 ± 26 μm; anterior lift-off: +12 ± 25 μm). Cementless tibial components report a high initial migration post-surgery (Koster et al., 2023), known as the settling in period, which may be captured within this quantified migration. This migration may also explain the lack of difference between the relative motion during the two activities. The tibial components may have achieved a certain level of stability after the first loading regime, providing increased stability for DKB. Unfortunately, with cadaveric specimens, it is difficult to test multiple parameters with the specimens in the same conditions (Yang et al., 2021).

Increased actual interference was related to reduced relative motion, thereby providing greater stability, in all but one load case (SD 2.5BW). Whilst reaching statistical significance, this relationship was relatively weak (R^2 = 0.109 – 0.248). There are limited papers that assess interference fit and primary stability for cementless tibial components. A recent study on cementless tibial components by Sánchez et al. (2021) reported no significant differences in the vertical relative motion of the tray in comparing clinically employed (350 μm) to increased (700 μm) interference during neither gait (p = 0.474) nor squat (p = 0.269). For other orthopaedic components, to the best of the author's knowledge, a consistent relationship between interference fit and primary stability has not been reported in the literature. Gebert et al. (2009) found that the torque capacity between acetabulum cup and underlying bone was independent on the interference fit altogether. Conversely, Norman et al. (2006) (bone cores and pegs), Curtis et al. (1992) (acetabulum and cups), Damm et al. (2015) and Damm et al. (2017) (bone cubes and implant surfaces), and Berahmani et al. (2015b) (femur and pegs) all found some positive

correlation between interference fit and fixation strength, whilst not always reaching statistical significance. In all the above cases these findings were dependent on additional parameters, such as implant surface finish, bone relaxation, implantation direction and bone density. It is important to note that all these studies tested the effect of interference fit by changing the nominal interference fit. The work presented in Chapter 5, and by others (Berahmani et al., 2018, Berahmani et al., 2017, Damm et al., 2015), find that the interference fit achieved differs to what is intended. Aside from the complexity of the environment, testing the nominal interference fit could in part explain the reported lack of reported statistical significance within these studies.

The found statistically significant relationship between increased interference and reduced relative motion comes after the tibiae underwent one freeze-thaw cycle (after implantation, the tibiae were returned to the freezer. The day before the time-elapsed mechanical load sequence, they were placed in a physiological saline bath to thaw and rehydrate). Other authors have found that the effect of an interference fit wanes with time, both in the short term (30 minutes (Berahmani et al., 2015a)) and longer term (24hrs (Norman et al., 2006)). Within this study, a significant relationship between actual interference fit and relative motion was still found on the second day of testing for all load steps, showing here that the effect of an interference was present not just after a substantial period, but also across loading and unloading cycles. This work therefore finds that the mechanical interlock provided by an interference may last longer than previously reported.

Conversely, a higher bone volume fraction was not found to reduce overall relative motion between the implant and bone. Bone volume fraction was calculated from the intact dataset, prior to resection and impaction. The bone volume in contact with the implant post impaction was therefore not quantified. Whilst the statistical analysis was undertaken on 77 VOIs, these come from seven tibiae (N = 7). There may therefore be an insufficient number of specimens to adequately assess its effect statistically. Future studies should look to increase the number of specimens and include those with physiological relevant diseases, such as osteoarthritis which is the primary pathology for receiving a TKA (AOANJRR, 2022). These limitations may in part explain the lack of statistical significance. Some authors have reported a relationship between bone density (normal and osteoporotic bone models: (Meneghini et al., 2011, Lee et al., 1991)) or bone stiffness (indentation tests: (Miura et al., 1990)) and micromotion, whilst others have not found such a relationship (CT derived BMD: (Sánchez et al., 2021)). RSA studies have reported a statistically significant correlation between patient BMD to continuous migration (Andersen et al., 2017), highlighting the importance of bone density to potential implant longevity.

Gaps were found between the resected surface and the Tray for all specimens. There was an apparent co-location between subsidence and gaps, whilst not reaching statistical significance in any load case for actual interference fit ($p > 0.09$) or percentage tray contact ($p > 0.05$). Part of the lack of statistical significance could be the distribution of gaps and the applied load. Gaps were

found in all regions across the seven specimens (Figure 6. 3 A), whilst loading was applied posteriorly for both activities. Where present, posterior regions with gaps were observed to have greater tray subsidence (posterior-medial region of Tibia F and G, posterior region of Tibia E) than posterior regions without gaps (Tibia A, C and D, Figure 6. 3). Some authors go as far as to term tray subsidence solely as gap closing (Sánchez et al., 2021), highlighting the importance of good tray contact for stability.

6.5 CONCLUSION

The relative motion between a commercially available cementless tibial TKA component and underlying cadaveric bone was quantified experimentally across the entire interface for the simulated motions of SD and DKB. A sagittal rocking motion of the tray was evident in both activities, with anterior lift-off and posterior subsidence. Lift-off was enhanced in the central and lateral anterior regions during DKB, where the load was applied more posteriorly. Posterior subsidence was the dominant motion of the tray across all seven specimens and in both activities, with up to -168 μm of subsidence quantified. By considering the limits of tolerable micromotion for osseointegration established previously within the literature, the tibial component's motion remained largely permissible to osseointegration and only began to exceed tolerable limits (150 μm) at 1.5BW loading. Greater anterior lift-off of the tray occurred during DKB, where the loading on the tibial tray occurs more posteriorly. Bone volume fraction and post-impaction residual strain were not related to the stability of the implant. The actual interference fit between the implant and bone was found to be related to the relative motion at the bone-implant interface, with greater interference providing greater stability in all but one load case. This statistically significant relationship was quantified after the specimens were exposed to a freeze-thaw cycle and multiple loading cycles over a two-day time period. This work therefore finds that the mechanical interlock provided by an interference may last longer (beyond 24 hrs) than previously reported, with the relationship between increased interference and reduced relative motion still found on the second day of testing.

Study 4: Quantifying the cancellous bone mechanical environment following TKA of cementless tibial trays during simulated stair descent and deep knee bend: full-field strain analysis through time-elapsed micro-CT imaging and DVC

The study presented in this chapter is the subject of the following paper:

Wearne LS, Rapagna S, Awadalla M, Keene G, Taylor M, Perilli E (2024). Quantifying the immediate post-implantation strain field of cadaveric tibiae implanted with cementless tibial trays: A time-elapsed micro-CT and digital volume correlation analysis during stair descent. *Journal of the Mechanical Behavior of Biomedical Materials*, 151: 106347.

Since this submission, the analysis has been extended to include 7 tibiae and the second activity, DKB.

Please refer to the Appendix at the end of this thesis for a detailed outline of the author's contribution to this study.

ABSTRACT

Primary stability, the mechanical fixation between implant and bone prior to osseointegration, is crucial for the long-term success of cementless tibial components. However, little is known about the mechanical interplay between the implant and bone internally, as experimental studies quantifying internal strain are limited. This study employed DVC to quantify the immediate post-implantation strain field of seven cadaveric tibiae implanted with a commercially available cementless titanium tibial component (Attune Affixium, DePuy Synthes). The tibiae were subjected to a two-day time-elapsed mechanical load sequence, replicating stair descent on the first day (0.0 – 2.5BW) and deep knee bend on the second (0.0-3.5BW). At each load step, concomitant time-elapsed micro-CT imaging was performed. With progressive loads, increased compression of trabecular bone was quantified, with the highest strains directly under the posterior region of the tibial component implant, dissipating with increasing distance from the bone-implant interface. At the final load steps of SD 2.5BW and DKB 3.5BW, the median compressive strain of bone in direct contact with the implant ranged from -2,193 to -22,028µε, with peak (90th percentile) compressive strain ranging from -3,165 to -73,612 µε. Furthermore, DVC analysis was undertaken on the two baseline (0.0BW) scans, capturing the residual strains after the first day of testing. Residual strains were observed in all of the seven tibiae and were confined to within 3.14 mm from the bone-implant interface, reflective of the observed initial migration of cementless tibial components reported in clinical studies. The presence of strains above the accepted yield strain of bone suggests that inelastic properties should be included within finite element models of the initial mechanical environment. This study provides a means to experimentally quantify the internal strain distribution of human tibia with cementless trays, increasing the understanding of the mechanical interaction between bone and implant.

KEYWORDS

Cementless tibial component, internal strain field, bone-implant interface, time-elapsed micro-CT scanning, digital volume correlation, primary stability.

7.1 INTRODUCTION

Whilst the importance of primary stability for long term fixation of cementless total knee arthroplasty (TKA) components is recognised, little is known about the initial mechanical environment of the cancellous bone surrounding the implant. Experimental studies on the strain field post-implantation have previously been restricted to external bone surface measurements (Completo et al., 2007, Completo et al., 2008, Gray et al., 2008, Kessler et al., 2006, Green et al., 2002, Small et al., 2010), preventing analysis of the internal cancellous bone. Finite element (FE) models are able to predict the internal deformations and strain distribution of tibiae with cementless tibial components (Hashemi and Shirazi-Adl, 2000, Kelly et al., 2013, Taylor et al., 1998, Dawson and Bartel, 1992, Chong et al., 2011), providing an insight into the possible initial mechanical environment under complex loading scenarios. However, the models are limited, often not including an interference fit (Taylor et al., 1998, Chong et al., 2011, Quevedo González et al., 2019), or modelling a fit smaller than used clinically (Dawson and Bartel, 1992, Hashemi and Shirazi-Adl, 2000), and are sensitive to chosen friction coefficients, material properties and contact conditions. Furthermore, without experimental data, it is difficult to validate these models (Yang et al., 2021), relying on external (surface) measurements (Completo et al., 2007, Completo et al., 2008, Gray et al., 2008, Quevedo González et al., 2019), or comparisons to failure and migration rates within joint replacement registries (Taylor et al., 1998, Perillo-Marcone et al., 2004) and the regional development of fibrous tissue from retrieval studies (Dawson and Bartel, 1992).

Chapter 3 and Chapter 4 report on the feasibility of experimentally assessing the internal strain distribution of cadaveric tibiae implanted with a cementless titanium TKA component through time-elapsed micro-CT scanning and digital volume correlation (DVC) (Wearne et al., 2022). The aim of the present study is to perform that analysis: quantifying the immediate post-implantation mechanical environment (strains) of seven cadaveric tibiae implanted with clinically employed cementless tibial components, when subjected to two time-elapsed mechanical load sequence that replicated stair descent (SD: from 0.0 to 2.5 BW) and deep knee bend (DKB: from 0.0 to 3.5 BW). These common everyday activities expose the tibial component to posterior loading, potentially detrimental to the stability of the implant. The residual strain present in the tibial cancellous bone after the first day of testing (SD max load of 2.5BW) was also quantified.

7.2 MATERIALS AND METHODS

This study utilised the micro-CT datasets obtained during the time-elapsed mechanical loading sequence for both SD and DKB (section: *4.4.3 Time-elapsed Micro-CT Imaging with Mechanical Loading*). During this set up, the tibiae were potted (4.4.2 Potting) and placed within the mechanical loading rig (*4.4.1 The Loading Rig*). All seven tibiae (*4.1 Specimens*) were included in this analysis. Please refer to sections listed for methodology details.

7.2.1 Internal Strain Quantification: DVC Analysis

The same co-registration undertaken within Chapter 6: *6.2.1 Co-Registration of Micro-CT Datasets* was employed for this study. Internal strain fields were extracted via DVC analysis (*4.5 Digital Volume Correlation Analysis*).

In summary, 10 full-field DVC datasets were produced for each tibia (nine load steps (SD: 0.5 – 2.5 BW; DKB: 0.5 – 3.5BW) and one residual). Normal (ε_{xx}, ε_{yy}, ε_{zz}) and shear (ε_{xy}, ε_{yz}, ε_{zx}) strain fields across the entire datasets were extracted. Principal strain components were calculated in MATLAB as the eigenvalues of the Cartesian strain matrix for subvolumes across the tibia, with the minimum principal strain component (Figure 7. 1B) describing apparent compression.

Tibial subvolumes, that had a BV/TV greater than 5%, within Radial 1 (within 0.00 – 1.56 mm from the bone-implant interface), Radial 2 (within 1.56 – 3.13 mm from the bone-implant interface) and Radial 3 (within 3.13 – 4.69 mm from the bone-implant interface) were extracted for this study (Figure 7. 1C). Please refer to *4.5.3 DVC Subvolume Masking* for masking details. Subvolumes more than 4.69 mm away from the bone-implant interface were not considered. The strain distributions for each of these radial VOIs were plotted and median and peak (90th percentile) compressive strain values calculated.
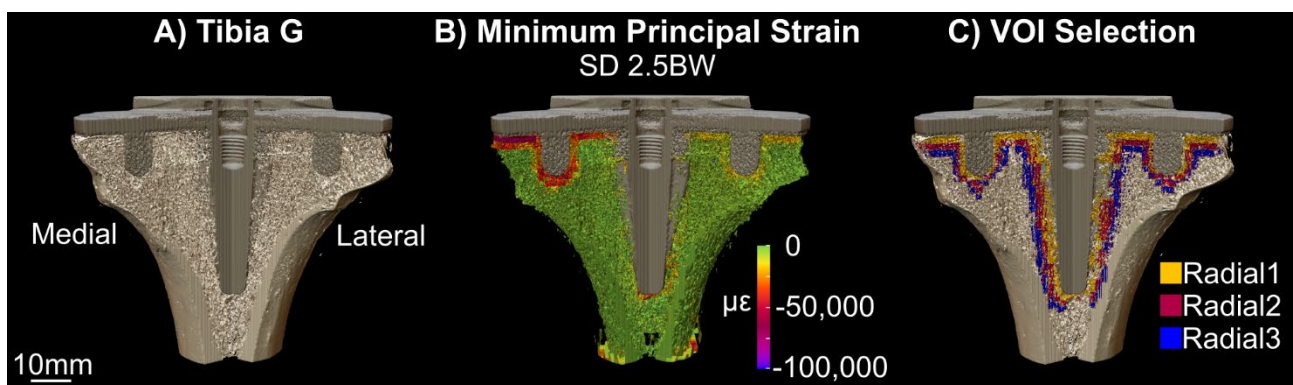
Figure 7. 1: 3D rendering of the image processing process. 3D rendering of Tibia G, virtually cut through the keel and two posterior pegs, B) DVC derived minimum principal strain component across the proximal tibia while loaded in stair descent (SD) at 2.5 BW, C) selected Volumes of Interest (VOIs), at three distances from the bone-implant interface: Radial 1, Radial 2 and Radial 3, corresponding to distances 0-1.56 mm, 1.56-3.13 mm and 3.13-4.69 mm, respectively.

7.3 RESULTS

All seven tibiae completed the time-elapsed mechanical testing sequence with concomitant micro-CT scanning for the two activities successfully. All tibiae showed increased minimum principal strain with progressive loading for the two activities (Figure 7. 2). Residual strain was captured after SD for all specimens. The regional strain distribution was comparable between SD and DKB for each tibia, with peak minimum principal strain occurring in the posterior medial region for five of the tibiae (A, B, E, F, G) for both activities (Figure 7. 3). Whereas for tibiae C and D peak minimum principal strain occurred within the posterior-lateral region, again for both acitivities.

Table 7. 1: Residual minimum principal strain calculated within Radial 1 (0.00-1.56 mm from bone-implant interface), Radial 2 (1.56-3.14 mm from bone-implant interface) and Radial 3 (3.14-4.69 mm from bone-implant interface) for each specimen. Residual strain is calculated between the baseline datasets of each activity (SD 0.0BW (PL2) to DKB 0.0BW), capturing the permanent damage inflicted on the specimens from the first day of testing. Median, standard deviation (std dev) and peak (90th Percentile) values reported.

Tibia	Residual Strain	Radial 1	Radial 2	Radial 3
A	Median ± Std Dev (με)	-1,240 ± 1,331	-827 ± 822	-851 ± 627
	Peak (με)	-3,165	-1,887	-1,709
B	Median ± Std Dev (με)	-2262 ± 3769	-,1063 ± 1,519	-829 ± 532
	Peak (με)	-8,926	-3,084	-1,468
C	Median ± Std Dev (με)	-1814 ± 4663	-900 ± 2,676	-669 ± 1,042
	Peak (με)	-10,114	-5,296	-1,667
D	Median ± Std Dev (με)	-3077 ± 5256	-1,209 ± 2,361	-906 ± 796
	Peak (με)	-12,144	-4,649	-1,677
E	Median ± Std Dev (με)	-2302 ± 2486	-1,151 ± 1,319	-1,010 ± 874
	Peak (με)	-6,627	-2,920	-1,952
F	Median ± Std Dev (με)	-15045 ± 20421	-3,248 ± 9,832	-1,152 ± 1,330
	Peak (με)	-53,548	-21,520	-2,628
G	Median ± Std Dev (με)	-5297 ± 4663	-1,474 ± 4,121	-891 ± 1,333
	Peak (με)	-24,538	-6,881	-1,786

There were large strain variations within and between tibiae and across load cases, Table 7. 1. The median minimum principal strain during SD ranged from -795 με (Tibia A, SD 0.5BW) to - 20,237 με (Tibia F, SD 2.5BW) for subvolumes in direct contact with the tibial component (Radial 1), and peak (90th percentile) minimum principal strain values ranged from -1,676 με (Tibia A, SD 0.5BW) to -71,726 με (Tibia F, SD 2.5BW). For DKB, median values for subvolumes within Radial 1 ranged from -802με (Tibia A, DKB 0,5BW) to -22,028 με (Tibia G, DKB 3.5BW), with peak values ranging from -9,411 με to -73,612 με (Tibia G, DKB 3.5BW)
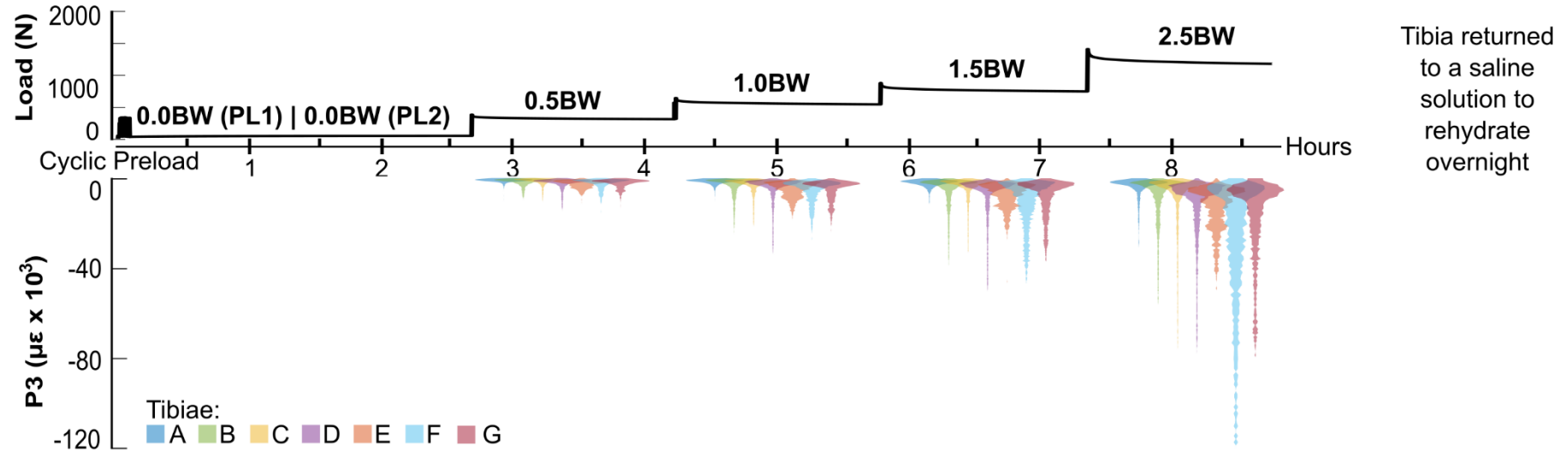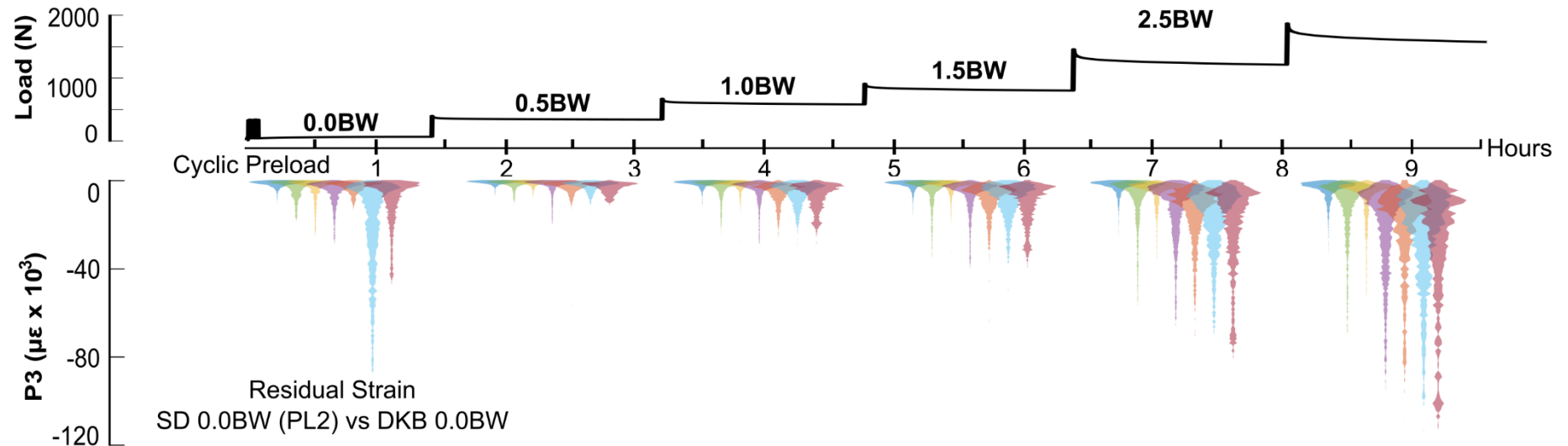
Figure 7. 2: Minimum principal strain (P3) extracted during the time-elapsed mechanical load sequence for stair descent (SD, top) and deep knee bend (DKB, bottom), with a representative load profile (Tibia G) included. Cyclic preload was applied at the start of both days. The minimum principal strain component extracted within Radial 1 (0.0-1.56mm from the bone-implant interface) of the seven tibiae at each load step are displayed. The residual strain inflicted from the first day of loading (SD 0.0BW (PL2) vs DKB 0.0BW) is also displayed.

Stair Descent 2.5BW   **Deep Knee Bend 3.5BW**

Median ± Std Dev (µε)   Median ± Std Dev (µε)
Peak (µε)   Peak (µε)

Tibia A

-2,193±4,573   -2,744±4,212
-8,806   -9,411

Tibia B

-4,132±10,919   -6,130±13,052
-23,668   -28,926

Tibia C

-3,713±14,057   -4,123±8,357
-26,434   -18,807

Tibia D

-6,537±14,444   -11,999±18,113
-30,464   -46,055

Tibia E

-10,341±9,833   -14,189±18,674
-27,605   -48,482

Tibia F

-20,237±27,822   -18,698±20,254
-71,726   -53,708

Tibia G

-9,509±17,997   -22,028±26,997
-45,294   -73,612

M   L   M   L

Minimum Principal Strain (µε)

10mm

-100,000   -80,000   -60,000   -40,000   -20,000   0

Figure 7. 3: Minimum principal strain distribution of cancellous bone within Radial 1 (0.00 – 1.56mm from the bone-implant interface) at maximum loads for stair descent (SD 2.5BW, left) and deep knee bend (DKB 3.5BW, right) of the seven tibiae. Median, standard deviation (Std Dev) and peak (90th percentile) values are reported

Highest minimum principal strain values occurred in subvolumes in direct contact with the tibial component (Radial 1) and diminished (dissipated) when moving away from the bone-implant interface (Radial 2 and Radial 3). Both median and peak strains diminished in magnitude with increasing distance from the bone-implant interface (Figure 7. 4). Within Radial 3 (3.13 – 4.69 mm from the bone-implant interface), both median (from -549 to -4,764 µε) and peak (from -1,097 to -7,476 µε) minimum principal strain values were within the elastic region of trabecular bone (less than -7,800 to -10,000 µε (Bayraktar et al., 2004)) for all load cases.
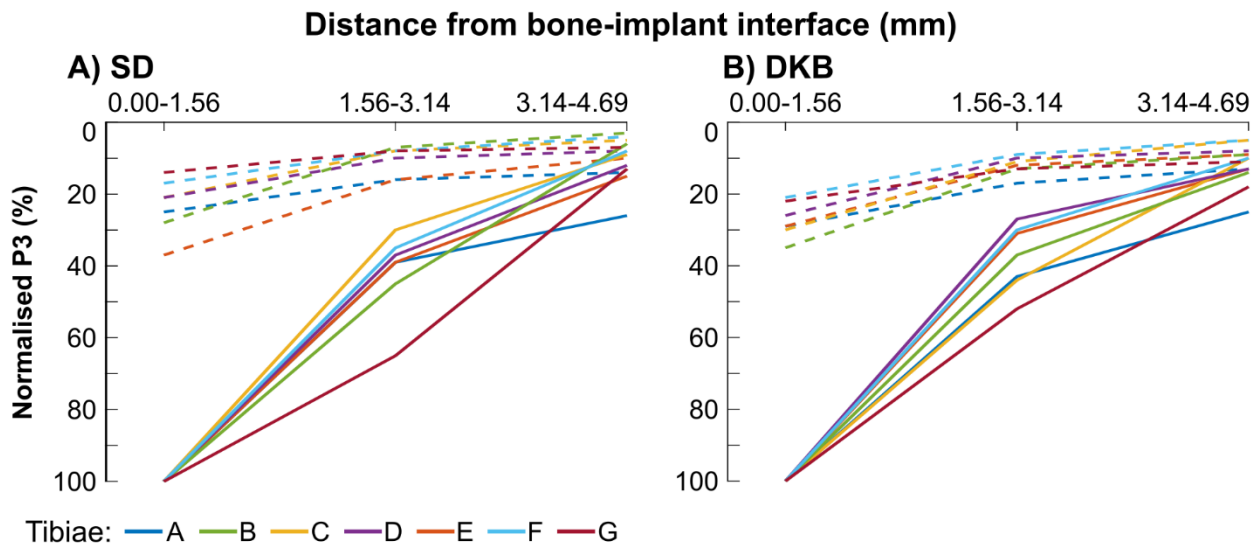
Figure 7. 4: Normalised minimum principal strain component (P3) for Radial 1, 2 and 3 during A) SD at 2.5BW and B) DKB at 3.5BW. The strain diminishes at increasing distance from the bone-implant interface. Normalised to the Radial 1 peak strain value. Normalised mean shown by the dashed line and normalised peak shown by the solid line.

Residual strain was quantified across all seven specimens (Table 7. 1, and Figure 7. 2), with peak minimum principal strain values between -3,165 to -53,548 µε (median: -10,728 µε). Such large values were limited to subvolumes in direct contact with the tibial component (Radial 1, within 0 – 1.56 mm from the bone-implant interface) for six of the tibiae (Tibia A, B, C, D, E and G), however, extended to Radial 2 (1.56 – 3.13 mm from the bone-implant interface) for Tibia F (peak strain -21,520 µε). No strain values exceeding the yield strain of bone were observed within Radial 3 (peak range: -1,468 to -2,628 µε). All tibiae went on to complete the second day of testing, where they were loaded to a maximum of 3.5BW in the DKB configuration. No tibia was observed to fail grossly across the loading protocol.

7.4 DISCUSSION

This study quantified the internal strain distribution of seven cadaveric tibiae implanted with a commercially available cementless tibial component when subjected to two time-elapsed mechanical load sequences with concomitant micro-CT imaging. The first sequence replicated SD, with loading from 0.0 – 2.5BW, and the second sequence DKB, with loading from 0.0BW – 3.5BW. With progressive loading there was increased compression of cancellous bone, particularly for bone close to the implant. At the highest applied loads for the two activities (SD 2.5BW and DKB 3.5BW), in all specimens the calculated peak strain of cancellous bone exceeded the yield strain of bone accepted in literature (Bayraktar et al., 2004).

Across the seven tibiae, the highest compressive strain consistently occurred in the posterior region for cancellous bone in direct contact with the tibial component (Radial 1). Furthermore, the strain distribution was comparable across the two activities for all specimens. For five tibiae (Tibia A, B, E, F and G) high strains were predominantly located in the posterior-medial region under the tray, whilst for two tibiae (Tibia C and D) this was observed in the posterior-lateral region. Peak compressive strains in the posterior-medial region reflect both the SD and DKB loading configuration, where the point of loading was posteriorly offset in relation to the centre of the implant, as seen within Tibia A, B, E, F and G. As included with *4.4.2.1 Alignment Errors*, alignment errors can be detected within the micro-CT datasets by looking at the impingement points of the protruding prongs. For tibiae C and D, peak strains occurred in the posterior-lateral region, which could be an experimental artefact due to alignment or due to the bone distribution of those tibiae. The static knee joint alignment and dynamic knee joint loads of the donors were not captured prior to the experiment, which may influence bone properties across the plateau (Roberts et al., 2018). The alignment error between the upper loading platen to tibial component for Tibia C and D were comparable to other specimens in both activities, however this does not account for a potential tilt of the implant (as found for Tibia C during SD).

It is difficult to compare the strain distribution observed here to other studies, due to differences in applied loading, implants employed, fixation technique and the metric quantified (with FE models often reporting stress or strain energy density distributions). Perillo-Marcone et al. (2004) developed patient-matched FE models for four individuals enrolled in an RSA study, to assess if the predicted risk ratio (calculated von Mises stress / ultimate compressive stress) and percentage volume of failing bone matched tibial component migration. For their patient-matched models of tibiae that received cementless tibial components (Patients 2 and 3), they reported peak risk in the posterior medial region directly under the tray, consistent with the regions of peak strain observed here for five of the tibiae. Quevedo González et al. (2023), in developing FE models of 12 cadaveric knees with cementless tibial components during stair ascent, reported risk of localised fatigue failure posteriorly across either plateau. This is similarly to this study, where large compressive strain was observed posteriorly across both medial and lateral plateaus of the tibiae.

In this study, large strain magnitude variations across the seven specimens were observed, with median minimum principal strains ranging from -2,193 µε (Tibia A) to -20,237 µε (Tibia E) for subvolumes in direct contact with the tibial component during SD 2.5BW loading and from - 4,135 µε (Tibia A) to -30,861 µε (Tibia G) during DKB 3.5BW loading. Yang et al. (2021), in their analysis of strain energy density across FE simulations of two tibiae with cemented tibial components, found that tibial anatomy had the largest impact on the post-implantation strain field across 144 varied simulations (other factors considered: posterior cruciate ligament balancing, surgical alignment and posterior slope), which could account for the large variation observed here. In the present study, Tibia A had a large posterior shelf (referred to as a "shelf" tibia (Yang et al., 2021)) and, from visually inspecting the micro-CT datasets, it was observed that the posterior-lateral peg was very close to the cortical bone underneath (Figure 7. 5B). Furthermore, there was overhang of the tibial component on the lateral and medial sides (Figure 7. 5C). Such contact with the medial and lateral cortex and proximity to the posterior shelf could explain the lower strain magnitudes observed. The reported benefits of the implant resting on cortical bone are limited (Quevedo González et al., 2023, Dalury, 2016).
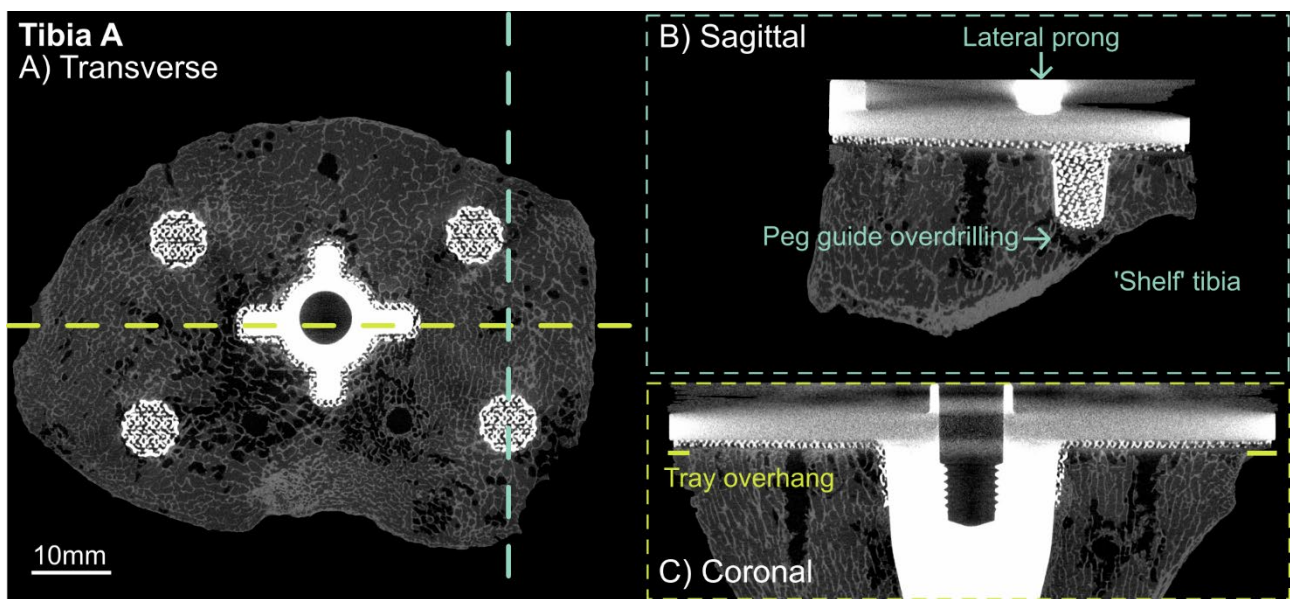
Figure 7. 5: Micro-CT images of Tibia A, a "shelf" tibia in the A) transverse, B) sagittal and C) coronal plane. Overdrilling of the peg guides, shown in B), was seen across all tibiae. Tibia A presented a large posterior shelf and overhang of the tibial component, medially and laterally (solid yellow lines shown in C). The lateral prong of the upper loading platen is also visible in B).

The extracted strain values during the time-elapsed mechanical load sequence were high. The 90th percentile strains for cancellous bone in direct contact with the tibial component (Radial 1) ranged from -1,676 to -73,612 µε across all load steps. With the yield strain of tibial trabecular bone reported in the published literature ranging between -7,800 to -10,000 µε (Bayraktar et al., 2004), peak strains exceeding this value were observed as early as 1.0BW loading (Tibiae D, E, F, G), with all seven tibiae exceeding it by 2.5BW loading in SD and 3.5BW in DKB. These high strains were predominantly contained for cancellous bone in direct contact with the tibial component (0 – 1.56 mm from the bone-implant interface, Radial 1). In five tibiae (Tibia C, D, E, F, G), peak strains

exceeding the yield strain of bone were observed further from the implant (within 1.56 – 3.13 mm from the bone-implant interface, Radial 2), however, at higher loads (at 1.5BW for Tibia F and 2.5BW for Tibiae C, D, E, G). Further than 3.13 mm from the bone-implant boundary, peak strains remained below the yield strain at all load steps considered. This regional dissipation of strain is comparable to other studies, whereby the highest strain associated with cementless devices are localised close to the implant surface, diminishing within 0.42 – 4.1 mm away from this interface (Dawson and Bartel, 1992, Rapagna et al., 2019, Berahmani et al., 2015a, Kelly et al., 2013).

The observed residual strain field across the tibiae (particularly Tibia C, D, F, G) further suggests the occurrence of permanent bone deformation, alluding to permanent damage. Despite the load had been removed and the tibia had time to recover in saline solution overnight, permanent compression of cancellous bone was detected by DVC the day after. The spatial distribution of the residual strains within the tibia reflected that of the loaded scans (Figure 7. 3).

The high strain values and the observed residual strain in this study were largely confined to within 1.56 mm from the bone-implant interface and may explain the high initial migration of cementless tibial components observed clinically (Andersen et al., 2017, Koster et al., 2023). A recent short-term RSA study reported over 1.00 mm of migration for Attune cementless tibial components (similar implant design as used here) in the first 3 months postoperatively. The tibial components went on to stabilise to 0.01 mm/year migration in the second year, comparable to a well-established and clinically successful device (0.06 mm/year: LCS Complete Knee System, DePuy Synthes, Koster et al., 2023). Furthermore, early registry revision rates for this device are promising (AOANJRR, 2020b, AOANJRR, 2020c). The mechanical environment quantified here is therefore of a potentially successful device. Similarly high internal strains that exceed the yield strength, and have an associated risk of localised bone failure, have been reported in FE studies assessing the primary fixation (prior to biological fixation) of tibial components (Perillo-Marcone et al., 2004, Taylor and Tanner, 1997, Hashemi and Shirazi-Adl, 2000, Quevedo González et al., 2023, Quevedo González et al., 2019). None of the tibiae here failed grossly and were still able to carry load during the following day of testing, accepting a maximum of 3.5BW during DKB. The ability of cancellous bone to still accept new load following large compressions (150,000 – 500,000 µε) has also been noted by others (Keaveny et al., 1994, Morgan et al., 2018). FE models should be reflective of this mechanical environment. Kelly et al. (2013), in their comparison of a plastic crushable foam model against a traditional von Mises stress model for cementless tibial components, concluded that, in order to accurately model the post-impaction period, induced damage must be included.

High strain values have been reported in other DVC studies for different anatomical sites. In their analysis of cadaveric scapula with glenoid implants, Boulanaache et al. (2020) reported a maximum compressive strain of -46,000 µε when loaded to 1500N. Danesi et al. (2016), for

vertebrae injected with cement, reported maximum compression of -14,000 $\mu\epsilon$ at 5 % sample compression, with up to -110,000 $\mu\epsilon$ at 15 % sample compression. Whilst for intact proximal femurs, Martelli et al. (2021) quantified localised peak compression of -160,000 $\mu\epsilon$ prior to fracture; well beyond the yield strain of trabecular bone.

This work presents, for the first time, the experimentally extracted internal strain field of cadaveric tibiae with metal cementless tibial components. Previous analysis of the strain field of tibiae with cementless tibial components (or, in general, bone at organ level with implants) has been limited to either external measurements, captured from strain gauges (Completo et al., 2007, Completo et al., 2008) or photoelastic resin (Berend et al., 2010, Kessler et al., 2006, Green et al., 2002), or predictions of the internal field made from finite element models (Dawson and Bartel, 1992, Perillo-Marcone et al., 2004, Taylor and Tanner, 1997, Hashemi and Shirazi-Adl, 2000, Quevedo González et al., 2023, Quevedo González et al., 2019). DVC, as employed here, permits the calculation of the continuous internal strain field at organ level in a non-destructive manner. Furthermore, as the procedure is based on acquired micro-CT datasets of the specimens in an unloaded and loaded condition, it allows visualisation of the bone-implant interplay internally.

7.5 CONCLUSION

This study has quantified the internal strain distribution for a commercially available cementless tibial component during the immediate post-implantation period while being subjected to a time-elapsed mechanical load sequence that replicated stair descent and deep knee bend. These results present the first time that the internal strain field has been quantified experimentally in such a scenario, whilst being able to visualise the bone-implant interaction through the micro-CT datasets. The extracted strain values were higher than anticipated. However, the observed distributions with peak strain occurring in the posterior region directly under the tibial component are reflective of elevated risk patterns reported in published FE studies. The large strain values and observed residual strain field, occurring predominately within 1.56 mm from the bone-implant boundary, also align with the initial migration reported clinically for cementless tibial components within the first 3 months postoperatively. This study provides a means to experimentally quantify the internal strain distribution of human tibia with cementless implants, increasing the understanding of the mechanical interaction between bone and implant.

CHAPTER 8: DISCUSSION AND FUTURE DIRECTIONS

The overarching aim of this thesis was to quantify the interference fit of a cementless tibial TKA component and the initial mechanical environment surrounding the implant following implantation, by extracting the internal strain field and relative motion between implant and bone. This was achieved via micro-CT imaging seven cadaveric tibiae when intact, after TKA preparation, impacted and when exposed to two time-elapsed mechanical load sequences that replicated SD and DKB. Specifically, this included:

1. Assessing the possibility of using DVC on micro-CT datasets of cadaveric tibiae with a commercially available cementless tibial component (Attune Affixium Cementless Fixed Bearing Knee, DePuy Synthes Joint Reconstruction) to experimentally quantify the immediate mechanical environment by extracting internal displacement vectors and strain fields (Chapter 3: Study 1, Chapter 4: Experimental Protocol).

2. Evaluating the actual interference fit achieved across seven cadaveric tibiae implanted with a commercially available cementless tibial component and assessing its effect on the post-impaction cancellous bone strain (Chapter 5: Study 2). Resected surface roughness, flatness, and percentage of tray in immediate contact with bone was also calculated.

3. Experimentally quantifying the relative motion across the entire bone-implant interface of a cementless tibial component and underlying bone for seven cadaveric specimens during SD and DBK (Chapter 6: Study 3). Relationships between the actual interference fit, percentage of tray-bone contact, residual post-impaction strain and bone volume fraction to the relative motion were assessed.

4. Extracting the compressive strains of seven cadaveric tibiae implanted with commercially available cementless tibial components when subjected to two time-elapsed mechanical load sequence that replicated SD and DKB (Chapter 7: Study 4). The residual strain present in the tibial cancellous bone after the first day of testing (SD, max load of 2.5BW) was also quantified.

8.1 PRINCIPAL FINDINGS

1) The initially high migration rate of cementless tibial components seen clinically may be explained by the limited immediate contact between tibial component and underlying bone, induced damage during implantation and high bone strains when first loaded.

Cementless tibial components have a higher initial migration compared to their cemented counterparts within the initial post-operative period, which typically settles by the second post-operative year (Pijls et al., 2018, Laende et al., 2019). This initial period can span from the first 6 weeks to 12 months post-operatively (Pijls et al., 2018, Laende et al., 2019).

A recent RSA study compared the migration of a clinically successful device (LCS, DePuy Synthes, 20 year survival rate over 90 % (AOANJRR, 2022)) to an implant similar to the component used within this study (Attune, DePuy Synthes) (Koster et al., 2023). For both implants, the majority of migration was reported to occur within the first 3 months postoperatively: the Attune migrated by 1.07 ± 0.2 mm, reaching a total of 1.17 ± 0.02mm migration within the first year. The implants went on to stablise, with only 0.01 mm migration for the Attune (and 0.06mm for the LCS) during the second post-operative year. No difference in migration rates were found between the two devices. High initial migration rates, that go on to stabilise (without continual migration), have likewise been reported elsewhere (Andersen et al., 2017, Fukuoka et al., 2000, Li and Nilsson, 2000, Pijls et al., 2018).

The findings from this work provides insight into why such high initial rates may exist for cementless tibial components. Firstly, limited immediate contact between the tibial component and bone was found, with only 54.4 ± 8.2% (range: 50.3 – 70.6 %) of the tibial tray in contact with underlying resected surface following impaction (Chapter 5). This was in part due to a rough resected surface, with the quantified peaks and low points preventing complete seating ($R^2 =$ 0.219, $p < 0.01$). The roughness (2.44 ± 0.41 mm) and flatness (0.180 ± 0.037 mm) of the resected surface within this study is comparable to values reported by others (roughness: 0.56-2.57 mm; flatness: 0.10-0.40 mm (Delgadillo et al., 2020, Toksvig-Larsen and Ryd, 1991, Toksvig-Larsen and Ryd, 1994)), highlighting that an uneven resected surface is common. To achieve complete seating of the tray, subsidence would need to occur. Within this study, a subsidence of 0.300mm would result in over 90 % (range: 80 – 97 %) of the tray in contact with the underlying bone. This would increase to over 97 % (range: 91 – 100%) with a subsidence of 0.500 mm. The lack of initial contact between implant and bone may therefore be a contributing factor to the high initial migration rate reported in the literature: **subsidence may occur in the early postoperative period to gain complete seating**.

Secondly, **permanent damage was induced in the peri-prosthetic bone during the impaction process that extended beyond the bone-implant interface**. High residual compressive strains were quantified following the impaction that extended up to 3.14 mm from the bone-implant

interface (Chapter 5). Such permanent deformation alters the mechanical properties of the cancellous bone in intimate contact with, and extending from, the implant. Based on the post-yield behaviour of trabecular bone (Keaveny et al., 2001), it is likely that this tissue would have reduced elastic modulus following the impaction.

When exposed to initial loads, through the time-elapsed mechanical load sequences that replicated SD and DKB, localised high compressive strain values were extracted close to the bone-implant interface that exceeded the yield strain of cancellous bone (reported as -7,800 µε (Bayraktar et al., 2004)) (Chapter 7). Across the seven tibiae studied, median compressive strain values ranged from -795 µε to -22,028 µε for bone in intimate contact with the tibial component (within 1.56 mm from the bone-implant interface), exceeding the yield stain of bone as early as 1.0BW loading. By the end of the loading sequences (SD: 2.5BW; DKB: 3.5BW), the peak bone strain values for all seven specimens within this region exceeded the yield strain of cancellous bone. High strain values were also captured further from the bone-implant interface (within 1.56-3.14 mm), however did not extend beyond 3.14 mm. **This concentration of high strain values for bone close to the implant could map the area at risk of permanently deforming, resulting in potential tray migration**.

Migration and residual strains were both quantified after the SD load sequence, **confirming that permanent deformation had occurred, with concomitant migration of the tibial tray** (Chapter 6 & 7). These observed phenomena could be a consequence of the bedding-in process described previously. As there was limited contact between the tray and underlying bone initially, the exposed bony peaks may have been subjected to a greater portion of the applied load, resulting in their flattening and subsequent tray migration (Taylor et al., 2012). Across the seven specimens, the median permanent tray subsidence was -8.47 ± 26.0 µm after this simulated activity. It could therefore be expected that additional migration would be captured with repeated load cycles to further increase the seating of the tray and hence distribution of the load across the entire resected surface.

Together, these experimental results provide a potential mechanism for the high initial migration rate of cementless tibial components reported in the literature: **by finding limited initial implant-bone contact, permanently deformed bone following implantation, and, high strains and subsequent tray migration when subjected to initial mechanical load**. Such results support the conjecture that cementless tibial components currently undergo a bedding-in period to obtain complete seating of the tray, which may be in part due to a rough resected surface. Six weeks was the earliest follow-up time in the 53 studies that Pijls et al. (2018) assessed in their systematic review and meta-analysis on the migration patterns of tibial components following primary TKA. The bedding-in process, potentially captured within this study, cannot yet be distinguished from the subsequent migration in these RSA studies as it would occur immediately following surgery. It is

important to note that high initial migration rates (particularly within the first three months) exist in clinically successful devices (such as the LCS) (AOANJRR, 2022, Koster et al., 2023) and here an insight is provided for the initial interaction between implant and bone.

2) The interference fit of cementless tibial components is related to both increased residual deformation of peri-prosthetic bone following impaction and reduced relative motion between implant and bone in subsequent loading.

Actual interference fit, as computed within the study, assesses the overlap between the prepared proximal tibia to the geometry of the implant. During impaction, this overlap either induces a compressive elastic response within the surrounding cancellous bone, becomes permanently damaged (through either abrasion and/or compaction (Berahmani et al., 2018, Damm et al., 2017, Bishop et al., 2014)) or a mixture of the two. Only the elastic response is reported within the literature as contributing to the primary stability of the tibial component (Gebert et al., 2009, Jepsen et al., 2009).

The extent of the mechanical tissue response, quantified through the post-impaction residual strain, was found to be related to the actual interference fit: **with increased interference there were greater compressive strains in the surrounding cancellous bone**. The relationship was strongest for bone in intimate contact with the implant (within 1.56 mm from the bone-implant interface: $R^2 = 0.450$, $p < 0.01$), however, extended beyond, up to 3.14 mm from the bone-implant interface ($R^2 = 0.269$, $p < 0.01$).

Furthermore, **with increased actual interference there was increased primary stability, with reduced relative motion across the bone-implant interface**. Other authors have likewise reported increased stability (increased push-out and pull-out force) with increased interference (Berahmani et al., 2015a, Norman et al., 2006). However, this increased stability waned with time; within 30 min to 24 hrs post-implantation there was no statistically significant difference in stability with increased interference (Berahmani et al., 2015a, Norman et al., 2006). In this study, there was an extended period in between implantation to testing, spanning multiple days during which the tibiae underwent a freeze-thaw cycle. Increased stability with increased actual interference fit was still found in 10 of the 11 load cases, **providing an increased mechanical interlock that lasted longer than previously reported**.

Interestingly, no significant relationship was found between the post-impaction residual strain and the relative motion in any load cases ($p > 0.256$). The residual strain quantified both the permanent damage inflicted and the elastic response of bone. The proposed benefits of an interference fit have previously been attributed to the induced elastic stresses within the surrounding bone, which would wane over time due to bone's viscoelastic behaviour (Dawson and Bartel, 1992, Curtis et al., 1992, Berahmani et al., 2015a, Norman et al., 2006). It could therefore be hypothesised that the mechanical response captured here is the permanent deformation of the peri-prosthetic bone and

may explain why no relationship was found. Whilst increased residual strain was not found to relate to increased implant stability, this permanent deformation could still be beneficial to the long-term success of the device by stimulating a quicker osteogenic response (Bosshardt et al., 2011).

These results show a complex interaction between the actual interference fit achieved, the post-impaction residual strain induced and the resulting primary stability of cementless tibial components. More work is needed to ascertain the separate components of the induced mechanical response; separating the permanent damage inflicted to the elastic response of bone. **Nevertheless, the mechanical interlock provided by the interference is beneficial to the stability of the tibial component and may last longer than previously reported, regardless of the permanent damage that it may induce.**

8.2 SIGNIFICANCE TO ORTHOPAEDIC RESEARCH

The mechanical environment surrounding cementless tibial components in the immediate post-operative period is essential to its long-term success, with sufficient primary stability required to facilitate osseointegration. During surgery, an interference fit is introduced, whereby there is an overlap of the resected tibia to the geometry of the tibial component. Theoretically, this firstly ensures contact between implant and bone and, secondly, induces an elastic response in the surrounding cancellous bone. Along with friction across the bone-implant interface, this elastic response is believed to establish primary stability. However, little is known about the interplay between the interference and the initial mechanical environment.

The interference fit achieved differs to the intended nominal interference due to surgical variation and induced damage (Berahmani et al., 2018, Damm et al., 2017). Previous experimental methods employed to quantify the initial mechanical environment, through either micromotion or strain analysis, have been limited to external measurements only (Navacchia et al., 2018, Small et al., 2016, Sánchez et al., 2021, Berend et al., 2010, Kessler et al., 2006, Green et al., 2002, Small et al., 2010, Han et al., 2020), and often at discrete locations (Lee et al., 1991, Miura et al., 1990, Kraemer et al., 1995, Stern et al., 1997, Sala et al., 1999, Meneghini et al., 2011, Bhimji and Meneghini, 2012, Bhimji and Meneghini, 2014, Chong et al., 2010, Van Valkenburg et al., 2016, Completo et al., 2008, Completo et al., 2007, Gray et al., 2008).

Furthermore, the effect of the interference is assessed by altering the nominal interference (Sánchez et al., 2021), which differs to what is achieved due to surgical variation and induced damage (Damm et al., 2015, Berahmani et al., 2018, Norman et al., 2006). FE models provide an insight into the internal environment surrounding a cementless tibial component, by extracting full-field strains, stresses, stress-energy densities and micromotion. However, an interference fit is often not included (Viceconti et al., 2006, Chong et al., 2010, Hashemi and Shirazi-Adl, 2000, Taylor et al., 2012, Taylor et al., 1998, Quevedo González et al., 2023, Fitzpatrick et al., 2014a, Quevedo González et al., 2019), or when one is modelled, it is often smaller than what is used clinically (Yang et al., 2021, Navacchia et al., 2018). Additionally, assumptions are made regarding the mechanical properties of bone and interface characteristics that need to be validated. The relevance of validating internal measurements to experimentally derived external measurements is questionable.

Digital volume correlation undertaken on micro-CT datasets provides an experimental means to extract full-field internal displacement vectors, from which relative motion across the entire bone-implant interface and internal strain can be extracted. Whilst micro-CT imaging and DVC analysis has been performed at organ level (Hussein et al., 2012, Tozzi et al., 2016, Boulanaache et al., 2020, Zhou et al., 2020b, Kusins et al., 2019, Kusins et al., 2022, Danesi et al., 2016, Palanca et al., 2016a), there is yet to be a study undertaken on a specimen as large as cadaveric tibiae and

with a metallic tibial component, which introduces additional complexities. This thesis confirms the possibility of undertaking such an analysis (**Chapter 3: Study 1** and **Chapter 4: Experimental Protocol**) (Wearne et al., 2022). The developed micro-CT and DVC protocol is also applicable to other anatomical sites and large orthopaedic components.

The work presented in this thesis is the first time, to the best of the author's knowledge, that a study has been able to visualise the interface between the cancellous bone of the tibia and a commercially available cementless tibial component, at organ level. By acquiring micro-CT datasets of these specimens, when intact, following TKA preparation and after impaction, a greater understanding of the initial mechanical environment surrounding a cementless tibial component has been established. Surgical variation across seven cadaveric tibiae was assessed, determining the actual interference fit, the proportion of initial bone-implant contact and the extent of mechanical response induced within the surrounding cancellous bone following implantation (**Chapter 5: Study 2**). Through two time-elapsed mechanical load sequences that replicated SD and DKB, the relative motion across the entire bone-implant interface (**Chapter 6: Study 3**) and the internal strain field of the cancellous bone surrounding the implant (**Chapter 7: Study 4**) was calculated.

8.3 LIMITATIONS AND RECOMMENDATIONS FOR FUTURE RESEARCH

1) Assessing the impact of tibial morphological characteristics and cancellous bone material properties to primary stability

There was large inter-specimen variation in the extracted strain values that could not be explained by surgical variation (resected surface roughness, actual interference fit), the post-impaction residual strain nor BV/TV. Other studies have likewise recognised that inter-specimen variability can be a major contributor to variations in result (Norman et al., 2006, Quevedo González et al., 2023, Costa et al., 2017, Oliviero et al., 2018, Taylor and Prendergast, 2015).

BV/TV was used to quantify regional variations in bone microarchitecture. In this thesis, BV/TV was not found to be related to resected surface roughness (p = 0.23), actual interference fit (p = 0.77), post-impaction residual strain at any distance from the implant (p = {0.45 : 0.89}), nor the relative motion at the bone-implant interface for any load case (p = {0.136 : 0.814}). BV/TV does not, however, capture gross tibia morphology and, only through regressions, can explain some mechanical properties (including ultimate strength (Perilli et al., 2008, Perilli et al., 2012), elastic modulus (Ulrich et al., 1997) and anisotropy (Ulrich et al., 1997)). This may, in-part, explain why no relationships were found in this study. For example, Tibia A was recognised as a "shelf" tibia, displaying a large posterior overhang (Yang et al., 2021) with the posterior pegs sitting close to the cortex. The strain values extracted from Tibia A during the time-elapsed mechanical load sequences were consistently smaller than the median across the other six tibiae, which could not be explained by the specimen's BV/TV (Tibia A BV/TV (median ± std dev) = 18.5 ± 4.25 %; other tibiae BV/TV = 18.4 ± 6.34 %).

Only seven cadaveric tibiae were employed in this study, displaying limited BV/TV variation, and making statistical analysis difficult. The number of specimens employed here, however, is in line with other experimental studies (Martelli and Perilli, 2018, Boulanaache et al., 2020, Rapagna et al., 2019, Martelli et al., 2021, Kusins et al., 2019, Zhou et al., 2020a, Zhou et al., 2020b). Future work should look to increase the number of specimens, and introduce those that have clinically relevant pathologies, such as osteoarthritis. Furthermore, specimen attributes, including morphological characteristics and material properties, should be quantified to assess their impact on the primary stability of cementless tibial components.

2) Assist in advancing assessment guidelines for new devices in their development phase

This study quantified the mechanical environment surrounding a cementless tibial component in the immediate post-operative period for seven cadaveric specimens. The work presented in this thesis is not able to predict the potential clinical success of these seven TKAs individually. There was large inter-specimen variation in the actual interference fit (median range: -0.368 to 1.51 mm), the post-impaction residual strain (-1,316 to -14,906 µε), and, during the time-elapsed mechanical load sequence, the relative motion (SD 2.5BW: 8.5 to 65.7 µm; DKB 3.5BW: 10.8 to 90.1 µm) and

minimum principal strain component (SD 2.5BW: -2,193 to -20,237 µε; DKB 3.5BW: -2,744 to -22,028 µε). The mechanical environment presented in this thesis, including the large inter-specimen variation, presents a baseline for a clinically successful device (AOANJRR, 2020a, AOANJRR, 2020b).

An short-term (2 year) RSA study found comparable rates between a device similar to that used within this study (Attune, DePuy Synthes) and a clinically well-performing device (LCS Complete Knee Systems, DePuy Synthes) (Koster et al., 2023). Furthermore, initial registry data for this device is promising, with a cumulative percentage revision of 1.2 % at 3 years (95 % confidence intervals (CI): 0.5, 2.8 %), comparable to that of the NexGen Complete Knee Solution (1.7 % (CI: 1.3, 2.2 %) Zimmer Biomet), which, has a 20-year survivorship of 94.3 % (CI: 92.9, 95.3 %) (AOANJRR, 2022). Furthermore, associations were made between the quantified relative motion at the bone-implant interface to limits established within the literature conducive to osseointegration (< 50 µm (Pilliar et al., 1986)) and fibrous tissue development (> 150 µm (Søballe et al., 1992)). Whilst there is some debate surrounding the use of such limits (Kohli et al., 2021), the majority of the bone-implant interface of all seven specimens remained within the reported limits permissible to osseointegration (Søballe et al., 1992), with at least 78.6 % (Tibia F) of the bone-implant interface remaining under 150 µm of relative motion.

Future work should look to understand the difference in the initial mechanical environment between clinically successful and clinically unsuccessful devices. This would involve performing similar analysis on devices that have long-term clinical data (RSA studies of 10+ years and registry data), for those that have both positive (low rates of continuous migration (Pijls et al., 2012), low revision rates) and negative results (high rates of continuous migration, high revision rates). This type of analysis would result in benchmarks for a favourable and potentially unacceptable initial mechanical environment. New devices entering the market could then be evaluated against such results, to ensure that they are performing comparatively as well or, ideally, better than their predecessors.

3) Computing the effect of inhomogeneous strains and discontinuous materials in DVC analyses

This study employed DVC, being the tool that permits experimental quantification of the internal displacement field in specimens while being mechanically tested and imaged volumetrically (in 3D). DVC extracts continuum level displacement vectors within subvolumes (Bay et al., 1999), from which subvolume strain values can be calculated. Material discontinuities arise in the current scenario of cadaveric tibiae with a cementless tibial component due to the bone-implant interface and the presence of bone debris caused by shearing of bone in the impaction. It is not known how such discontinuities affect the accuracy of these calculations.

The standard for error analysis (and as undertaken within this study), is a zero-strain scenario, where a homogeneous load case (zero-strain) is assessed (Dall'Ara and Tozzi, 2022). Other authors have also virtually applied non-zero homogeneous strains (0.5 % (Boulanaache et al., 2020) and 1 % (Zhou et al., 2020a)) to assess accuracy. However, in all of these scenarios the effect of having separate bodies is not captured.

Any inaccuracies introduced due to either the bone-implant interface or debris would be largest for subvolumes in direct contact with the tibial component (Radial 1) and reduce further away. This was observed in this study, where the correlation coefficient was lowest in Radial 1, in comparison to Radial 2 and Radial 3. Future work is needed to assess the impact that an introduced boundary has on DVC calculations, particularly when there is a heterogeneous strain field. How far any errors propagate from the introduced boundary should also be quantified.

To mitigate any effect, the micro-CT datasets (see *4.5.1 Image Preparation for DVC Analysis*) were shifted in superior-inferior direction, so that the bone-implant interface under the tibial component was aligned to a DVC subvolume boundary. Within each subvolume there was consequently a continuous material (either bone or implant). Whilst this could be achieved for subvolumes directly under the tibial component (requiring translation of the datasets along only one axis (vertical)), around the pegs and keel it could not be achieved, as it was not possible to align the four pegs and keel from the image datasets to the subvolume grid system of DVC.
The impact of bone debris was also mitigated by masking regions where bone debris accumulation was known to occur (the distal tips of the pegs). However, other studies have reported debris accumulation in the pores of implant surfaces and neighbouring trabeculae (Damm et al., 2017, Berahmani et al., 2018). Such instances were not masked in this study.

Whilst limitations of a zero-strain error analysis have been expressed above, it is currently best practice (Tozzi et al., 2017, Roberts et al., 2014). By this standard, the zero-strain error analysis undertaken within this study quantified errors (MAER: 307 – 528 µε; SDER: 116 – 307 µε) that are sufficiently low for analysis of bone within its elastic region, by being less than 10% of the yield strain of bone (Liu and Morgan, 2007, Roberts et al., 2014), and analysis of micromotions permissible to osseointegration, by being less than 10 % of permissible limits (Viceconti et al., 2001, Søballe et al., 1992). Other studies have likewise employed DVC to quantify the internal strain field at the interface of augmented or implanted specimens (Tozzi et al., 2017, Le Cann et al., 2017, Le Cann et al., 2020, Palanca et al., 2016a, Boulanaache et al., 2020, Danesi et al., 2016, Du et al., 2015, Zhou et al., 2020a, Zhou et al., 2020b).

A recent study by Valmalle et al. (2022) employed what they termed "local-global" DVC to assess the damage onset of a dis-continuous pantographic material. By augmenting DVC with FE, point constraints were set at a structural level of the material that permitted separate bodies to be treated as such. Strain fields were extracted across hinge-joints where the bodies were weakly

constrained to one another. However, the extracted strain field was not sufficiently accurate for analysis within the elastic region. That work highlights the potential in combining DVC with FE. Future work is needed to improve the accuracy of such a system and extend its use to assessing the union of orthopaedics components and bone.

4) Exploring dynamic and complex loading scenarios

When comparing the induced relative motion between the tibial component and underlying bone in SD to DKB, few statistically significant differences were found. This contrasts to other authors who have reported differences in micromotion values depending on the activity undertaken, though not always statistically tested (Han, Chong 2010, Yang, Quevedo Gonzalez, 2019, Van Valkenburg, Taylor 2012). There are several reasons why such differences may not have been found in this work.

SD and DKB are highly dynamic and complex activities, that involve all six degrees of freedom across the knee. Due to the requirements of micro-CT imaging and the mechanical loading rig used within this work, these activities were replicated statically and with one degree of freedom (axial compression). Whilst the vertical component is the largest contributor to resultant force acting across the knee in both activities (Kutzner et al., 2010), peak micromotion has been correlated to instances that couple low axial load with high flexion-extension and varus-valgus moments (Fitzpatrick and Rullkoetter, 2014, Taylor et al., 2012, Quevedo González et al., 2019). Here, the flexion of the knee in these activities was represented by posteriorly offsetting two prongs, the position of which mimicked the medial and lateral femoral condyles on the tibial plateau in each activity, which introduced an additional flexion-extension moment. However, these values were neither measured, nor directly controlled, and potting errors occurred (*4.4.2.1 Alignment Errors*). Alternate mechanical loading rigs and hexapod robots, which offer 6 degrees of freedom measurements, have been used for time-elapsed mechanical loading of large specimens with concurrent micro-CT imaging (Bennett et al., 2022, Martelli and Perilli, 2018, Martelli et al., 2021, Kusins et al., 2019). The possibility of using those systems for cadaveric tibiae with titanium tibial components would need to be assessed, due to the presence of the large metallic component and the force required (the hexapod robot referenced is limited to 1,500N (Kusins et al., 2019)). If deemed possible, future work should be undertaken to compare the results of this study, with one degree of freedom (and additional moments added due to the offset of the prongs), to those of more complex loading configurations.

To the best of the author's knowledge, there currently does not exist a volumetric imaging modality with a sufficiently short scan time to permit *dynamic* analysis with DVC of bone and implant at organ level. DVC has been undertaken on high-resolution peripheral quantitative computer tomography (HR-pQCT) image datasets of cadaveric (*in-vitro*) femurs before and after impaction of a femoral component (Rapagna et al., 2019). HR-pQCT can offer shorter scan times in comparison

to micro-CT systems (Mys et al., 2019), whilst still being able to obtain relatively high spatial resolution (such as 60.7 μm/pixel (Rapagna et al., 2019)). However, such systems have a relatively small gantry space (Mys et al., 2019), requiring multiple scans to fit the specimen into the field of view (Rapagna et al., 2019), and, have limited X-ray source power (68 kVp, 100 W for Scanco Xtreme CTII (Scanco Medical, 2023)), which becomes problematic with high density metallic components at organ level, as is the case in this study. The aforementioned study by Rapagna et al. (2019) mitigated this issue by removing the femoral component prior to performing the post-implantation scan.

Advances have been made in incorporating artificial intelligence and deep-learning networks with DVC. So far, these have assisted in enhancing computational efficiency and hence lowering processing time (Duan and Huang, 2022), whilst, as of yet not addressing scanning times. The reliance of DVC on relatively slow imaging modalities in bone research has been highlighted as an overall limitation (Dall'Ara and Tozzi, 2022, Buljac et al., 2018).

Within this study, the time-elapsed mechanical load sequence that represented SD was undertaken on the first day of testing for each specimen, followed by DKB on the second. Residual strain, alluding to permanent deformation, and migration of the tray was captured following SD and, as such, the specimens were not in the same condition for each day of testing. This may be a contributing factor as to why no statistically significant difference in relative motion was found between the replicated loading activities. It is difficult to assess the contribution of individual factors through *ex-vivo* testing. Specimen damage could have been avoided by reserving specimens for one activity only, however, at the expense of introducing additional inter-specimen variation (Martelli and Perilli, 2018, Danesi et al., 2016). Likewise, inter-specimen variation could have been eliminated by using sawbones (Cristofolini and Viceconti, 2000), but these do not properly represent the mechanical properties of bone (Berend et al., 2010). This is a limitation of *ex-vivo* testing, which is well recognised within the literature (Yang et al., 2021, Cristofolini et al., 2010b).

Initial permanent migration of cementless tibial trays (the "settling-in period") has likewise been quantified by Han et al. (2020) after 500 cycles of preload through the use of DIC. However, as it was using DIC, that analysis was limited to peripheral measurements (see *2.4 Limitations in Assessing Primary Stability*) and the preload, similar to this study, only had a vertical component ($-F_z$). Further research could look to quantify permanent tray migration and permanent cancellous bone deformation after multiple load cycles by loading the specimen outside of the micro-CT gantry. Micro-CT scans could be acquired before and after loading, permitting DVC analysis. Without the space and X-ray penetration limitations discussed above, this may permit the use of loading devices that can achieve multiple degrees of freedom, such as hexapod robots and functional activity simulators used by others (Van Valkenburg et al., 2016, Navacchia et al., 2018, Han et al., 2020, Yang et al., 2020, Sánchez et al., 2021), whilst still permitting internal analysis.

The insights gained from this study, in terms of the initial mechanical environment surrounding cementless tibial components, can now be used to build and validate FE models. With such a model, systematic studies could then be undertaken (Cristofolini et al., 2010b). The impact of implant design features, loading patterns, surgical variation and specimen characteristics could be individually assessed.

5) Including damage criteria in FE models when simulating the initial mechanical environment

Extracted compressive strains during the time-elapsed mechanical load sequences of SD and DKB were high and concentrated to within 3.14mm the bone-implant interface. The strain values exceeded the yield strain of bone as early as 1.0BW during both activities. Residual strain was captured following the first time-elapsed mechanical load sequence (being SD, where a maximum of 2.5BW was applied), alluding to permanent deformation of bone. This was supported by the simultaneous migration of the component. All specimens were still able to receive load the following day, where a maximum of 3.5BW was applied in a DKB configuration.

Due to the consistency of post-yield mechanical behaviour of cancellous bone, Keaveny et al. (1994) stipulated that this behaviour should be treated as a material property. However, few FE studies have implemented such characteristics, rather modelling bone as linear elastic with no failure criteria (Chong et al., 2011, Chong et al., 2010, Perillo-Marcone et al., 2004, Dawson and Bartel, 1992, Hashemi and Shirazi-Adl, 2000, Quevedo González et al., 2023, Fitzpatrick et al., 2014a, Quevedo González et al., 2019). The results of this thesis further highlight the need to include such material properties in FE models, particularly when modelling the immediate post-operative period. As captured collectively within this study, bone in immediate contact with the implant is subjected to permanent deformation during the impaction and proceeds to undergo high levels of deformation upon loading. Extracted strain values exceeded the yield strain of bone and resulted in further permanent deformation, as captured by the residual strain field following the first time-elapsed mechanical load sequence. Importantly though, the specimens were still functional, and no specimen failed grossly. Recent studies have found that crushable foam (CF) models, whereby a failure criterion is introduced through isotropic hardening (Soltanihafshejani et al., 2021), are able to better capture the immediate post-operative period (Kelly et al., 2013). With this work, the internal strain calculations derived from those models can now be validated directly against experimentally values. This work therefore provides an opportunity to assess the assumptions made regarding chosen material properties, boundary conditions and friction coefficients.

6) Aiding in the development of cementless-TKA specific rehabilitation guidelines

Currently, to the best of the author's knowledge, there is no established rehabilitation protocol following TKA (Mistry et al., 2016, Dalury, 2016, Castrodad et al., 2019). The published guidelines

reviewed focused on increasing patient knee range of motion, increasing joint functionality and achieving normal gait mechanics. Early rehabilitation has been defined as the period from the first post-operative day until 6 weeks (Castrodad et al., 2019). It is often encouraged that relatively high flexion angles are achieved in the immediate period following TKA, with recommendations to achieve 90° of passive flexion at hospital discharge (typically days), 80° active flexion at the initial out-patient review (typically 1-2 weeks post surgery), and, functional tasks and weight bearing by 3-6 weeks post-surgery (Mistry et al., 2016, Castrodad et al., 2019). These time points occur before osseointegration of the cementless tibial component would have occurred (Bosshardt et al., 2017). The reviewed rehabilitation studies did not differentiate between cementless TKA and cemented TKA, even though the fixation of the devices differ (Mistry et al., 2016, Castrodad et al., 2019). The primary stability of cementless tibial components required for osseointegration needs to be considered, as unlike cemented tibial components, a secure fixation is not achieved immediately following the operation. This thesis considered two ADLs that have a high degree of flexion and result in posterior loading of the tibial component. High compressive strains (> 7,800 µε) and potentially detrimental relative motion at the bone-implant interface (> 50 µm), which could be unsatisfactory conditions for osseointegration, first occurred at 1.0BW loading for both SD and DKB. Based on these results, and considering the fixation of the tibial component only, it could be recommended to reduce or limit either loading and/or high flexion angles in the immediate post-operative period. However, the whole replaced joint needs to be considered in the rehabilitation protocol. More work is needed to establish clinical guidelines that consider the fixation of cementless tibial components during this period, in additional to the functional outcome of the joint.

8.4 CONCLUDING STATEMENT

The work in this thesis provides greater insight into the interaction between a cementless tibial component and the underlying bone in the immediate post-operative period through time-elapsed mechanical loading with concomitant micro-CT imaging and digital volume correlation (DVC). The initial mechanical environment was quantified, experimentally, by assessing the actual interference fit between implant and bone, the post-implantation residual strain field, and, when loaded, the relative motion across the entire bone-implant interface and the minimum principal strain component in the surrounding cancellous bone. The actual interference fit between implant and bone was found to be related to both the post-impaction residual strain, and, relative motion at the bone-implant interface, with greater interference relating to higher residual strains and also greater implant stability. Post-impaction residual strain and high minimum principal strain values during time-elapsed loading, with subsequent permanent deformation, were extracted in the cancellous bone surrounding the implant. This highlights the need for FE analyses to include failure properties when modelling this initial period. Taken together, these results provide a comprehensive analysis of the initial mechanical environment following the implantation of a clinically successful cementless tibial tray and provide insight into the possible mechanisms resulting in the high initial migration rates of cementless tibial trays seen clinically.

ACKNOWLEDGEMENTS

APPENDICES

STATEMENTS OF CONTRIBUTION: CHAPTER 3, STUDY 1

Full publication details:

Wearne, LS, Rapagna, S, Taylor, M & Perilli, E 2022. Micro-CT scan optimisation for mechanical loading of tibia with titanium tibial tray: A digital volume correlation zero strain error analysis. *Journal of the Mechanical Behavior of Biomedical Materials, 134, 105336*.

Outline of the author's contribution to the publication:

In this paper, LS Wearne was the main contributor to the study conceptualisation, study methodology, data acquisition, formal analysis and interpretation, graphical representation, writing-original draft and subsequent editing.

LS Wearne was involved in micro-CT imaging and cross-section reconstruction of the cadaveric tibia for all scanning configurations. LS Wearne developed the masking protocol for mitigating the influence of marrow movement. LS Wearne developed and undertook the DVC analysis and subsequent analysis of the results, including the statistical tests. LS Warne wrote the draft manuscript, which was then edited by co-authors (S Rapagna, M Taylor and E Perilli).

STATEMENTS OF CONTRIBUTION: CHAPTER 5, STUDY 2

Full publication details:

Wearne LS, Rapagna S, Keene G, Taylor M, Perilli E. Quantifying the interference fit of cementless tibial trays and its effect on the initial mechanical environment. *In preparation for submission to a peer-reviewed journal*.

Outline of the author's contribution to the publication:

In this paper, LS Wearne was the main contributor to the conceptualisation, formal analysis, investigation, methodology and writing (original draft and editing).

LS Wearne was involved in the micro-CT imaging of the specimens when intact, resected and impacted. LS Wearne developed the methodology for quantifying the actual interference fit and resected surface analysis and undertook all subsequent analysis. LS Wearne developed and undertook the DVC analysis and masking of extracted results. LS Wearne performed all data analyses and interpretation of results. LS Wearne wrote the original draft manuscript, which was edited by her supervisors (M Taylor, E Perilli).

STATEMENTS OF CONTRIBUTION: CHAPTER 6, STUDY 3

Full publication details:

Wearne LS, Rapagna S, Awadalla M, Keene G, Taylor M, Perilli E. Quantifying the contribution of interference fit to the primary stability of cementless tibial trays: a micro-CT and Digital Volume Correlation analysis. *In preparation for submission to a peer-reviewed journal.*

Outline of the author's contribution to the publication:

In this paper, LS Wearne was the main contributor to the conceptualisation, formal analysis, investigation, methodology and writing (original draft and editing).

LS Wearne (with M Taylor and E Perilli) designed the experimental protocol, including the representative activities (SD and DKB) and load steps. LS Wearne developed and performed the potting procedure. LS Wearne (with S Rapagna and E Perilli) undertook the time-elapsed mechanical load sequence with concomitant micro-CT imaging and image reconstruction. LS Wearne developed and undertook the DVC analysis, including masking techniques (segmenting subvolumes of the tibia with BV/TV > 5%, segmenting implant subvolumes, isolating subvolumes in direct contact with the implant (Radial 1)). LS Wearne performed all data analysis and initial interpretation of results, including statistical tests. LS Wearne wrote the original draft manuscript, which was edited by her supervisors (M Taylor, E Perilli).

STATEMENTS OF CONTRIBUTION: CHAPTER 7, STUDY 4

Full publication details:

Wearne LS, Rapagna S, Awadalla M, Keene G, Taylor M, Perilli E. Quantifying the immediate post-implantation strain field of cadaveric tibiae implanted with cementless tibial trays: a time-elapsed micro-CT and Digital Volume Correlation analysis during stair descent. *Journal of the Mechanical Behavior of Biomedical Materials*, 2023. *In revision*.

Outline of the author's contribution to the publication:

In this paper, LS Wearne was the main contributor to the conceptualisation, formal analysis, investigation, methodology and writing (original draft and editing).

LS Wearne (with M Taylor and E Perilli) designed the experimental protocol, including the representative activities (SD and DKB) and load steps. LS Wearne developed and performed the potting procedure. LS Wearne (with S Rapagna and E Perilli) undertook the time-elapsed mechanical load sequence with concomitant micro-CT imaging and image reconstruction. LS Wearne developed and undertook the DVC analysis, including masking techniques (segmenting subvolumes of the tibia with BV/TV > 5%, segmenting implant subvolumes, isolating subvolumes in Radial 1, Radial 2, and 3 (Radial 3) subvolumes). LS Wearne performed all data analysis and initial interpretation of results. LS Wearne wrote the original draft manuscript, which was edited by co-authors (S Rapagna, M Awadalla, M Taylor and E Perilli).

REFERENCES

AJRR 2022. American Joint Replacement Registry Annual Report 2022. *In:* American Academy of Orthopaedic Surgeons (ed.). Rosemont, Illinois.

Andersen, MR, Winther, NS, Lind, T, Schrøder, HM, Flivik, G & Petersen, MM 2017. Low preoperative BMD is related to high migration of tibia components in uncemented TKA—92 patients in a combined DEXA and RSA study with 2-year follow-up. *The Journal of Arthroplasty,* 32**,** 2141-2146.

Andriacchi, TP, Stanwyck, TS & Galante, JO 1986. Knee biomechanics and total knee replacement. *The Journal of Arthroplasty,* 1**,** 211-219.

AOANJRR 2020a. Automated Industry Report System (AIRS), ID No. 2124 for DePuy Synthes, ATTUNE CR/ATTUNE Total Knee, (procedures from 1 September 1999-17 February 2020). Adelaide, Australia.

AOANJRR 2020b. Automated Industry Report System (AIRS), ID No. 2125 for DePuy Synthes, ATTUNE PS/ATTUNE Total Knee, (procedures from 1 September 1999-17 February 2020). Adelaide, Australia.

AOANJRR 2020c. Hip, Knee & Shoulder Arthroplasty: 2020 Annual Report. Adelaide: Australian Government Department of Health.

AOANJRR 2022. Australian Orthopaedic Association National Joint Replacement Registry. Hip, Knee & Shoulder Arthroplasty: 2022 Annual Report. Adelaide, Australia: Australian Government Department of Health.

Baker, P, Khaw, F, Kirk, L, Esler, C & Gregg, P 2007. A randomised controlled trial of cemented versus cementless press-fit condylar total knee replacement: 15-year survival analysis. *The Journal of bone and joint surgery. British volume,* 89**,** 1608-1614.

Baldwin, MA, Clary, CW, Fitzpatrick, CK, Deacy, JS, Maletsky, LP & Rullkoetter, PJ 2012. Dynamic finite element knee simulation for evaluation of knee replacement mechanics. *Journal of Biomechanics,* 45**,** 474-483.

Bargren, JH, Blaha, J & Freeman, M 1983. Alignment in total knee arthroplasty. Correlated biomechanical and clinical observations. *Clinical orthopaedics and related research***,** 178-183.

Barrett, J & Keat, N 2004. Artifacts in CT: Recognition and Avoidance. *Radiographics,* 24**,** 1679-1691.

Bay, BK, Smith, TS, Fyhrie, DP & Saad, M 1999. Digital volume correlation: Three-dimensional strain mapping using X-ray tomography. *Experimental Mechanics,* 39**,** 217-226.

Bayraktar, HH, Morgan, EF, Niebur, GL, Morris, GE, Wong, EK & Keaveny, TM 2004. Comparison of the elastic and yield properties of human femoral trabecular and cortical bone tissue. *Journal of Biomechanics,* 37**,** 27-35.

Bennett, KJ, Callary, SA, Atkins, GJ, Martelli, S, Perilli, E, Bogdan Solomon, L & Thewlis, D 2022. Ex vivo assessment of surgically repaired tibial plateau fracture displacement under axial load using large-volume micro-CT. *Journal of Biomechanics,* 144**,** 111275.

Berahmani, S, Hendriks, M, de Jong, JJA, van den Bergh, JPW, Maal, T, Janssen, D & Verdonschot, N 2018. Evaluation of interference fit and bone damage of an uncemented femoral knee implant. *Clin Biomech (Bristol, Avon),* 51**,** 1-9.

Berahmani, S, Hendriks, M, Wolfson, D, Wright, A, Janssen, D & Verdonschot, N 2017. Experimental pre-clinical assessment of the primary stability of two cementless femoral knee components. *Journal of the Mechanical Behavior of Biomedical Materials,* 75**,** 322-329.

Berahmani, S, Janssen, D, van Kessel, S, Wolfson, D, de Waal Malefijt, M, Buma, P & Verdonschot, N 2015a. An experimental study to investigate biomechanical aspects of the initial stability of press-fit implants. *Journal of the mechanical behavior of biomedical materials,* 42**,** 177-185.

Berahmani, S, Janssen, D, Wolfson, D, Rivard, K, de Waal Malefijt, M & Verdonschot, N 2015b. The effect of surface morphology on the primary fixation strength of uncemented femoral knee prosthesis: a cadaveric study. *The Journal of arthroplasty,* 30**,** 300-307.

Berend, ME, Small, SR, Ritter, MA & Buckley, CA 2010. The effects of bone resection depth and malalignment on strain in the proximal tibia after total knee arthroplasty. *The Journal of arthroplasty,* 25**,** 314-318.

Berger, RA, Lyon, JH, Jacobs, JJ, Barden, RM, Berkson, EM, Sheinkop, MB, Rosenberg, AG & Galante, JO 2001. Problems with cementless total knee arthroplasty at 11 years followup. *Clinical Orthopaedics and Related Research®,* 392**,** 196-207.

Bergmann, G, Bender, A, Graichen, F, Dymke, J, Rohlmann, A, Trepczynski, A, Heller, MO & Kutzner, I 2014. Standardized loads acting in knee implants. *PloS one,* 9**,** e86035.

Bhimji, S & Meneghini, RM 2012. Micromotion of cementless tibial baseplates under physiological loading conditions. *The Journal of Arthroplasty,* 27**,** 648-654.

Bhimji, S & Meneghini, RM 2014. Micromotion of cementless tibial baseplates: keels with adjuvant pegs offer more stability than pegs alone. *The Journal of arthroplasty,* 29**,** 1503-1506.

Bishop, NE, Hohn, JC, Rothstock, S, Damm, NB & Morlock, MM 2014. The influence of bone damage on press-fit mechanics. *J Biomech,* 47**,** 1472-8.

Bloebaum, RD, Bachus, KN, Mitchell, W, Hoffman, G & Hofmann, AA 1994. Analysis of the bone surface area in resected tibia: Implications in tibial component subsidence and fixation. *Clinical Orthopaedics and Related Research (1976-2007),* 309**,** 2-10.

Bosshardt, DD, Chappuis, V & Buser, D 2017. Osseointegration of titanium, titanium alloy and zirconia dental implants: current knowledge and open questions. *Periodontology 2000,* 73**,** 22-40.

Bosshardt, DD, Salvi, GE, Huynh-Ba, G, Ivanovski, S, Donos, N & Lang, NP 2011. The role of bone debris in early healing adjacent to hydrophilic and hydrophobic implant surfaces in man. *Clinical Oral Implants Research,* 22**,** 357-364.

Bottlang, M, Erne, OK, Lacatusu, E, Sommers, MB & Kessler, O 2006. A mobile-bearing knee prosthesis can reduce strain at the proximal tibia. *Clinical Orthopaedics and Related Research®,* 447.

Boulanaache, Y, Becce, F, Farron, A, Pioletti, DP & Terrier, A 2020. Glenoid bone strain after anatomical total shoulder arthroplasty: In vitro measurements with micro-CT and digital volume correlation. *Medical Engineering & Physics,* 85**,** 48-54.

Brånemark, R, Öhrnell, L-O, Nilsson, P & Thomsen, P 1997. Biomechanical characterization of osseointegration during healing: an experimental in vivo study in the rat. *Biomaterials,* 18**,** 969-978.

Buljac, A, Jailin, C, Mendoza, A, Neggers, J, Taillandier-Thomas, T, Bouterf, A, Smaniotto, B, Hild, F & Roux, S 2018. Digital volume correlation: review of progress and challenges. *Experimental Mechanics,* 58**,** 661-708.

Burgers, T, Mason, J, Squire, M & Ploeg, H-L 2010. Time-dependent fixation and implantation forces for a femoral knee component—An in vitro study. *Medical engineering & physics,* 32, 968-973.

Camine, VM, Rüdiger, H, Pioletti, D & Terrier, A 2016. Full-field measurement of micromotion around a cementless femoral stem using micro-CT imaging and radiopaque markers. *Journal of biomechanics,* 49**,** 4002-4008.

Camine, VM, Rüdiger, HA, Pioletti, DP & Terrier, A 2018. Effect of a collar on subsidence and local micromotion of cementless femoral stems: in vitro comparative study based on micro-computerised tomography. *International orthopaedics,* 42**,** 49-57.

Campi, S, Mellon, SJ, Ridley, D, Foulke, B, Dodd, CAF, Pandit, HG & Murray, DW 2018. Optimal interference of the tibial component of the cementless Oxford Unicompartmental Knee Replacement. *Bone & Joint Research,* 7**,** 226-231.

Capozza, RF, Feldman, S, Mortarino, P, Reina, PS, Schiessl, H, Rittweger, J, Ferretti, JL & Cointry, GR 2010. Structural analysis of the human tibia by tomographic (pQCT) serial scans. *Journal of Anatomy,* 216**,** 470-481.

Carlsson, L, Röstlund, T, Albrektsson, B & Albrektsson, T 1988. Implant fixation improved by close fit cylindrical implant–bone interface studied in rabbits. *Acta Orthopaedica Scandinavica,* 59**,** 272-275.

Castrodad, IMD, Recai, TM, Abraham, MM, Etcheson, JI, Mohamed, NS, Edalatpour, A & Delanois, RE 2019. Rehabilitation protocols following total knee arthroplasty: a review of study designs and outcome measures. *Annals of translational medicine,* 7.

Chong, DY, Hansen, UN, Van der Venne, R, Verdonschot, N & Amis, AA 2011. The influence of tibial component fixation techniques on resorption of supporting bone stock after total knee replacement. *Journal of Biomechanics,* 44**,** 948-954.

Chong, DYR, Hansen, UN & Amis, AA 2010. Analysis of bone–prosthesis interface micromotion for cementless tibial prosthesis fixation and the influence of loading conditions. *Journal of Biomechanics,* 43**,** 1074-1080.

Choy, W-S, Yang, D-S, Lee, K-W, Lee, S-K, Kim, K-J & Chang, S-H 2014. Cemented versus cementless fixation of a tibial component in LCS mobile-bearing total knee arthroplasty performed by a single surgeon. *The Journal of arthroplasty,* 29**,** 2397-2401.

Ciarelli, M, Goldstein, S, Kuhn, J, Cody, D & Brown, M 1991. Evaluation of orthogonal mechanical properties and density of human trabecular bone from the major metaphyseal regions with materials testing and computed tomography. *Journal of Orthopaedic Research,* 9**,** 674-682.

Comini, F, Palanca, M, Cristofolini, L & Dall'Ara, E 2019. Uncertainties of synchrotron microCT-based digital volume correlation bone strain measurements under simulated deformation. *Journal of Biomechanics,* 86**,** 232-237.

Completo, A, Fonseca, F & Simões, JA 2007. Finite element and experimental cortex strains of the intact and implanted tibia. *Journal of Biomechanical Engineering,* 129**,** 791-797.

Completo, A, Fonseca, F & Simões, JA 2008. Strain shielding in proximal tibia of stemmed knee prosthesis: Experimental study. *Journal of Biomechanics,* 41**,** 560-566.

Costa, MC, Tozzi, G, Cristofolini, L, Danesi, V, Viceconti, M & Dall'Ara, E 2017. Micro finite element models of the vertebral body: validation of local displacement predictions. *PloS one,* 12**,** e0180151.

Cowin, SC 2001. *Bone mechanics handbook*, CRC press.

Cristofolini, L, Cappello, A & Toni, A 1994. Experimental errors in the application of photoelastic coatings on human femurs with uncemented hip stems. *Strain,* 30**,** 95-104.

Cristofolini, L, Conti, G, Juszczyk, M, Cremonini, S, Sint Jan, SV & Viceconti, M 2010a. Structural behaviour and strain distribution of the long bones of the human lower limbs. *Journal of Biomechanics,* 43**,** 826-835.

Cristofolini, L, Schileo, E, Juszczyk, M, Taddei, F, Martelli, S & Viceconti, M 2010b. Mechanical testing of bones: the positive synergy of finite–element models and in vitro experiments. *Philosophical Transactions of the Royal Society A: Mathematical, Physical and Engineering Sciences,* 368**,** 2725-2763.

Cristofolini, L & Viceconti, M 2000. Mechanical validation of whole bone composite tibia models. *Journal of Biomechanics,* 33**,** 279-288.

Croom, B, Burden, D, Jin, H, Vonk, N, Hoefnagels, J, Smaniotto, B, Hild, F, Quintana, E, Sun, Q & Nie, X 2020. Interlaboratory study of digital volume correlation error due to X-Ray computed tomography equipment and scan parameters: an update from the DVC challenge. *Experimental Mechanics***,** 1-16.

Culley, J. 2022. *Unicompartmental knee replacement* [Online]. Available: https://www.medicalstockimages.net/collections/surgery/products/knee-replacement-unicompartmental [Accessed September 2023].

Curtis, M, Jinnah, R, Wilson, V & Hungerford, D 1992. The initial stability of uncemented acetabular components. *The Journal of bone and joint surgery. British volume,* 74**,** 372-376.

Dall'Ara, E, Barber, D & Viceconti, M 2014. About the inevitable compromise between spatial resolution and accuracy of strain measurement for bone tissue: A 3D zero-strain study. *Journal of Biomechanics,* 47**,** 2956-2963.

Dall'Ara, E, Peña-Fernández, M, Palanca, M, Giorgi, M, Cristofolini, L & Tozzi, G 2017. Precision of digital volume correlation approaches for strain analysis in bone imaged with micro-Computed Tomography at different dimensional levels. *Frontiers in Materials,* 4.

Dall'Ara, E & Tozzi, G 2022. Digital volume correlation for the characterization of musculoskeletal tissues: Current challenges and future developments. *Frontiers in Bioengineering and Biotechnology,* 10.

Dalton, JE, Cook, SD, Thomas, KA & Kay, JF 1995. The effect of operative fit and hydroxyapatite coating on the mechanical and biological response to porous implants. *JBJS,* 77.

Dalury, D 2016. Cementless total knee arthroplasty: current concepts review. *The bone & joint journal,* 98**,** 867-873.

Damm, NB, Morlock, MM & Bishop, NE 2015. Friction coefficient and effective interference at the implant-bone interface. *Journal of biomechanics,* 48**,** 3517-3521.

Damm, NB, Morlock, MM & Bishop, NE 2017. Influence of trabecular bone quality and implantation direction on press-fit mechanics. *Journal of Orthopaedic Research,* 35**,** 224-233.

Danesi, V, Tozzi, G & Cristofolini, L 2016. Application of digital volume correlation to study the efficacy of prophylactic vertebral augmentation. *Clinical Biomechanics,* 39**,** 14-24.

Dawson, J & Bartel, D 1992. Consequences of an interference fit on the fixation of porous-coated tibial components in total knee replacement. *JBJS,* 74**,** 233-238.

Delgadillo, LE, Jones, HL, Ismaily, SK, Han, S & Noble, PC 2020. How flat is the tibial osteotomy in total knee arthroplasty? *The Journal of Arthroplasty,* 35**,** 870-876.

Den Buijs, JO & Dragomir-Daescu, D 2011. Validated finite element models of the proximal femur using two-dimensional projected geometry and bone density. *Computer methods and programs in biomedicine,* 104**,** 168-174.

DePuy Synthes 2016. ATTUNE Knee System: Surgical Technique Featuring the ATTUNE Fixed Bearing Porous Knee. *In:* Orthopaedics, D (ed.). Warsaw, USA.

DePuy Synthes. 08 June 2023. *RE: RE: Attune Affixium Nominal Interference.* Type to Wearne, LS.

Dreyer, MJ, Trepczynski, A, Nasab, SHH, Kutzner, I, Schütz, P, Weisse, B, Dymke, J, Postolka, B, Moewis, P & Bergmann, G 2022. European Society of Biomechanics SM Perren Award 2022: Standardized tibio-femoral implant loads and kinematics. *Journal of Biomechanics,* 141**,** 111171.

Du, J, Lee, J-H, Jang, AT, Gu, A, Hossaini-Zadeh, M, Prevost, R, Curtis, DA & Ho, SP 2015. Biomechanics and strain mapping in bone as related to immediately-loaded dental implants. *Journal of biomechanics,* 48**,** 3486-3494.

du Plessis, A, Broeckhoven, C, Guelpa, A & le Roux, SG 2017. Laboratory x-ray micro-computed tomography: a user guideline for biological samples. *GigaScience,* 6.

Duan, X & Huang, J 2022. Deep learning-based digital volume correlation. *Extreme Mechanics Letters,* 53**,** 101710.

Eggermont, F, Verdonschot, N, van der Linden, Y & Tanck, E 2019. Calibration with or without phantom for fracture risk prediction in cancer patients with femoral bone metastases using CT-based finite element models. *PLoS One,* 14**,** e0220564.

Engh, CA, O'connor, D, Jasty, M, McGovern, TF, Bobyn, JD & Harris, WH 1992. Quantification of implant micromotion, strain shielding, and bone resorption with porous-coated anatomic medullary locking femoral prostheses. *Clinical orthopaedics and related research***,** 13-29.

Feldkamp, LA, Davis, LC & Kress, JW 1984. Practical cone-beam algorithm. *Journal of the Optical Society of America A,* 1**,** 612-619.

Finlay, JB, Bourne, RB & McLean, J 1982. A technique for the in vitro measurement of principal strains in the human tibia. *Journal of Biomechanics,* 15**,** 723-739.

Fitzpatrick, CK, Clary, CW, Cyr, AJ, Maletsky, LP & Rullkoetter, PJ 2013. Mechanics of post-cam engagement during simulated dynamic activity. *Journal of Orthopaedic Research,* 31**,** 1438-1446.

Fitzpatrick, CK, Clary, CW & Rullkoetter, PJ 2012. The role of patient, surgical, and implant design variation in total knee replacement performance. *Journal of Biomechanics,* 45**,** 2092-2102.

Fitzpatrick, CK, Hemelaar, P & Taylor, M 2014a. Computationally efficient prediction of bone–implant interface micromotion of a cementless tibial tray during gait. *Journal of Biomechanics,* 47**,** 1718-1726.

Fitzpatrick, CK, Komistek, RD & Rullkoetter, PJ 2014b. Developing simulations to reproduce in vivo fluoroscopy kinematics in total knee replacement patients. *Journal of biomechanics,* 47**,** 2398-2405.

Fitzpatrick, CK & Rullkoetter, PJ 2014. Estimating total knee replacement joint load ratios from kinematics. *Journal of Biomechanics,* 47**,** 3003-3011.

Freeman, MAR & Pinskerova, V 2005. The movement of the normal tibio-femoral joint. *Journal of Biomechanics,* 38**,** 197-208.

Frost, HM 1987. The mechanostat: a proposed pathogenic mechanism of osteoporoses and the bone mass effects of mechanical and nonmechanical agents. *Bone Miner,* 2**,** 73-85.

Fukuoka, S, Yoshida, K & Yamano, Y 2000. Estimation of the migration of tibial components in total knee arthroplasty: a Roentgen stereophotogrammetric analysis. *The Journal of Bone and Joint Surgery. British volume,* 82**,** 222-227.

Galloway, F, Kahnt, M, Ramm, H, Worsley, P, Zachow, S, Nair, P & Taylor, M 2013. A large scale finite element study of a cementless osseointegrated tibial tray. *Journal of Biomechanics,* 46**,** 1900-1906.

Gao, X, Fraulob, M & Haïat, G 2019. Biomechanical behaviours of the bone–implant interface: a review. *Journal of the Royal Society Interface,* 16**,** 20190259.

Gebert, A, Peters, J, Bishop, NE, Westphal, F & Morlock, MM 2009. Influence of press-fit parameters on the primary stability of uncemented femoral resurfacing implants. *Medical Engineering & Physics,* 31**,** 160-164.

Gillard, F, Boardman, R, Mavrogordato, M, Hollis, D, Sinclair, I, Pierron, F & Browne, M 2014. The application of digital volume correlation (DVC) to study the microstructural behaviour of trabecular bone during compression. *Journal of the Mechanical Behavior of Biomedical Materials,* 29**,** 480-499.

Glisson, RR, Musgrave, DS, Graham, RD & Vail, TP 2000. Validity of Photoelastic Strain Measurement on Cadaveric Proximal Femora. *Journal of Biomechanical Engineering,* 122**,** 423-429.

Gortchacow, M, Wettstein, M, Pioletti, DP & Terrier, A 2011. A new technique to measure micromotion distribution around a cementless femoral stem. *Journal of Biomechanics,* 44**,** 557-560.

Grassi, L & Isaksson, H 2015. Extracting accurate strain measurements in bone mechanics: A critical review of current methods. *Journal of the Mechanical Behavior of Biomedical Materials,* 50**,** 43-54.

Gray, HA, Taddei, F, Zavatsky, AB, Cristofolini, L & Gill, HS 2008. Experimental Validation of a Finite Element Model of a Human Cadaveric Tibia. *Journal of Biomechanical Engineering,* 130.

Green, GV, Berend, KR, Berend, ME, Glisson, RR & Vail, TP 2002. The effects of varus tibial alignment on proximal tibial surface strain in total knee arthroplasty: the posteromedial hot spot. *The Journal of arthroplasty,* 17**,** 1033-1039.

Haddad, FS & Plastow, R 2020. Is it time to revisit cementless total knee arthroplasty? *The bone & joint journal,* 102**,** 965-966.

Han, S, Patel, RV, Ismaily, SK, Jones, HL, Gold, JE & Noble, PC 2020. Micromotion and migration of cementless tibial trays under functional loading conditions. *The Journal of Arthroplasty*.

Hara, T, Tanck, E, Homminga, J & Huiskes, R 2002. The influence of microcomputed tomography threshold variations on the assessment of structural and mechanical trabecular bone properties. *Bone,* 31**,** 107-109.

Harada, Y, Wevers, H & Cooke, T 1988. Distribution of bone strength in the proximal tibia. *The Journal of arthroplasty,* 3**,** 167-175.

Hasan, S, van Hamersveld, KT, Marang-van de Mheen, PJ, Kaptein, BL, Nelissen, RG & Toksvig-Larsen, S 2020. Migration of a novel 3D-printed cementless versus a cemented total knee arthroplasty: two-year results of a randomized controlled trial using radiostereometric analysis. *The bone & joint journal,* 102**,** 1016-1024.

Hashemi, A & Shirazi-Adl, A 2000. Finite element analysis of tibial implants—effect of fixation design and friction model. *Computer Methods in Biomechanics and Biomedical Engineering,* 3**,** 183-201.

Helgason, B, Gilchrist, S, Ariza, O, Chak, J, Zheng, G, Widmer, R, Ferguson, S, Guy, P & Cripton, PA 2014. Development of a balanced experimental–computational approach to understanding the mechanics of proximal femur fractures. *Medical engineering & physics,* 36**,** 793-799.

Helgason, B, Perilli, E, Schileo, E, Taddei, F, Brynjolfsson, S & Viceconti, M 2008. Mathematical relationships between bone density and mechanical properties: a literature review. *Clin Biomech (Bristol, Avon),* 23**,** 135-46.

Hendee, WR & Ritenour, ER 2003. *Medical Imaging Physics,* New York, John Wiley & Sons, Inc.

Hildebrand, T & Rüegsegger, P 1997. A new method for the model-independent assessment of thickness in three-dimensional images. *Journal of Microscopy,* 185**,** 67-75.

Hsu, R, Himeno, S, Coventry, MB & Chao, EY 1990. Normal axial alignment of the lower extremity and load-bearing distribution at the knee. *Clinical Orthopaedics and Related Research (1976-2007),* 255**,** 215-227.

Hubbell, J & Seltzer, S 1996. NIST standard reference database 126. *Gaithersburg, MD: National Institute of Standards and Technology*.

Huiskes, R 1993. Failed innovation in total hip replacement: diagnosis and proposals for a cure. *Acta Orthopaedica Scandinavica,* 64**,** 699-716.

Hussein, AI, Barbone, PE & Morgan, EF 2012. Digital volume correlation for study of the mechanics of whole bones. *Procedia IUTAM,* 4**,** 116-125.

Hvid, I 1988. Mechanical strength of trabecular bone at the knee. *Dan Med Bull,* 35**,** 345-65.

Hvid, I & Hansen, SL 1985. Trabecular bone strength patterns at the proximal tibial epiphysis. *J Orthop Res,* 3**,** 464-72.

Inacio, MCS, Paxton, EW, Graves, SE, Namba, RS & Nemes, S 2017. Projected increase in total knee arthroplasty in the United States – an alternative projection model. *Osteoarthritis and Cartilage,* 25**,** 1797-1803.

Innocenti, B, Truyens, E, Labey, L, Wong, P, Victor, J & Bellemans, J 2009. Can medio-lateral baseplate position and load sharing induce asymptomatic local bone resorption of the proximal tibia? A finite element study. *Journal of orthopaedic surgery and research,* 4**,** 26-26.

Jackman, TM, Hussein, AI, Curtiss, C, Fein, PM, Camp, A, De Barros, L & Morgan, EF 2016. Quantitative, 3D visualization of the initiation and progression of vertebral fractures under compression and anterior flexion. *Journal of Bone and Mineral Research,* 31**,** 777-788.

Jepsen, KJ, DDavy, DT & Akkus, O 2009. Observations of Damage in Bone. *In:* Cowin, SC (ed.) *Bone Mechanics Handbook.* 2 ed. New York: Informa Healthcare.

Karbowski, A, Schwitalle, M, Eckardt, A & Heine, J 1999. Periprosthetic bone remodelling after total knee arthroplasty: early assessment by dual energy X-ray absorptiometry. *Archives of orthopaedic and trauma surgery,* 119**,** 324-326.

Keaveny, TM 2001. Strength of Trabecular Bone. *In:* Cowin, SC (ed.) *Bone Mechanics Handbook.* second ed. Boca Raton: CRC Press.

Keaveny, TM, Morgan, EF, Niebur, GL & Yeh, OC 2001. Biomechanics of trabecular bone. *Annual review of biomedical engineering,* 3**,** 307-333.

Keaveny, TM, Wachtel, EF, Ford, CM & Hayes, WC 1994. Differences between the tensile and compressive strengths of bovine tibial trabecular bone depend on modulus. *Journal of biomechanics,* 27**,** 1137-1146.

Kelly, N, Cawley, D, Shannon, F & McGarry, JP 2013. An investigation of the inelastic behaviour of trabecular bone during the press-fit implantation of a tibial component in total knee arthroplasty. *Medical engineering & physics,* 35**,** 1599-1606.

Kessler, O, Lacatusu, E, Sommers, MB, Mayr, E & Bottlang, M 2006. Malrotation in total knee arthroplasty: effect on tibial cortex strain captured by laser-based strain acquisition. *Clinical Biomechanics,* 21**,** 603-609.

Kohli, N, Stoddart, JC & van Arkel, RJ 2021. The limit of tolerable micromotion for implant osseointegration: a systematic review. *Scientific Reports,* 11**,** 1-11.

Koster, LA, Rassir, R, Kaptein, BL, Sierevelt, IN, Schager, M, Nelissen, RGHH & Nolte, PA 2023. A randomized controlled trial comparing two-year postoperative femoral and tibial migration of a new and an established cementless rotating platform total knee arthroplasty. *The Bone & Joint Journal,* 105-B**,** 148-157.

Kraemer, WJ, Harrington, IJ & Hearn, TC 1995. Micromotion secondary to axial, torsional, and shear loads in two models of cementless tibial components. *The Journal of Arthroplasty,* 10**,** 227-235.

Kurtz, SM, Lau, E, Ong, K, Zhao, K, Kelly, M & Bozic, KJ 2009. Future young patient demand for primary and revision joint replacement: National projections from 2010 to 2030. *Clinical Orthopaedics and Related Research®,* 467**,** 2606-2612.

Kusins, J, Knowles, N, Ryan, M, Dall'Ara, E & Ferreira, L 2019. Performance of QCT-Derived scapula finite element models in predicting local displacements using digital volume correlation. *Journal of the Mechanical Behavior of Biomedical Materials,* 97**,** 339-345.

Kusins, J, Knowles, N, Targosinski, J, Columbus, M, Athwal, GS & Ferreira, L 2022. 3D strain analysis of trabecular bone within the osteoarthritic humeral head subjected to stepwise compressive loads. *Journal of the Mechanical Behavior of Biomedical Materials,* 125**,** 104922.

Kutzner, I, Heinlein, B, Graichen, F, Bender, A, Rohlmann, A, Halder, A, Beier, A & Bergmann, G 2010. Loading of the knee joint during activities of daily living measured in vivo in five subjects. *Journal of Biomechanics,* 43**,** 2164-2173.

Kuzyk, PR & Schemitsch, EH 2011. The basic science of peri-implant bone healing. *Indian journal of orthopaedics,* 45**,** 108-115.

Laende, EK, Astephen Wilson, JL, Mills Flemming, J, Valstar, ER, Richardson, CG & Dunbar, MJ 2019. Equivalent 2-year stabilization of uncemented tibial component migration despite higher early migration compared with cemented fixation: an RSA study on 360 total knee arthroplasties. *Acta orthopaedica,* 90**,** 172-178.

LaVision 2017. Digital Volume Correlation: Product-Manual (Item-Number(s): 1105020). *In:* Anna-Vandenhoeck-Ring (ed.). Gottingen, Germany.

Le Cann, S, Tudisco, E, Perdikouri, C, Belfrage, O, Kaestner, A, Hall, S, Tägil, M & Isaksson, H 2017. Characterization of the bone-metal implant interface by Digital Volume Correlation of in-situ loading using neutron tomography. *Journal of the Mechanical Behavior of Biomedical Materials,* 75**,** 271-278.

Le Cann, S, Tudisco, E, Tägil, M, Hall, SA & Isaksson, H 2020. Bone damage evolution around integrated metal screws using X-Ray Tomography—in situ pullout and digital volume correlation. *Frontiers in Bioengineering and Biotechnology,* 8**,** 934.

Lee, C-S, Lee, J-M, Youn, B, Kim, H-S, Shin, JK, Goh, TS & Lee, JS 2017. A new constitutive model for simulation of softening, plateau, and densification phenomena for trabecular bone under compression. *Journal of the mechanical behavior of biomedical materials,* 65**,** 213-223.

Lee, RW, Volz, RG & Sheridan, DC 1991. The role of fixation and bone quality on the mechanical stability of tibial knee components. *Clin. Orthop. Rel. Res.***,** 177-183.

Lewis, RA 2005. Medical applications of synchrotron radiation in Australia. *Nuclear Instruments and Methods in Physics Research Section A: Accelerators, Spectrometers, Detectors and Associated Equipment,* 548**,** 23-29.

Li, H, Zhang, H, Tang, Z & Hu, G 2008. Micro-computed tomography for small animal imaging: Technological details. *Progress in natural science,* 18**,** 513-521.

Li, JY, Pow, EHN, Zheng, LW, Ma, L, Kwong, DLW & Cheung, LK 2014. Quantitative analysis of titanium-induced artifacts and correlated factors during micro-CT scanning. *Clinical oral implants research,* 25**,** 506-510.

Li, MG & Nilsson, KG 2000. The effect of the preoperative bone quality on the fixation of the tibial component in total knee arthroplasty. *The Journal of Arthroplasty,* 15**,** 744-753.

Linde, F, Nørgaard, P, Hvid, I, Odgaard, A & Søballe, K 1991. Mechanical properties of trabecular bone. Dependency on strain rate. *Journal of Biomechanics,* 24**,** 803-809.

Liu, L & Morgan, EF 2007. Accuracy and precision of digital volume correlation in quantifying displacements and strains in trabecular bone. *Journal of biomechanics,* 40**,** 3516-3520.

Loeser, RF, Goldring, SR, Scanzello, CR & Goldring, MB 2012. Osteoarthritis: a disease of the joint as an organ. *Arthritis and rheumatism,* 64**,** 1697.

Martelli, S, Giorgi, M, Dall' Ara, E & Perilli, E 2021. Damage tolerance and toughness of elderly human femora. *Acta Biomaterialia,* 123**,** 167-177.

Martelli, S & Perilli, E 2018. Time-elapsed synchrotron-light microstructural imaging of femoral neck fracture. *Journal of the Mechanical Behavior of Biomedical Materials,* 84**,** 265-272.

Marter, A, Burson-Thomas, C, Dickinson, A, Rankin, K, Mavrogordato, M, Pierron, F & Browne, M 2020. Measurement of internal implantation strains in analogue bone using DVC. *Materials,* 13**,** 4050.

Martin, RB & Sharkey, NA 2001. Mechanical effects of postmortem changes, preservation, and allograft bone treatments. *Bone Mechanics Handbook, Second Edition***,** 20-1-20-24.

Mathieu, V, Vayron, R, Richard, G, Lambert, G, Naili, S, Meningaud, J-P & Haiat, G 2014. Biomechanical determinants of the stability of dental implants: Influence of the bone–implant interface properties. *Journal of biomechanics,* 47**,** 3-13.

Meneghini, RM, Daluga, A & Soliman, M 2011. Mechanical stability of cementless tibial components in normal and osteoporotic bone. *The journal of knee surgery,* 24**,** 191-196.

Meric, G, Gracitelli, GC, Aram, LJ, Swank, ML & Bugbee, WD 2015. Variability in distal femoral anatomy in patients undergoing total knee arthroplasty: Measurements on 13,546 computed tomography scans. *J Arthroplasty,* 30**,** 1835-8.

Miller, MA, Terbush, MJ, Goodheart, JR, Izant, TH & Mann, KA 2014. Increased initial cement–bone interlock correlates with reduced total knee arthroplasty micro-motion following in vivo service. *Journal of Biomechanics,* 47**,** 2460-2466.

Mistry, JB, Elmallah, RD, Bhave, A, Chughtai, M, Cherian, JJ, McGinn, T, Harwin, SF & Mont, MA 2016. Rehabilitative guidelines after total knee arthroplasty: a review. *The journal of knee surgery***,** 201-217.

Mittra, E, Rubin, C, Gruber, B & Qin, Y-X 2008. Evaluation of trabecular mechanical and microstructural properties in human calcaneal bone of advanced age using mechanical testing, μCT, and DXA. *Journal of Biomechanics,* 41**,** 368-375.

Miura, H, Whiteside, LA, Easley, JC & Amador, DD 1990. Effects of screws and a sleeve on initial fixation in uncemented total knee tibial components. *Clinical Orthopaedics and Related Research®,* 259**,** 160-168.

Monti, L, Cristofolini, L, Toni, A & Ceroni, RG 2001a. In vitro testing of the primary stability of the VerSys enhanced taper stem: A comparative study in intact and intraoperatively cracked femora. *Proceedings of the Institution of Mechanical Engineers, Part H: Journal of Engineering in Medicine,* 215**,** 75-83.

Monti, L, Cristofolini, L & Viceconti, M 1999. Methods for quantitative analysis of the primary stability in uncemented hip prostheses. *Artificial organs,* 23**,** 851-859.

Monti, L, Cristofolini, L & Viceconti, M 2001b. Interface biomechanics of the Anca Dual Fit hip stem: An in vitro experimental study. *Proceedings of the Institution of Mechanical Engineers, Part H: Journal of Engineering in Medicine,* 215**,** 555-564.

Morgan, EF, Bayraktar, HH & Keaveny, TM 2003. Trabecular bone modulus–density relationships depend on anatomic site. *Journal of Biomechanics,* 36**,** 897-904.

Morgan, EF & Keaveny, TM 2001. Dependence of yield strain of human trabecular bone on anatomical site. *Journal of Biomechanics,* 34**,** 569-577.

Morgan, EF, Unnikrisnan, GU & Hussein, AI 2018. Bone mechanical properties in healthy and diseased states. *Annual review of biomedical engineering,* 20**,** 119-143.

Mueller, TL, Basler, SE, Müller, R & van Lenthe, GH 2013. Time-lapsed imaging of implant fixation failure in human femoral heads. *Medical Engineering & Physics,* 35**,** 636-643.

Mys, K, Varga, P, Gueorguiev, B, Hemmatian, H, Stockmans, F & van Lenthe, GH 2019. Correlation between cone-beam computed tomography and high-resolution peripheral computed tomography for assessment of wrist bone microstructure. *Journal of Bone and Mineral Research,* 34**,** 867-874.

Navacchia, A, Clary, CW, Wilson, HL, Behnam, YA & Rullkoetter, PJ 2018. Validation of model-predicted tibial tray-synthetic bone relative motion in cementless total knee replacement during activities of daily living. *Journal of Biomechanics,* 77**,** 115-123.

Nelissen, RGHH, Valstar, ER & Rozing, PM 1998. The effect of hydroxyapatite on the micromotion of total knee prostheses. A prospective, randomized, double-blind study*. *JBJS,* 80.

Nikon Metrology, I 2018. X-Tek X-ray and CT Inspection: Inspect-X 5.3 - 3D Computed Tomography (CT) Operator Manual. Geldenaaksebaan, Leuven, Belgium: Nikon Meterology.

Nikon Metrology, I. 2020. *XT H 225 for all-purpose X-ray and CT inspection* [Online]. Available: https://www.nikonmetrology.com/en-us/product/xt-h-225 [Accessed December 2020].

Norman, TL, Ackerman, E, Smith, T, Gruen, T, Yates, A, Blaha, J & Kish, V 2006. Cortical bone viscoelasticity and fixation strength of press-fit femoral stems: an in-vitro model.

Odgaard, A 1997. Three-dimensional methods for quantification of cancellous bone architecture. *Bone,* 20**,** 315-328.

Oliviero, S, Giorgi, M & Dall'Ara, E 2018. Validation of finite element models of the mouse tibia using digital volume correlation. *Journal of the Mechanical Behavior of Biomedical Materials,* 86**,** 172-184.

Pal, B & Gupta, S 2020. The relevance of biomechanical analysis in joint replacements: A review. *Journal of The Institution of Engineers (India): Series C,* 101**,** 913-927.

Palanca, M, Cristofolini, L, Dall'Ara, E, Curto, M, Innocente, F, Danesi, V & Tozzi, G 2016a. Digital volume correlation can be used to estimate local strains in natural and augmented vertebrae: An organ-level study. *Journal of biomechanics,* 49**,** 3882-3890.

Palanca, M, De Donno, G & Dall'Ara, E 2021. A novel approach to evaluate the effects of artificial bone focal lesion on the three-dimensional strain distributions within the vertebral body. *Plos one,* 16**,** e0251873.

Palanca, M, Tozzi, G & Cristofolini, L 2016b. The use of digital image correlation in the biomechanical area: a review. *International biomechanics,* 3**,** 1-21.

Parfitt, AM, Drezner, MK, Glorieux, FH, Kanis, JA, Malluche, H, Meunier, PJ, Ott, SM & Recker, RR 1987. Bone histomorphometry: standardization of nomenclature, symbols, and units: report of the ASBMR Histomorphometry Nomenclature Committee. *Journal of bone and mineral research,* 2**,** 595-610.

Parratte, S, Pagnano, MW, Trousdale, RT & Berry, DJ 2010. Effect of postoperative mechanical axis alignment on the fifteen-year survival of modern, cemented total knee replacements. *JBJS,* 92.

Paschos, NK & Prodromas, CC 2019. Knee. *In:* Paschos, NKB, George (ed.) *General Orthopaedics and Basic Science.* 1 ed. Switzerland: Cham: Springer International Publishing.

Peña Fernández, M, Cipiccia, S, Dall'Ara, E, Bodey, AJ, Parwani, R, Pani, M, Blunn, GW, Barber, AH & Tozzi, G 2018. Effect of SR-microCT radiation on the mechanical integrity of trabecular bone using in situ mechanical testing and digital volume correlation. *Journal of the Mechanical Behavior of Biomedical Materials,* 88**,** 109-119.

Perilli, E, Baleani, M, Öhman, C, Fognani, R, Baruffaldi, F & Viceconti, M 2008. Dependence of mechanical compressive strength on local variations in microarchitecture in cancellous bone of proximal human femur. *Journal of biomechanics,* 41**,** 438-446.

Perilli, E, Baruffaldi, F, Bisil, MC, Cristofolini, L & Cappello, A 2006. A physical phantom for the calibration of three-dimensional X-ray mircotomograpohy examination. *Journal of Microscopy,* 22**,** 124-134.

Perilli, E, Briggs, AM, Kantor, S, Codrington, J, Wark, JD, Parkinson, IH & Fazzalari, NL 2012. Failure strength of human vertebrae: prediction using bone mineral density measured by DXA and bone volume by micro-CT. *Bone,* 50**,** 1416-1425.

Perillo-Marcone, A, Barrett, D & Taylor, M 2000. The importance of tibial alignment: finite element analysis of tibial malalignment. *The Journal of arthroplasty,* 15**,** 1020-1027.

Perillo-Marcone, A, Ryd, L, Johnsson, K & Taylor, M 2004. A combined RSA and FE study of the implanted proximal tibia: correlation of the post-operative mechanical environment with implant migration. *Journal of Biomechanics,* 37**,** 1205-1213.

Perillo-Marcone, A & Taylor, M 2007. Effect of varus/valgus malalignment on bone strains in the proximal tibia after TKR: an explicit finite element study.

Pijls, BG, Plevier, JW & Nelissen, RG 2018. RSA migration of total knee replacements: a systematic review and meta-analysis. *Acta orthopaedica,* 89**,** 320-328.

Pijls, BG, Valstar, ER, Nouta, K-A, Plevier, JW, Fiocco, M, Middeldorp, S & Nelissen, RG 2012. Early migration of tibial components is associated with late revision: a systematic review and meta-analysis of 21,000 knee arthroplasties. *Acta orthopaedica,* 83**,** 614-624.

Pilliar, RM, Lee, JM & Maniatopoulos, C 1986. Observations on the effect of movement on bone ingrowth into porous-surfaced implants. *Clinical orthopaedics and related research***,** 108-113.

Prendergast, PJ 2001. Bone Prostheses and Implants. *In:* Cowin, SC (ed.) *Bone Mechanics Handbook.* 2 ed. Washington, D.C.: CRC Press.

Purcell, RL, Baral, EC, Slaven, SE, Wright, TM & Westrich, GH 2022. Bone ongrowth of contemporary cementless tibial components: a retrieval analysis. *Arthroplasty Today,* 13**,** 149-153.

Quevedo González, FJ, Lipman, JD, Lo, D, De Martino, I, Sculco, PK, Sculco, TP, Catani, F & Wright, TM 2019. Mechanical performance of cementless total knee replacements: It is not all about the maximum loads. *Journal of Orthopaedic Research®,* 37**,** 350-357.

Quevedo González, FJ, Sculco, PK, Kahlenberg, CA, Mayman, DJ, Lipman, JD, Wright, TM & Vigdorchik, JM 2023. Undersizing the Tibial Baseplate in Cementless Total Knee Arthroplasty

has Only a Small Impact on Bone-Implant Interaction: A Finite Element Biomechanical Study. *The Journal of Arthroplasty,* 38**,** 757-762.

Rao, AS, Engh, JA, Engh, GA & Parks, NL 2010. Mechanical Stability of Well-Functioning Tibial Baseplates From Postmortem-Retrieved Total Knee Arthroplasties. *The Journal of Arthroplasty,* 25**,** 481-485.

Rapagna, S, Berahmani, S, Wyers, CE, van den Bergh, JPW, Reynolds, KJ, Tozzi, G, Janssen, D & Perilli, E 2019. Quantification of human bone microarchitecture damage in press-fit femoral knee implantation using HR-pQCT and digital volume correlation. *J Mech Behav Biomed Mater,* 97**,** 278-287.

Rapagna, S, Roberts, BC, Solomon, LB, Reynolds, KJ, Thewlis, D & Perilli, E 2021. Tibial cartilage, subchondral bone plate and trabecular bone microarchitecture in varus-and valgus-osteoarthritis versus controls. *Journal of Orthopaedic Research®,* 39**,** 1988-1999.

Rapagna, S, Roberts, BC, Solomon, LB, Reynolds, KJ, Thewlis, D & Perilli, E 2022. Relationships between tibial articular cartilage, in vivo external joint moments and static alignment in end-stage knee osteoarthritis: A micro-CT study. *Journal of Orthopaedic Research®,* 40**,** 1125-1134.

Rawson, SD, Maksimcuka, J, Withers, PJ & Cartmell, SH 2020. X-ray computed tomography in life sciences. *BMC biology,* 18**,** 1-15.

Restrepo, S, Smith, EB & Hozack, WJ 2021. Excellent mid-term follow-up for a new 3D-printed cementless total knee arthroplasty. *The Bone & Joint Journal,* 103**,** 32-37.

Roberts, BC, Perilli, E & Reynolds, KJ 2014. Application of the digital volume correlation technique for the measurement of displacement and strain fields in bone: a literature review. *J Biomech,* 47**,** 923-34.

Roberts, BC, Solomon, LB, Mercer, G, Reynolds, KJ, Thewlis, D & Perilli, E 2018. Relationships between in vivo dynamic knee joint loading, static alignment and tibial subchondral bone microarchitecture in end-stage knee osteoarthritis. *Osteoarthritis Cartilage,* 26**,** 547-556.

Roberts, BC, Thewlis, D, Solomon, LB, Mercer, G, Reynolds, KJ & Perilli, E 2017. Systematic mapping of the subchondral bone 3D microarchitecture in the human tibial plateau: Variations with joint alignment. *Journal of Orthopaedic Research,* 35**,** 1927-1941.

Rueckel, J, Stockmar, M, Pfeiffer, F & Herzen, J 2014. Spatial resolution characterization of a X-ray microCT system. *Applied Radiation and Isotopes,* 94**,** 230-234.

Ryd, L, Albrektsson, B, Carlsson, L, Dansgard, F, Herberts, P, Lindstrand, A, Regner, L & Toksvig-Larsen, S 1995. Roentgen stereophotogrammetric analysis as a predictor of mechanical loosening of knee prostheses. *The Journal of bone and joint surgery. British volume,* 77**,** 377-383.

Ryd, L, Hansson, U, Blunn, G, Lindstrand, A & Toksvig-Larsen, S 1999. Failure of partial cementation to achieve implant stability and bone ingrowth: A long-term Roentgen stereophotogrammetric study of tibial components. *Journal of Orthopaedic Research,* 17**,** 311-20.

Sala, M, Taylor, M & Tanner, KE 1999. Torsional stability of primary total knee replacement tibial prostheses: A biomechanical study in cadaveric bone. *The Journal of Arthroplasty,* 14**,** 610-615.

Sánchez, E, Schilling, C, Grupp, TM, Giurea, A, Verdonschot, N & Janssen, D 2021. No effect in primary stability after increasing interference fit in cementless TKA tibial components. *Journal of the Mechanical Behavior of Biomedical Materials,* 118**,** 104435.

Sanyal, A, Gupta, A, Bayraktar, HH, Kwon, RY & Keaveny, TM 2012. Shear strength behavior of human trabecular bone. *J Biomech,* 45**,** 2513-9.

Saxby, DJ, Modenese, L, Bryant, AL, Gerus, P, Killen, B, Fortin, K, Wrigley, TV, Bennell, KL, Cicuttini, FM & Lloyd, DG 2016. Tibiofemoral contact forces during walking, running and sidestepping. *Gait & Posture,* 49**,** 78-85.

Scanco Medical. 2023. *XtremeCT II* [Online]. Switzerland: SCANCO Medical AG. Available: https://www.scanco.ch/xtremectii.html [Accessed 11 2023].

Sharkey, PF, Hozack, WJ, Rothman, RH, Shastri, S & Jacoby, SM 2002. Why are total knee arthroplasties failing today? *Clinical Orthopaedics and Related Research®,* 404**,** 7-13.

Small, S, Rogge, R, Malinzak, R, Reyes, E, Cook, P, Farley, K & Ritter, M 2016. Micromotion at the tibial plateau in primary and revision total knee arthroplasty: fixed versus rotating platform designs. *Bone & joint research,* 5**,** 122-129.

Small, SR, Berend, ME, Ritter, MA & Buckley, CA 2010. A comparison in proximal tibial strain between metal-backed and all-polyethylene anatomic graduated component total knee arthroplasty tibial components. *The Journal of Arthroplasty,* 25**,** 820-825.

Small, SR, Berend, ME, Ritter, MA, Buckley, CA & Rogge, RD 2011. Metal Backing Significantly Decreases Tibial Strains in a Medial Unicompartmental Knee Arthroplasty Model. *The Journal of Arthroplasty,* 26**,** 777-782.

Søballe, K, Brockstedt-Rasmussen, H, Hansen, ES & Bünger, C 1992. Hydroxyapatite coating modifies implant membrane formation. *Acta Orthopaedica Scandinavica,* 63**,** 128-140.

Soltanihafshejani, N, Bitter, T, Janssen, D & Verdonschot, N 2021. Development of a crushable foam model for human trabecular bone. *Medical engineering & physics,* 96**,** 53-63.

Soltanihafshejani, N, Peroni, F, Toniutti, S, Bitter, T, Tanck, E, Eggermont, F, Verdonschot, N & Janssen, D 2023. The application of an isotropic crushable foam model to predict the femoral fracture risk. *Plos one,* 18**,** e0288776.

Steiner, JA, Ferguson, SJ & van Lenthe, GH 2015. Computational analysis of primary implant stability in trabecular bone. *Journal of Biomechanics,* 48**,** 807-815.

Stern, SH, Wills, RD & Gilbert, JL 1997. The effect of tibial stem design on component micromotion in knee arthroplasty. *Clinical orthopaedics and related research***,** 44-52.

Stock, SR 2009. *Microcomputed tomography: methodology and applications*, CRC press.

Sukjamsri, C, Geraldes, DM, Gregory, T, Ahmed, F, Hollis, D, Schenk, S, Amis, A, Emery, R & Hansen, U 2015. Digital volume correlation and micro-CT: an in-vitro technique for measuring full-field interface micromotion around polyethylene implants. *Journal of biomechanics,* 48**,** 3447-3454.

Sumner, DR, Kienapfel, H, Jacobs, JJ, Urban, RM, Turner, TM & Galante, JO 1995. Bone ingrowth and wear debris in well-fixed cementless porous-coated tibial components removed from patients. *The Journal of Arthroplasty,* 10**,** 157-167.

Takechi, H 1977. Trabecular architecture of the knee joint. *Acta Orthopaedica Scandinavica,* 48**,** 673-681.

Taylor, M, Barrett, DS & Deffenbaugh, D 2012. Influence of loading and activity on the primary stability of cementless tibial trays. *Journal of Orthopaedic Research,* 30**,** 1362-1368.

Taylor, M & Prendergast, PJ 2015. Four decades of finite element analysis of orthopaedic devices: Where are we now and what are the opportunities? *Journal of Biomechanics,* 48**,** 767-778.

Taylor, M & Tanner, K 1997. Fatigue failure of cancellous bone: a possible cause of implant migration and loosening. *The Journal of Bone and Joint Surgery. British volume,* 79**,** 181-182.

Taylor, M, Tanner, KE & Freeman, MAR 1998. Finite element analysis of the implanted proximal tibia: a relationship between the initial cancellous bone stresses and implant migration. *Journal of Biomechanics,* 31**,** 303-310.

Toksvig-Larsen, S & Ryd, L 1991. Surface flatness after bone cutting: A cadaver study of tibial condyles. *Acta Orthopaedica Scandinavica,* 62**,** 15-18.

Toksvig-Larsen, S & Ryd, L 1994. Surface characteristics following tibial preparation during total knee arthroplasty. *The Journal of arthroplasty,* 9**,** 63-66.

Tozzi, G, Dall'Ara, E, Palanca, M, Curto, M, Innocente, F & Cristofolini, L 2017. Strain uncertainties from two digital volume correlation approaches in prophylactically augmented vertebrae: local analysis on bone and cement-bone microstructures. *Journal of the mechanical behavior of biomedical materials,* 67**,** 117-126.

Tozzi, G, Danesi, V, Palanca, M & Cristofolini, L 2016. Elastic full-field strain analysis and microdamage progression in the vertebral body from digital volume correlation. *Strain,* 52**,** 446-455.

Turunen, MJ, Le Cann, S, Tudisco, E, Lovric, G, Patera, A, Hall, SA & Isaksson, H 2020. Sub-trabecular strain evolution in human trabecular bone. *Scientific reports,* 10**,** 1-14.

Ulrich, D, Hildebrand, T, Van Rietbergen, B, Müller, R & Rüegsegger, P 1997. The quality of trabecular bone evaluated with micro-computed tomography, FEA and mechanical testing. *Stud Health Technol Inform,* 40**,** 97-112.

Valmalle, M, Vintache, A, Smaniotto, B, Gutmann, F, Spagnuolo, M, Ciallella, A & Hild, F 2022. Local–global DVC analyses confirm theoretical predictions for deformation and damage onset in torsion of pantographic metamaterial. *Mechanics of Materials,* 172**,** 104379.

Van Valkenburg, SM, Werner, FW, Bhimji, S, White, BF & Asseman, FB 2016. Assessment of physiological load testing of total knee implants. *Journal of Testing and Evaluation,* 44**,** 258-267.

Viceconti, M, Brusi, G, Pancanti, A & Cristofolini, L 2006. Primary stability of an anatomical cementless hip stem: A statistical analysis. *Journal of Biomechanics,* 39**,** 1169-1179.

Viceconti, M, Monti, L, Muccini, R, Bernakiewicz, M & Toni, A 2001. Even a thin layer of soft tissue may compromise the primary stability of cementless hip stems. *Clinical Biomechanics,* 16**,** 765-775.

Viceconti, M, Muccini, R, Bernakiewicz, M, Baleani, M & Cristofolini, L 2000. Large-sliding contact elements accurately predict levels of bone–implant micromotion relevant to osseointegration. *Journal of Biomechanics,* 33**,** 1611-1618.

Viceconti, M, Olsen, S, Nolte, L-P & Burton, K 2005. Extracting clinically relevant data from finite element simulations. *Clinical Biomechanics,* 20**,** 451-454.

Waygate Technologies. 2023. *Pheonix V|tome|x L 300* [Online]. Baker Hughes Company. Available: https://www.bakerhughes.com/waygate-technologies/industrial-radiography-and-ct/industrial-3d-precision-metrology-ct/phoenix-vtomex-l300 [Accessed 13/09/2023 2023].

Wazen, RM, Currey, JA, Guo, H, Brunski, JB, Helms, JA & Nanci, A 2013. Micromotion-induced strain fields influence early stages of repair at bone–implant interfaces. *Acta Biomaterialia,* 9**,** 6663-6674.

Wearne, LS, Rapagna, S, Taylor, M & Perilli, E 2022. Micro-CT scan optimisation for mechanical loading of tibia with titanium tibial tray: A digital volume correlation zero strain error analysis. *Journal of the Mechanical Behavior of Biomedical Materials,* 134**,** 105336.

Wearne LS, Rapagna S, Awadalla M, Keene G, Taylor M, Perilli E (2024). Quantifying the immediate post-implantation strain field of cadaveric tibiae implanted with cementless tibial trays: A time-elapsed micro-CT and digital volume correlation analysis during stair descent. *Journal of the Mechanical Behavior of Biomedical Materials*, 151: 106347.

Wennerberg, A & Albrektsson, T 2009. Effects of titanium surface topography on bone integration: a systematic review. *Clinical Oral Implants Research,* 20**,** 172-184.

Werner, FW, Ayers, DC, Maletsky, LP & Rullkoetter, PJ 2005. The effect of valgus/varus malalignment on load distribution in total knee replacements. *Journal of biomechanics,* 38**,** 349-355.

Whitehouse, W 1974. The quantitative morphology of anisotropic trabecular bone. *Journal of microscopy,* 101**,** 153-168.

Winsor, C, Li, X, Qasim, M, Henak, CR, Pickhardt, PJ, Ploeg, H & Viceconti, M 2021. Evaluation of patient tissue selection methods for deriving equivalent density calibration for femoral bone quantitative CT analyses. *Bone,* 143**,** 115759.

Yang, H, Bayoglu, R, Clary, CW & Rullkoetter, PJ Impact of patient, surgical, and implant design factors on predicted tray-bone interface micromotions in cementless total knee arthroplasty. *Journal of Orthopaedic Research,* n/a.

Yang, H, Bayoglu, R, Clary, CW & Rullkoetter, PJ 2021. Impact of surgical alignment, tray material, PCL condition, and patient anatomy on tibial strains after TKA. *Medical Engineering & Physics,* 88**,** 69-77.

Yang, H, Bayoglu, R, Renani, MS, Behnam, Y, Navacchia, A, Clary, C & Rullkoetter, PJ 2020. Validation and sensitivity of model-predicted proximal tibial displacement and tray micromotion in cementless total knee arthroplasty under physiological loading conditions. *Journal of the Mechanical Behavior of Biomedical Materials,* 109**,** 103793.

Zeiss. 2023. Germany: Carl Zeiss Microscopy GmbH, . Available: https://www.zeiss.com/microscopy/en/products/x-ray-microscopy/xradia-versa.html#Versa_510 [Accessed 13/09/2023 2023].

Zhou, K, Yu, H, Li, J, Wang, H, Zhou, Z & Pei, F 2018. No difference in implant survivorship and clinical outcomes between full-cementless and full-cemented fixation in primary total knee arthroplasty: A systematic review and meta-analysis. *International Journal of Surgery,* 53**,** 312-319.

Zhou, Y, Gong, C, Hossaini-Zadeh, M & Du, J 2020a. 3D full-field strain in bone-implant and bone-tooth constructs and their morphological influential factors. *journal of the mechanical behavior of biomedical materials,* 110**,** 103858.

Zhou, Y, Gong, C, Lewis, GS, Armstrong, AD & Du, J 2020b. 3D full-field biomechanical testing of a glenoid before and after implant placement. *Extreme Mechanics Letters,* 35**,** 100614.